Design and Performance Evaluation of a Rotary Flow Control Valve for Independent Metering Hydraulics

The thesis submitted in partial fulfilment of the requirements of
Bournemouth University for the degree of
Doctor of Philosophy in Mechanical Engineering

Ivan Okhotnikov

Department of Design and Engineering at
Bournemouth University in collaboration with
Hydreco Hydraulics Ltd.

May, 2018

Copyright Statement

Abstract

Off road heavy machinery is the second largest contributor to air pollution in terms of the levels of fossil fuel consumption after road cars. This is partly attributed to inefficient power hydraulic systems used to drive these machines' tools or instruments. A relatively recent idea of an independent metering technology has become a major topics in improving efficiency, reducing fuel consumption and saving energy. Current research and development of independent metering applied to fluid power systems enables energy recuperation capabilities of hydraulics. However, actual industrial implementation cases are still rare, especially in application requiring high flow rates.

Flow control valves are used in flow regulation and controlling of hydraulic actuators' speed. The speed control occurs through throttling, which causes large power losses. Moreover, the substantial flow forces acting on the throttling parts of the valve in high flow rate regimes has resulted in the application of sophisticated multi-staged servo valves. An alternative one-stage design can resolve these issues, but such proposals and studies are still scarce in the literature.

This research looks at new design ideas as the means to improve hydraulic valve performance and efficiency. The novelty is also to enable single staged valves to be used in high flow rate applications. The main approach is to simplify and perform a complete redesign of the valve geometrical structure to replace the existing spool and seat valve configuration.

The novel design proposed in this thesis is based on a rotary tubular structure, which is less bulky and much lighter. The focus of this investigation has been on the study of the flow characteristics and fluid structure interaction of the new valve's moving parts using a combination of theoretical, simulation-based and experimental studies. A prototype of the final design was manufactured and tested to validate the simulated data. Test results provided a good experimental validation of analytical and numerical models employed in this investigation.

Detailed analysis of the performance of the new suggested valve proved its viability as a strong candidate to replace the existing in-efficient industry standard spool and seat valves. The metering characteristics of the new valve has demonstrated that alternatively designed one-staged flow control valves can create smaller pressure drops, hence, consume less power than the industry standard benchmark.

The thesis presents the research, investigation and detailed analysis of a novel unconventional valve design suitable for the independent metering architecture. This research demonstrates the feasibility of the independent metering architecture for use in high flow rates applications. This research further consolidates the position of this new valve can have within the fluid power industry, further expands its range of application paving the way for industry adoption to replace old valves with a new and more efficient valve system.

Acknowledgements

I would firstly like to thank my academic supervisors at Bournemouth University, Professor Siamak Noroozi and Dr Philip Sewell, for their invaluable support, thorough guidance and patience over the course of the project.

Secondly, I would like to express gratitude to Hydreco Hydraulics Ltd. for match-funding this project alongside Bournemouth University. In particular, I would like to recognise the assistance provided by Philip Godfrey and John Ineson in designing, developing and especially testing of the rotary valve. Without their industrial insights, advice on best practice, helpful suggestions and experience, this project simply would not have been possible.

Finally, none of this would have been possible without the support of my family and friends. I am grateful for their patience and constant encouragement throughout the project.

Contents

Copyright Statement **i**

Abstract **iii**

Acknowledgements **iv**

Contents **viii**

List of Figures **xi**

List of Tables **xii**

Nomenclature **xiii**

1 Introduction **1**

1.1 Motivation . . . 1
1.2 Background . . . 3
1.3 Hypothesis . . . 4
1.4 Objectives . . . 4
1.5 Contributions . . . 5
1.6 Limitations . . . 6

2 Literature Review **7**

2.1 Valve Control . . . 7
2.1.1 Open Centre Systems . . . 8
2.1.2 Constant Pressure System . . . 9
2.1.3 Load Sensing . . . 9
2.2 Valveless Control . . . 10
2.2.1 Displacement Control . . . 11
2.2.2 Secondary Control . . . 12
2.3 Digital Hydraulics . . . 12
2.3.1 Digital Valve Systems . . . 12
2.3.2 Digital Hydraulic Machines . . . 13
2.4 Independent Metering . . . 13
2.4.1 Definition . . . 13
2.4.2 Concept Development . . . 14
2.4.3 IM Circuits . . . 15
2.4.4 IM Valves . . . 16
2.5 Spool Valves . . . 17
2.5.1 Rotary Valves . . . 19
2.6 Knowledge Gaps . . . 20

3 Methodology **23**

3.1 Mechanical Design Process . . . 23
3.1.1 Product Definition . . . 23
3.1.2 Conceptual Design . . . 25
3.1.3 Design Development . . . 26
3.2 Initial Valve Design . . . 28
3.2.1 Single Valve . . . 28
Orifice Area . . . 31
Dimensioning . . . 32
Actuation . . . 35
3.2.2 Four-Valves Assembly . . . 37
Check Valves . . . 39
3.3 Chapter Conclusions . . . 39

4 Fluid Mechanics Modelling **40**
4.1 Preprocessing . . . 40
4.1.1 Geometric Model . . . 41
4.1.2 Turbulence Model . . . 41
Wall Function . . . 42
4.1.3 Mesh . . . 43
Grid Independence . . . 44
4.1.4 Boundary Conditions . . . 45
Fluid Model . . . 46
4.1.5 Goals . . . 46
4.2 Postprocessing . . . 48
4.2.1 Outflow . . . 48
4.2.2 Volume Flow Rate . . . 51
Discharge Coefficient . . . 52
4.2.3 Reynolds Number . . . 53
4.2.4 Pressure Losses . . . 54
Temperature Rise . . . 55
4.2.5 Steady Flow Torque . . . 56
4.2.6 Jet Angles . . . 61
Graphical Estimation . . . 61
4.3 Cavitation . . . 63
4.4 “Closed-State” Leakage . . . 65
4.5 Chapter Conclusions . . . 67

5 Solid Mechanics Modelling **69**
5.1 Preprocessing . . . 69
5.1.1 Geometric Model . . . 70
5.1.2 Stress-Strain Model . . . 70
5.1.3 Mesh . . . 71
Grid Independence . . . 72
5.1.4 Boundary Conditions . . . 74
Material Model . . . 74
Loads . . . 74
Fixtures . . . 75
5.2 Postprocessing . . . 75
5.2.1 Spool Strength . . . 76
Steady Flow Torque Effect . . . 76
Pressurized Oil Effect . . . 76

Combined Effect . . . 78
5.2.2 Prototype Assembly Strength . . . 78
Factor of Safety . . . 80
5.3 Chapter Conclusions . . . 81

6 Experiments **82**
6.1 Prototype Valve . . . 82
6.1.1 Original Parts . . . 82
6.1.2 "Off-the-shelf" Parts . . . 83
Stepper Motor . . . 83
Accessories . . . 84
6.1.3 Standard Parts . . . 84
6.1.4 Assembly . . . 84
6.2 Data Acquisition System . . . 85
6.2.1 Hydraulic Test Rig . . . 86
6.2.2 Instrumentation . . . 87
6.3 Test Procedure . . . 88
6.4 Test Results . . . 88
6.4.1 Volume Flow Rate . . . 89
6.4.2 Pressure Losses . . . 90
6.4.3 Leakage . . . 90
Internal Leakage . . . 91
"Closed-State" Leakage . . . 91
6.5 Correlations with Modelling . . . 92
6.5.1 Corrected Model . . . 93
6.6 Chapter Conclusions . . . 95

7 Concept Refinement **96**
7.1 Redesign . . . 96
7.1.1 Separator . . . 96
7.1.2 Collecting Channel . . . 97
Sleeve . . . 98
Body . . . 98
7.1.3 Results . . . 98
7.2 Influence of the Orifice Shape . . . 101
7.2.1 Orifice Area . . . 101
7.2.2 Pressure Losses . . . 103
7.2.3 Results . . . 104
7.3 Benchmark . . . 104
7.4 Chapter Conclusions . . . 105

8 Conclusions **106**
8.1 Discussion . . . 106
8.2 Conclusions . . . 107
8.3 Contribution to Knowledge . . . 108
8.4 Future Work . . . 108

References **110**

Appendices **119**

A Drawings of the Prototype **120**

B Prototype Assembly Scheme **131**

C Stepper Motor Specification **133**

D Mathematical Model of the Valve **138**

E Data Analysis Code **143**

F Published Article **146**

List of Figures

1.1 Petroleum consumption in the US, (Fichmann 2012). 1
1.2 Petroleum consumption in the US by the industrial sector, (Fichmann 2012). . . . 2
1.3 Petroleum consumption in the US by the transportation sector, (Fichmann 2012). 2
1.4 Examples of NRMM 2
1.5 The general block-scheme of a fluid power system. 3

2.1 Open centre system. 8
2.2 Constant pressure system. 8
2.3 A hydraulic scheme with pressure rails. 9
2.4 Load sensing system. 10
2.5 Displacement control system. 11
2.6 Digital hydraulics control system. 12
2.7 A scheme of digital displacement machine. 13
2.8 Independent metering system. 14
2.9 Number of studies related to IM for the last three decades. 15
2.10 The IM circuits classification 16
2.11 The Eaton's Ultronics™ 17
2.12 The open centre spool control valve (Bosch Rexroth 2016). 18
2.13 Examples of the tubular-spool valves. 21

3.1 The mechanical design process, (Ullman 2009). 23
3.2 The main phases of the mechanical design process followed in the thesis, (Ullman 2009). 24
3.3 Suggested concepts. 25
3.4 The adopted concept. 26
3.5 Single valve design development. 27
3.6 Four-valves assembly design development. 27
3.7 The hydraulic symbol of the valve. 28
3.8 The throttling parts and the outflow scheme. 29
3.9 The extreme states of the valve 29
3.10 Location and area measurement of the single orifice 30
3.11 Projection plane and orifice profile projection. 31
3.12 Total orifice area function, $A(\phi)$. 32
3.13 Total perimeter of throttling orifices, $S(\phi)$. 32
3.14 The cutaway section of the single valve 33
3.15 The main dimensions of the throttling parts. 35
3.16 The hydraulic mounting surface. 36
3.17 The hydraulic scheme of the four valves assembly. 37
3.18 The four valve assembly block. 38

4.1 The fluid domain of the single valve. 43

4.2 The mesh . . . 43
4.3 Grid independence study results . . . 44
4.4 The location of the boundary openings . . . 45
4.5 Viscosity $\nu(T)$, $\mu(T)$ and density $\rho(T)$ functions . . . 46
4.6 Spool metering surfaces . . . 47
4.7 The planes for analysis. . . . 48
4.8 The velocity field distributions . . . 49
4.9 Turbulence intensity in the flow region. . . . 50
4.10 Volume flow rate $Q(\phi)$ . . . 51
4.11 Discharge coefficient $C_d(\phi)$ . . . 51
4.12 Volume flow rate $Q(\Delta p)$ . . . 52
4.13 Volume flow rate function $Q(\phi, \Delta p)$ . . . 53
4.14 Reynolds number function $\mathrm{Re}(\Delta p, \phi)$ . . . 54
4.15 Pressure losses $p_{loss}(Q)$ . . . 54
4.16 Power losses $P_{loss}(Q)$ . . . 55
4.17 Fluid temperature function $T_{gl.}(\phi, \Delta p)$ . . . 56
4.18 The outflow scheme and steady flow torques . . . 57
4.19 Vector diagrams of steady flow torques formation. . . . 58
4.20 Opening and closing steady flow torques $T_{st.fl}(\phi)$ . . . 59
4.21 Total steady flow torque function $T_{st.fl}(\phi)$ . . . 60
4.22 Orifice steady flow torques $T_{st.fl.i}(\phi)$ . . . 60
4.23 Jet angles $\alpha_i(\phi)$ . . . 61
4.24 The graphical method . . . 62
4.25 Total steady flow torque function $T_{st.fl.}(\phi, \Delta p)$ . . . 63
4.26 Cavitation numbers σ . . . 64
4.27 Location of the leakage channels. . . . 65
4.28 The unfolded view on the leakage channels. . . . 65
4.29 Flow trajectories visualisation of the “closed-state” leakage . . . 67
4.30 The “closed-state” leakage function $Q_L(\Delta p)$ . . . 67
4.31 The percentage difference between the leakage estimation results . . . 67

5.1 The general geometric model . . . 70
5.2 The mounting surface on the bottom plane. . . . 70
5.3 Examples of a standard uniform mesh. . . . 71
5.4 Examples of a curved-based mesh. . . . 71
5.5 Simulation steps and results. Flow torque effect. . . . 72
5.6 Grid independence results. . . . 73
5.7 Effect of pressurized oil on the spool . . . 77
5.8 The deformed spool. . . . 78
5.9 Effect of the pressurized oil on the valve assembly. . . . 79
5.10 Results of the screws strength check. . . . 80

6.1 The main manufactured parts of the prototype valve . . . 83
6.2 Encoder operation scheme (Oriental Motors 2017). . . . 83
6.3 The model of the prototype valve assembly . . . 85
6.4 The block scheme of the data acquisition system. . . . 86
6.5 The scheme of the hydraulic test rig. . . . 86
6.6 The photos of the used hydraulic test rig. . . . 87
6.7 Experimental volume flow rate $Q_e(\phi)$ . . . 89
6.8 Percentage difference between simulated and tested volume flow rates . . . 89
6.9 Experimental pressure loss $p_{e.loss}$ . . . 90

6.10 Percentage difference between simulated and tested pressure drops 91
6.11 Internal leakage channels. 91
6.12 Experimental internal leakage volume flow rate $Q_{int.leak.}(\Delta p)$ 92
6.13 Internal leakage portion in the total volume flow rate at $\phi = 90°$. 92
6.14 Corrected geometric model and fluid sub domain. 93
6.15 Flow path in the corrected model 94
6.16 Correlation of study results for $\phi = 90°$. 94
6.17 Percentage difference between simulated and test results of the pressure drop . . . 95

7.1 The separator of the modified spool. 97
7.2 Redesign of the collecting channels. 98
7.3 The cross section of the modified valve. 99
7.4 The fluid domain of the modified valve. 99
7.5 The mesh of the modified valve 99
7.6 The velocity field distributions in the redesigned valve. 100
7.7 Pressure losses of the modified valve at $\phi =$ const. 101
7.8 Pressure drop reduction in the modified valve 101
7.9 Studied orifice shapes at the fully open state. 102
7.10 Total orifice area functions for different shapes. 102
7.11 Pressure losses for the circular ⌀13 mm orifice at $\phi =$ const. 103
7.12 Pressure losses for the triangular “tip-to-tip” orifice at $\phi =$ const. 103
7.13 Tecnord’s SJ-MRA rotary flow control valve, (Tecnord 2017). 104
7.14 Test data of the pressure drop of SJ-MRA (Tecnord 2017). 104
7.15 Throttling loss reduction in the initial and redesigned RTSV 105

8.1 Spool single opening geometry. 139

List of Tables

2.1 Eligible study criteria. 7

3.1 The main geometrical and mass parameters of the throttling mechanism. 35

4.1 The main physical properties of the fluid. 46
4.2 Preprocessing settings of the CFD model. 47
4.3 Geometric parameters of the leakage channels. 66

5.1 Mechanical properties of the AA 7075-T651. 74
5.2 Preprocessing setting of the solid model. 75

6.1 List of the original valve parts. 83
6.2 Key characteristics of the SM RKS5913, (Oriental Motors 2017). 84
6.3 List of standard parts. 85
6.4 Instrumentation. 88
6.5 Test plan. 89
6.6 Results of the “closed-state” leakage measurement. 92

Nomenclature

Latin symbols

a	Thermal expansion coefficient, K^{-1}
A	Area, mm^2
A_v	Van Driest coefficient
b_i	Seal width, mm
c	Gap clearance, mm
C_d	Discharge coefficient
$C_{\varepsilon 1}$, $C_{\varepsilon 2}$, C_μ, C_B	Closure coefficients in the $k-\varepsilon$ turbulence model
d, D	Diameter, mm
D_h	Hydraulic diameter, mm^2
e	Specific internal energy, $J\,kg^{-1}$
E	Elasticity modulus, GPa
$\hat{E}$	Effective elasticity modulus, GPa
f	Factor of safety
f_1, f_2, f_μ	Lam and Bremhost's damping functions in $k-\varepsilon$ turbulence model
F	Force, N
$g(\omega)$	Coulomb and Stribeck effect function
G	Shear modulus, GPa
h	Height of the tubular cylinder in the spool opening, mm
h_s	Specific enthalpy, $J\,kg^{-1}$
I	Moment of inertia, $kg\,mm^2$
k	Turbulent kinetic energy, $m^2\,s^{-2}$
K	Karman constant
l, L	Length, characteristic length, mm
m	Mass, kg
n	Number of the balancing grooves
N	Number of cells in a mesh
p	Pressure, MPa
P	Power, W
Pr	Prandtl number
q	Heat flux vector, $W\,m^{-2}$
Q	Volume flow rate, $l\,min^{-1}$
r, R	Radius, mm
Re	Reynolds number
S	Perimeter, mm
t	Time, s
T	Torque, N m
u_i	The i-th component of the fluid velocity vector, $m\,s^{-1}$
u^+	Dimensionless longitudinal velocity
v, V	Average, characteristic velocity, $m\,s^{-1}$
y	Distance from the wall surface, m

y^+	Dimensionless wall distance
x_i	The i-th component of the coordinate vector, m
w	Width of the balancing groove, mm
z	Average deflection of the asperities on two contacting surfaces, mm

Greek symbols

α	Jet angle,°
β	Minimum overlap angle,°
γ	Maximum overlap angle,°
δ_i	Displacement along i axis, µm
δ_{ij}	Kronecker function
ε	Turbulent dissipation rate, $\mathrm{m^2\,s^{-2}}$, strain
λ	Angle covering the spool opening, °
μ	Dynamics viscosity, Pa s
μ_t	Turbulent eddy viscosity coefficient
μ_w	Dry friction coefficient
ν	Kinematic viscosity, $\mathrm{m^2\,s^{-1}}$, Poisson ratio
ρ	Density, $\mathrm{kg\,m^{-3}}$
σ	Cavitation number, standard deviation
σ_i	Coefficients in the Lu-Gre friction model
σ_{ii}	Stresses, MPa
σ_k, σ_ε, σ_B	Closure coefficients in the $k-\varepsilon$ turbulence model
τ	Shear stress, MPa
τ_{ij}	Reynolds stress tensor, MPa
τ_w	Wall shear stress, MPa
ϕ	Spool angular position, °
ω	Angular velocity, $\mathrm{rad\,s^{-1}}$
ω_S	Stribeck characteristic angular velocity, $\mathrm{rad\,s^{-1}}$

Notation

$\dot{x}$	First time derivative of x
$\overrightarrow{x}$	Vector quantity
$\overline{x}$	Mean value of x

Acronyms

AA	Aluminum Alloy
AEM	Asynchronous Electric Motor
BOM	Bill of Materials
CFD	Computational Fluid Dynamics
CNC	Computer Numerical Controlled
CV	Control Volume
DAQ/DAS	Data Acquisition System
DC	Direct Current
DCV	Directional Control Valve
DFCU	Digital Flow Control Unit
DFX	Design for X (cost, manufacture, assembly, etc.)
DIMV	Digital Independent Metering Valve
EHPV	Electro-Hydraulic Poppet Valve
FEA	Finite Element Analysis
FM	Flow Meter
FOS	Factor of Safety
FSI	Fluid Structure Interaction
ICE	Internal Combustion Engine
IM	Independent Metering

LS	Load Sensing
NRMM	Non-Road Mobile Machinery
PLC	Programmable Logic Controller
PRV	Pressure Relief valve
PT	Pressure Transducer
RTSV	Rotary Tubular Spool Valve
SM	Stepper Motor
SW	SolidWorks
TT	Torque Transducer
UK	United Kingdom
US	United States
VAC	Volts of Alternating Current
VDC	Volts of Direct Current
VFD	Variable-Frequency Drive

Chapter 1

Introduction

This chapter reviews the background, scope and objectives of the research presented in the thesis. The need for reasonable natural resources consumption and its optimisation in the industrial sector are discussed. These represent the prerequisites to outline the scope of the thesis, to define the hypothesis and the objectives to be accomplished to answer the research question.

1.1 Motivation

Over the last half century, the transport and industrial sectors have remained the main consumers of petroleum and diesel in the UK, the US and worldwide. Not only these have kept the largest share in a demand for oil products, their portion has been growing in last decades both in the UK (Department for Business Energy & Industrial Strategy 2017) and the US (Fichmann 2012), see the Figures 1.1, 1.2 and 1.3. One of the largest end user of oil based fuels is the non-road mobile machinery (NRMM).

NRMM include a wide range of mobile working machines and transportable industrial equipment in which an internal combustion engine (ICE) is installed (European Parliament 2016). These are widely used in construction, agriculture, material handling, oil and gas, forestry and mining industries. Typical examples of these machines are backhoes, excavators, harvesters, tractors, cranes, container or log staggers, mine loaders, see the Figure 1.4.

Because of such omnipresence of mobile working machines, the energy consumed as well as emissions caused per year are immense. For instance, in the US in 2008 mobile hydraulics spent up to 1.3 quads (or 3.3 million tonnes of oil equivalent) and produced up to 92 million metric tonnes of CO_2 (Love et al. 2012).

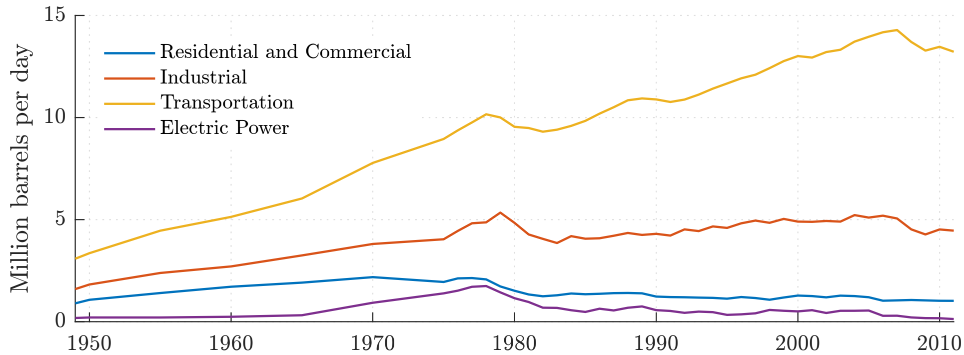

Figure 1.1: Petroleum consumption in the US, (Fichmann 2012).

NRMM are usually used to perform a specific function with an installed implement. The most common drive of these instruments is hydraulics. In fact, in the US the NRMM fluid power

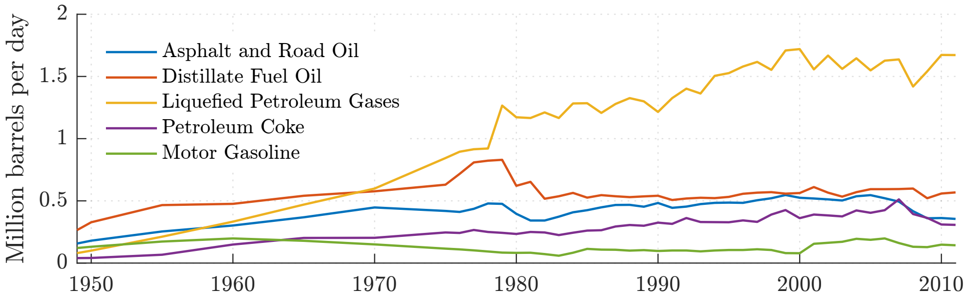

Figure 1.2: Petroleum consumption in the US by the industrial sector, (Fichmann 2012).

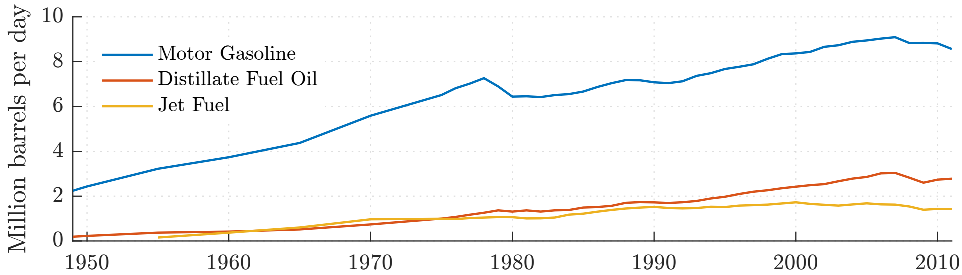

Figure 1.3: Petroleum consumption in the US by the transportation sector, (Fichmann 2012).

(a) Wheel loader. (b) Medium excavator. (c) Telehandler.

Figure 1.4: Examples of NRMM, (Caterpillar 2017).

hydraulics makes up around two thirds of hydraulic component units sold yearly. Among this type of hydraulics, construction and agriculture applications account for 75% (Lynch and Zigler 2017).

Fluid power offers a series of advantages unavailable to other drives, especially in applications requiring significant mechanical power output. Among the assets are high power density, reliability and a lower operating cost compared to competing technologies. Power hydraulics has a wide operating bandwidth. That enables fast starts, stops, and reversals. Working fluid in these systems performs power transmission, lubricating and heat averting functions (Merritt 1968). Moreover, due to the large bulk modulus of hydraulic mineral oil, fluid power is less sensitive to impact loads, provides natural damping and, thus, is more reliable than mechanical transmissions (Eriksson 2010). All these factors have made hydraulics indispensable for NRMM applications and ensured its dominance among power drive technologies.

However, fluid power possesses several drawbacks. Tight clearances between mechanical parts require extremely clean working fluid free from solid particles, dissolved gasses and air. It necessitates regular and strict supervision of the liquid's contamination level during an exploitation period. Other shortcomings are low flexibility and high non-linearity of hydraulic control relative to electromagnetic counterparts (Merritt 1968). Hydraulics is also prone to oil leakage through seals, mechanical contacts and connections (Burrows 2004), which can cause spillages and environmental pollution.

Despite their widespread use and substantial amounts of energy consumption and exhaust emissions of these machines, not much work has been undertaken to improve systems efficiency. The average efficiency of fluid powered systems is still around 22% (Love et al. 2012). Some estimates suggest in mobile hydraulics only ten per cent of the energy stored in the fuel is converted to mechanical power (Vukovic and Murrenhoff 2015). Thus, improving energy efficiency in the field of NRMM fluid power systems still remains one of the main areas of research in mechanical engineering.

Due to growing environmental concerns and tight legislation imposed on the permissible emissions levels produced by these machinaries (European Parliament 2016), the manufacturers are now required to develop more efficient and environmentally friendly systems meeting these regulations (Schneider et al. 2016).

1.2 Background

A fluid power system represents a set of interconnected devices and tools, see the Figure 1.5, designed to generate, control and transmit power by means of confined, pressurized liquid and thereby drive machines and mechanisms (Durfee and Sun 2009). It transfers power by converting it from mechanical to fluid form, and then back to mechanical one. The reason to employ fluid as a power transmitting medium is the convenience of energy transportation to a new location, as liquid bearing hoses or pipes can have complex and long routes passing around any physical obstacle. Hydraulic drives employ Pascal's principle that states that pressure exerted on an enclosed liquid volume is conveyed and distributed equally along all directions in it.

A diesel engine in NRMM provides a motive force for a vehicle as well as power for fluid actuated devices and other auxiliary systems. A fluid power system of such machines typically contains a single hydraulic power source that regulates multiple output implements through valves. A typical hydraulic architecture of a working machine consists of hydraulic power sources, i.e. pumps, hydraulic drivers, motors, and corresponding control valves.

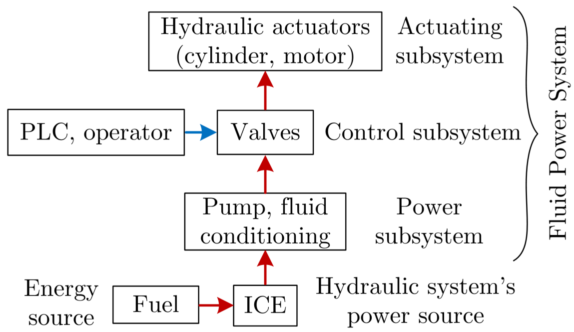

Figure 1.5: The general structural block-scheme of a fluid power system. The red arrows – power flow, the blue arrow – control signal.

One of the promising approaches to tackle economic and environmental challenges in hydraulics is to use alternative architectures and controls of fluid power systems as these contribute heavily to power losses in NRMM (Wang and Wang 2014). Attempts to reconsider hydraulic circuitries have led to development of several advanced fluid power transmission schematics and corresponding research trends (Murrenhoff et al. 2014).

In recent years, researchers of fluid power systems in mobile machines have shifted their focus on improvement of efficiency, controllability and miniaturisation of a hydraulic system as a whole rather than individual components (Vukovic and Murrenhoff 2015). This holistic approach has proved its viability, for efficiency of modern hydraulic components is relatively high, reaching 95% in the case of piston pumps. Normally, performance of hydraulic systems can be enhanced by minimising throttling losses, applying energy regeneration and recuperation schemes and avoiding inefficient operating regimes (Murrenhoff et al. 2014).

Another approach to increase efficiency of hydraulics architecturally is hybridisation that is implementation of energy storage by changing its nature. The most common way to implement it is to resort to electrical energy and use batteries as storing devices. This trend is gaining recognition as application cases are reported in hydraulics of industrial mobile transmission systems (Rydberg 2015).

Nevertheless, among different architectures of power hydraulics, the valve-controlled class is still dominant due to use of a single centralised fluid power source and, hence, their relative low cost and high reliability (Axin 2013). In these systems, a valve's opening causes controlled resistance to the fluid flow, which governs the speed of a hydraulic motor, an actuator. The position of the spool inside a valve body determines an extent, to which the throttling orifice is open, and the flow is "stifled". The opening area defines the amount of fluid passing through the valve per a unit of time or a volume flow rate. Finally, the speed of the actuator is directly proportional to the volume flow rate pumped to it through the valve.

The precise value of resistance imposed on the fluid flow depends predominantly on the geometry, or the exact design, of the valve's inner parts, which form flow passages. Internal galleries formed by the valve parts account for how intricate and complex the flow streamlines are, how many changes to a flow cross-section and its direction take place along a flow passage. Since the valve design plays such an important role in hydraulic efficiency, attempts to reconsider a structural design of directional control valves (DCVs) to improve their efficiency seem worthwhile.

Controlling an operation of a hydraulic actuator is conventionally accomplished using a single spool type proportional directional control valve per one hydraulic actuator (McCloy and Martin 1973), (Merritt 1968). The spool regulates simultaneously flows to and from the actuator by a single control signal – the spool position. Thus, the inlet and outlet flows are mechanically coupled (Shenouda 2006). This mechanical linkage of supply and exhaust orifices can cause cavitation on overrunning loads, extra throttling losses at the meter-out, which thereby adversely affects energy efficiency of an entire machine.

Thus, disengaging these orifices is a viable method improving a mechanical design for reduction of flow energy losses. Moreover, mechanical orifices decoupling opens an opportunity to recuperate potential energy of heavy loads. These considerations motivated inception of the independent metering (IM) concept.

Numerous studies investigated this concept and proved not only high energy saving potential of this architecture (Choi et al. 2015), (Chen and Zhao 2017), (Liu et al. 2016), but indicated benefits to smoother and more responsive control of an hydraulic actuator (Das et al. 2015), (Xu et al. 2015), (Ding et al. 2016). Furthermore, the failure tree analysis and estimation of failure probability per hour have shown that this system layout meets safety and reliability requirements to NRMM's hydraulics (Beck and Weber 2017).

1.3 Hypothesis

The purpose of this research is to propose and examine a way to improve the energy efficiency of a valve-controlled working fluid power system in mobile machinery. The method approach to achieve the stated aim and satisfy mentioned restraints is to propose a specific control valve design and its application as part of a hydraulic system.

It is hypothesised, that the new design of the flow control valve and the applied system architecture improve the energy efficiency of hydraulically driven implements in mobile construction machinery.

1.4 Objectives

The more specific purpose of the present investigation is to analyse the performance of the proposed valve, compare and verify its inferred characteristics with a reference, industry standard system commonly used in fluid power control. The objectives are then to assess basic efficiency, design and manufacturability properties of the proposed valve system through building the necessary models for simulations, models' validation according to the test results on prototypes. It is also desired to evaluate the performance of the suggested valve system during operation within a hydraulic system at realistic operating regimes.

The following objectives are to be accomplished to answer the hypothesis and fill identified knowledge gaps from the literature review:

1. Conduct a critical literature review of design concepts, configurations, architectures and performance of hydraulic control system. This is needed to analyse, select or propose an architectural concept in which the proposed control valve is intended to operate;
2. To propose an exact new design of a control valve with an alternative structure that exceeds the requirements of safe, smooth and fast operation of an output hydraulic actuator;
3. Performance characteristics of a suggested design solution should be identified and examined in the modelled environment. The characteristics' behaviour should be described mathematically by constructing an accurate mathematical model from first principles. The model is expected to account for as many physical phenomena occurring in the proposed valve system as possible. Simulation methodologies used in the development of fluid power systems and individual constituents should be investigated. The most appropriate modelling approaches should be chosen and vindicated;
4. The expected performance and final simulation models should be verified and validated experimentally. This can be done by comparing existing fluid power control systems and industry standards with the proposed system. Properties of interest are energy efficiency, leak-tightness, resistance to cavitation, durability qualities of the valve's most loaded parts and relative design simplicity. Available manufacturing methods and technologies used in the production of hydraulic components should be considered during the development of the three-dimensional geometrical model and working drawings of the valve. Manufacturability assessment of the proposed design of the flow control valve system should be conducted before production of prototypes.

1.5 Contributions

The novelty in the thesis consists in the following aspects. The research seeks an alternative to commonly used hydraulic control valves with the linearly sliding spools. The theory and utilisation of sliding spools have been firmly established over past decades. However, industry still lacks valve configurations based on unconventional approaches to design throttling parts and orifices.

Original and atypical design configurations of throttling surfaces of valve parts could potentially obviate deficiencies of the valve's throttling mechanism, which currently prevails the market, especially of high-flow rate hydraulic systems. The usual drawbacks here are structural complexity of servo- and multi-staged valves, issues with oscillatory dynamics and possible cavitation due to intricate channelling and mechanical coupling of the valve inlet and outlet flows. This research looks for design ways to expand operational regimes of a single-staged control valve to high-flow rates domains.

The second contribution to knowledge consists in the further development of the chosen advanced control architecture of IM. The concept development is realized through proposal of a valve assembly incorporating four two-way valves, which allows to use IM hydraulics in high-flow rate applications. Owing to advantages IM lends to power hydraulics, the concept has been drawing attention of researchers for a long time. It has resulted in exhaustive theoretical studies of its performance, as well as multiple practical validation examples. However, there is still a lack of studies aimed at design implementation of that approach in fluid power systems operating in high flow rate regimes. The undertaken research addresses this need and suggests a way to expand application of IM industrially. Further industrial expansion of the concept enables further research of IM characteristics for various machines and regimes of operation. Its promising features would allow significant reduction in fuel consumption of a working machine, extending its lifetime and shortening a work cycle.

Full implementation of IM combined with the new valve if adopted will have a significant impact on reduction of greenhouse gases emission and fuel consumption of these machinaries. While at the same time, it will extend the lifecycle of these systems due to decreasing of load intensities and stresses.

1.6 Limitations

The present research concerns only mobile working multi-axis hydraulic systems of a valve-controlled type. Vehicle fluid power systems of transmission, chassis, suspension and propulsion applications, as well as stationary hydraulic equipment of industrial plants, as presses, metalworking machines and clamping tools, are not investigated in the thesis.

Systems, which are based on engine- or displacement-controlled schemes, are not considered in the dissertation except in a literature review in the following chapter. Digital hydraulics concept, as well as the application of magneto- and electrorheological working fluids, is not included in the proposed design solution of the control valve.

The thesis is also limited to mechanical design ways to improve the efficiency of the hydraulic valve and system design. It does not include the development of a controller, its design and an electrical control circuitry. Serial manufacturing, marketing prospects are not considered. The research investigates valve's durability characteristics and a mathematical model for a dynamic behaviour study as complementary studies.

Chapter 2

Literature Review

To meet the first research objective of the thesis, in this chapter the state of the art of fluid power systems and appropriate technologies are identified and reviewed. The chapter also addresses the second objective inspecting designs and structures of valves, which are commonly applied in industry, as well as new, unconventional design proposals. The review allows for informed design choices to be made in development of an alternative valve design.

Generally, working fluid power systems of mobile machines can be divided based on the actuators' control principle on resistive, or throttling, and displacement regulated. In this classification, there are two main groups of systems, which differ according to the presence of a DCV as the main actuator' speed regulating unit.

The review of literature on the subject starts with search, selection, critical analysis of published academic articles, patents, manufacturers' catalogues. Three databases were searched: patent database Espacenet, Science Direct and Web of Science. The advanced search strategy was employed in all three sources using keywords. Exact set of keywords varied depending on the search topic. For instance, the retrieved articles on independent metering included a combination of following terms in a body or a title of a study: "independent" or "decoupled" in conjunction with either "metering", "valve", "control system", "hydraulic" or "fluid power". Within the found selection of articles the eligibility filter was applied, see the Table 2.1.

Section	Criteria
Language	Studies published in English
Publication type	Peer-reviewed journal articles of primary research, manufacturers catalogues, excluding literature reviews, letters to the editor, commentaries and the like
Publication date	Database inception: prior September 2017

Table 2.1: Eligible study criteria.

2.1 Valve Control

The presence of a valve, which modulates the output force and velocity of the hydraulic actuator, remains the main design feature of the state of the art power hydraulic systems due to robustness and relatively low cost of such solution (Axin 2015).

Flow- and pressure-regulating valves enable a link between the source of hydraulic power and its consumers making it possible to implement the complex logic of actuators operation and working cycles. Great repairability distinguishes valve-controlled systems from valveless. It takes much less effort and cost to replace faulty valve parts or an entire valve without special tools even in field conditions.

Valve controlled systems is the subject of studies and design improvements, which are primarily being done by manufacturers. Current ubiquity of this type of systems on the market makes introduction of new ideas less resource- and time-demanding than launching a radically new technology. Often, to confirm feasibility of novel designs, few replacements of components or modifications are sufficient leaving the main hydraulics intact.

The common trait of valve-controlled systems is prevalence of throttling losses due to a resistive nature of flow regulation. Excessive fluid power in this type of flow control is dissipated in a form of heat since the flow is being restrained.

2.1.1 Open Centre Systems

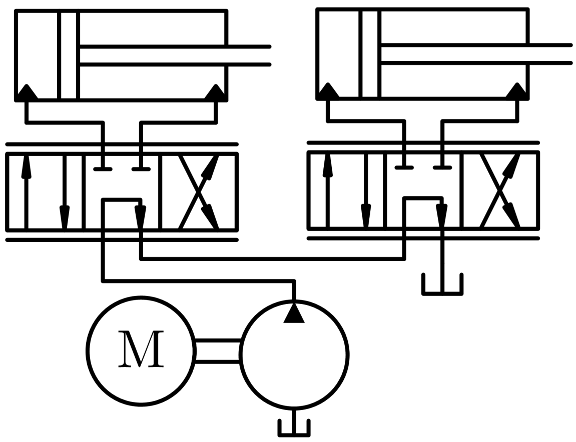

Figure 2.1: Open centre system.

In open centre systems, in the neutral or non-activated state of a DCV, working fluid flows from a pump through a valve's bypass channel to a tank or to the next DCV in the case of multiple actuators, see the Figure 2.1. In these systems, if none of the DCVs is activated, the whole pump flow rate passes through all valves towards a tank. This allows maintaining low standby pressure and using fixed-displacement pumps, which are considerably simpler and cheaper than variable-displacement. The use of fixed-displacement, alongside with the manual valve control method makes the complete open centre hydraulic system more robust, simple in servicing and maintenance comparing with competing system architectures.

According to the Bernoulli's principle and given the pump pressure is constant, the flow rate to an actuator, and consequently the actuator's speed, depends on both the load pressure and the spool position. The flow dependency on the workload gives open centre systems high damping qualities, which are perfect in handling large inertia loads (Eriksson 2007). At the same time, highly-damped systems tend to have an increased response time to a step input signal, hence, slower operation, which adversely affects work cycle time of an entire machine.

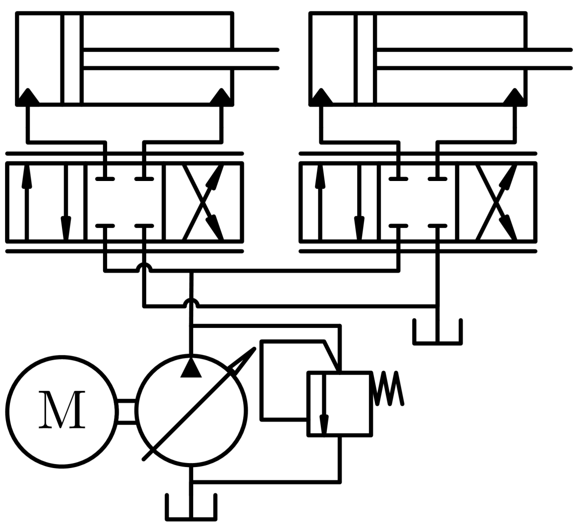

Figure 2.2: Constant pressure system.

Activation of several valves simultaneously leads to an effect taking place in multi-functional open centre systems – loads interaction, which causes open centre systems to have even slower responsiveness (Axin et al. 2014). It becomes more noticeable when load types and magnitudes differ drastically between actuators. The effect occurs due to the serial arrangement of valves, when flow from the pump goes through every flow control valve until it reaches the tank. Therefore, the effect of load variations are transmitted between actuators. As an example, an impact load from one actuator makes an otherwise steady operation of another actuator discontinuous. Moreover, the flow passing through all DCVs accumulates hydraulic losses from every actuator's branch, which creates large pressure drops. It consequently results in the significant power dissipation in heat and requires a more powerful pump to control multi axis open centre systems.

2.1.2 Constant Pressure System

Constant pressure systems solve the load dependency by utilizing in the power subsystem a pressure relief (PRV) or safety valve, which is installed in the parallel bypass to the variable displacement pump, see the Figure 2.2. The main DCV in this case has the closed centre, which does not allow the flow through when it is in the neutral position. The PRV contains an adjustable spring, which determines the stand-by and the upper limit pressure levels of the whole system. If the closed centre DCV is not activated, the pump's regulator reduces its flow rate to minimum. The residual flow rate is then bypassed to the tank through the PRV.

In constant pressure systems with a variable displacement pump and a non-activated DCV the pump-inbuilt regulator restricts the flow by shortening machine's displacement, i.e. de-swashes or de-strokes the pump, as soon as the pressure reaches the set level. In the case the flow demand from the load is lower than pump's output, excessive fluid is diverted through the PRV to the tank or the pump's displacement is adapted to the required flow demand.

The constant pressure systems with fixed displacement pumps tend to generate significant fluid heating, since when the DCV is closed, the whole pump's flow is diverted through the PRV. Oil temperature rise in systems with large-displacement pumps may lead to destructive consequences. Due to amounts of produced heat, these systems find limited applications and require introduction of heat exchangers and coolers in the hydraulic tank design.

Another embodiment of constant pressure systems is a class of hydraulics, which uses three or more pressure rails. A pressure rail is a hydraulic line, i.e. a hose or a pipe, which contains oil under a specific and constant pressure level, see the Figure 2.3. This arrangement allows fast switching between different pressure according to the load's demand. A great advantage of these consists in compatibility with another advanced actuator controlling schematics (Vukovic et al. 2016).

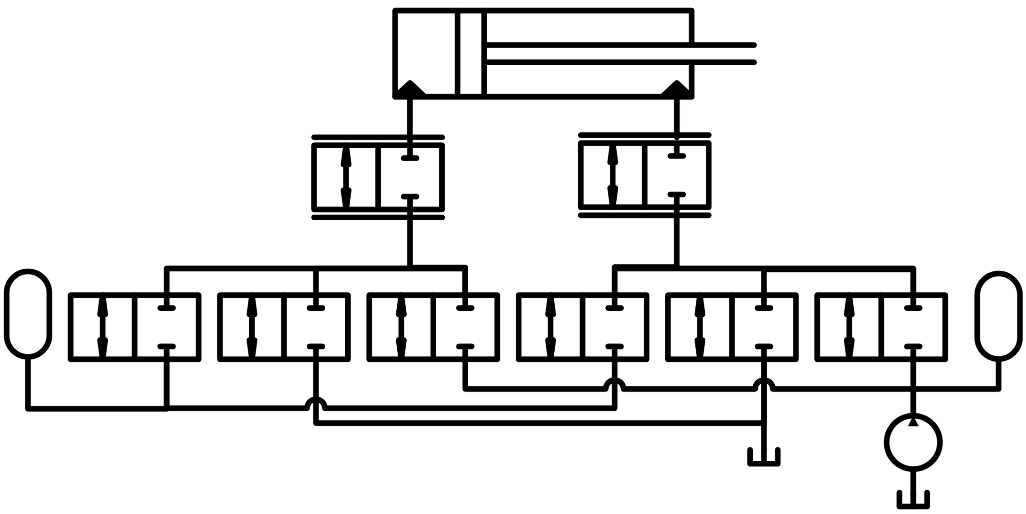

Figure 2.3: A hydraulic scheme with pressure rails.

2.1.3 Load Sensing

Unlike constant pressure systems, in load sensing (LS) systems the pump pressure is being continuously adjusted to the highest load (Lantto 1994). This could be accomplished using either the variable displacement pump or the fixed displacement one together with overflow or unloading valves. Usually the concept realisation also requires a pressure reducing valve, which keeps a constant pressure drop across the DCV, regardless of the load behaviour. The constant pressure drop across the flow control valve is kept by adjusting either the pump's displacement or pressure

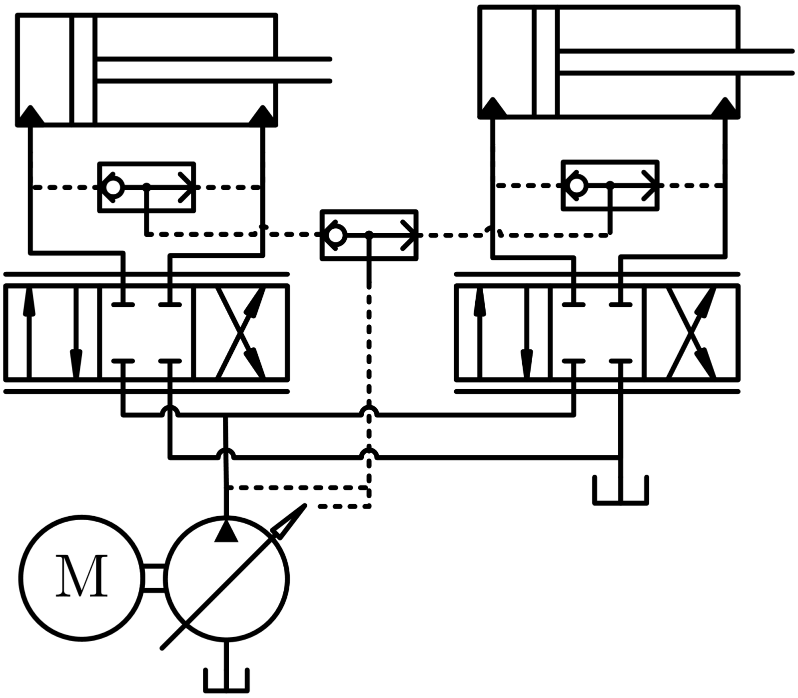

Figure 2.4: Load sensing system.

reducing valves. The pump pressure is pre-set with a margin of 20-30 bars and held higher than the flow demand of the most loaded actuator (Axin 2013).

The pressure setting in LS systems is based on a set of shuttle valves, which compare loads from all actuators, picks the highest one and sends this pressure as the pilot one to the pressure regulation mechanism of either the unloading valve or the variable displacement pump, see the Figure 2.4. In the case of variable displacement pumps, the pilot load pressure is sent to the pump's pressure regulator (McWilliams 1991).

The pump flow rate is controlled by the differential pressure between the pump supply port and the load. LS is based on a mechanically implemented feedback, which compares load pressures from actuators and sends the biggest to the pressure regulator. Thus, only the required flow and power are being fed to the loads.

The inherent flaw of LS is that its dynamic behaviour can become oscillatory and unstable due to transient nature of a pilot pressure (Sakurai et al. 2002). The regulating pressure is based on the load signal, which often is highly-variable in time and oscillatory. Fast response times in movement of high inertia loads may create a shock waves in hydraulic ducts as well machine structures. Therefore, appropriate measures to damp and soften oscillations needs to be undertaken. These are usually implemented in selection of shock absorbers and dampers with spring and damping coefficients being selected according to intended use and loads.

Multi actuator LS systems suffer from loads cross interaction too, unless pressure compensators are used for each actuator. In this case, faster and more accurate response can be achieved at the expense of low damping. A general method to avoid unstable operational regimes in LS systems is the employment of intelligent control algorithms such as active energy regeneration systems (Marani et al. 2008).

2.2 Valveless Control

As the name implies, any hydraulic control system that governs the actuator speed without control valves belongs to this architectural class. The valveless control implements hydraulic motor's speed regulation by means of modulation of the characteristic displacement of a variable displacement machine as pumps, rotary motors, and transformers, which are used as the main driving or actuating part of the valveless hydraulic system.

In applications where a controlled hydraulic motor is supposed to work for the most part of a working cycle of NRMM, this method is the most common one. It is applied to closed hydraulic systems of propulsion and steering in hydrostatic transmissions and aircraft rudder control. Common traits of these systems are speed regulation of the motor through varying the machines' displacement and returning of the exhaust motor's flow to the pump's intake instead of the tank, see the Figure 2.5.

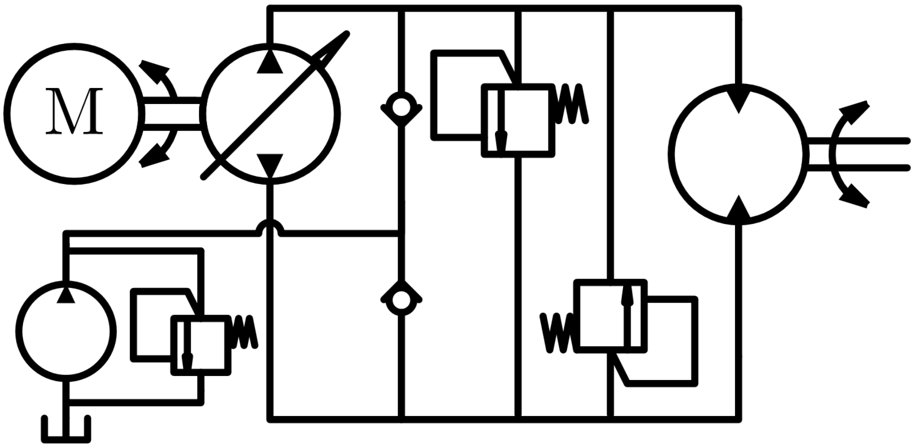

Figure 2.5: Displacement control system.

2.2.1 Displacement Control

In the displacement controlled actuation, one variable displacement hydraulic pump is used for each actuator (Hippalgaonkar and Ivantysynova 2013). This type of control allows to control actuators of both the rotary and linear nature. If the hydraulic motor is rotary, it is normally non-variable one. Its speed is controlled by the variable pump. In the case of multiple actuators, there are several closed circuits containing variable displacement pumps.

The solution provides high energy efficiency, for only needed flow is supplied for a service actuator. However, displacement control requires complex mechanical control of a variable displacement machine, which are also more expensive than fixed displacement. The pump regulator adds an supplementary hydraulic contour to control the pump's displacement. Hence, overall displacement controlled hydraulic system becomes less reliable and serviceable than valve-controlled analogues.

Displacement controlled systems in multi-axis arrangements often include hydraulic accumulators to store excessive hydraulic energy. Such decentralized systems with accumulators to store regenerated energy from a lifted load increases efficiency even more (Lodewyks and Zurbrügg 2016). At the same time, it requires several high-cost variable hydraulic machines, advanced controls, and maintenance. Such control technique is applied in electrohydraulic actuator systems of aircraft controls (Lin et al. 2013), (Habibi 1999).

The displacement control principle can be implemented with the IM arrangement of DCVs in an open circuit (Heybroek 2008). For each actuator, there is a variable displacement pump and four two-way valves. In a sense, the displacement controls finds its application in digital hydraulic power management systems too (Heikkilä and Linjama 2013). Here, control of actuator's speed is still realized through adjustments in pumping element, but in an incremental manner.

Velocity control of actuators by the pump displacement has low bandwidth, which influences dynamic properties of the whole system. Methods to overcome this shortcoming include shortening hydraulic hoses length, introduction of specific nonlinear controllers (Wang and Li 2012).

2.2.2 Secondary Control

Displacement control of a variable displacement pump is also referred as primary displacement control. Normally secondary controlled hydrostatic transmission is used in closed-loop systems with regulated rotary motors. The speed control of a motor is realized by adjustment of hydraulic motor's displacement instead of pump's one. Examples of such systems are a cabin swing drive (Pettersson and Tikkanen 2009), aircraft high lift systems (Geerling and Biedermann 1998).

The main incentive to resort to such control technique is the presence of high-inertia loads and braking regimes in operation. With secondary controlled systems it is possible to recuperate load's kinetic energy by charging high-pressure accumulators when motor works in a pump mode (Ho and Ahn 2012). Thus, secondary controlled schemes often feature high-pressure common rail with the hydraulic accumulators and pump-motor hydraulic units connected to the load. Despite engine fuel savings, precise position and velocity control in these systems is challenging. To overcome it and compensate nonlinear characteristics as dead-zone input, application of specific control method can be used with an adaptive fuzzy controller (Do et al. 2014).

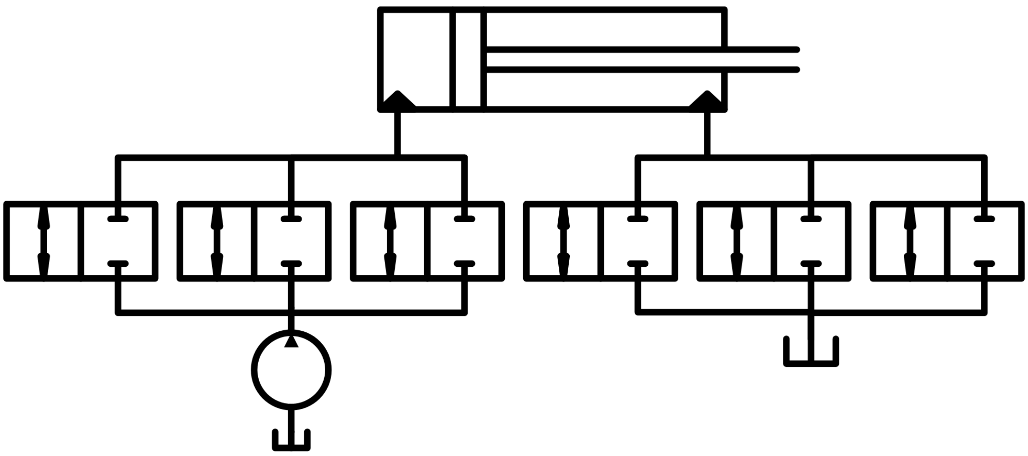

Figure 2.6: Digital hydraulics control system.

2.3 Digital Hydraulics

Digital fluid power could be defined as following: digital fluid power means hydraulic and pneumatic systems having discrete valued component(s) actively controlling system output (Linjama 2011). Realization of that concept is represented in control of individual valves connected in a parallel arrangement and individual control of the piston chambers in pumps or motors through switching technology. These concepts can be combined by a common name of digital hydraulic power management system (Linjama and Huhtala 2010). These also enable system architectures with fixed displacement pumps.

This technology is a relatively new and broad research subject, which promises to reduce losses and dynamic shortcomings of present-day hydraulics at the expense of complicated control codes and increased number of control components of the total system.

2.3.1 Digital Valve Systems

Arranging several low-cost on-off valves in parallel enables precise flow control of a hydraulic actuator (Linjama et al. 2003). This concept necessitates many fast switching on-off valves with different flow cross-sections, see the Figure 2.6. That has motivated many research studies of such valves and their possible arrangements.

Among examples is a hydraulic hybrid actuator, where a set of on-off valves are combined with accumulators to attain only mean power supply to an actuator, thus, developing further energy regenerative capabilities of hydraulics (Linjama et al. 2015). Development of a digital hydraulic actuator system (Dell' Amico et al. 2013) is another step forward in the concept's evolution. Such arrangement with multiple valves changing their state with fast frequencies can create adverse pressure pulses, which can be perceived by an actuator and a load. Incorporation valves in a single laminated valve body with the cartridge, screw-in principle reduces remarkably package sizes and mass of the flow control unit without compromising leakage and durability features (Paloniitty et al. 2012), (Paloniitty et al. 2015).

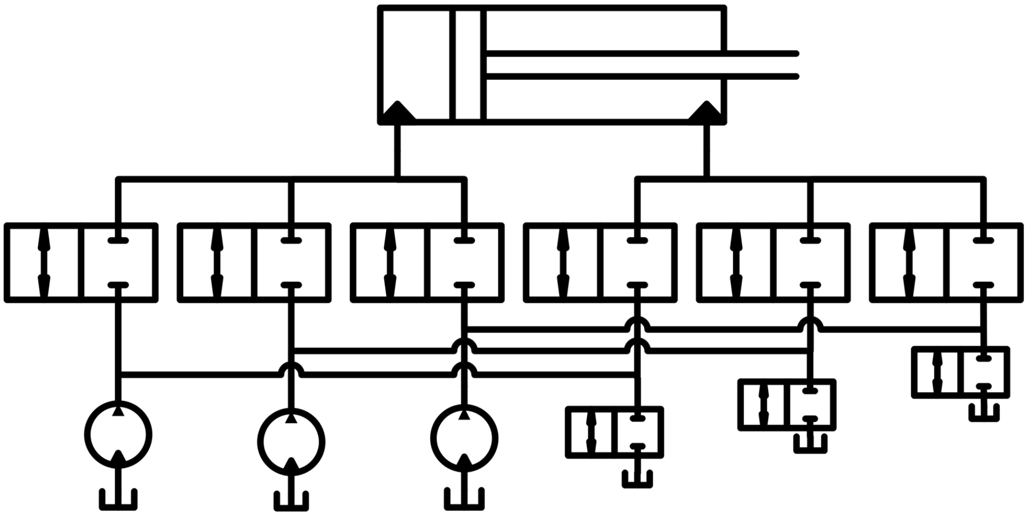

Figure 2.7: A scheme of digital displacement machine.

2.3.2 Digital Hydraulic Machines

The idea of independent pressure regulation for each piston chamber of positive displacement hydraulic machine found its application in gearless drives of wind turbines (Rampen 2006). Artemis IP successfully developed and industrialized their digital displacement concept also in hybrid vehicles' transmissions (Taylor et al. 2011). The ground principle in these machines relies on active on/off valves control to regulate the fluid flow into and from a pumping element – piston chamber of displacement machines (Linjama and Huhtala 2009).

The concept of digital displacement fluid power machines has caused a large number of research studies of compact, fast-switching, on/off valves (Roemer et al. 2013), which are indispensable to implement the concept. Two biggest challenges to overcome in order to apply digital hydraulic in a displacement machine are related to adding extra two active on/off valves to every chamber of a displacement machine. Firstly, these valves need to be fit and packaged compactly in the piston's chamber. Often it would lead to smaller walls of a pump housing, increased internal stress in its material and consequently less structural strength of the part. Secondly, the valves need to be controlled actively, with high-speed dynamics. For this, fine control of valve opening timing needs to implemented. Additionally, the valves must be able let all piston's flow rate though in very short amount of time.

2.4 Independent Metering

2.4.1 Definition

On the early stages of the concept development, a term "decoupled metering" was used as a synonym to IM. Researchers aimed at dividing a flow rate and a pressure levels of actuator speed control, but not physical control orifices within a valve. Although an initial idea differs from the definition of IM used in the review, mechanical design embodiments of flow rate-pressure isolated systems look exactly as IM systems with the disjoined mechanical linkage between flow passages.

The numbers of found published articles are estimates as sometimes papers deal with IM in an indirect way or have an overlap with alternative hydraulic architectures or even other disciplines. The number of patents considering IM is approximate too. Often it is challenging to evaluate contribution of a patent on the concept development. The poster sessions are excluded. The total number of publications reached a maximum in 2016 amounting to 17.

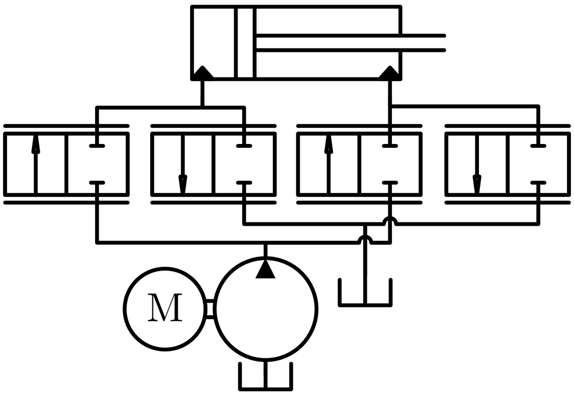

Figure 2.8: Independent metering system.

In this review, the IM concept refers to the separation of the mechanical coupling between meter-in and meter-out orifices (Shenouda 2006). In a broader sense, the term covers any valve arrangement within a hydraulic system where actuator's supplying and diverting flows are controlled individually (Eriksson 2010). Thus, IM systems inherently possess two or more degrees of freedom in control process.

Independent and coordinated control of two or more valves makes electrical actuation the main option to regulate valves and ensure full functionality of a hydraulic actuator. Hence, IM is an example of a mechatronic approach to constructing power hydraulics as its effective implementation depends on seamless and smooth integration between mechanical, electrical and control engineering systems.

2.4.2 Concept Development

Hydraulic architectures matching the definition of IM given above can be traced in industrial patents and academic papers back as far as the late 1960s. The list of references can be incomplete as it is hard to find the older research studies.

The idea to improve the efficiency of fluid power systems by disconnecting flows from a pump to an actuator and from an actuator to a tank came from an industrial background. The first mentioning of an idea to allocate a single valve per an actuator's port dates back to 1969 in the patent by Koehring Co., currently Terex Corp (Tennis 1969). The patent proposes to divide a spool inside a control valve in two separate spools for each port of a hydraulic actuator. Although this invention was mainly motivated by a problem of warpage of lengthy spools, it has still introduced the idea later termed IM.

In 1990 it was first suggested to decouple meter-in and meter-out orifices in mobile hydraulics using readily available poppet or seat valves (Jansson and Palmberg 1990). The authors pointed that mobile machines could have benefited from adopting the IM arrangement of seat valves, which had already been used in stationary industrial applications. Later, this idea had drawn considerable attention from the academic community what resulted in extensive research work on programmable valves (Book and Goering 1999).

Later it was observed that the commonly used DCVs with a single spool had been designed to optimise the control of the pump-to-actuator fluid flow only. Because of that, such spool is unable adequately throttle the actuator-to-tank fluid flow, especially in overrunning loads (Crosser 1992). This patent claims a design employing two three-way proportional pilot controlled valves to regulate an actuator's supply and exhaust. Additionally, hydraulic piloting is implemented through two 3/2 proportional solenoid valves per main flow control valve what totals to six proportional valves.

The first actual claim for a independently operable flow metering solenoid valve was made in 1997 by Caterpillar Inc. The invention was used to prioritise a tilt function over lifting in a hydraulic control system of a wheel loader (Koehler and Krone 1997).

The term “independent metering valve” was first coined by Aardema and Koehler (Choi et al. 2015), (Aardema and Koehler 1999) of Caterpillar Inc. In this patent, possible modes of circuit operation and corresponding states of the valves were discussed and summarized the first time. In the same year, Smith suggested using a system of four poppet solenoid actuated valves custom designed for an IM arrangement (Smith 1999).

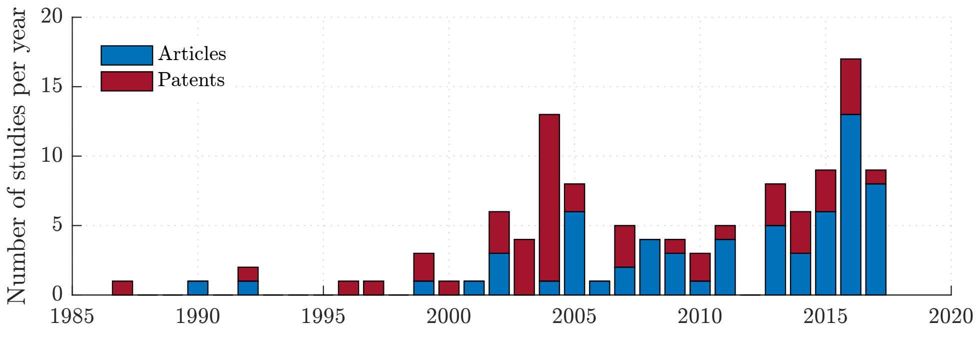

Figure 2.9: Number of studies related to IM for the last three decades.

The Figure 2.9 shows the number of publications related to IM and its development. While industry created and clearly signalled a strong demand for IM systems, the concept has been gradually gaining more attention within the academic community especially during the last decade. A ratio of patents and scientific papers in the total number of publications indicates that interest to the concept has recently shifted from industry to academia.

The observable growth in IM research is not monotonous but steady. Most academic studies of IM were presented in conferences and industrial expositions. It substantiates irregularity in academic publications appearance for most of the conferences are biannual or occur in even longer time intervals.

2.4.3 IM Circuits

Sitte suggests classification of IM hardware layouts on symmetric and asymmetric circuits (Sitte and Weber 2013), see the Figure 2.10. Symmetric one is constructed using only one valve type. The system built out of 2/2 proportional valves can be assembled in either the Wheatstone bridge arrangement or via five valves, where the additional fifth valve connects the actuator ports.

In the last decade there has been attempts to merge IM with digital hydraulics. In some cases, the IM concept overlaps with digital hydraulics. According to the definition of digital hydraulics given by Linjama, the idea of digital fluid power consists in controlling system output, that usually is a volume flow rate, by discrete valued components (Linjama 2011). As an example, the most common execution of digital hydraulics is an allocation of one or more digital flow control units (DFCU) per hydraulic actuator’s port (Linjama et al. 2003), which makes the whole hydraulic system belonging to the IM.

The energy performance comparison of DFCUs in the IM arrangement, what authors called the digital hydraulic IM valve (DIMV), with the industry standard load-sensing system has been conducted on a Volvo’s 21-ton excavator during truck loading and grading cycles (Ketonen and Linjama 2017).

The latest steps forward in the development of IM systems are adding a pressure compensation capability to the entire hydraulic system and a set of shuttle valves. The latter allows selecting the maximum pressure level from all actuators as a pilot signal for a pressure compensator thereby enabling load sensing flow control.

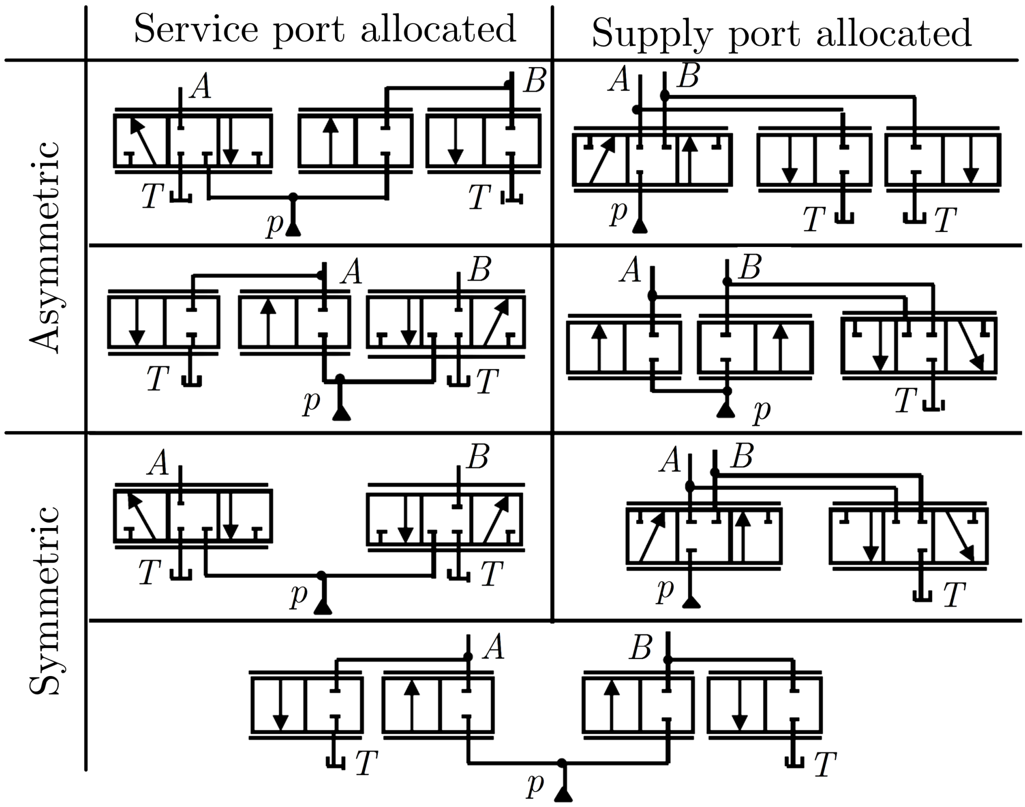

Figure 2.10: The IM circuits classification according to (Sitte and Weber 2013).

2.4.4 IM Valves

Currently, the most common types of control valves being used to implement an IM are 2/2 and 3/3 proportional spool valves, although many studies consider the application of poppet valves as more favourable to design simplicity, system dynamics and leak tightness.

Aardema defines the IM valve as a set four independently operable, electronically controlled metering valves (Aardema and Koehler 1999). The separate metering can be accomplished through a variety of schemes involving various kinds and numbers of control valves as shown above.

Since the IM concept pertains primarily to hydraulic architectures, naturally initial research studied fluid power systems built exclusively from already available, off the shelf valve design solutions. But in recent years there have been proposed many alternative mechanical designs developed specifically for application within IM systems.

To this day major industrial contributors to the IM development are Caterpillar Inc., its supplier HUSCO and later Incova Technologies, Parker Hannifin, Eaton, Bosch, Moog Inc., Sauer-Danfoss, Deere & Company. Research done by these hydraulics manufacturers spans across multiple disciplines involved in the physical realization of IM: electronics, control systems theory, mechanical engineering of IM valves, hydraulic architectures and performance investigation of a whole construction machine. Today there are two industrial companies which managed to launch production of IM valves.

The HUSCO's INCOVA™, an acronym from Intelligent Control Valve, represents one of the successful implementation of IM systems in the off-highway automotive sector. The INCOVA™ system uses four independently controlled electro-hydraulic poppet valves (EHPVs) configured in a Wheatstone bridge arrangement with pressure sensor feedback (HUSCO 2007).

The Eaton's Ultronics™ is another example of the applied IM concept in the industry. The system employs a twin spool architecture where a two-stage electro-hydraulic valve comprises two spools which are hydraulically controlled by another two pilot spools (EATON 2010), see the Figure 2.11.

2.5 Spool Valves

Considering advantages valve-controlled systems provide, the closer look at the exact structure of a control spool valve is needed in order to identify ways to effectively improve its design. The valve control implies actuator's speed regulation through throttling adjustment of the DCV's spool position. The position of a spool modulates areas of orifices that determine valve's hydraulic resistance. Flow rates to and from an actuator are changing according to these areas.

Since throttling control is of a resistive type, excessive fluid energy is being dissipated in the form of viscous friction in whirls occurring after any obstacle to the flow. Friction also makes oil temperature to raise. Generated heat is absorbed by working liquid, usually behind meter-in and meter-out slits of a spool or a poppet, for these regions of a fluid subdomain are the most prone to formation of vortices and high-speed jets.

Structurally control valves used in fluid power systems consist of a spool and a sleeve as the key flow regulating components together with a spool actuating mechanism. The typical design contains the cylindrical sliding spool with multiple shoulders and the sleeve with several openings on it. The sleeve holes connect both supply, or pump, p and return, or tank, T lines to actuator's service ports A and B. In absence of a sleeve, these channels are ensured by a valve's body, see the Figure 2.12.

The driving signal from actuating mechanism defines axial position of the spool inside the fixed sleeve. In turn, spool's axial location determines the extent of overlap between the sleeve apertures and the spool lands. Therefore, relative displacement of the spool inside the sleeve regulates the orifice area and the flow rate passing through these throttling elements.

Proportional control valves provide infinite positioning of the spool within its stroke depending on the control signal from the spool driving mechanism. On-off valves, which have a certain number of states, determine flow direction only. The flow rate regulation requires additional flow control valves. In the case of on-off control, directional and control functions are split between different valves.

Remarkable achievements of electrical motion control systems have ensured that electromagnetic linear motors became the most common devices governing spool location in proportional valves. However, solenoids, voice coils, and other electromagnetic linear drivers have limited use in the presence of large flow forces usually acting on the spool at large flow rates. These forces can cause a backlash in the system, limit smoothness of the operation of hydraulic drives and actuators. Moreover, the motion of the moving part in the valve can only be maintained, when the actuation force can overcome the flow force acting on the moving parts. Therefore, the magnitude and the direction of the flow force becomes key information for fluid power engineers who design hydraulic valves.

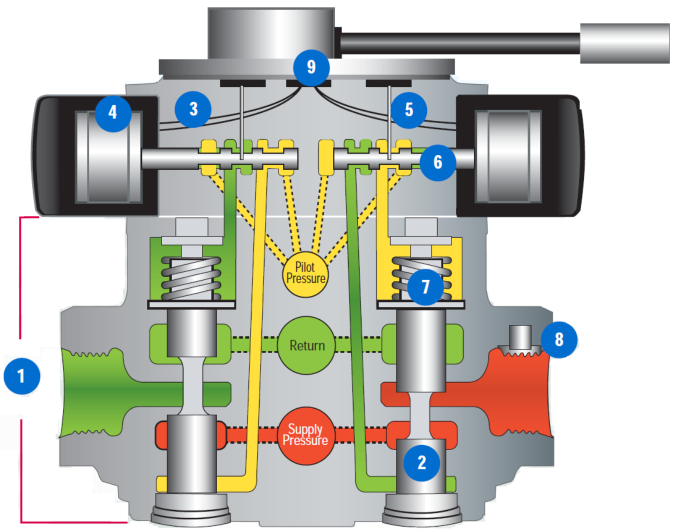

Figure 2.11: The Eaton's Ultronics™ twin independent spool valve (EATON 2010). 1 – main stage valve block, 2 – independent spool for metering, 3 – pilot valve, 4 – low power voice coil actuator, 5 – centering spring, 6 – pilot spool, 7 – position sensor, 8 – thin film pressure sensor, 9 – embedded micro electronics.

To overcome these large resisting forces, an indirect pilot hydraulic actuation of the main sliding spool is employed. Such design of a flow control valve lacks mechanical reliability due to the introduction of the additional hydraulic spool to control the main spool. It results in immense pressure losses, poor energy efficiency and rigorous requirements to the level of oil contamination due to sophisticated and narrow channelling (Filho and De Negri 2013). Furthermore, production of such multiple-stage valves demands high-precision manufacturing process what increases the overall cost of these flow control units. Manual assembly of torque motor driven two-stage valves and their adjustment motivates for investigating alternative technologies (Plummer 2016).

To solve efficiency issues in valves in general and reduce pressure losses, optimisation of the flow paths through the valve and thereby lessening flow disturbances are employed. A promising method to enhance valve performance and simplify valves geometrically for manufacturability is to implement a specially profiled sliding spools.

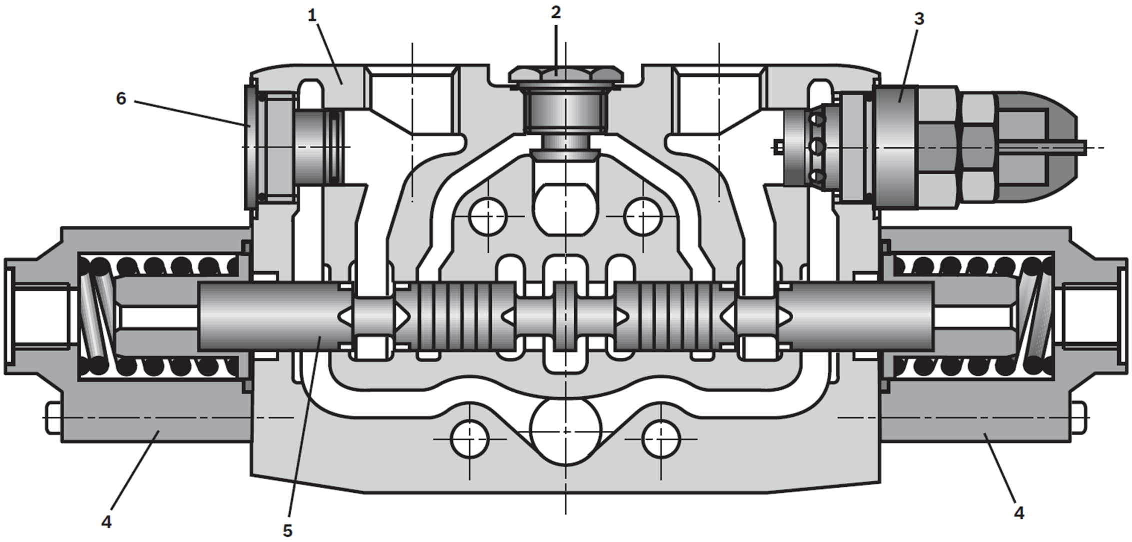

(a) The cross section.

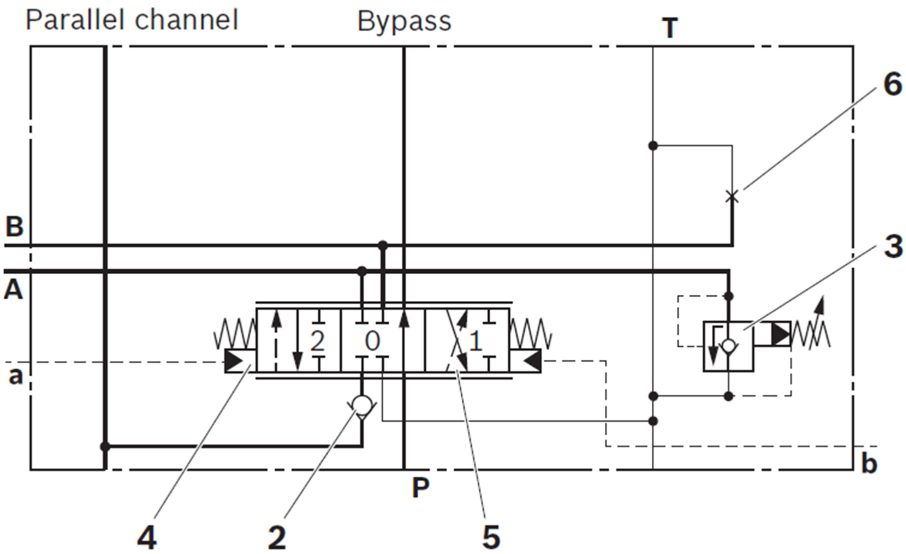

(b) The hydraulic symbol.

Figure 2.12: The open centre spool control valve (Bosch Rexroth 2016). Ports: P – pump, T – tank, A, B – actuator. Parts: 1 – housing, 2 – check valve, 3 – secondary valve, 4 – operating, or spool actuating, element, 5 – spool, 6 – plug screw.

Many studies have shown the positive impact of smoother spool geometry on fluid's rate of change of momentum, hence reducing the flow forces experienced by the spool's driver. The introduction of compensation profile on the sliding spool's shaft diminishes the flow forces by creating a pressure drop in the downstream cavity (Amirante et al. 2007). It was proved experimentally, that geometrical optimization of central conical surfaces on the spool shank can provide higher inlet velocities on opposite sides of the spool. That alleviates a net flow force, and lowers an overshoot in the dynamic study (Amirante et al. 2016). Cone surfaces on the spool's control edges and making oil jet return back in spool's cavity on the meter-out edges enables application of direct actuation of the spool for larger nominal valve sizes (Herakovič 2009).

Adding supplementary parallel channel to the return line in valve's body allows extension of the valve's operational flow range by improving the carrying capacity of the drain line without resorting to more powerful solenoids (Lisowski et al. 2013). The geometrical optimization of the flow regulating parts has a significant effect on flow forces in seat valves as well (Simic and Herakovic 2015). Other viable ways to obviate the negative effect of flow forces are improvement of electromagnetic actuator's performance (Reichert 2010), advanced regulation of spring rates of return mechanism and geometrical optimization of spool's ambient parts, channels, inlet and outlet spool chambers (Abdalla et al. 2011) to make them less prone to vortices and flow disturbances formation.

2.5.1 Rotary Valves

Despite the vast number of design studies all looking to minimise the flow forces and static pressure losses, examinations of conceptually alternative constructions of throttling elements and their arrangements are still rare in current literature. The use of valves with rotary spools is an example of studies on design variations of the valve structure to solve the problems associated with large flow-generated forces.

The current research has been inspired by numerous computational fluid dynamics (CFD) studies of flow characteristics of currently used spool valves, which predominantly include flow velocity fields and flow trajectories visualisations. Judging by flow streamlines in the conventionally used spool and seat valves (Lisowski et al. 2013), (Bordovsky et al. 2016), (Herakovič 2015), (Lisowski and Filo 2016a), (Lisowski and Filo 2016b), it has been concluded that, firstly, exact geometry of a valve is a sole factor defining flow trajectories and, hence, pressure losses and efficiency of a valve; secondly, streamlining of flow paths' geometry is a way to improve efficiency of a valve; and finally, the easiest way to implement streamlining is to remove unnecessary U-turns and sudden cross-section changes of flow paths, which are in abundance in linear spool valves. These considerations let to infer that rotary valves could provide more streamlined flow trajectories and ease of valve operation. Unlike conventional linear spool configurations, a rotating spool design would also create a much smaller net area of surfaces subjected to the flow forces, hence, making power consumption of a valve switching mechanism smaller.

So far, employment of such rotary spools industrially is restricted to manually driven on-off valves, flow dividers, steering valves and plug valves. In these ball valves, usually a rotary spool is spherical in a cross section with drilled through holes serving as flow paths. In valves with cylindrically shaped spools, flow paths are milled on the external cylinder of the spool, imposing sudden changes in direction and a cross sections of flow paths.

However, there are alternative proposals to implement rotary valves. In a study of a three-way electronically driven hydraulic rotary valve, a detailed mathematical model of a DC-driven spool was presented (Yang et al. 2010). In the research of direct drive servo valves, a single axisymmetric spool works with a similar principle as a 4/3 directional valve. It modulates proportionally and simultaneously flow areas of both meter-in and meter-out hydraulic lines of an actuator (Yu et al. 2014), (Yu et al. 2015). Spool shoulders contain several axially oriented grooves overlapping with corresponding holes on the static bush. In these structures, the single spool incorporates several fluid paths in it. That makes the structure of the spool larger for the same volume or mass flow rate application and generates tangible pressure drops of the whole valve. A similar approach to the spool design was described in the analysis of a rotary directional control valve driven by a servo motor (Wang et al. 2016). The common drawback in the mentioned design solutions is a spool incorporating a few axial flow paths in it, which results in a bulky spool requiring large power to operate it. At the same time, U-turns are preserved for both flows passing through these valves, meter-in and meter-out. This makes valves to dissipate substantial flow energy.

The introduction of switched inertia hydraulic systems provokes numerous studies of rotary fast-switching valves since the rotary arrangement of spools proved to be easier to shift between open and closed states. This concept is analogous with an electric buck converter and inherent fluid inertia in hydraulic tubes to control supply pressure and flow to a motor (Pan et al. 2013). Experimental study of switched inertia suggests fast switching can cause noise and cavitation problems (Pan et al. 2015), (Johnston and Pan 2015).

The above-mentioned studies comprise detailed CFD and experimental analyses of driving torques of spools at flow rates not exceeding $150\,\mathrm{l\,min^{-1}}$. For noted design solutions, the formation of lateral or radial forces on the spool causing flexion, stiction and jamming of the spool inside the bush seems to be a common potential problem.

Minimisation of the mobile surfaces subjected to the flow forces as an approach to overcome flow forces was used in the research of an axial flow valve with rotational metering (Ansaloni et al. 2008). The proportional two-way, two-position valve in this study has an in-line setup of regulating parts. The valve design implies inbuilt hydraulic control of the rotor's angle by means of the reducer ring sliding along helical grooves in a gap between the stator and the rotor. The suggested design might pose problems of rotor blocking and internal leakages.

Among multitude patents dedicated to the rotary valve structures, there are design solutions suggesting a tubular spool as the main throttling part. Embodying the approach of mobile surfaces minimisation and using rotary control motion, these concepts represent a promising and under-studied class of control valve designs. The first found patents proposing such structures were filed in the middle of the last century, (Husley 1962) and (Erwin and Husley 1958). The sectional views of these valves are illustrated in the Figure 2.13.

There is a proposal in the study of the three-way pulse-width-modulated directional valve to harvest the fluid flow energy by embedded turbines in order to establish the spool's translational and rotary positions (Tu et al. 2012) and eventually modulate its duty ratio (Wang and Li 2009). This design features a self-spinning turbine with rhombic slots forming throttling orifices (Wang et al. 2010), (Tu et al. 2007), (Rannow et al. 2010) and finds application in virtually variable displacement pump/motors (Tu et al. 2011).

2.6 Knowledge Gaps

After analysis of the possible hydraulic architectures done in the first part of the Literature Review, it has been noted that several architectural concepts of power hydraulics still exist only as a proposal to schematically resolve efficiency issues. The reviewed sources show a clear lack of physical embodiments of advanced circuitries of fluid power systems, especially for the high flow rates applications. That applies to the independent metering concept too, which is considered by the author as the most promising hydraulic architecture in terms of possibilities for energy recuperation and regeneration without compromising structural and control complexity.

It has also been concluded after the review of current technological trends in fluid power systems, that among available control principles valve-based control remains the most flexible and reliable one. Displacement control still requires significant investments in design, development, introduction, subsequent expensive maintenance and servicing of such systems. Among valve-controlled systems, the IM offers a compromise between energy saving capabilities of digital hydraulics and architectural simplicity of constant pressure and open centre systems.

This study attempts to advance the innovative concept of IM and expand its application to high flow rate applications of fluid power systems. The research presents a strong case for that architectural approach to be the most suitable valve system in the specified domain of power

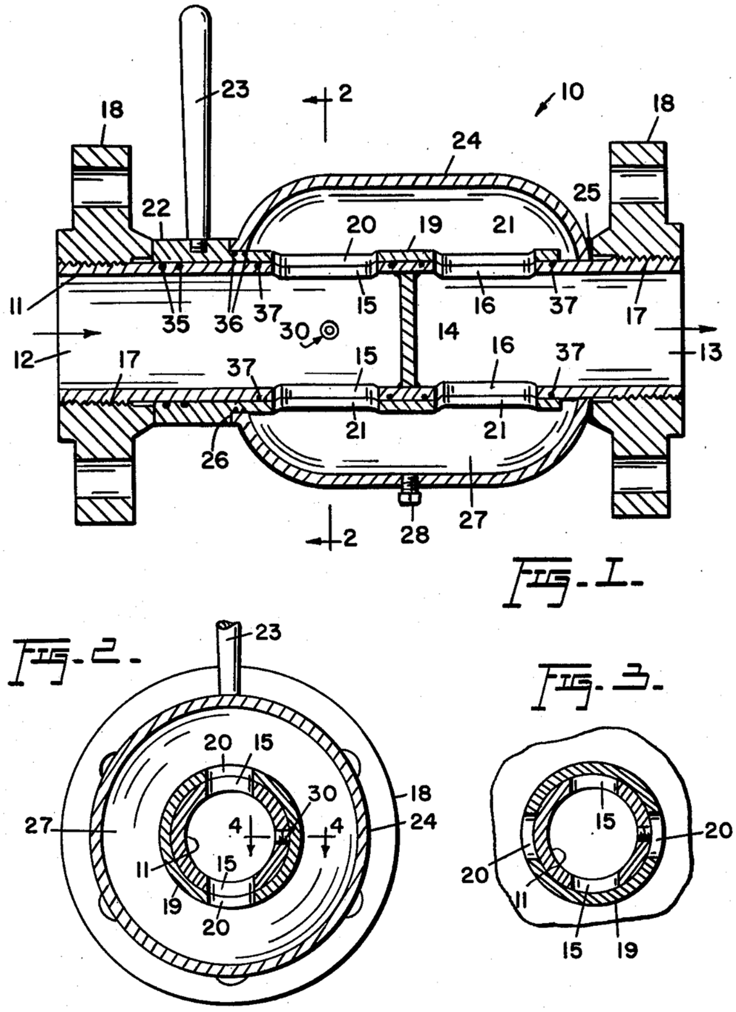

(a) Rotary control valve (Husley 1962).

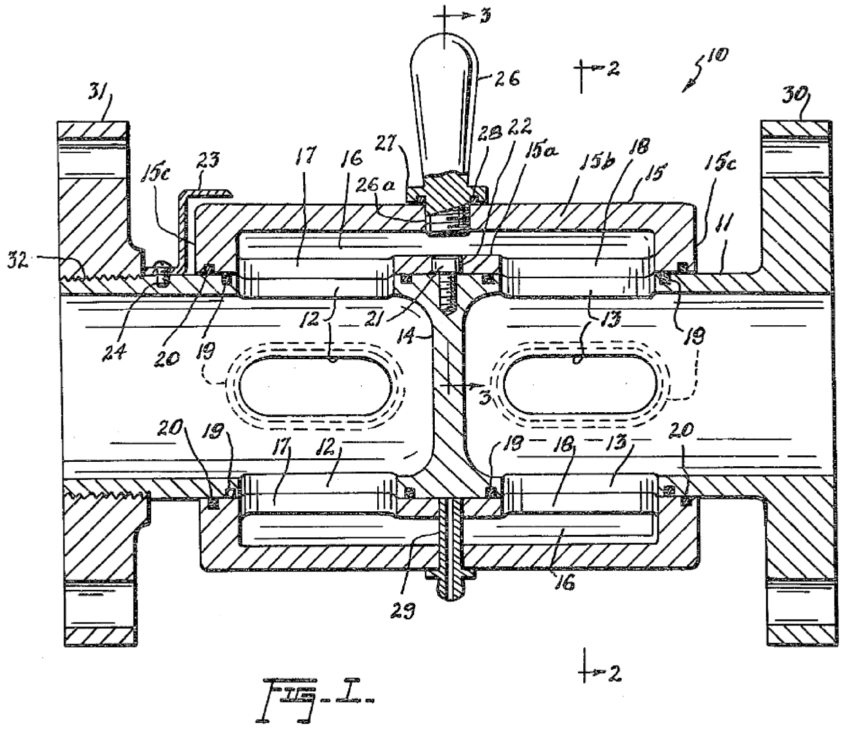

(b) Rotary sleeve valve (Erwin and Husley 1958)

Figure 2.13: Examples of the tubular-spool valves.

hydraulics. Application of high-flow rate IM could also address one of the biggest challenges in the design of fluid power systems, namely the size, or compactness, and weight of the components (Yang and Pan 2015), which influences entire energy efficiency, work cycle of the mobile machines carrying power hydraulics.

According to the reviewed literature on valve design of the spool type, the common issue of the control valves consists in high flow forces acting on the spool. That fact makes application of advanced design and control methods to compensate the effect of the flow forces inevitable. The studied literature presents scarce alternative design solutions to overcome the issue of increased flow forces. The studied academic and industrial literature shows, that slight attention has been paid by researchers so far to the actual design of constituents of the hydraulic valves to enable the single-stage, or directly operated, valves in high-flow rate applications.

Current research proposes to further develop the concept of reduction of flow forces in high flow rate applications through the implementation of the novel design of the throttling orifice. The main approach for this research is the detailed investigation of the structural design to minimise the number of spool's surfaces exposed to the flow forces and the implementation of direct control of spool position.

The true potential of rotary valves, in this perspective, does not seem to have been fully realised. This particularly applies to tubular spool valves. Initial consideration of this design has concluded their similarity with blade of knife valves of fluid transportation industry. Tubular structure could present a set of advantages, which are insufficiently explored. Further design development of their structure could resolve efficiency issues of hydraulic valves and lessen flow forces acting on the spool. With advances in electrical rotary drives, implementation of one-staged rotary valve seems a viable substitute for the linear sliding spool.

In this research, the emphasis is placed on the actual geometrical design of the valve's throttling elements. The aim is by better design to produce slow and gradual opening, closing and flow variation to enable smoother operation of the actuator, improve valves' reliability due to simpler construction, and better their controllability by alleviating the influence of the flow forces. In overall, these measures would greatly simplify valves' manufacturing and lessen exploitation cost in the longer term.

Chapter 3

Methodology

This chapter outlines the methodology used in the mechanical design and development process of the new valve. Several viable design options were considered and analysed. The valve design for further development and performance evaluation was selected based on the preliminary design evaluation.

The quantitative evaluation of the new concept and its performance was the methodology adopted for this research. This chapter discusses the parameters defining the performance of the valve as well as the methods of parameters' evaluation, which needs to be applied in order to address the research question.

3.1 Mechanical Design Process

As it is hypothesized that it is possible to improve performance of the valve-controlled fluid power systems through implementation of alternative design solutions, i.e. rotary motion-based spools, the mechanical design process was adopted and followed in order to design, develop and analyse the new valve. The thesis encompasses the third, fourth and fifth phases in the six-phases mechanical design process illustrated in the Figure 3.1.

The design process scheme, see the Figure 3.1, sets the framework for the design investigation and performance evaluation. The Product Definition, Conceptual Design and Product Development phases are divided further into the sub-phases, which became the methodological framework of the research.

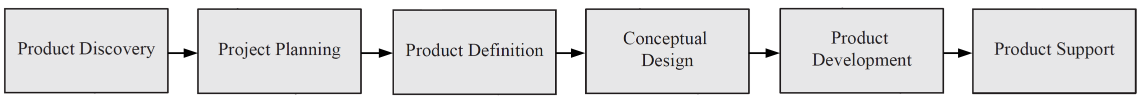

Figure 3.1: The mechanical design process, (Ullman 2009).

3.1.1 Product Definition

During the process of the Product Definition, the potential customers, the requirements, the competing technologies and preliminary engineering specification of the new valve were identified.

As it is shown in the Literature Review and the Introduction, the targeted customers include designers, developers and manufacturers of hydraulic components, fluid power systems and entire working machines, NRMM in agricultural, forestry and construction industries. Due to economic considerations and the tightening regulations imposed on the emission level, they are in a clear demand for more efficient, controllable and environmentally friendly heavy machinery and their components. The same applies in particular to hydraulic systems of these machines. These constitute main customers and general product requirements.

The previous chapter also listed the competing technologies, which are under development, which could potentially resolve these issues. Besides the novel alternatives, there are reliable and time-tested "off-the-shelf" solutions, which are also considered as competing technologies.Among them there are industry standard load sensing and open centre hydraulic architectures. Component-wise, the main competing valve configurations include sliding spool and poppet valves.

The main design problem associated with currently used flow control valve can be described as the mechanical linkage between the meter-in and meter-out ports of the spool valve. To address this problem, the IM arrangement of the valves was adopted. The second design issue of the spool valves is high pressure drops created by these valves, which causes large power consumption of the entire hydraulic system. To solve this problem, the novel geometrical configuration of the valve throttling parts was suggested as a result of the conceptual design development.

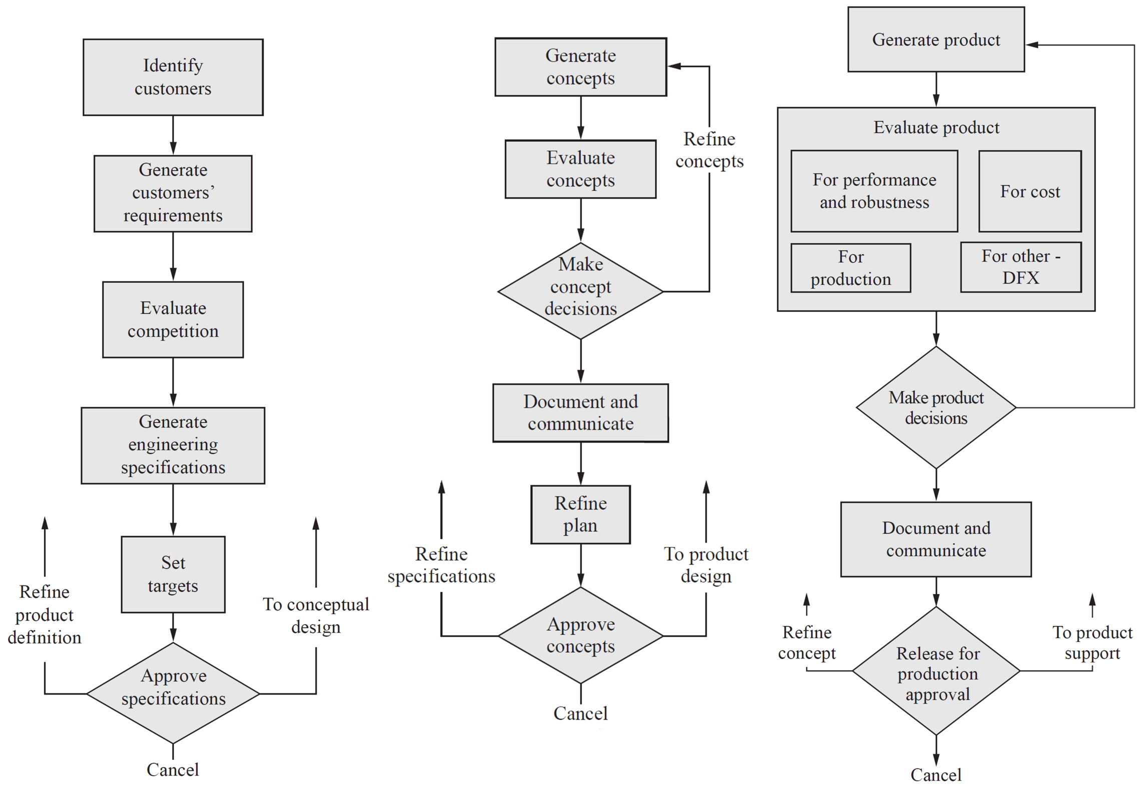

(a) The Product Definition phase. (b) The Conceptual Design phase. (c) The Product Development phase.

Figure 3.2: The main phases of the mechanical design process followed in the thesis, (Ullman 2009).

The key design requirements for the new valve design determined after the detailed Literature Review are summarized as follows:

- Valves are arranged in the IM configuration, see the Figure 2.8
- Single valve has a 2/2 configuration of the possible positions and hydraulic lines
- The anti-cavitation function of the IM valve assembly is ensured for the cylinder chambers
- Spool actuation is implemented through rotation
- Spool return to the neutral position is ensured

For the engineering specification and targets development, the pressure drop created by the single valve in the IM layout was selected as the main parameter for improvement. It is a measure of energy efficiency of the developed design solution. The bench marking will compare the metering characteristics of the new valve with the available industry standard and valves. Additionally, the actuation effort needed to change the valve orifice area, and, hence, implement flow control, will be studied in following chapters. These form engineering specification for the product development.

Estimation of the the key parameters and their comparison with the competing technologies is described in the following chapters.

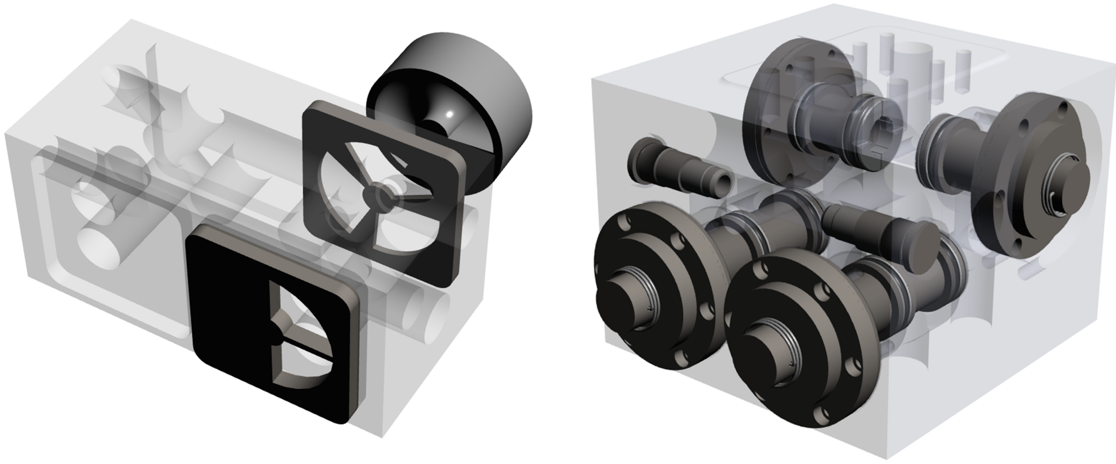

(a) The sectorial spool concept.

(b) The tubular spool concept.

Figure 3.3: Suggested concepts.

3.1.2 Conceptual Design

The main purpose of the Concept Development is to suggest exact geometric forms, which would ensure the design operates as anticipated, performs the planned functions and addresses the design requirements. It also guarantees design compliance with the intended outcome and meeting all functional criteria. Concepts must be refined enough to allows evaluating the technologies, which are needed to realize them, to evaluate their basic architecture and their manufacturability (Ullman 2009).

The reviewed literature on flow control valves revealed the potential of rotary valves to resolve common issues associated with the valves geometry. Within rotary valves, little consideration has been given to the exact structure of valves using a tubular spool. However, the new design compared to common solid rotary spools could require less power to actuate the valve, i.e. to change the spool angular position. The main reason for this consists in minor moment of inertia of a hollow circle, a tube, that forms a cross-section of such spools comparing with the solid circle (Budynas et al. 2006). At the same time, flow passages of a common solid rotary spool are milled on the external surface of the spool. That makes their moment of inertia larger, their structure becomes bulkier and harder, more power-demanding to rotate. Therefore, the hollow, or tubular, spool concept was adopted as the main differentiating design feature of the valve under development.

Before the adoption of the hollow spool as the main regulating part of the valve, a few design concepts were generated and two of them were evaluated, see the Figure 3.3. The developed concepts addressed the above mentioned key design requirements. Between the two suggested concepts, the tubular spool concept was considered as worthy of the further investigation and eventually was adopted. From initial brief evaluation, the sectorial spool concept would require bigger actuation efforts to rotate the spool due its larger size for the same hydraulic line diameter. Another reason to discard this concept is more complicated internal geometry of the sectorial spool to manufacture and control.

The principal design scheme, which reflects implementation of the required functions in the exact geometrical representation, is depicted in the Figure 3.4. The scheme ensures four valves are hydraulically connected in the IM arrangement through the set of internal channels. But the differentiating factor between parallel and perpendicular spool axes layouts is the size of a spool driver – a stepper motor. The perpendicular arrangement will result in bigger overall sizes of the entire assembly. For this reason the more favourable concept is the parallel layout.

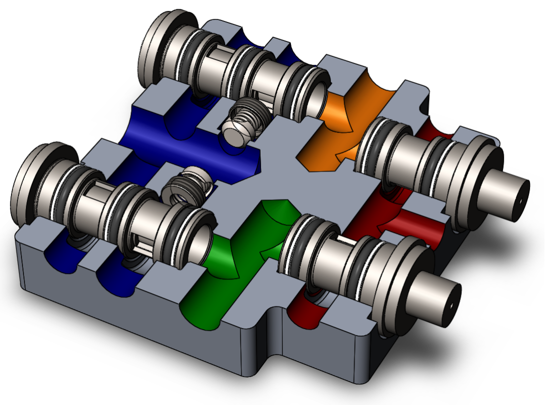

(a) Parallel spool axes.

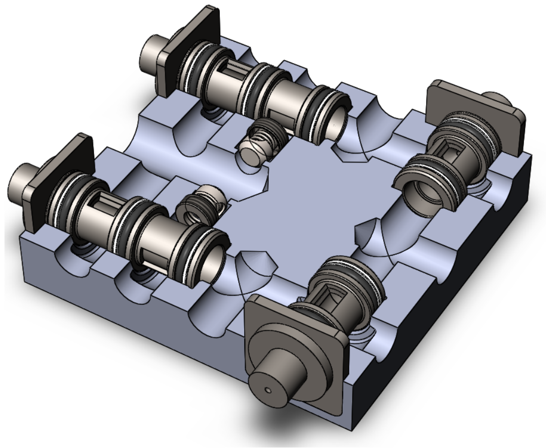

(b) Perpendicular spool axes.

Figure 3.4: The adopted concept. Different axes orientations.

3.1.3 Design Development

Once the concepts was finalised, the exact design, or the product, development commenced. The process consisted in suggesting, elaborating and selecting exact design solutions, which would meet requirements of manufacturing, assembly and use. In other words, on this stage every mechanical part and the entire assembly in the concepts start to take specific shapes and forms in order to satisfy requirements of performance, production, minimal cost, manufacturability, according to the followed process, see the Figure 3.2. Therefore, at this stage the design for cost (DFC), design for assembly (DFA) and design for manufacturability (DFM) techniques were considered.

The overall goal was to ensure the set of parts in the final assembly includes minimal necessary parts. This will provide the minimal mass, size and, hence, cost of the product. Moreover, DFM implies every mechanical part can be manufactured with existing and available technological methods. Part's design features do not include complicated profiles. While seeking exact dimensions of the assembly and the parts, it is necessary to keep intended valve functionality.

In this phase, two separate design development processes were undertaken simultaneously. The first design process considered the design of the single valve. It resulted in the creation of several design variants, see the Figure 3.5. During this process the valve design was evolving, changing after every design iteration. Design variations continued until the moment when the design contained the minimal number of constituent parts and it was deemed feasible to manufacture without compromising the key functions and requirements.

The Figure 3.5 illustrates design variants, which were discarded after anticipated performance and manifacturability considerations. For example, variants 2 and 3 have been considered unfavourable due to the fact that the sleeve in these designs is a separate part which needs to be fixed from turning and axial movement. In the variant 1, the sleeve is a single part, which is assembled with the body. Similar design analysis consideration enabled design evolution until the design was deemed simple enough to study and prototype manufacturing, at the same time capable of carry out intended functions.

Parallel to this process, the development of the four-valves assembly was being performed, see the Figures 3.4 and 3.6. The main goal was to ensure the valve body's internal canalisation implements the IM configuration. Moreover, the valve body needed to incorporate the set of anti-cavitation check valves, enough space to locate spool drivers with minimal required material.

At this point, the concept design is considered ready for the Design Evaluation. As a part of the Design Development phase, performance evaluation parameters were identified. For the

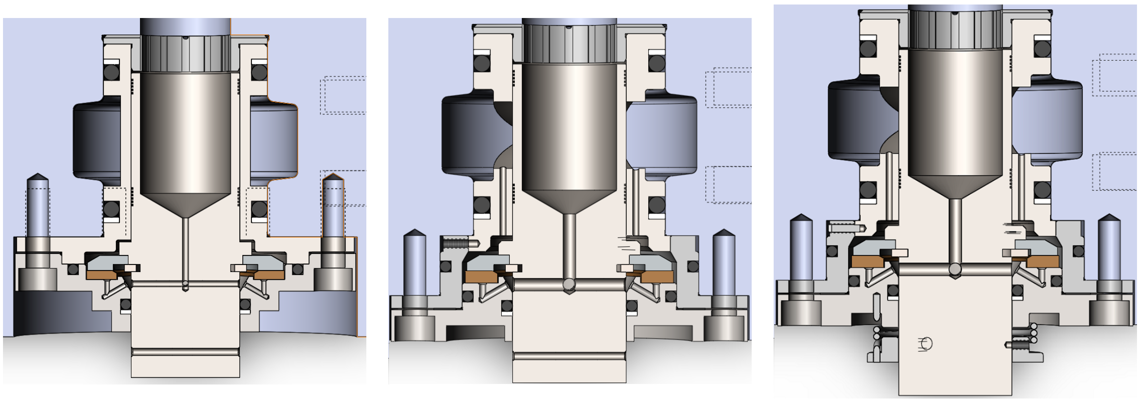

(a) Variant 1 (b) Variant 2 (c) Variant 3

Figure 3.5: Single valve design development. Different variants of the single valve design.

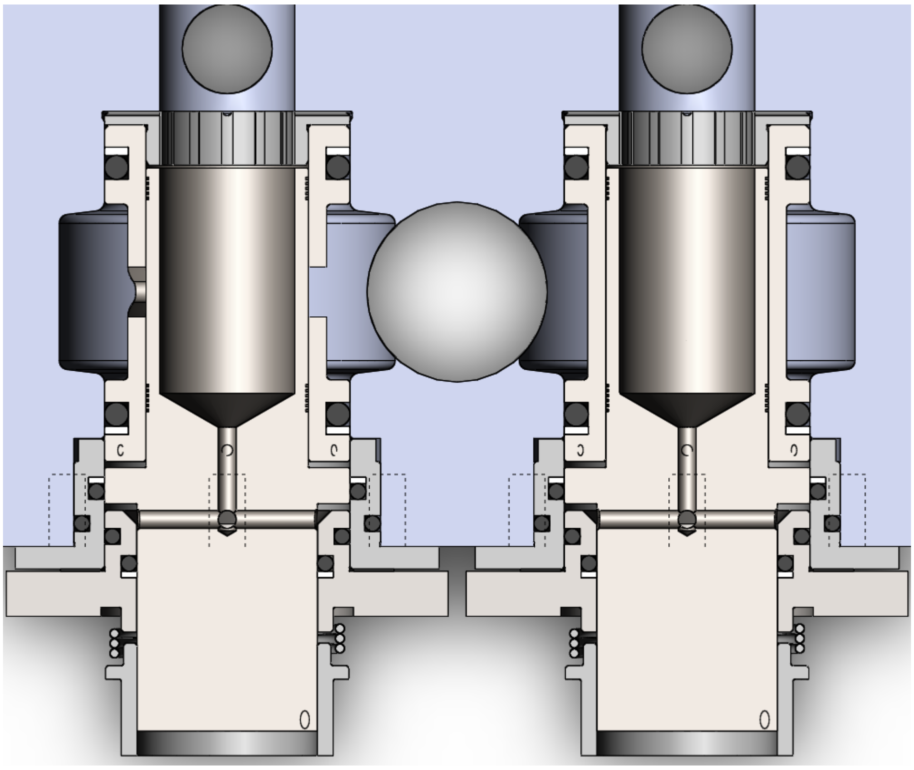

(a) Valves in the exhaust (tank) branch

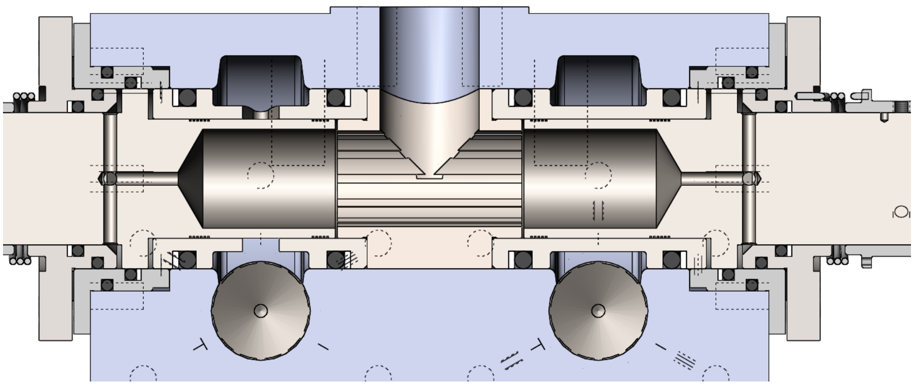

(b) Valves in the discharge (pump) branch

Figure 3.6: Four-valves assembly design development.

hydraulic valves, the key parameters are metering characteristics, actuating efforts and a created pressure drop due to throttling. These factors along with others were studied in this thesis numerically, experimentally and analytically. Description of the evaluation process and its results are discussed in the following chapters.

The quantitative evaluation of the identified performance parameters of the new valve through a mixture of analytical, numerical and experimental modelling techniques constitutes the methodology of the research as these allow to verify and to validate the proposed research question.

3.2 Initial Valve Design

This section outlines the initial proposed design of the rotary tubular spool valve (RTSV) and the assembly of four valves in the IM arrangement. It gives a detailed description of the design geometry for the single valve as well as the valve assembly for the further analysis. The chapter also summarizes the key operational principle of the selected concept and results of the design development of the valve.

3.2.1 Single Valve

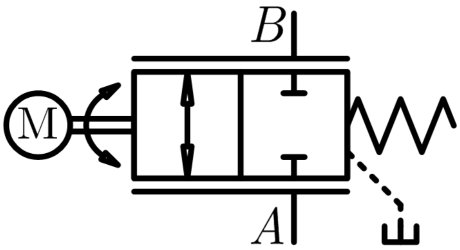

Figure 3.7: The hydraulic symbol of the valve.

The design of the new flow control unit represents a normally closed two-position, two-way flow control valve with direct electromagnetic proportional control of the spool and a non-variable spring return mechanism to the valve's closed state. Applying terms and symbols of BS ISO 1219-1:2012, the graphical symbol for the valve is illustrated on the Figure 3.7.

All key parts are housed in a valve's casing. It ensures supply of working fluid to the spool, collection and guidance of oil to the hydraulic actuator via built-in channels after the flow passes throttling orifices. The valve design implies a cartridge assembly method allowing multi-valve arrangement in a single body given enough valve socket ports and matching internal channelling. Manufacturers favour such assembly method because cartridge valves are easy and fast to manufacture, assemble, repair, maintain or replace in the event of a mechanical failure.

In this new proposed valve's structure, liquid enters the hollow cylindrical spool's central cavity through the end face opening from the supply channel at the A port. Then it outflows from the two specially profiled cut-outs on the outer surface of the spool's cylinder and passes through the sleeve windows to the collecting chamber of the valve body, see the Figure 3.8. The flow rate is regulated by the opening area, which is formed by the overlap between the slots of the spool and the sleeve, see the Figure 3.10. The total orifice area is also a function of each window profile. Consequently, the angular position of the spool in the sleeve defines the output oil's flow rate.

To minimise and compensate the reactive transverse, radial flow forces originating from the flow momentum change, which could lead to bending and jamming of the cantilevered spool inside the sleeve, two throttling orifices are located on the diametrically opposite sides of the spool's cylindrical surface, Figure 3.9. The axisymmetric profile also increases the strength of the spool by reducing the mechanical stress in the material of the part, compared to a case with a single larger orifice or multiple smaller cut-outs.

The suggested spool works under torsion conditions from a steady flow torque. Its throttling cross-section in a double-orifice arrangement has a higher polar, or second moment of inertia than a single orifice design with the same throttling opening area. Additionally, a two slot configuration halves the total discharge passing through the single orifice, which in turn increases the valve's throughput and lowers pressure drop across the valve.

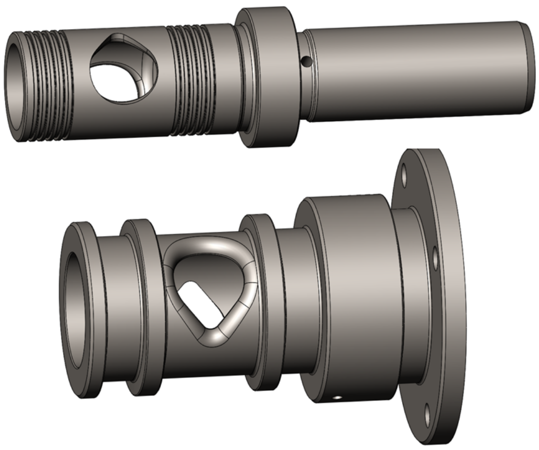

(a) The throttling parts of the valve.
Top – movable spool, bottom – static sleeve.

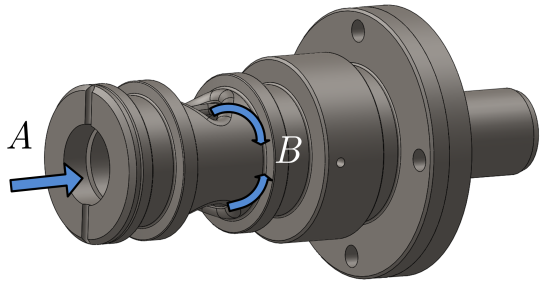

(b) The outflow scheme from throttling elements.

Figure 3.8: The throttling parts and the outflow scheme.

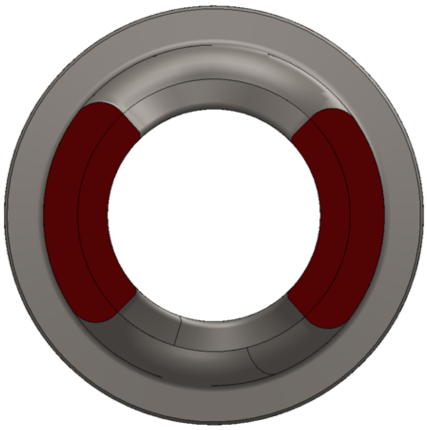

(a) The open state of the valve, ϕ=90°.

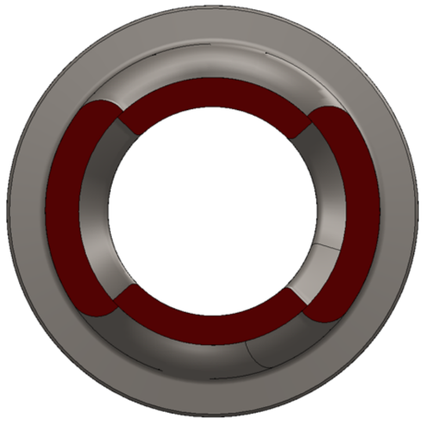

(b) The closed state of the valve, ϕ=0°.

Figure 3.9: The extreme states of the valve. The inner part – the spool, the outer – the sleeve.

The spool incorporates two sets of circumferential grooves cut on both sides of the throttling holes, see Figure 3.8a. The purpose of the grooves is to lower coulomb friction in the spool-sleeve assembly and prevent silting of the spool inside the sleeve due to the small radial clearance between those parts (Merritt 1968). The grooves also play a role of labyrinth sealing, which prevents leakages to spool bearing housing and flow over to the supply channel.

The Figure 3.8b shows the guiding sleeve located at the entrance to the spool central cavity. The part guides the flow into the spool's central chamber. The inner cylindrical surfaces of the sleeve could be smooth or incorporate a set of longitudinal splines to prevent transversal flow circulation. In the studied design the smooth option has been chosen to facilitate manufacturing of the part. The sleeve also has two semicircular slots shown on the Figure 3.8b. These allow for simple dismantling of the assembly.

The profile of the sleeve's throttling holes is identical in shape to the spool's windows, but the openings on the spool and the sleeve are pointed towards each other. In the current study, drop-shaped windows are used on both the spool and the sleeve. This allows a very smooth increase of the opening area when throttling begins. In turn, this ability provides the smooth start of actuation, as well as accurate velocity control of a hydraulic actuator.

Location of the throttling windows on the cylindrical surfaces makes it easier to cut complex

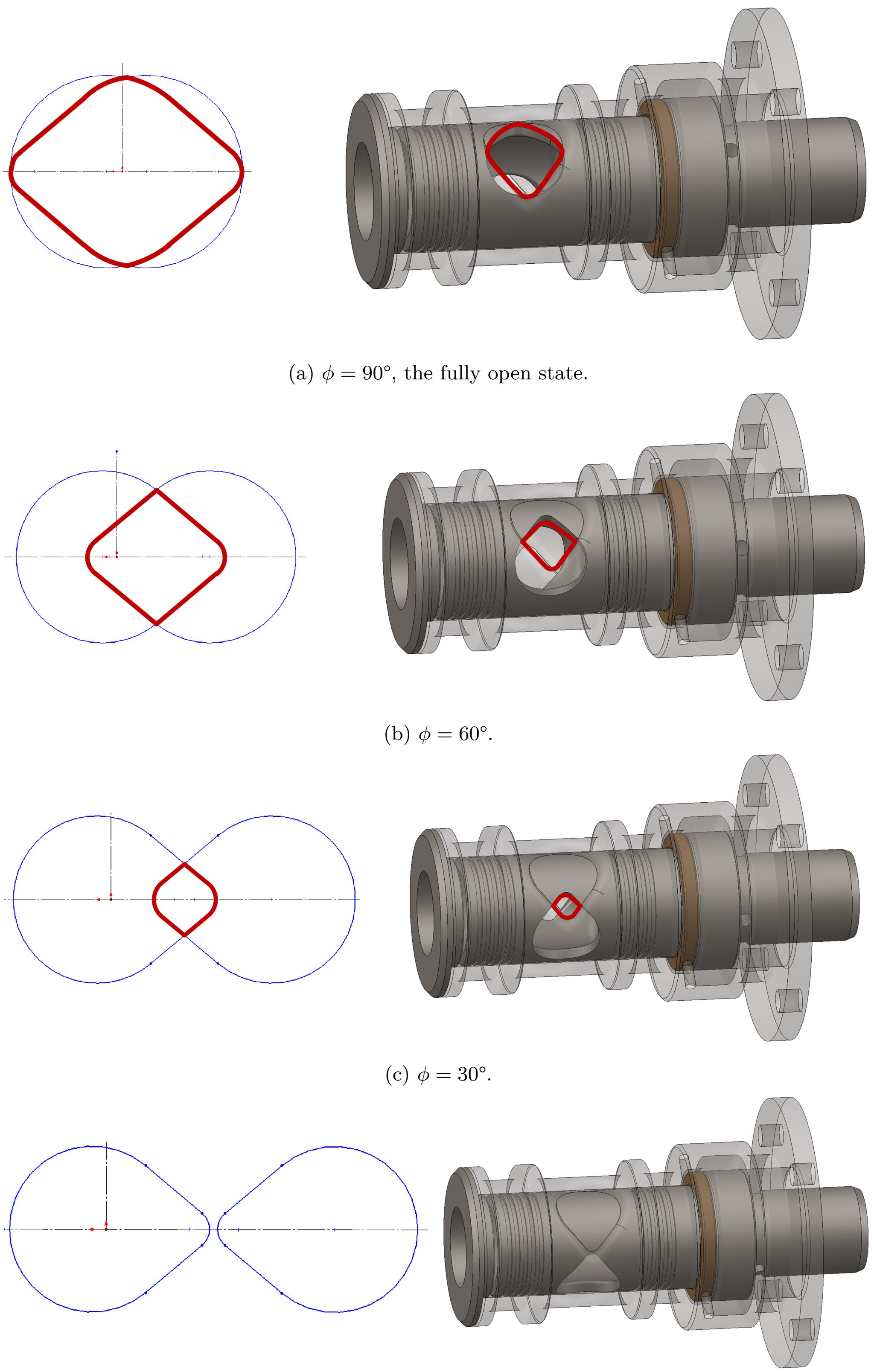

(a) $\phi = 90°$, the fully open state.

(b) $\phi = 60°$.

(c) $\phi = 30°$.

(d) $\phi = 0°$, the fully closed state.

Figure 3.10: Location and area measurement of the single orifice at different spool angular positions. The sleeve is transparent.

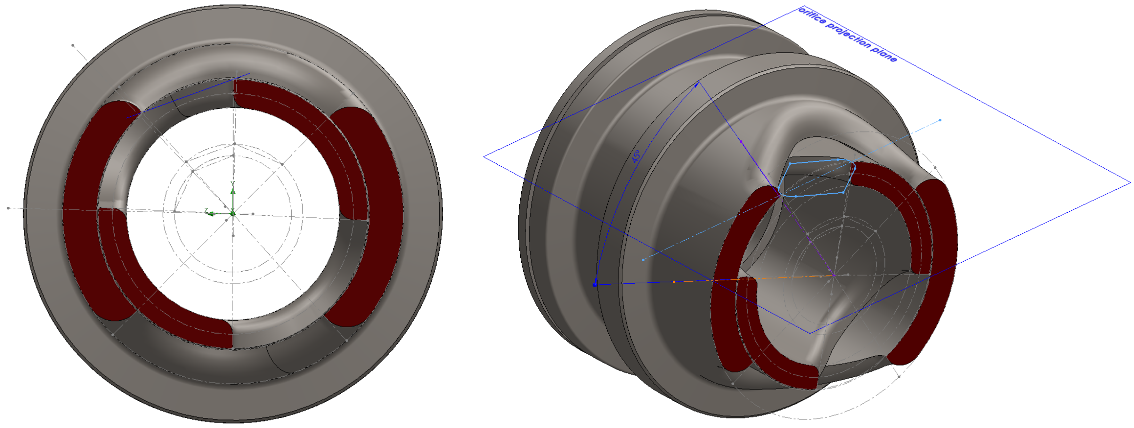

(a) Projection plane for $\phi = 45°$ on a section view.

(b) Projection plane and single orifice projection for $\phi = 45°$ on an isometric view.

Figure 3.11: Projection plane and orifice profile projection.

opening profiles, which improves manufacturability of the flow regulating parts. The combination of the windows' shapes, nonlinear nature of the total orifice area, the stroke angle and the rate of spool rotation makes the developed orifices' arrangement unique in its class. This flow regulation potential is currently unobtainable by any ordinary linear sliding spools. The required flow rate can be achieved in this valve through the specific orifice area, which depends on the input control signal.

Orifice Area

In order to determine the relation between the single orifice area and the angular position of the spool, swept or unrolled profiles of the windows have been used in a planar study, see Figure 3.10. By overlaying spool and sleeve profiles and replacing angular displacement with linear one, the intersection area on a projection plane can be measured, which is equal to the single orifice area $A_{sing.or.}$. Doubling intersection area of the single orifice yields the total orifice area of the valve depending on the spool position, which is referred further on as the valve opening area.

$$A(\phi) = A_{tot.or.}(\phi) = 2A_{sing.or.}(\phi) \tag{3.1}$$

To measure the orifice area the spool and sleeve orifice profiles were projected on the plane parallel to the spool axis and passing through the most distant points on the spool and sleeve profiles forming the profiles, see the Figure 3.11a and the Figure 3.11b. On these figures, the projections plane is coloured in blue.

The orifices on the sleeve and the spool provide the opening area function shown on the Figure 3.12. The increase of the area is non linear with more gradual increment at lower angles of opening. The slow non-linear change in the area at the start of actuation is a special design feature of the rotary valve. The dependency at $\phi > 50°$ of the spool angular position is steeper and much closer to a linear rate of opening, reaching the total orifice opening of $A_{tot.or.} = 186.99\,\mathrm{mm}^2$.

Projecting the orifice profiles also allowed measuring the total length, or perimeter S, of the projection lines forming the throttling opening. This was later used in calculation of the opening's hydraulic diameter D_h and Reynolds numbers Re for different spool angular positions ϕ. The result of the perimeter measurement is shown in the Figure 3.13.

To model mathematically valve performance, curve fitting and interpolation have been performed via MATLAB curve fitting application. The power law has been used that gave the following goodness of fit. The sum of squares due to error 27.714, R-square 0.99, root mean squared error 0.9306. The resultant area function and power law coefficients with 95% confidence bounds are

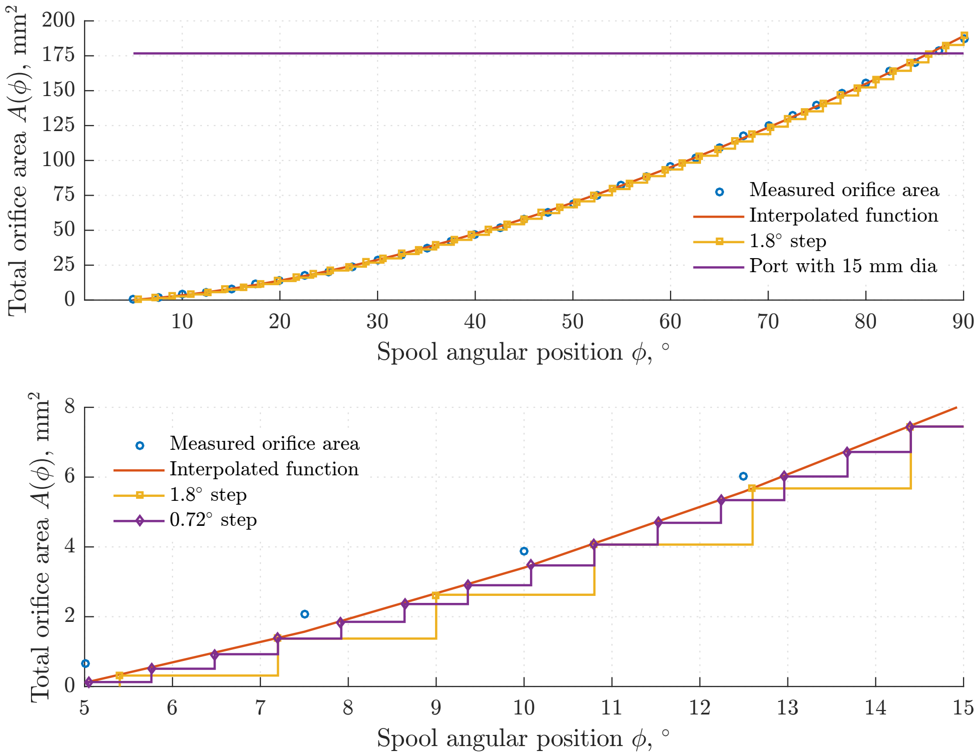

Figure 3.12: Total orifice area function, $A(\phi)$.

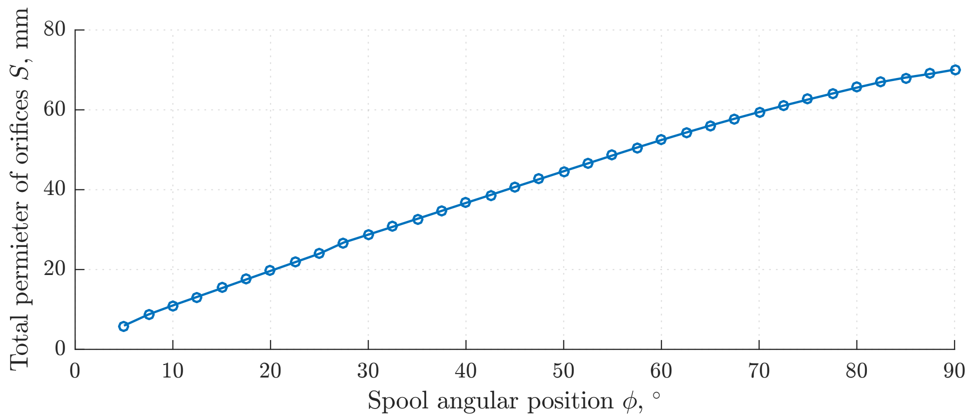

Figure 3.13: Total perimeter of throttling orifices, $S(\phi)$.

$$A(\phi) = \begin{cases} 0.1015\phi^{1.675} - 1.397 & \text{if } 0 < \phi \leq 90° \\ 0 & \text{otherwise} \end{cases} \tag{3.2}$$

Dimensioning

The sizing process of valve parts included exact dimensioning of the throttling parts and maintaining the same cross-sectional area of the entering flow A_{in} throughout the valve up to the exit port with the area A_{out}. This approach ensures the constant cross section of the flow and reduces flow disturbances. Since there are two throttling orifices on the spool and the total flow is split in two jets, the annular area of the flow A_{an} needs to be equal to a half of A_{in}, i.e.

$$A_{in} = A_{out} = 2A_{an}. \tag{3.3}$$

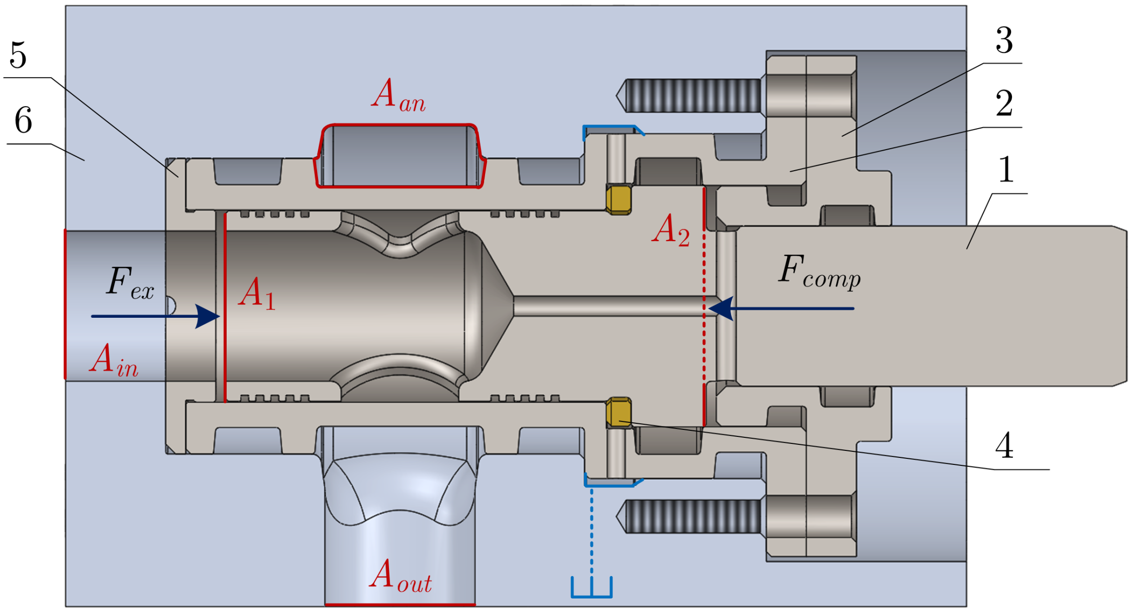

Figure 3.14: The cutaway section of the single valve. Original parts: 1 – spool, 2 – sleeve, 3 – lid, 4 – thrust bearing, 5 – guiding sleeve, 6 – valve body. The region inside the spool to the right of the area A_1 – the spool central chamber or cavity. The annular region with the cross section of A_{an} – the cross-section of the single branch of the collecting channel or chamber. A_{in} and A_{out} – inlet, supply and outlet, service ports respectively. A_2 – the annular area of the spool back, or compensating chamber.

This criterion determines the external diameter of the sleeve d_4, the diameter of the annular gallery d_5 and its length l_{an} inside the body of the valve and the diameters of the inlet d_1 and outlet d_8 ports, as shown in Figure 3.14 and Figure 3.15. Therefore, it is possible to approximate the flow area of the single branch of the collecting chamber as a rectangle with the area as follows:

$$A_{an} = l_{an} \left(\frac{d_5 - d_4}{2} \right). \tag{3.4}$$

Then according the Equation 3.3, the requirement for the constant flow cross-section can be rewritten as following:

$$\frac{\pi {d_1}^2}{4} = \frac{\pi {d_8}^2}{4} = l_{an} \left(d_5 - d_4 \right). \tag{3.5}$$

The tubular spool inside the valve is always subjected to the supply or pump pressure p_{pump} acting on the spool's circular surface A_1. The pump pressure p_{pump} acting on the area A_1 generates the extruding force F_{ex} that pushes the spool out from the valve body.

$$A_1 = \frac{\pi {d_2}^2}{4} \tag{3.6}$$

$$F_{ex} = p_{pump} A_1 \tag{3.7}$$

In order to compensate this force and stabilize the spool in a certain axial position, the working fluid is supplied through the axial channel inside the the spool to its back chamber. There, hydraulic oil under the high pump pressure p_{pump} acts on the annular area A_2 and creates the counter-, or compensating force F_{comp}.

$$A_2 = \frac{\pi \left({d_7}^2 - {d_6}^2 \right)}{4} \tag{3.8}$$

$$F_{comp} = p_{pump} A_2 \tag{3.9}$$

Therefore, assuming pressure levels are equal in the central and the back chambers of the valve, the spool stabilization criterion is

$$F_{comp} \geq F_{ex} \tag{3.10}$$

$$A_2 \geq A_1 \tag{3.11}$$

$${d_7}^2 - {d_6}^2 \geq {d_2}^2 \tag{3.12}$$

It is possible to design the spool such that $A_2 > A_1$ and the compensating force exceeds the ejecting force, i.e. $F_{comp} > F_{ex}$. In this case, the spool is pushed against the brass thrust bearing. The material is selected in order to ensure a low friction pair between the spool and the bearing, i.e. austenitic steel with brass. The thrust bearing features radial grooves to allow the oil leakage from the spool-sleeve clearance to drain to the tank. In the Figure 3.14, the blue slot cut in the body collects this leakage and drains it to the tank.

The most critical dimensions of the valve moving parts are spool internal d_1, spool external d_2 and sleeve internal d_3 diameters. These determine the maximum amount of flow that the valve can modulate without cavitation as well as amount of internal leakage at the closed state, viscous friction exerted on the spool in motion and eventually manufacturing requirements. Since these dimensions are of significant importance, geometric form requirements are imposed on these surfaces, i.e. requirements of cylindricity and circular run-out, which combines straightness and roundness demands. The exact dimensions can be found in the Table 3.1 and the Appendix A.

The combination of the external spool d_2 and the internal sleeve d_3 diameters defines tightness properties of the valve, i.e. amount of possible leakage that can occur at the closed valve. At the same time, the radial clearance c determines a magnitude of viscous friction the fluid in the gap imposes to the spool and eventually to the spool drive. The clearance c also influences ease of manufacturing and assembling of the valve for the tighter tolerances of these surfaces would require more complicated technological techniques.

$$c = \frac{d_3 - d_2}{2} \tag{3.13}$$

The selected diameters of the spool also determine the nominal diameters of hydraulic hoses and pipes, connecting clamps and mounting surfaces. To ensure smooth entering to the central chamber and exit from the valve, the nominal diameter of the hydraulic connector port has been selected equal to the nominal value of the internal spool diameter d_1. The connecting surfaces have been designed according to the standard BS ISO 6162-1 used for high pressure applications that are up to 35 MPa. In this design, the closest standardized diameter has been selected to diameter d_1. In the standard port four threaded M8 holes are used to secure the connecting clamp positioning, see the Figure 3.16.

It was also intended during the design development to avoid, reduce or eliminate altogether where feasible anticipated stress concentrations by preventive design measures. The methods consists in smoothing edges with sharp and right angles, exclusion unnecessary corners, holes and changes of cross-sectional areas of the objects without compromising valve structural functionality.

To conclude, form and location tolerances were assigned to the most responsible surfaces and geometrical elements of the part and assembly design. The surfaces of parts, which form rubbing pairs, were specified with roughness requirements to decrease friction between them. The full package of the developed design documentation, i.e. the assembly and working drawings for the proposed design, the prototype assembly scheme, is appended in the Appendix A and the Appendix B correspondingly.

Contacting surfaces of all mechanical parts are sealed with rubber o-rings and anti-extrusion plastic backup rings to prevent squeezing and extrusion of soft O-rings out due to high oil pressure acting on them. Selection of o-ring sizes, particularly their cross-sectional and landing diameters as well as housing grooves is done according to the BS ISO 3601.

To secure the axial position of the sleeve-spool assembly inside the valve, the sleeve and the lid

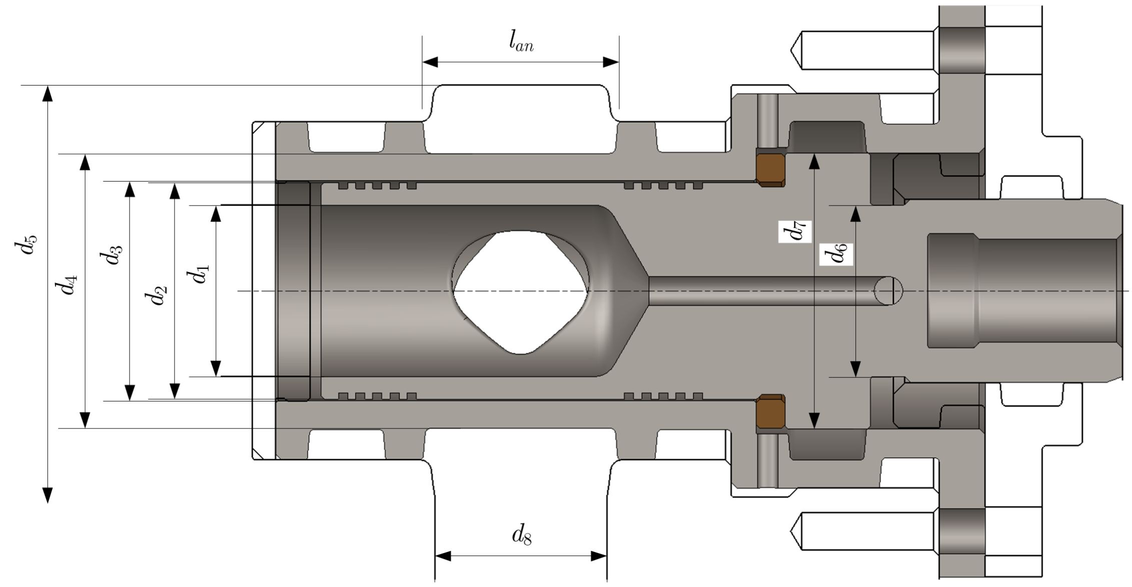

Figure 3.15: The main dimensions of the throttling parts.

Parameter	Symbol	Value	Units
Internal spool diameter; nominal dia of inlet, outlet ports	d_1, d_8	$15^{+0.027}$	mm
External spool diameter	d_2	$19_{-0.033}$	mm
Internal sleeve diameter	d_3	$19.2^{+0.033}$	mm
External sleeve diameter	d_4	$24.1_{-0.084}$	mm
Diameter of the collecting chamber	d_5	$36^{+0.1}$	mm
Spool shaft diameter in the back chamber	d_6	$15^{0}_{-0.1}$	mm
Spool shoulder diameter in the back chamber	d_7	$24.1^{-0.02}_{-0.041}$	mm
Length of the collecting chamber	l_{an}	16	mm
Area of the inlet and the outlet ports	A_{in}, A_{out}	176.71	mm^2
Spool total circular area, the front chamber	A_1	283.53	mm^2
Spool annular area, the back chamber	A_2	279.45	mm^2
Cross-sectional area of the collecting chamber	A_{an}	95.2	mm^2
Area of total orifice opening	$A_{tot.or.}$	186.99	mm^2
Radial clearance of the sleeve-spool gap	c	$0.1^{+0.033}$	mm
Spool moment of inertia (keyway, AISI 4340)	I_{sp}	5.43	$kg\,mm^2$
Spool mass (keyway, AISI 4340)	m_{sp}	97.2×10^{-3}	kg
Spool stroke range	ϕ	0...90	°

Table 3.1: The main geometrical and mass parameters of the throttling mechanism.

are screwed in the housing with a set of four screws M4x20. The full list of the required standard parts is cataloged in the bill of materials (BOM), which can be found in the general assembly drawing in the Appendix A.

Actuation

The flow regulation is attained by turning the spool to a pre-set angle. The spool is controlled by a rotary electric motor. The spool angular position corresponds to a finite value of the opening area that can be calculated and established in accordance with the required metering characteristics by a controller. In this proposed new design solution, the rotational movement of the spool is accomplished via a stepper motor.

The electromechanical motor must ensure accurate positioning of the spool. It also must

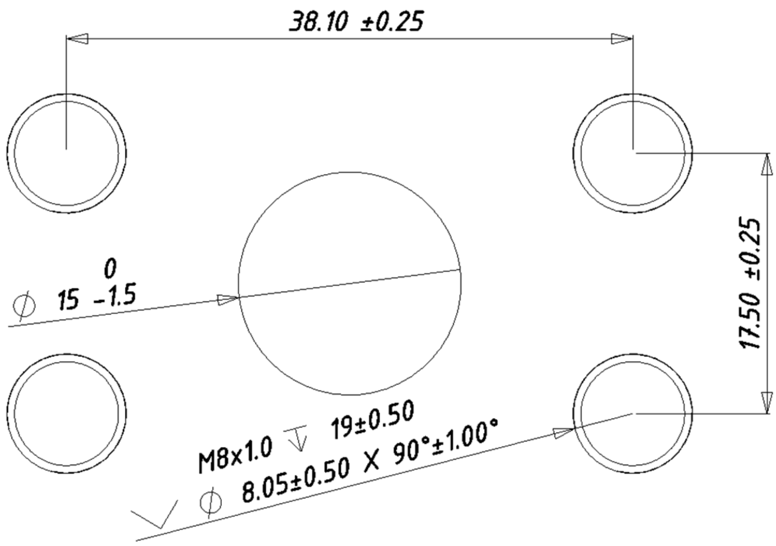

Figure 3.16: The hydraulic mounting surface.

maintain a specified angle even in the presence of significant disturbing fluctuating torques originated from fluid flow, inertia torques in rotary transmission and both mechanical and viscous friction factors. Furthermore, it should transmit the input signal quickly and with minimal deviations from the intended values. The complex, mutable and unsteady nature of the controlled medium favours application of stepper motors with a high holding torque. Other requirements for the spool driver is its ability to withstand a high holding torque providing short settling time during state switch.

Among electrical motors, stepper are notorious for the highest available torque at a set position, the holding torque. Since the operation of the valve is quasi-static, the combination of the high holding torque and the fast switching dynamics makes the stepper an ideal choice for the spool drive in rotary valve.

To be able to maintain the exact angular position of the spool at the steady flow regime, the driver holding torque T_{hold} must exceed the torques induced by the flow, viscous friction torque in the spool cavity and in the annular gap between the spool and the sleeve as well as the spring torque turning the spool into the initial, closed position. For that reason, the holding torque is the main characteristic affecting the selection of the stepper motor. Thus, the motor selection criterion is as follows

$$T_{hold} \geq f_s \sum T_{dist}, \tag{3.14}$$

where f_s – is the factor of safety (FOS), providing a torque safety margin.

In conventional valves, the spool's return to a neutral state is performed with compression centering springs. This is used to ensure, that in the absence of an input signal on the spool actuator or its failure the spool closes all hydraulic ports of the valve. That will guarantee there is no flow between them during the no-control condition.

This spring fulfils a safety function. In the rotary valve, a torsion spring is used for the same purpose. Selection of the torsion spring is based on maximum torque needed at the extreme angular positions. The spring must possess enough stiffness to generate a return elastic torque and be able to overcome the torques originated from oil flow, viscous and Coulomb friction between contacting parts in order to close the valve.

The application of the stepper as the spool actuator makes the valve opening stepped as well, see the Figure 3.12. Depending on the resolution or the steps, the opening increment can differ between different stepping motors. However, the range of controllers and microstepping technique are able to achieve the step angles of 1 microdegree.

To reduce a length of the valve-stepper assembly, it is possible to cut a keyway aperture in the spool's shaft, opposite the central chamber. Although introduction of the keyway shortens the structure, decreases the inertial load on the stepper motor and reduces the overall weight of the assembly, such design feature could be challenging for manufacturing, quality control and servicing. As both configurations were under consideration, graphical figures could illustrate both options. These should be viewed as equivalent design solutions.

Among the listed above torque disturbances acting on the spool, steady flow torque is considered as the most prominent. In force terms, for sliding spools steady flow force prevails over the rest force factors and affects the selection of the spool driver mechanism and its control method. Modelling and quantification of the listed disturbances are carried out in following chapters.

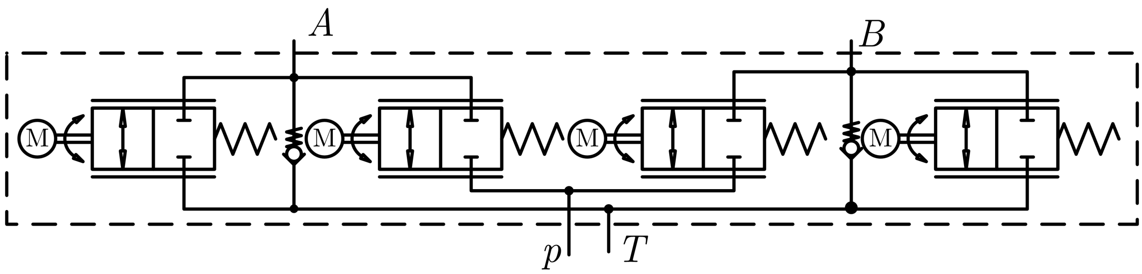

Figure 3.17: The hydraulic scheme of the four valves assembly.

3.2.2 Four-Valves Assembly

To implement the IM concept and auxiliary functions within a single valve unit, it is necessary to design a body housing. This housing should contain four valves, two check valves, mounting surfaces with threaded holes to install stepper motors and the entire assembly on the designated place in a mobile machine.

The valve system location within a machine can be an undercarriage, in the cabin floor or even on a boom of a manipulator for digging machines. The valve block can also be located close to the actuator it is controlling. This may reduce pipework as each valve block would be supplied on a ring main with only short hoses to the actuator. The valve-actuator pipework can be eliminated all together if the valve block is directly mounted onto the actuator. In this case no hoses are needed between the valve block and the actuator.

Presence of six valves in total within a single block makes the fluid subdomain of the full assembly of four valves more intricate than for the single valve, see Figure 3.18c. For this reason, the manufacturing process selected for the valve body in series production is casting as it allows for complicated internal geometry of the parts with multiple galleries, chambers and connecting channels. The initial material for the casing is cast iron. For the prototype testing purposes, the design assumes aluminum alloy as the main material of the main parts as it would allow to ensure complicated internal canalisation through metal cutting processes, milling and turning, thereby, facilitating the production of few prototype parts.

Alternatively, the valves can have individual bodies mounted separately in vicinity of each other and then connected with high-pressure hydraulic pipes or hoses. Although this is one of possible design solutions, it would hinder maintenance and service of the assembly since it increases a required number of connecting clamps, hoses and fittings. Furthermore, introduction of additional mechanical components containing high pressure oil makes it less leak tight as every connection point needs to be sealed.

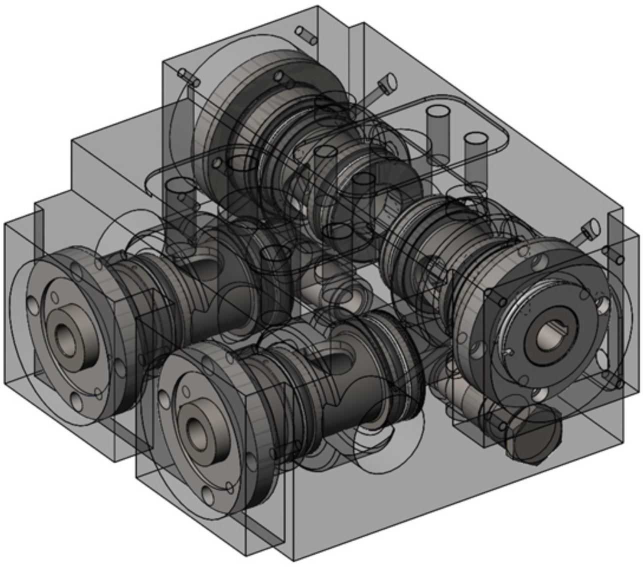

(a) The initial four valve assembly block design.

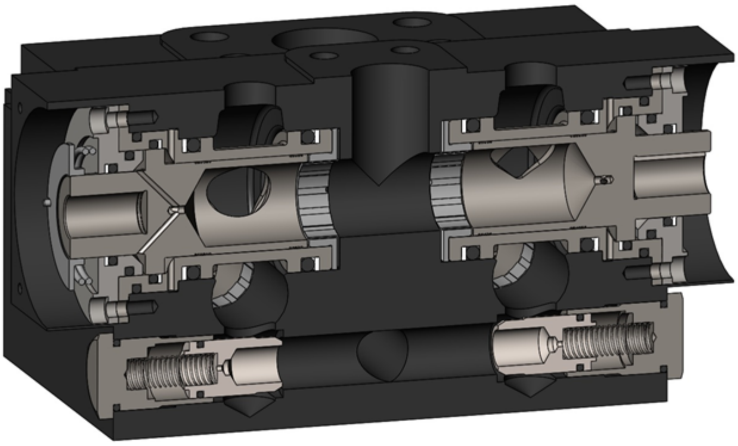

(b) The cut away section of the four valve block.

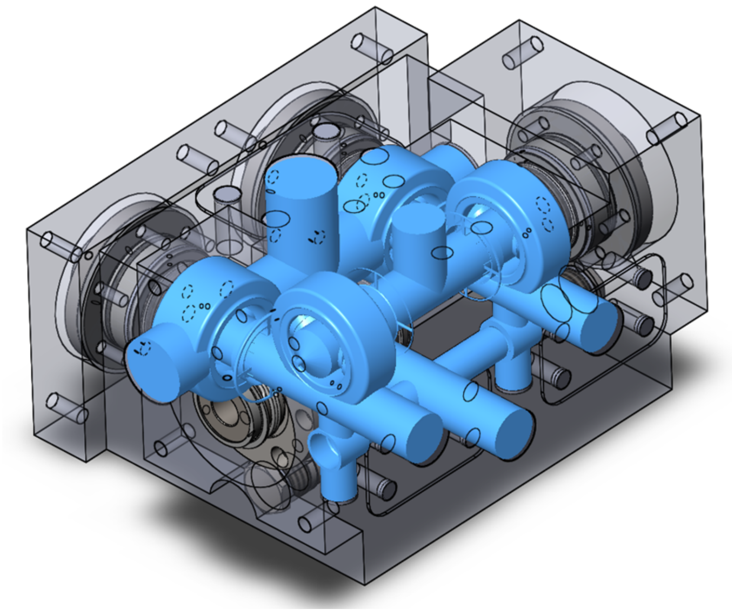

(c) The fluid subdomain of the four-valves assembly.

Figure 3.18: The four valve assembly block.

Check Valves

The designed initial body block incorporates four described above proportional rotary flow control valves, which are driven by four stepper motors, and two check valves. The purpose of check valves is to address cavitation in the cylinder's chambers. If the chamber pressure becomes lower than the pressure in the return or tank line, working fluid is sucked in through these valves to the actuator. Thus, these valves carry out anti-cavitation, safety functions. A full production solution will also need the option with relief valves to protect individual service ports.

3.3 Chapter Conclusions

This chapter described the process of concept generation and evaluation, which is employed throughout the thesis. The key phases of the process were described in more details in application to the flow control valves. Following the first three phases of the mechanical design process, the general product definition was drawn up, main customers and key their requirements were identified. To address these requirements, critical valve functions were specified.

Then, to implement the functions, two design concepts, representing how selected geometric shapes ensure the functions, were suggested and evaluated. According to the brief design comparison, the rotary-tube concept was chosen for the following detailed performance evaluation. Key parameters for evaluation were selected. This chapter commences the concept evaluation, which continues in the following chapters in a form of numerical modelling and experimental testing.

Chapter 4

Fluid Mechanics Modelling

This chapter starts performance evaluation of the valve described in the previous chapter. The goal is to compare the performance of the design to the engineering specifications developed earlier in the design project. It is needed to evaluate the product design relative to the numerical targets of the developed design (Ullman 2009). The design is considered to be refined to the point that numerical engineering measurements can be made.

This chapter discusses hydraulic performance evaluation of the valve. In the thesis, for the main performance parameters study two methods were employed to examine a posed hydraulic problem: numerical, or computational, and experimental. Although an analytical method to solve hydraulic problems is not applicable for the current research project mainly due to high geometrical complexity and a turbulent nature of flows inside the valve, the analytical method was applied for leakage estimation, where the flow is assumed laminar. Analytically estimated leakage was compared with the modelling results.

In this chapter, a parametric computational fluid dynamics (CFD) analysis of the new hydraulic valve is employed since this method makes it possible to obtain performance characteristics of the valve theoretically and optimise them before prototype production and experimental investigation. This approach significantly reduces design and development process. Due to its advantages before purely experimental investigation, it has become an industry benchmark in recent years. The purpose of the CFD in this study is to establish the performance of the proposed valve design by computing metering characteristics and steady flow torques in a modelled environment.

4.1 Preprocessing

In the case of the control valves, the main area of interest are the pressure differential imposed on the hydraulic system and the magnitudes of steady flow torques on the rotary spool under steady-state regimes. This torque is perceived by the spool driver. The magnitude of the flow torques is also the main criterion in selecting the spool motor. These torques are the predominant active load acting on the spool actuator. To estimate these, a series of parametric simulations and analysis of the modelling results have been performed.

Postprocessing visualisation capabilities of the used CFD package help to identify internal fluid flow behaviour within the new valve. Its original geometry of internal channels and chambers defines areas of further geometrical improvement. CFD simulations also allow the visualisation of the changing flow paths corresponding to different spool's angular positions while maintaining the same overall fluid subdomain intact. At any given angular position of the spool, a new fluid subdomain is extracted from the geometrical solid model simulating the effect of change in the orifice area of the valve.

4.1.1 Geometric Model

According to the preceding description of the new design concept, a detailed three-dimensional solid geometrical model of the valve was constructed using the SolidWorks (SW) software suite by Dassault Systems SolidWorks Corp., Waltham, Massachusetts, USA. To study the flow around orifices, a full three-dimensional flow model was utilised instead of a simplified planar fluid subdomain or an axis-symmetrical flow model. This approach eliminates all assumptions made in the two dimensional flow analysis case such as uniformity of the flow paths in any adjacent planes without compromising calculation accuracy (Amirante et al. 2014).

A series of parametric CFD analyses was conducted using the Flow Simulation module of SW. Based on the depicted valve's geometrical model, the internal regions occupied by the oil, which is the fluid subdomain, are modelled. The Figure 4.1 shows the flow paths throughout the fluid sub domain of the single valve, which has been studied further in this chapter.

To facilitate and speed up multiple parametric simulations, the geometry simplification has been implemented. The fluid sub-domain has been reduced to regions directly engaged into the throttling process. Technological clearances and channels fulfilling auxiliary functions, such as axial balancing of the spool, have been omitted. The main simplification has been applied to the spool-sleeve clearance, which was ignored. Therefore, the effect of the sealing grooves on spool lateral balancing was neglected.

4.1.2 Turbulence Model

In the expected application of the developed valve, which is high pressures and high flow rates, the fluid flow inside the valve is considered as turbulent. In the Flow Simulation module, the Favre-averaged Navier-Stokes equations are used, where the effects of the flow turbulence on the mass-averaged flow parameters are considered. The applied Favre averaging method also accounts for fluctuations of fluid density and temperature. The instantaneous equations governing conservation of mass, momentum and energy are as follows (Wilcox 2006):

$$\frac{\partial \rho}{\partial t} + \frac{\partial}{\partial x_i}(\rho u_i) = 0 \tag{4.1}$$

$$\frac{\partial}{\partial t}(\rho u_i) + \frac{\partial}{\partial x_j}(\rho u_i u_j) = -\frac{\partial p}{\partial x_i} + \frac{\partial \tau_{ij}^R}{\partial x_j} \tag{4.2}$$

$$\frac{\partial}{\partial t}\left[\rho\left(e + \frac{1}{2}u_i u_j\right)\right] + \frac{\partial}{\partial x_j}\left[\rho u_j\left(h_s + \frac{1}{2}u_i u_i\right)\right] = \frac{\partial}{\partial x_j}\left(u_i \tau_{ij}^R\right) - \frac{\partial q_j}{\partial x_j} \tag{4.3}$$

where e is specific internal energy, h_s is specific enthalpy, which is defined as following:

$$h_s = e + \frac{p}{\rho} \tag{4.4}$$

To close this system of equations, transport equations for the turbulent kinetic energy and its dissipation rate are employed, the $k - \varepsilon$ model (Wilcox 2006). The adopted model meets accuracy and reliability requirements in the considered valve study and performs satisfactorily in solving fluid power problems (Palumbo et al. 1996).

In SW Flow Simulation the classical two-equations $k - \varepsilon$ empirical model for simulating turbulence effects in fluid flow CFD simulation (Wilcox 2006) is used as it requires the minimum amount of additional information to define the flow (SolidWorks 2013b). The modified $k - \varepsilon$ turbulence model with damping functions (Lam and Bremhorst 1981) describes laminar, turbulent, and transitional flows of homogeneous fluids consisting of the following turbulence conservation laws (Sobachkin and Dumnov 2013):

$$\frac{\partial \rho k}{\partial t} + \frac{\partial \rho k u_i}{\partial x_i} = \frac{\partial}{\partial x_i}\left(\left(\mu + \frac{\mu_t}{\sigma_k}\right)\frac{\partial k}{\partial x_i}\right) + \tau_{ij}^R - \rho\varepsilon + \mu_t P_B, \tag{4.5}$$

$$\frac{\partial \rho\varepsilon}{\partial t} + \frac{\partial \rho\varepsilon u_i}{\partial x_i} = \frac{\partial}{\partial x_i}\left(\left(\mu + \frac{\mu_t}{\sigma_\varepsilon}\right)\frac{\partial \varepsilon}{\partial x_i}\right) + C_{\varepsilon 1}\frac{\varepsilon}{k}\left(f_1 \tau_{ij}^R \frac{\partial u_i}{\partial x_j} + C_B \mu_t P_B\right) - f_2 C_{\varepsilon 2}\frac{\rho\varepsilon^2}{k}. \tag{4.6}$$

Here P_B represents turbulence generation due to buoyancy and can be written as

$$P_B = -\frac{g_i}{\rho\sigma_B}\frac{\partial \rho}{\partial x_i}, \tag{4.7}$$

where g_i is the component of gravitational acceleration in direction of x_i. In this research, flow simulation in the rotary valve was conducted without consideration of an effect of gravity on a fluid flow since in power hydraulics applications surfaces forces from pressure tend to greatly exceed body forces from gravity and inertia. Therefore, in this research the buoyancy term was neglected.

The empirical $k - \varepsilon$ constants have the following typical values (SolidWorks 2015): $\sigma_k = 1$, $\sigma_B = 0.9$, $\sigma_\varepsilon = 1.3$, $C_\mu = 0.09$, $C_{\varepsilon 1} = 1.44$, $C_{\varepsilon 2} = 1.92$ and constant $C_B = 1$ if $P_B > 0$, and 0 otherwise.

Following Boussinesq assumption, the Reynolds-stress tensor for Newtonian fluids has the following form:

$$\tau_{ij}^R = \mu\left(\frac{\partial u_i}{\partial x_j} + \frac{\partial u_j}{\partial x_i} - \frac{2}{3}\delta_{ij}\frac{\partial u_k}{\partial x_k}\right) - \frac{2}{3}\delta_{ij}\rho k. \tag{4.8}$$

Here δ_{ij} is the Kronecker delta function (it is equal to unity when $i = j$, and zero otherwise), μ is the dynamic viscosity coefficient, k is the turbulent kinetic energy and μ_t is the turbulent eddy viscosity coefficient, which is determined from

$$\mu_t = \frac{f_\mu C_\mu \rho k^2}{\varepsilon}. \tag{4.9}$$

Here f_μ is the turbulent viscosity factor. It is determined by the expression

$$f_\mu = \left(1 - e^{-0.0165 R_y}\right)^2 \left(1 + \frac{20.5}{R_T}\right), \tag{4.10}$$

$$R_y = \frac{\rho\sqrt{k}y}{\mu}, \qquad R_T = \frac{\rho k^2}{\mu\varepsilon} \tag{4.11}$$

Here y is the distance from from a point to the wall and Lam and Bremhorst's damping function f_1 and f_2 are determined from

$$f_1 = 1 + \left(\frac{0.05}{f_\mu}\right)^3, \qquad f_2 = 1 - e^{{R_T}^2} \tag{4.12}$$

Lam and Bremhorst's damping functions f_μ, f_1, f_2 decrease turbulent viscosity and turbulence energy and increase the turbulence dissipation rate when the Reynolds number R_y based on the average velocity of fluctuations and distance from the wall becomes too small. When $f_\mu = 1$, $f_1 = 1$, $f_2 = 1$ the approach obtains the original $k - \varepsilon$ model.

The heat flux vector, q_j, is defined by

$$q_j = \left(\frac{\mu}{\mathrm{Pr}} + \frac{\mu_t}{\sigma_c}\right)\frac{\partial h}{\partial x_j} \tag{4.13}$$

where Pr is the Prandtl number, $\sigma_c = 0.9$ is the constant in the $k - \varepsilon$ model.

Wall Function

To simulate fluid boundary layer effects near solid bodies, to solve the Navier-Stokes equations with the two-equation $k - \varepsilon$ turbulence model and to evaluate skin friction in these regions a "wall function" approach (Launder and Spalding 1974) is utilized in the Flow Simulation module. Instead of a logarithmic profile, SW Flow Simulation employs Van Driest's profiles (Driest 1956). Additionally, a "two-scale wall functions" approach to describe a turbulent boundary layer and fit a fluid's boundary layer profile relative to the main flow's properties is employed (SolidWorks 2013b).

When the number of cells across the boundary layer is sufficient (more than 10) the simulation of laminar boundary layers is done via Navier-Stokes equations as part of the core flow calculation. For turbulent boundary layers proceeding from the Van Driest mixing length (Driest 1956) SW Flow Simulations uses following dependency of the dimensionless longitudinal velocity u^+ on the dimensionless wall distance y^+ (SolidWorks 2013b)

$$u^+ = \frac{u}{\sqrt{\frac{\tau_w}{\rho}}} = \int_0^{y^+} \frac{2d\eta}{1 + \sqrt{1 + 4K^2\eta^2\left(1 - e^{-\frac{\eta}{A_v}}\right)^2}}. \tag{4.14}$$

Here $K = 0.4504$ is the Karman constant and the Van Driest coefficient is $A_v = 26$.

4.1.3 Mesh

Before processing, a mesh, or a grid, the fluid subdomain needs to be built. The Flow Simulations module enables splitting the fluid domain into cells with adjustable resolution. Then, the governing partial differential equations, that are the Navier-Stokes and transport equations, are solved in nodes, in centres of the mesh cells. The Flow Simulation solves the governing equations with a discrete numerical technique based on the finite volume discretization method as it satisfies requirements of conservation nature of the governing differential equations.

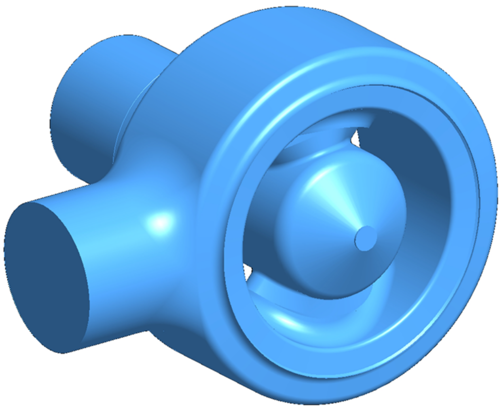

Figure 4.1: The fluid domain of the single valve.

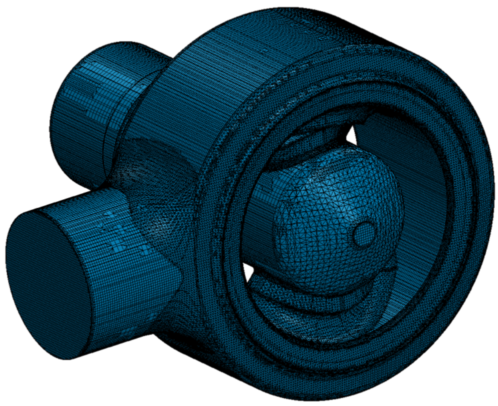

Figure 4.2: The mesh with ≈ 1 million fluid cells.

The mesh cells are rectangular parallelepipeds with orthogonal faces, which are parallel to the specified axes of the Cartesian coordinate system. The near-boundary cells are fractions of the original parallelepiped cells that are cut by the solid matter geometry boundary. Thus, the resulting near-boundary cells are polyhedrons with both axis-oriented and arbitrary oriented plane faces, partial cells. All physical and inertial parameters are referred to the mass centres of the cells within the control volume (SolidWorks 2015).

The module uses the immersed body meshing approach and yields the structured and uniformed Cartesian mesh with an irregular distribution of the mesh cells, which results in the faster calculation of mesh-based information required by the solver. The approach also speeds up the search for data associated with neighbour cells. The Cartesian-based method has been shown to deliver the lowest local truncation error when the Navier-Stokes equations are discretized onto the mesh, to simplify navigations on the mesh and to ensure robustness of the differencing scheme by the absence of secondary skewed faces (SolidWorks 2013a).

Automatically constructed initial meshes in SW vary in level of fineness, i.e. cell sizes. The SW built-in mesh generating algorithms enable on-the-fly mesh optimisation and obtaining the fine enough mesh for purposes of valves design and simulation without resorting to any further mesh refinement. In these parametric studies, the minimum gap size and minimum wall thickness of the mesh were assigned to 1 mm and 0.01 mm respectively. Both parameters influence the characteristic cell's size and computational domain resolution in narrow channels. Flow Simulation generates the mesh to have a minimum of two cells per the specified minimum gap size. The wall thickness parameter defines the refinement level of the mesh at the fine geometrical elements such as sharp edges and small protrusions (SolidWorks 2015).

Applied solution-adaptive refinement process allows splitting the mesh cells into the high-gradient flow regions, which cannot be resolved prior to the calculation and merging the mesh cells in the low-gradient regions. It serves to minimize the spatial error arising from the discretization of the governing differential equations (SolidWorks 2013a).

Mesh cells are not uniform in sizes across the fluid subdomain but maintain the Cartesian structure with the orthogonal faces. Areas adjacent to the throttling orifices are subjected to further automated solution adaptive refinement with the aim to optimize mesh distribution by increasing the number of fluid cells in areas with significant changes of variables and flow restrictions.

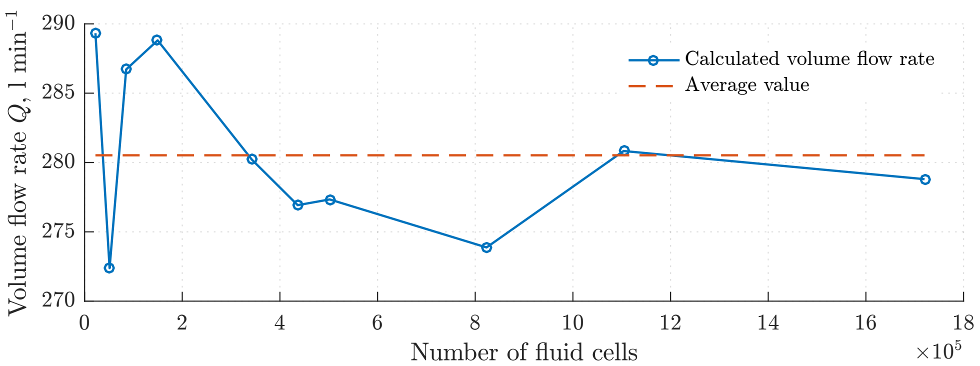

Figure 4.3: Grid independence study results. The mean value $\overline{Q} = 280.46\,\mathrm{l\,min^{-1}}$, the standard deviation $\sigma = 5.97\,\mathrm{l\,min^{-1}}$, which is 2.13% deviation from the mean value.

Grid Independence

A grid independence study has been conducted for the case of $\Delta p = 1\,\mathrm{MPa}$ pressure differential between inlet and outlet openings of the valve and the spool angular position $\phi = 90°$, the full open state. For specified conditions, several meshes have been created differing in a number of fluid cells from 22 000 to 1 100 000. The average value of the computed flow rate between different meshes is equal to $Q_{av} = 280.46\,\mathrm{l\,min^{-1}}$ with 3.13% fluctuations of the extreme values around the average one. Then, the standard deviations was calculated according to the expression

$$\sigma = \sqrt{\frac{1}{N}\sum_{i=1}^{N}\left(Q_i - \overline{Q}\right)^2}, \tag{4.15}$$

where $N = 10$ – total number of mesh resolutions studied, $\overline{Q} = 280.46\,\mathrm{l\,min^{-1}}$ – the mean volume flow rate, Q_i – the volume flow rate computed with the ith mesh.

The standard deviation is $5.97\,\mathrm{l\,min^{-1}}$, which is considered as an acceptable value to conclude that the obtained values ensure the convergence of the solution regardless of the mesh resolution. The applied mesh resolutions provide acceptable accuracy of the computed results. The result of the mesh independence study is shown in Figure 4.3.

The meshing algorithm for further parametric studies was selected providing on average 1.1 million fluid cells and three million partial cells on the bordering surfaces of solid matter. The maximum cell size of the basic mesh before the refinement process commences is 0.8 mm. The chosen meshing setting guarantees a reasonable trade-off between computational time and accuracy for the simulations described further.

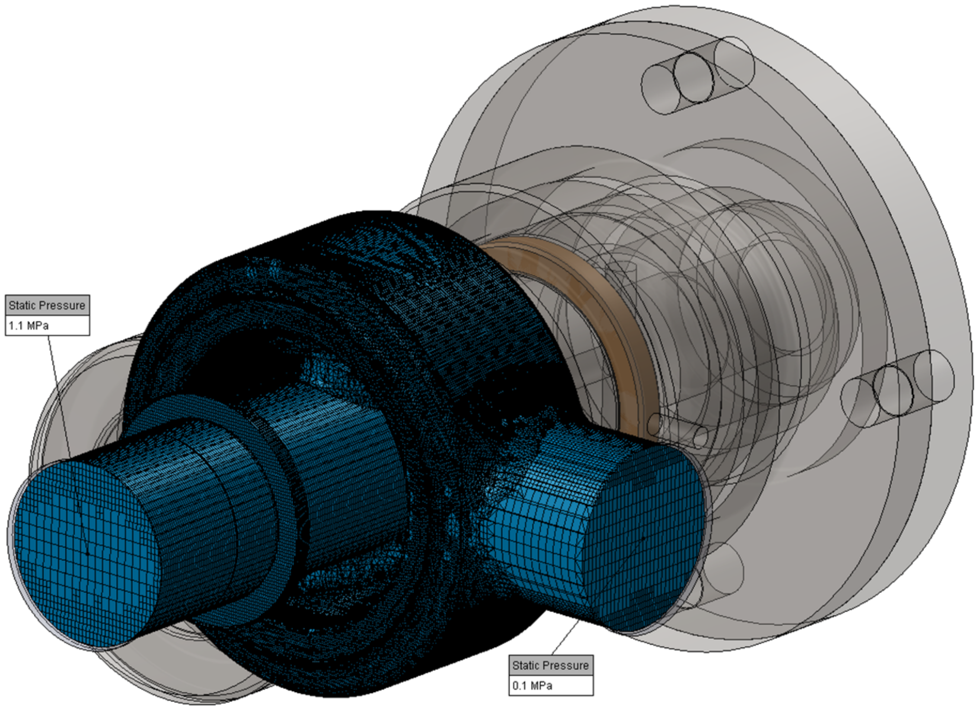

Figure 4.4: The location of the boundary openings on the used mesh. The left opening – inlet, the right – outlet.

4.1.4 Boundary Conditions

The specification of the boundary conditions establishes the hydraulic problem for the Flow Simulation module. It consists of assigning the desired magnitude of the flow parameters in the fluid subdomain's openings. In this study, a wall roughness and slip conditions were not imposed. It is also considered that there are no leakages through external sealing lids of the valve's fluid domain.

The first objective is to gain an understanding of the hydraulic performance of the valve and to predict areas needing further geometrical optimisation to reduce hydraulic pressure losses. A feature of particular interest is the valve's discharge coefficient. Along with the orifice area, the coefficient, as the orifice area, depends on the spool stroke. These complete the geometrical description of the valve in the Bernoulli equation and allows further mathematical modelling of the valve performance in the dynamics study.

The second goal is to set a criterion for selection of the spool driving mechanism. Here, it is desired to evaluate a jet angle of the single orifice as the determining factor that influences the magnitude of flow torques. Calculating a pair of steady flow torques exerted on the spool's metering surfaces, see the Figure 4.6, allows derivation of the jet angle function.

In both parametric simulations, Dirichlet boundary conditions for the steady state fluid flow were used. Namely, boundary conditions for the valve inlet were selected as the static pressure of $p_{in} = 0.35\,\mathrm{MPa}$, $0.6\,\mathrm{MPa}$ and $1.1\,\mathrm{MPa}$. The valve outlet opening was subjected to the invariant static pressure of $p_{out} = 0.1\,\mathrm{MPa}$. It corresponds to an unpressurized tank pressure of one atmosphere.

Thus, the boundary condition of the adopted pressure differential makes up a set of $\Delta p = 0.25\,\mathrm{MPa}$, $0.5\,\mathrm{MPa}$ and $1\,\mathrm{MPa}$ pressure differentials. The magnitudes of the pressure differential were selected according to an usual margin of pressure levels in load sensing systems, which is in a range 10-20 bars (Dell 2017), (Nielsen 2005). The location of the inlet and the outlet openings of the valve overlapped on the used mesh is depicted on the Figure 4.4.

This set of hydraulic boundary conditions provided varying values of the pressure difference, dictating the volume flow rate passing through the orifice. For each variation of the specified input, the angular position of the spool was added as the geometrical parameter varying from 10° to full open state of 90° with a 5° step.

Also the boundary conditions at the inlet and outlet have to be specified for the turbulent quantities, which in this study were the turbulence intensity of 2% and the turbulence length scale, the hydraulic diameter of the inlet and outlet.

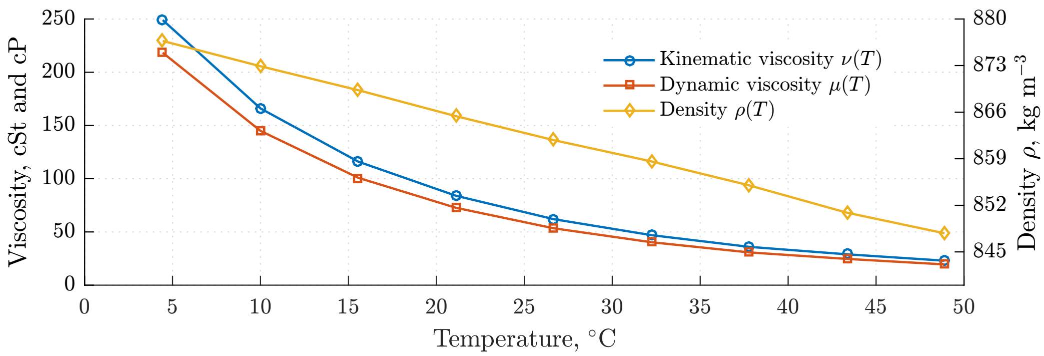

Figure 4.5: Viscosity $\nu(T)$, $\mu(T)$ and density $\rho(T)$ functions of the used fluid model (CITGO 2015).

Property	Symbol	Units	Value
Initial temperature	T_{in}	°C	45
Density at T_{in}	ρ	kg m^{-3}	850
Kinematic viscosity at T_{in}	ν	cSt	29
Dynamic viscosity at T_{in}	μ	cP	24.68
Vapour pressure at 20 °C (CITGO 2015)	$p_{v.20}$	Pa	0.06
Vapour pressure at 45 °C (Command 1971)	$p_{v.45}$	Pa	13

Table 4.1: The main physical properties of the fluid.

Fluid Model

The oil used in the CFD study is the petroleum-based anti-wear mineral hydraulic oil, grade 32. It has been treated as a compressible fluid, i.e. viscosity- and density-temperature characteristics were used by the Flow Simulation solver, see the Figure 4.5. Although, the temperature increase has been proven to be local in small areas next to the throttling edges (Ji et al. 2011).

The temperature field in the fluid subdomain is non-uniform. The initial oil temperature was taken equal to $T_{in} = 318\,\mathrm{K}(45\,°\mathrm{C})$ that corresponds to normal operational conditions of fluid power systems. For this value of oil temperature, according to manufacturer's datasheet (CITGO 2015), the kinematic viscosity $\nu(T_{in}) = 29$ cSt ($10^{-6}\,\mathrm{m^2\,s^{-1}}$), dynamics viscosity $\mu(T_{in}) = 24.68$ cP ($10^{-3}\,\mathrm{N\,s\,m^{-2}}$) and density $\rho(T_{in}) = 850\,\mathrm{kg\,m^{-3}}$. The full list or physical properties are specified in the Table 4.1.

The preprocessing setting of the CFD model is summarized in the Table 4.2 below.

4.1.5 Goals

The final step in the Flow Simulation module's pre-processing stage is goals specification, which are physical parameters of interest at points, on surfaces or in the specified volumes. The module initially considers any steady-state flow problem as a time-dependent problem. The solver module

Simulation type	Internal steady-state flow simulation
Geometric model	Discrete spool openings $\phi = 10°$ to $90°$ with $5°$ step
Fluid model	Single-phase flow, mineral hydraulic oil ISO VG 32 at 45 °C • $\rho = 850\,\mathrm{kg\,m^{-3}}$ • $\nu = 29$ cSt, • $\mu = 24.68$ cP
Mesh	Adaptive finite volume discretization, rectangular parallelepipeds with initial maximum size 0.8 mm, $N \approx 1.1$ million
Turbulence model	$k - \varepsilon$ turbulence model
Boundary conditions	Static pressure at the inlet and the outlet: • $p_{in} = 0.35\,\mathrm{MPa}$, $0.6\,\mathrm{MPa}$ and $1.1\,\mathrm{MPa}$ • $p_{out} = 0.1\,\mathrm{MPa}$ Pressure differentials: • $\Delta p = 0.1\,\mathrm{MPa}$ to $1\,\mathrm{MPa}$ with $0.1\,\mathrm{MPa}$ step Other simulation conditions: • No-slip, smooth, adiabatic wall • Two-scale wall function • Turbulence intensity 2% • Turbulence length 0.1 mm • Fluid temperature 45 °C

Table 4.2: Preprocessing settings of the CFD model.

iterates on an internally determined time step to seek a steady state flow field, so it is necessary to have a criterion for determining that a steady state flow field is obtained to stop the calculations. Convergence of the goals is considered as attaining a steady state solution as well as a condition for finishing the calculation (SolidWorks 2015). For chosen features, convergence studies are conducted automatically for every simulation with automatically set criterion values, which are 3% of the computed value.

Depending on a nature of the simulation, the goals vary. In the case of the analysis of the metering characteristics of the valve, the volume flow rate of the outlet opening has been selected and measured. The boundary conditions for this set of simulations are pressure differences, the orifices area, and fluid's parameters. The obtained volume flow rate completes the Bernoulli equation for calculation of the discharge coefficient of the valve relatively to the spool angular position.

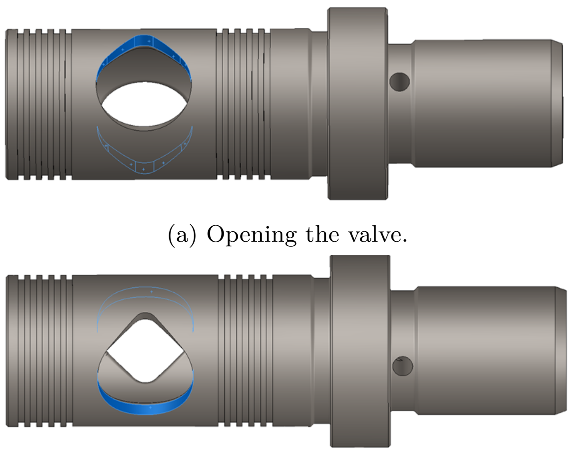

(a) Opening the valve.

(b) Closing the valve.

Figure 4.6: Spool metering surfaces perceiving the steady flow torques.

Using the same set of boundary conditions, but different goals, i.e. torques on the spool metering faces relative to its axis, see the Figure 4.6, CFD results in parameters for determining the jet angle of the orifice, both graphically through the the velocity vector field and analytically through the mathematical formula for steady state torque derived in the following section.

The chosen set of boundary conditions and the goals provide a complete description of the functionality for the designed valve structure at any hydraulic operational regime. These parameters set a basis for the further detailed development of the valve and optimisation of its geometry. Analysis of the derived discharge coefficients as well as jet angles are described in the subsequent sections.

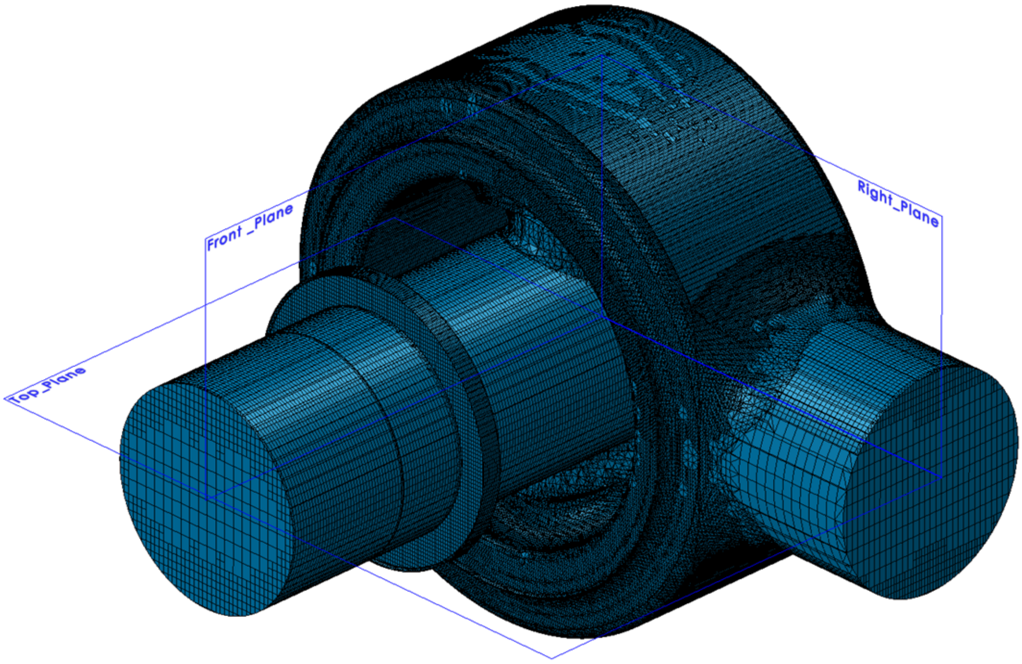

Figure 4.7: The planes for analysis.

4.2 Postprocessing

The results of the CFD study provide information about the distribution of the flow paths, the velocity field, and the velocity vector field inside the valve structure, throughout the entire fluid subdomain. Although the outflow is three dimensional, the plots of the flow parameters distributions have been built in front, right and top planes with the origin in the center of the spool's chamber. The choice of the planes for analysis is vindicated as these give better visualisation of the flow pattern at the orifice as will be demonstrated below. The location of the selected planes about the fluid domain is illustrated on the Figure 4.7.

4.2.1 Outflow

According to the depicted flux model in the right plane, Figure 4.8a, the fluid flows radially to the throttling area inside the spool's inner cavity. Two jets are being formed with maximum fluid velocity inside them reaching values of $45\,\mathrm{m\,s^{-1}}$ depending on the opening area and volume flow rate passing the orifices. After passing the sleeve orifices the jets hit the housing walls and then the flow splits. Streamlines stick to the casing surface due to Coanda effect (Trancossi 2011). This effect coupled with the collision of the jets with the walls at almost right angles results in multiple points of jets inflexions, flow separations and swirls.

Due to to this effect, in the right plane, one portion of the flow from the single jet is guided to the valve's outlet. The other part of the jet is routed to the area opposite to the sink channel. Due to the jet's separation, there are multiple areas of the fluid subdomain, which are highly prone to the formation of significant fluid circulations and subsequently highly turbulent regions, see the Figure 4.8a.

The oil streamlines of the jets are not parallel to the jet central line, the jet axis, but twisted along it. In fact, because fluid enters the spool central chamber at high velocities, it collides,

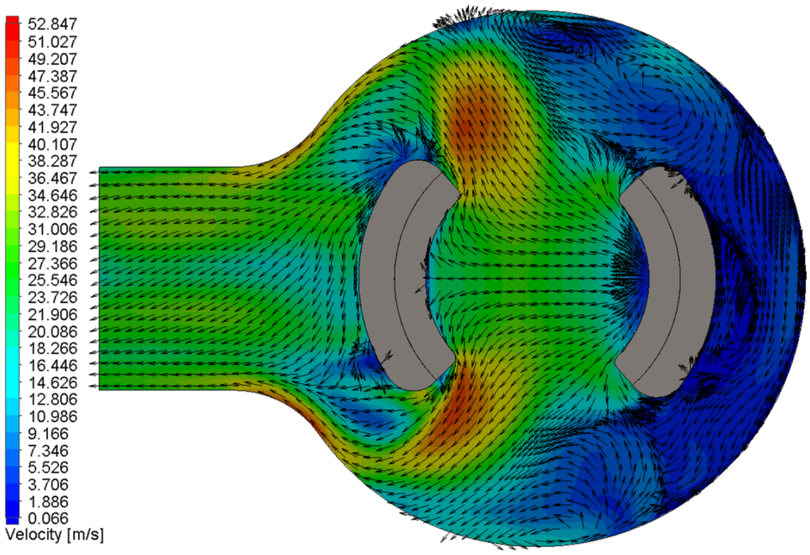

(a) The right plane.

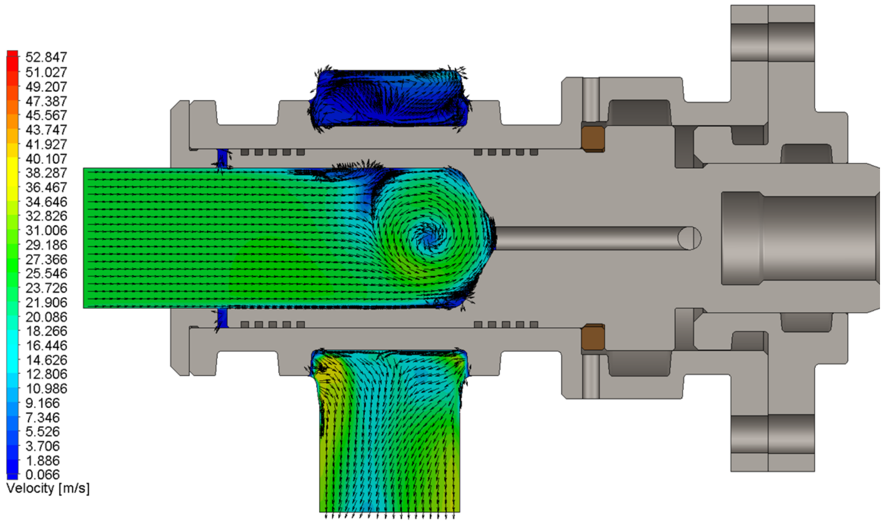

(b) The top plane.

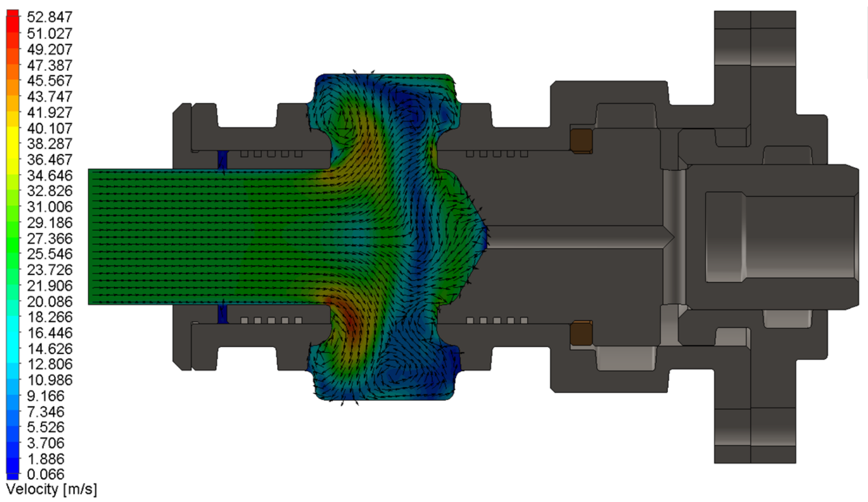

(c) The front plane.

Figure 4.8: The velocity field distributions in the main planes at the fully open state $\phi = 90°$ and $\Delta p = 1$ MPa pressure differential across the valve.

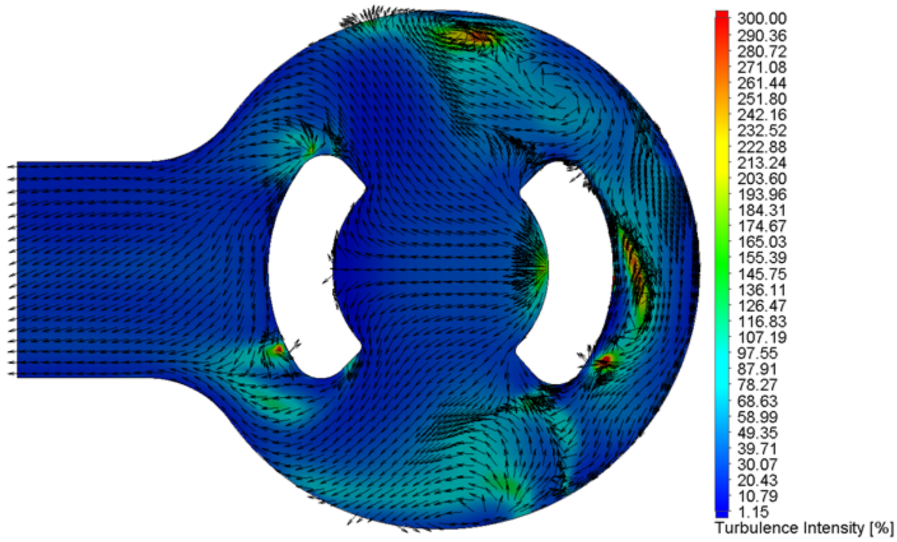

(a) The right plane.

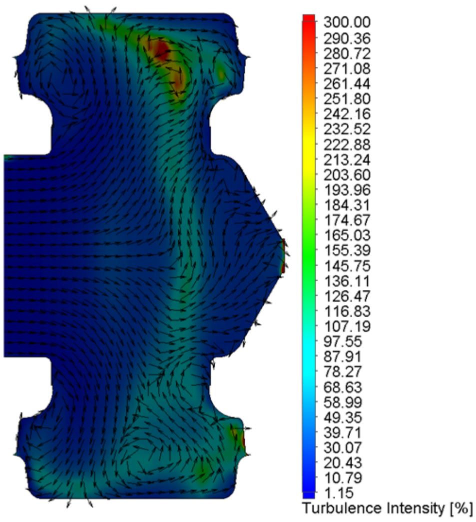

(b) The front plane.

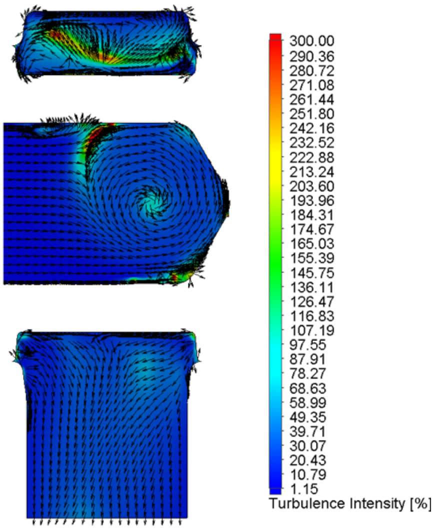

(c) The top plane.

Figure 4.9: Turbulence intensity in the flow region.

bounces of the spool's conical surface and forms a large swirl, see the Figure 4.8b. Depending on the initial flow conditions, it can occupy almost entire spool chamber. The swirl plane is perpendicular to the jet central line.

The region opposing the sink channel, the domains of merging fluid streamlines exiting the sleeve orifices, where flow separations take place, account for flow energy losses due to viscous friction in multiple swirls formed there. These are the regions of high turbulent intensity. Fluctuating local fluid particle velocities in the swirls reach 300% of time averaged velocity, what is reflected on the graph of the turbulence intensity or the level of the turbulence (Munson et al. 2012), see the Figure 4.9. Computed turbulent time or the period of the velocity fluctuations (the ratio of the turbulent kinetic energy k to its dissipation rate ε) and the turbulent length in the specified areas equal to values up to 0.003 s and 2.5 mm respectively.

These regions of high turbulence may become the regions of cavitation inception. A fluid nuclei may find itself in the core of a vortex, where the pressure level is lower than the mean. Therefore, increased vorticity could promote premature cavitation (Brennen 1995).

It is also been noted, based on the CFD visualization, that areas around the sleeve metering edges, especially at the sink side are prone to flow separation especially at high velocities and small opening areas. All above mentioned regions are subjects of further geometrical optimization to improve fluid flow trajectories by introduction geometry smoothing parts, geometrical objects such as fillets and chamfers.

Due to vorticity in the inner cavity of the spool, there is a deviation from the assumption of equality of the volume flow rates passing through the orifices. Another contributing factor to this is linked with the asymmetric location of the orifices about the sink channel on the small angular displacement of the spool. The partition ratio of the flow is not constant throughout the spool range. Up to 50°, the left orifice's area contains a larger domain of high fluid velocity compared to the right one since this orifice is located closer to the sink channel and constitutes lower resistance to the flow. However, inequality of the flows passing through two orifices does not affect the derivation of the analytical expression of the steady flow torques. Furthermore, at the fully open state the location of the valve's orifices becomes symmetric relative to the axis of the sink channel as well as the flow model.

4.2.2 Volume Flow Rate

During the CFD simulation studies of the valve, the spool angular position is considered as the main geometric parameter ranging from $\phi = 10°$ to $90°$ with an increment of 5°. The pressure differential across the orifice had definite values of $\Delta p = 0.25\,\text{MPa}$, $0.5\,\text{MPa}$ and $1\,\text{MPa}$. The volume flow rate $Q_{CFD}(\phi)$ as a function of the spool position has been simulated for the specified pressure differentials. Interpolation plots for discrete data points of CFD calculated flow rates are illustrated in Figure 4.10.

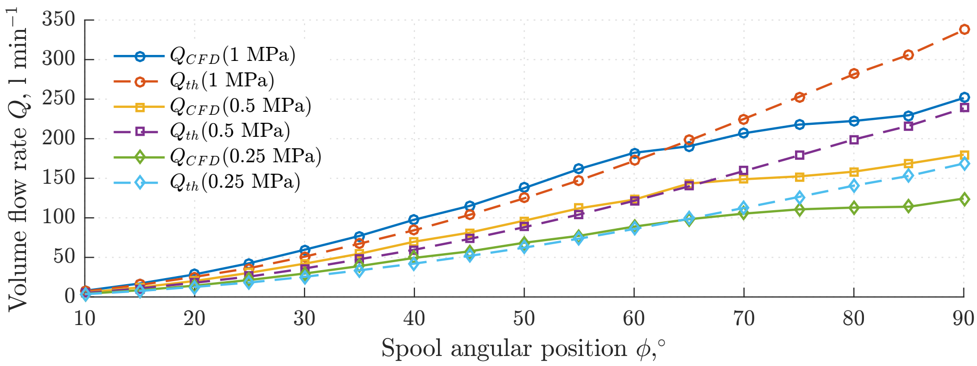

Figure 4.10: Volume flow rate $Q(\phi)$ at $\Delta p = 0.25;\ 0.5;\ 1\,\text{MPa}$

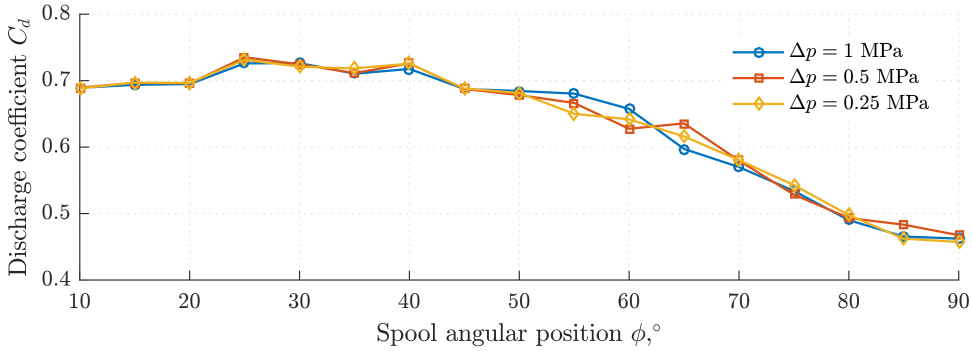

Figure 4.11: Discharge coefficient $C_d(\phi)$ at $\Delta p = 0.25;\ 0.5;\ 1\,\text{MPa}$

The Figure 4.10 also shows the theoretical volume flow rate functions $Q_{th}(\phi)$ for the constant pressure differentials Δp. The theoretical flow rate function is calculated according to the Bernoulli equation for the turbulent flow though the sharp-edged orifice:

$$Q_{th}(\phi) = C_d A(\phi)\sqrt{\frac{2\Delta p}{\rho}} \tag{4.16}$$

In this equation the measured area functions $A(\phi)$, see the Figure 3.12, was used. The discharge coefficient was considered constant, $C_d = 0.62$. It is a conventional value for the sharp-edge orifices in analytical engineering calculations (Merritt 1968).

Both volume flow rates, CFD simulated Q_{CFD} and analytically calculated Q_{th}, increase as the orifice area grows. From $\phi = 25°$ to $60°$ of the spool angular position the volume flow rate exhibits an almost linear rise. In the regions of extreme spool positions simulation results are less steady, with fluctuations due to increased flow instability. According to the simulated results, domains close to the maximum and minimum spool positions have more gradual flow rate gains. This benefits controllability of a hydraulic actuator at small and maximum speed regimes.

In the region of large valve openings $\phi > 60°$, the theoretically calculated and simulated data points start to deviate. At the maximum opening, $\phi = 90°$, the deviations reach values of around 25%. This can be attributed to the variable orifice shape for different spool positions, see the Figure 3.10. Differences in the orifice shapes between distinct spool positions causes the deviation from the assumption of the constant discharge coefficient. The coefficient heavily depends on the orifice geometry and does not keep the constant magnitude across the spool stroke.

Discharge Coefficient

Simulated flow rate characteristic Q_{CFD} of the valve has allowed calculation of the discharge coefficient of the orifice for any given spool angular position according to the Bernoulli equation 4.16.

$$C_d = \frac{Q_{CFD}}{A\,(\phi)}\sqrt{\frac{\rho}{2\Delta p}} \tag{4.17}$$

For every pressure differential across the valve, computed discharge coefficient curves follow the same trend, i.e. decreasing as the valve opens. The maximum value of the coefficient is $C_{d.max} = 0.735$ at $\phi = 25°$, the minimal value is $C_{d.min} = 0.457$ at the valve's open state, $\phi = 90°$. With the predetermined orifice area and the discharge coefficient relation, hydraulic behaviour of the valve can be predicted for any operational regime of the hydraulic system.

Since the $C_d(\phi)$ function does not heavily depend on the imposed pressure differential Δp, any curve can be used further. In the following sections the $C_d(\Delta p = 1\,\text{MPa})$ is used. Based on the found $A(\phi)$ function, it is possible to predict the theoretical $Q_{th}(\Delta p)$ characteristic of the valve for any pressure differential Δp and spool angular position ϕ.

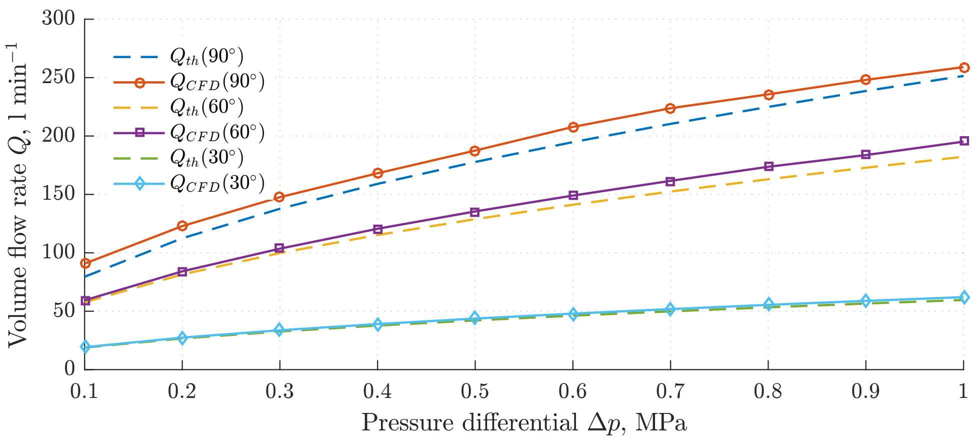

Figure 4.12: Volume flow rate $Q(\Delta p)$ at $\phi = 30°; 60°; 90°$.

The Figure 4.12 illustrates the valve flow rate dependency on the pressure differential $Q(\Delta p)$ for a given set of spool angular positions, which are $\phi = 30°$, $60°$ and $90°$. It shows the monotonous increase of both theoretical flow rate $Q_{th}(\Delta p)$ as well as results of the direct CFD simulation $Q_{CFD}(\Delta p)$. The calculated according to the Bernoulli equation flow rate Q_{th} used the derived discharge coefficient function $C_d(\phi)$ and the measured orifice area function $A(\phi)$. With the Figure 4.12, the correctness of the conducted CFD simulations can be verified and confirmed as the Q_{th} and Q_{CFD} curves follow the same trend with minimal deviations, which can be explained by variability of CFD results due to truncation errors during simulations.

With the calculated discharge coefficient function $C_d(\phi)$, which depends on the spool position as well as the area $A(\phi)$, the volume flow rate function $Q(\phi, \Delta p)$, see the Equation 4.16, can be mapped as the two-variable function, see the Figure 4.13. With the known spool position ϕ and pressures of the load and the pump, it is possible to predict the resultant volume flow rate Q. The reverse sequence of calculations can be performed by the controller to estimate needed opening of the valve ϕ for a given operational regime, which is a combination of flow parameters p_{load}, p_{pump} and Q.

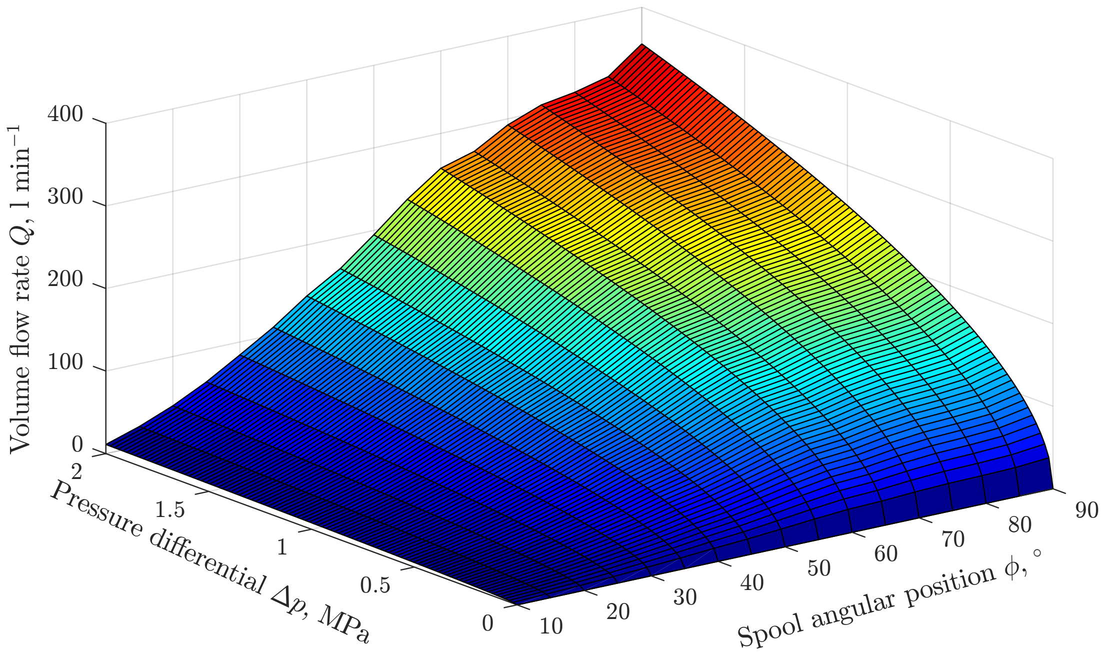

Figure 4.13: Volume flow rate function $Q(\phi, \Delta p)$

4.2.3 Reynolds Number

To predict a flow pattern of the oil motion in the valve for different spool angular positions, estimation of the Reynolds number Re has been performed according to the equations below:

$$\mathrm{Re} = \frac{\rho V L}{\mu} = \frac{V L}{\nu} \tag{4.18}$$

where V and L are characteristic velocity and length scales of the flow, ρ, μ and ν – fluid's density, dynamic and kinematic viscosity respectively, (White 1999).

For circular conduits, the Reynolds number can be expressed through the volume flow rate Q, the flow area A and the hydraulic diameter D_h, which is the same as the pipe diameter or the characteristic length L, (Durfee and Sun 2009). The more general formula for the hydraulic diameter, which accounts for noncircular pipes and hoses as the drop-shaped orifice, is

$$D_h = \frac{4A}{S} \tag{4.19}$$

where S is the perimeter of the flow cross-section. For the case of the initially chosen drop-shaped orifices, the total orifice perimeter S and area A were measured. The results are demonstrated in the Chapter 3, see the figures 3.13 and 3.12 respectively. Therefore, it was possible to calculate the hydraulic diameter D_h of the orifice and use it further to estimate the Reynolds number.

The formula used for Reynolds number estimation is derived from the equation 4.18 through the hydraulic diameter D_h in equation 4.19 and the volume flow Q rate and the area A.

$$\mathrm{Re} = \frac{QD_h}{A\nu} \tag{4.20}$$

The results of the Reynolds number calculations for different pressure differentials Δp and spool angular positions ϕ are illustrated in the Figure 4.14. The figure confirms, that for considered values of the valve opening and the pressure differential, the valve operates with the turbulent flow pattern since the Reynolds number exceeds the critical value of 2300 at almost all simulated design points.

It also can be concluded, that in the range of small valve openings, when the spool is positioned at $\phi < 30°$, the flow can take transitional nature in the throttling orifice areas as in this band the Reynolds number is within 1000<Re<4800.

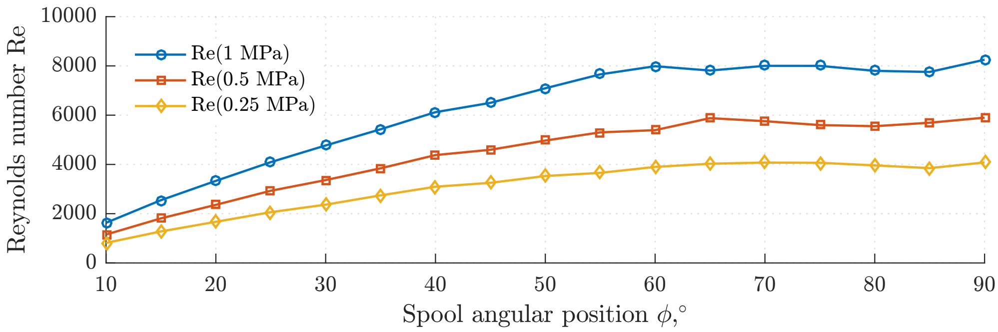

Figure 4.14: Reynolds number function $\mathrm{Re}(\Delta p, \phi)$

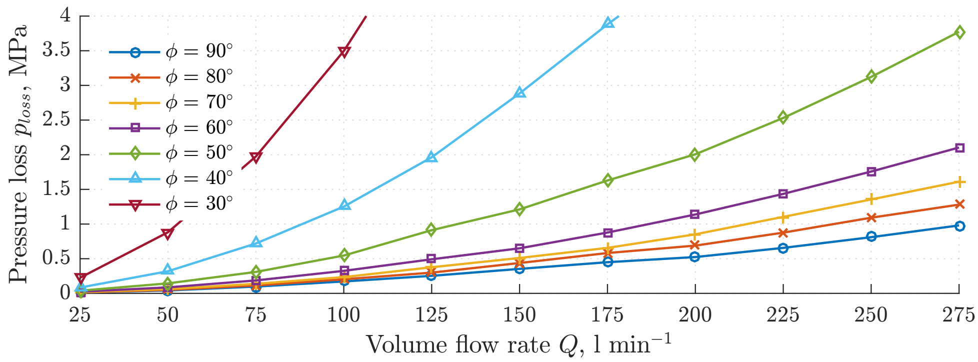

Figure 4.15: Pressure losses $p_{loss}(Q)$ at $\phi = \mathrm{const.}$

4.2.4 Pressure Losses

In order to estimate the pressure loss p_{loss} imposed by the valve to the hydraulic circuit it is installed in, another set of simulations has been conducted. In this case, the volume flow rate Q passing through the valve and the outlet pressure $p_{out} = 0.101\,325\,\mathrm{MPa}$ have been selected

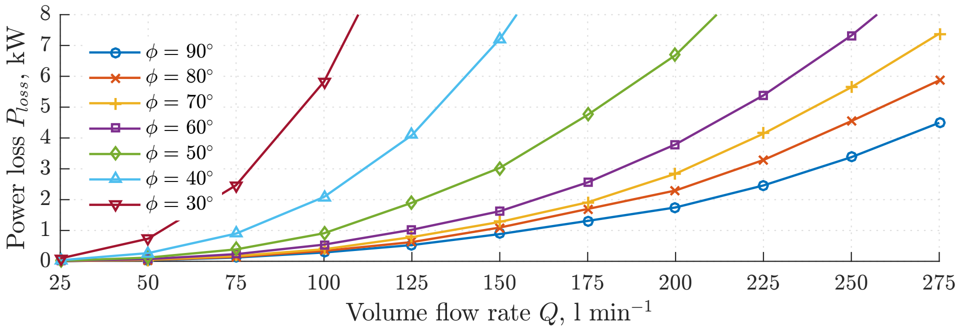

Figure 4.16: Power losses $P_{loss}(Q)$ at $\phi = \text{const}$.

as the hydraulic boundary conditions. Volume flow rate here alters from $Q_{min} = 25\,\mathrm{l\,min^{-1}}$ to $Q_{max} = 275\,\mathrm{l\,min^{-1}}$ with a step of $Q_{step} = 25\,\mathrm{l\,min^{-1}}$. The spool angular position ranges from $\phi_{min} = 40°$ to $\phi_{max} = 90°$ with $\phi_{step} = 10°$. The measured goal is the magnitude of inlet pressure p_{in}. Hence, the pressure loss is defined by the difference

$$p_{loss} = p_{in} - p_{out}. \tag{4.21}$$

The resultant pressure loss curves, i.e. $p_{loss}(Q)$ at $\phi = $const, for specified flow rates increase nonlinearly, with the dependency close to exponential. The maximum p_{loss} does not exceed 1 MPa at the fully open state of the valve and the maximum flow rate through it, i.e. at $Q(\phi_{max})$, see the Figure 4.15.

The obtained pressure loss function $p_{loss}(Q)$ allows further calculation of the power losses due throttling, see the Figure 4.16, according to the formula below. This power is consumed by fluid friction and increases the internal energy of the fluid (Merritt 1968).

$$P_{loss} = p_{loss}Q. \tag{4.22}$$

Temperature Rise

To confirm the increase of the fluid internal energy, the CFD simulation of the temperature across the entire fluid subdomain has been conducted. During the temperature rise modelling, estimation of the global maximum temperature $T_{gl.}$ has been done for the range of spool angular positions $\phi = 10°$ to $90°$ and the pressure differential ranging from $\Delta p = 0.1\,\mathrm{MPa}$ to $2\,\mathrm{MPa}$. The initial fluid temperature has been specified as $T_{in} = 45\,°\mathrm{C}$.

According to the modelling results, see the Figure 4.17, the temperature $T_{gl.}$ rises monotonously along with the rise of the pressure differential Δp and, hence, the volume flow rate Q through the valve. However, the rate of the temperature rise along the Δp axis varies for different spool positions ϕ. It has been noted, that small valve openings yield more gradual temperature rise. This fact accounts for the smaller power dissipation in the region $\phi < 50°$, comparing to the right half of the $\phi - \Delta p$ plane, where the fluid temperature reaches its maximum value of $T_{gl.max} = 47.5\,°\mathrm{C}$ at $\phi = 90°$. It has been also confirmed that the domains that generate the temperature increase are the regions of the highest velocity magnitude, fluid jets around the orifices.

Flow-generated heat can be also transferred to the valve structure, which is contact with oil, causing the fluid-surrounding parts to distort. These parts are the spool-sleeve assembly and the valve body. The clearance between the sleeve and the spool is chosen in a way to compensate heat-induced deformation of the spool-sleeve assembly and prevent a jam fault. Studies of radial deformations, due to flow-induced heat, in sliding spools with a comparable geometry showed values of thermal displacement do not exceed several tens of microns (Deng et al. 2009), (Ji et al. 2011). Such values do not lead to the heat-induced jam fault in the studied design.

Since the temperature increase does not exceed $2.5\,°\mathrm{C}$, the change in the fluid properties can

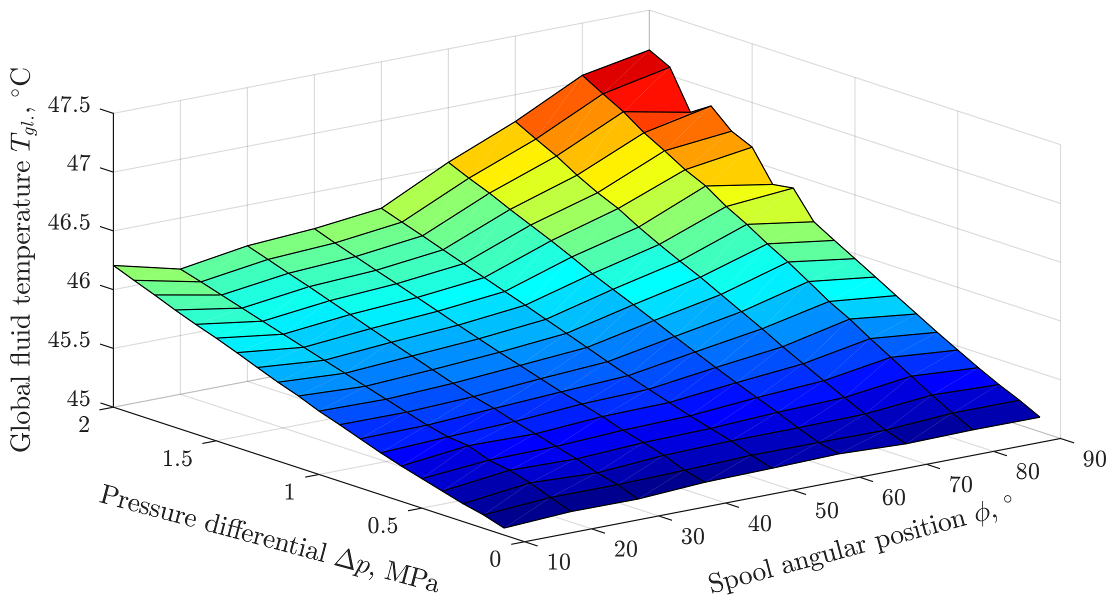

Figure 4.17: Fluid temperature function $T_{gl.}(\phi, \Delta p)$

be considered negligible and not affecting the derived above the metering characteristics of the valve and its performance on the studied regimes.

4.2.5 Steady Flow Torque

As the flow passes through the spool throttling edges, it generates in total four torques, which act on the spool from the steadily flowing fluid. These torques can be grouped in two, acting in opposite directions: opening $T_{st.fl.op.}$ and closing $T_{st.fl.cl.}$ the valve, see the green arrows on the Figure 4.18. The sum of these, allowing for a difference in directions and, hence, signs, amounts to the total steady flow torque acting on the spool. This torque is then being transmitted through the spool and the coupling to the shaft of the driver.

$$T_{st.fl.} = T_{st.fl.op.} + T_{st.fl.cl.} \tag{4.23}$$

Another way to group steady flow torques acting on the metering edges of the spool is an orifice-specific approach. Here all torques acting on the single orifice amount to the steady flow torque $T_{st.fl.i}$, where $i = 1, 2$ is the orifice number. For the further analysis the orifice-specific approach in torques classification has been employed. The total steady flow torque is a sum of torques acting on each orifice, i.e.

$$T_{st.fl.} = T_{st.fl.1} + T_{st.fl.2} \tag{4.24}$$

The formation of the steady flow torque can be described analytically through application of the law of the fluid momentum change in the control volumes. The control volumes were chosen to cover the regions, where the largest changes in the flow parameters are anticipated. The velocity plots, see the Figure 4.8, confirmed that the orifice domains, which are the cylindrical shells elements bound by the throttling drop-like profiles on the spool, contain more prominent variations of the fluid velocity, larger velocity gradients, comparing to the rest of the fluid subdomain. Therefore, in the Figure 4.19 the regions captured between the arcs BC, $B'C'$ and AD, $A'D'$ of the spool's external and internal circumferences respectively and the orifices projections constitute the chosen control volumes.

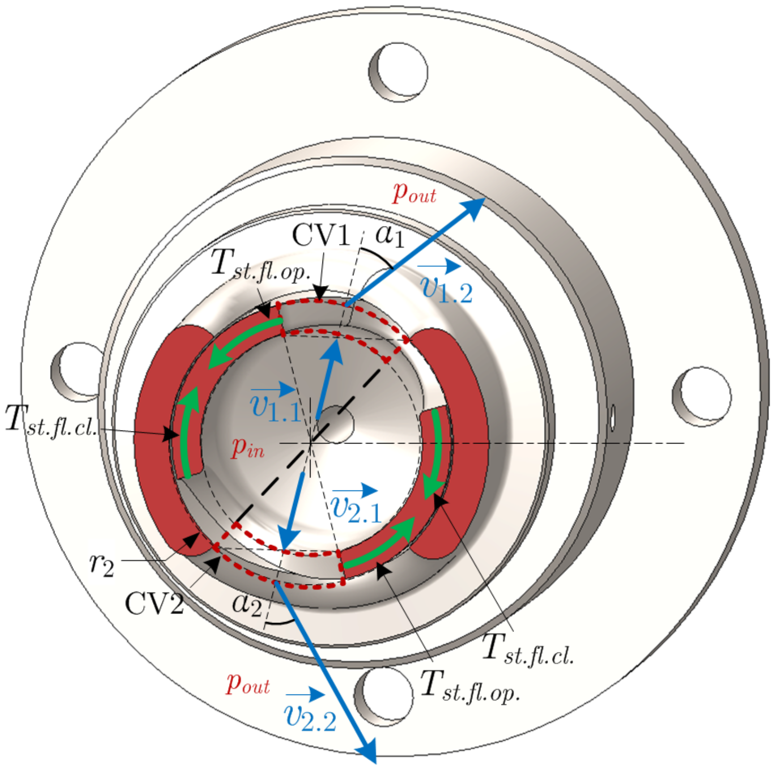

Figure 4.18: The outflow scheme and steady flow torques at $\phi = 60°$; $\overrightarrow{\vartheta}_{1.1}, \overrightarrow{\vartheta}_{1.2}$ – average velocities of the flow entering and leaving the control volume CV1, outlined by the red dashed line, α_1, α_2 – the jet angles, the black thick dashed line – the stationary orifice edge.

The fluid flow entering the control volume CV1 with the average velocity $\overrightarrow{\vartheta}_{1.1}$, see the Figure 4.18, then changes its direction and the velocity value to $\overrightarrow{\vartheta}_{1.2}$. The direction change is characterised by the jet angles α_1 for the control volume CV1 and α_2 for the CV2. The jet angle is the angle between the velocity vectors $\overrightarrow{\vartheta}_{i.1}$, $\overrightarrow{\vartheta}_{i.2}$, where i signifies the control volume. The velocity vector change means the momentum has changed as well, which is the reason for the steady flow torques formation. Therefore, to model the steady torques the second Newton law of the momentum conservation can be applied to the control volumes CV1 and CV2 respectively

$$\overrightarrow{F}_{st.fl.1} = \dot{m}(\overrightarrow{\vartheta}_{1.1} - \overrightarrow{\vartheta}_{1.2}) \tag{4.25}$$

$$\overrightarrow{F}_{st.fl.2} = \dot{m}(\overrightarrow{\vartheta}_{2.1} - \overrightarrow{\vartheta}_{2.2}). \tag{4.26}$$

In the above equations, $\overrightarrow{F}_{st.fl.i}$ is the vector of the net steady flow force, which acts of the fluid stream passing through the i-th control volume and causes a change of fluid flow's directions; $\dot{m}$ is the change of fluid mass in the control volume in time or the mass flow rate.

As the fluid density is considered constant in this study, ρ =const, the mass flow rate through the single orifice becomes equal to

$$\dot{m} = \rho Q_s, \tag{4.27}$$

where Q_s is the volume flow rate through the single orifice. It is assumed the total volume flow rate Q_t is split evenly between two orifices, i.e.

$$Q_t = 2Q_s. \tag{4.28}$$

According to the third Newton's law, from each control volume the spool perceives the force that is equal but opposite in direction to the net steady flow force $\overrightarrow{F}_{st.fl.i}$. The net force $\overrightarrow{F}_{st.fl.i}$ can be broken down in the radial $\overrightarrow{F}^{r}_{st.fl.i}$ and the tangential $\overrightarrow{F}^{\tau}_{st.fl.i}$ components, see the Figure

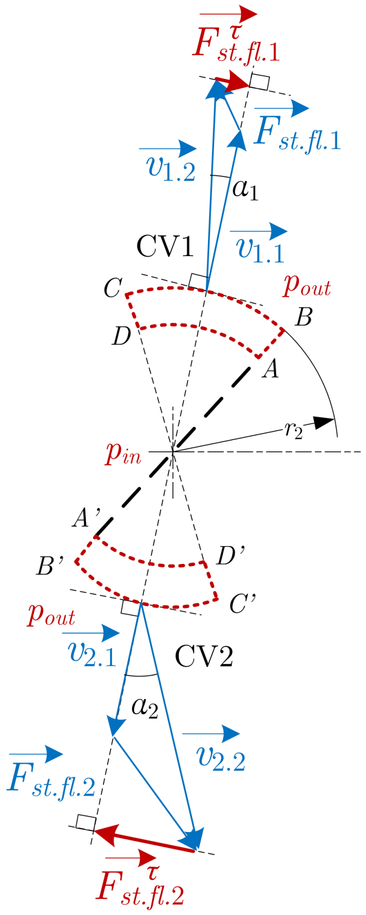

(a) $\phi = 60°$.

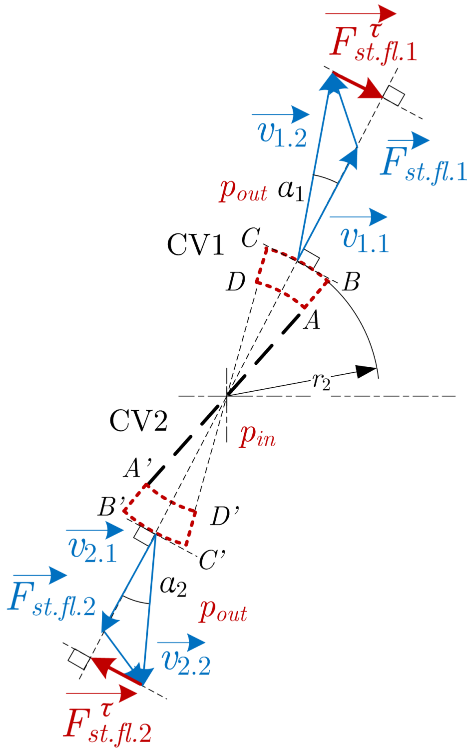

(b) $\phi = 30°$.

Figure 4.19: Vector diagrams of steady flow torques formation.

4.19. The radial projection does not contribute to formation of the steady flow torque as its vector intersects with the spool axis. Therefore, multiplying the tangential projections of the steady flow forces with opposite sign by the spool external radius $r_2 = d_2/2$ results in the steady flow torque

$$T_{st.fl.} = (F^{\tau}_{st.fl.1} + F^{\tau}_{st.fl.2})r_2. \tag{4.29}$$

To find the scalar value of the resultant tangential steady flow force $F^{\tau}_{st.fl.i}$, the assumption of a centrifugal nature of the flow in the right plane inside the spool central chamber has been made. In other words, it is assumed that the vector of the average velocity $\overrightarrow{v}_{i.1}$ of the fluid entering the i-th control volume crosses the spool axis. Therefore, its tangential projection is null and the scalar form of the momentum change in the control volumes CV1 and CV2 in equations 4.25 and 4.26 becomes

$$F^{\tau}_{st.fl.i} = \rho Q_s v_{i.2} \sin \alpha_i. \tag{4.30}$$

Due to the assumption of equality of the volume flow rates passing through the control volumes CV1 and CV2, the exit velocities $v_{i.2}$ are same and the i index can be neglected. The velocity $v_{i.2}$ leaving the i-th control volume can be expressed through the single orifice volume flow rate Q_s, which holds the same value for both orifices, and the area of the single orifice $A_{sing.or.}$.

$$v_{i.2} = v_2 = \frac{Q_s}{A_{sing.or.}} \tag{4.31}$$

Therefore, the expression for the total steady flow torque $T_{st.fl}(Q_s, \alpha_i)$ function becomes

$$T_{st.fl.}(Q_s, \alpha_i) = \frac{\rho Q_s^2 r_2}{A_{sing.or.}} \sum_{i=1}^{2} \sin \alpha_i \tag{4.32}$$

According to the Equations 4.28 and 3.1, the previous formula can be expressed in the more convenient form using the total volume flow rate across the valve Q_t and total opening area $A_{tot.or.}$ as follows:

$$T_{st.fl.}(Q_t, \alpha_i) = \frac{\rho Q_t^2 r_2}{2A_{tot.or.}} \sum_{i=1}^{2} \sin \alpha_i \tag{4.33}$$

This expression can be further transformed into the function $T_{st.fl.}(\Delta p, \phi)$ using the Bernoulli equation 4.16 and neglecting the subscript *tot.or.*

$$T_{st.fl}(\phi, \Delta p) = {C_d}^2 A \Delta p r_2 \sum_{i=1}^{2} \sin \alpha_i(\phi) \tag{4.34}$$

Substituting the equation 4.31 into 4.30 and rearranging the latter around the jet angle produces the equation allowing to derive the jet angles for both orifices. The following formula enables CFD results of the steady flow torque simulations to be processed in order to obtain the jet angle – the intrinsic property of the new valve and its internal flow pattern.

$$\alpha_i = \arcsin\left(\frac{F^{\tau}_{st.fl.i} A_{sing.or.}}{\rho Q_s^2}\right) \tag{4.35}$$

The calculations of steady flow torques and jet angles have been performed for the same range of pressure differentials and spool positions as computations of the volume flow rate, i.e. $\Delta p =$ 0.25 MPa, 0.5 MPa and 1 MPa and $\phi =$10° to 90°. The only difference is the set of goals. In this case, the flow torques on the metering faces of the spool, Figure 4.6, have been measured for both orifices.

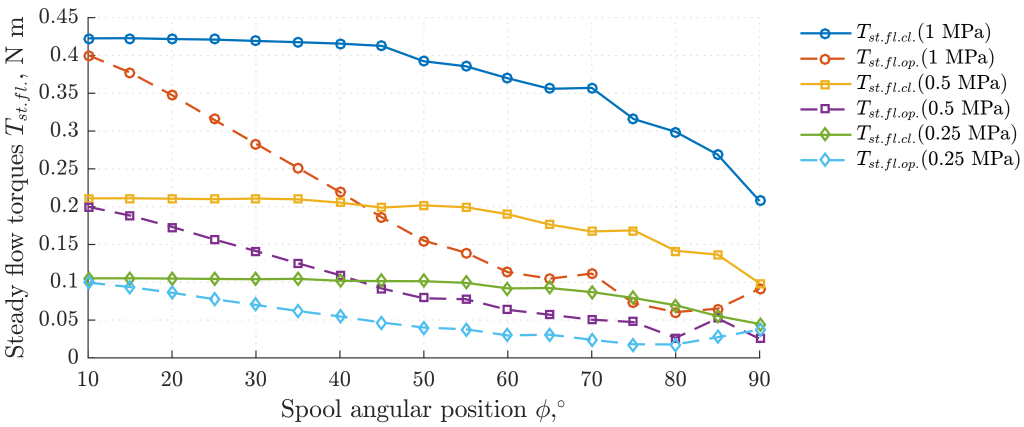

Figure 4.20: Opening and closing steady flow torques $T_{st.fl}(\phi)$ at $\Delta p = 0.25$; 0.5; 1 MPa

The selected four spool faces are features of interest since the rest of the spool surfaces are cylindrical and subjected to the same pressure. Therefore, these axisymmetric surfaces do not contribute to the steady flow torque formation. Measurement of the torques was performed on all four selected surfaces relative to the axis of the spool.

The values of the steady flow torques acting on each of the selected surfaces have been obtained through CFD and grouped according to the opening/closing direction, see the Figure 4.20. Since the modeled data contains the information of the torques on all four surfaces, it is possible to assess the torques created on each orifice and the total steady flow torque, see the Figure 4.21, which is perceived by the spool and transmitted to the spool driver.

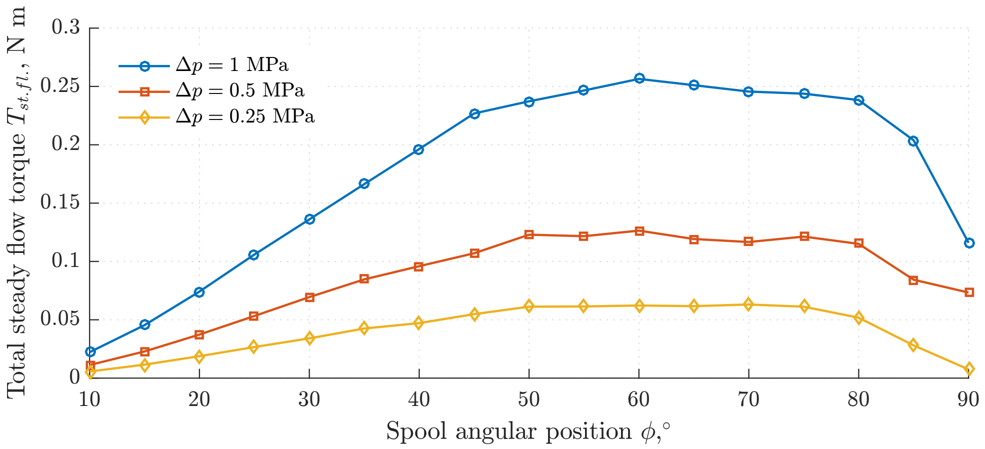

Figure 4.21: Total steady flow torque function $T_{st.fl}(\phi)$ at $\Delta p = 0.25$; 0.5; 1 MPa

This Figure 4.20 demonstrates behaviour of the absolute values of the steady flow torques. The torque direction difference is accounted by the subscripts "opening"and "closing". The results of the CFD simulations have shown that the closing torque $T_{st.fl.cl.}$ created on the both orifices prevails over the opening torque $T_{st.fl.op.}$ across entire spool stroke. This can be explained by the fact that the spool metering faces, which perceive the closing torque, are subjected to the higher total fluid pressure than the surfaces on which the opening torque is being formed.

The resultant steady flow torque $T_{st.fl.}$ has a dependency close to parabolic relative to the spool position. It follows from subtracting the opening torque $T_{st.fl.op.}$ from the closing one $T_{st.fl.cl.}$. The similar parabolic dependency of the steady flow torque on the spool angular position $T_{st.fl.}(\phi)$ has been reported for the rotary directional valve (Wang et al. 2016). The parabolic torque function separates the rotary spools from other valve classes as these valves tend to be over compensated.

The maximum value of the flow torque is observed when the spool is positioned in the middle of its stroke, which is the region of ϕ =55° to 65°. This domain of spool positions distinguishes itself due to the influence of the high magnitude of the volume flow rates and the deflection angles of the jets both reaching their maximums. The largest steady flow torque for the $\Delta p_{max} = 1$ MPa pressure difference across the valve does not exceed $T_{st.fl.max} = 0.26$ N m. This value serves as the criterion for the selection of the spool driver, the stepping motor. The motor's holding torque should exceed the total steady flow torque with a safety margin. That will ensure the spool is keeping its position in presence of the largest active load.

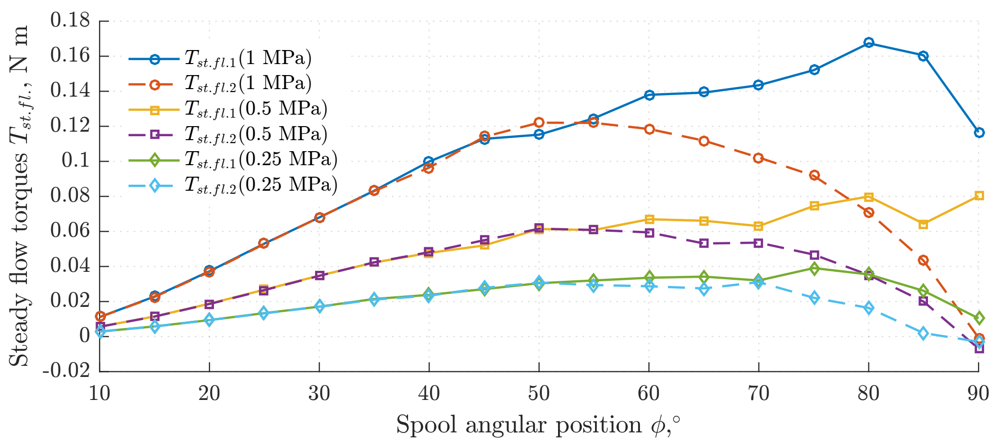

Figure 4.22: Orifice steady flow torques $T_{st.fl.i}(\phi)$ at $\Delta p = 0.25$; 0.5; 1 MPa

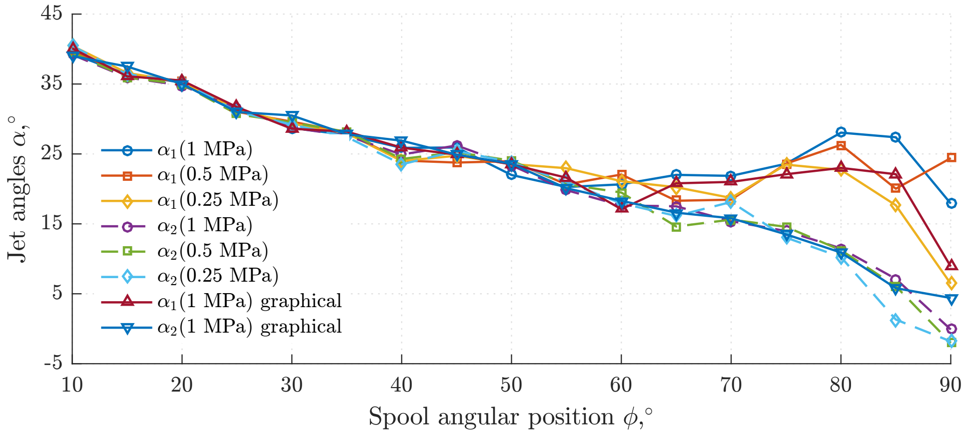

Figure 4.23: Jet angles $\alpha_i(\phi)$ at $\Delta p = 0.25; 0.5; 1\,\mathrm{MPa}$

4.2.6 Jet Angles

Based on the obtained values of the flow torques at each orifice, see the Figure 4.22, it is possible to calculate the jet angles α_i of the flow for any given spool position ϕ, according to the equation 4.35. According to this equation, the jet angles α_i are derived from the tangential flow forces $F^{\tau}_{st.fl.i}$ generated at the i-th control volume or the i-th orifice. Therefore, the simulated torques were recalculated to yield the total torque at each orifice, i.e. $T_{st.fl.i}$, see the Figure 4.22. Then, the jet angles were obtained and plotted, the Figure 4.23.

It has been noted that the jet angles, i.e. the directions of the diverted streamlines, do not change much, especially in the beginning and the middle of the spool stroke where the spool angular position does not exceed 60°. In this region the curves for the jet angles α_1 and α_2 effectively coincide for the different pressure differentials. Therefore, the flow pattern in this domain of spool angular positions ϕ does not depend on the flow characteristics (the flow rate through the valve Q and the imposed pressure differential Δp).

The jet angles curves for both orifices monotonously decrease from $\alpha_i = 40°$ at the onset of throttling at $\phi = 10°$ down to the $\alpha_2 = 0°$ and $\alpha_1 \approx 15°$ at the fully open state of $\phi = 90°$. But, the graphs of the jet angles of the first orifice α_1 exhibit larger fluctuations in the region of $\phi = 70°$ to 90° comparing with the second orifice α_2. The plots of α_2 decrease in a more stable manner.

The described relation of the jet angles to the spool position $\alpha_i(\phi)$ applies for the chosen arrangement of the throttling parts, their windows' profiles, and the housing geometry. The main housing geometrical parameters affecting the jet angles are the cross-section shape of the annular collecting channels, i.e. the shape of rectangles with the area A_{an} in the Figure 3.14, and the location of the outlet service port relative to the throttling orifices. Among these factors, the location of the sink channel, or outlet service port, has more significant effect.

The influence of the pressure differential value Δp on the jet angles α_i, see the Figure 4.23 as well as on the discharge coefficient C_d, see the Figure 4.11 is negligible. The same conclusion has been reported in a similar study of DCVs by a direct numerical flow simulation (Posa et al. 2013). The jets angles' independence on the pressure was also previously reported in the study looking at application of flow forces to implement pressure compensation in the proportional DCV with the sliding spool (Lisowski et al. 2015).

Graphical Estimation

With the use of the CFD study of flow torques, an alternative, graphical method has been employed to quantify the jet angle functions $\alpha_i(\phi)$. The method was used in a number of studies evaluating the jet angles in flow control valves to determine flow forces acting on the valve's regulating elements (Lisowski and Filo 2016b), (Lisowski et al. 2015), (Amirante et al. 2007), (Wang et al. 2016). For

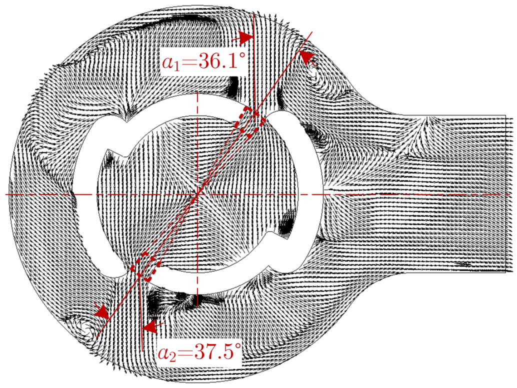

(a) $\phi = 15°$.

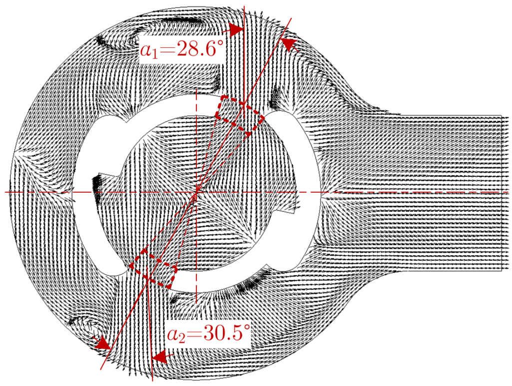

(b) $\phi = 30°$.

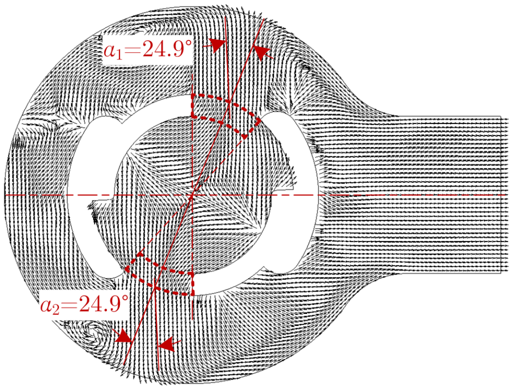

(c) $\phi = 45°$.

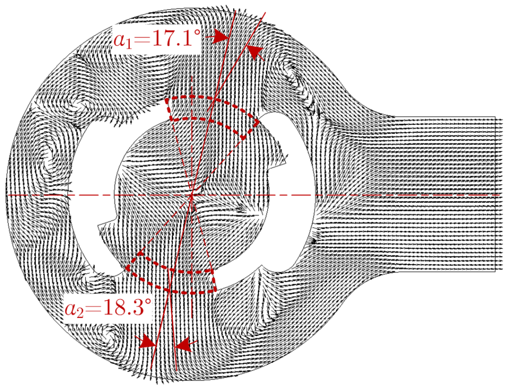

(d) $\phi = 60°$.

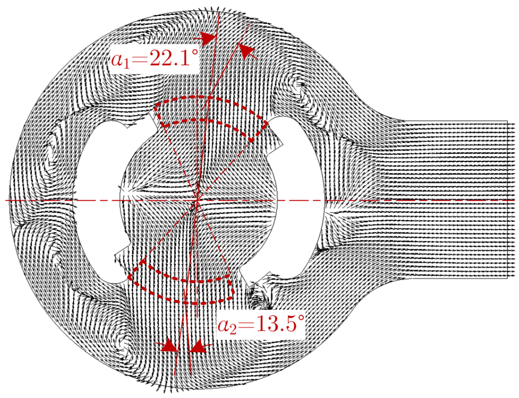

(e) $\phi = 75°$.

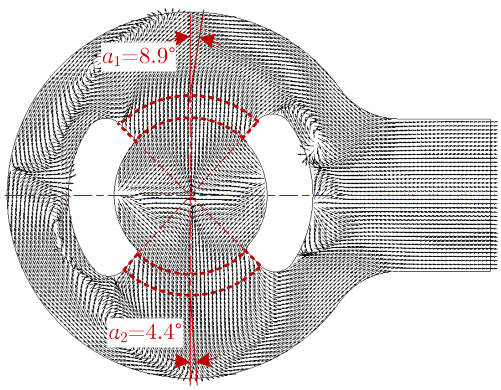

(f) $\phi = 90°$.

Figure 4.24: The graphical method to estimate the jet angles for different spool positions ϕ.

conventional valves with a spool- or poppet-based throttling mechanism, importance of the jet angle is stipulated by the fact that it directly influences on the amount of a flow force. Due to importance of this quantity and difficulty of obtaining its values, the graphical method has been widely adopted in the scientific community.

The method requires distributions of the flow velocity vectors for the series of the spool positions in the range $\phi = 10°$ to $90°$. For each spool position the plot of the velocity vector field has been created fro the case of $\Delta p = 1\,\text{MPa}$ pressure differential. The deflection angle of the flow has been measured and so the jet angle has been quantified. The radial direction of the fluid flow in the spool central chamber in the right plane is considered as the orientation of the inlet velocity $\overrightarrow{v}_{i.1}$ to the i-th control volume. Then directions of the outlet velocities $\overrightarrow{v}_{i.1}$ were drawn coinciding with the velocity vectors at the outlet of the orifices. Thus, the angle between the radial

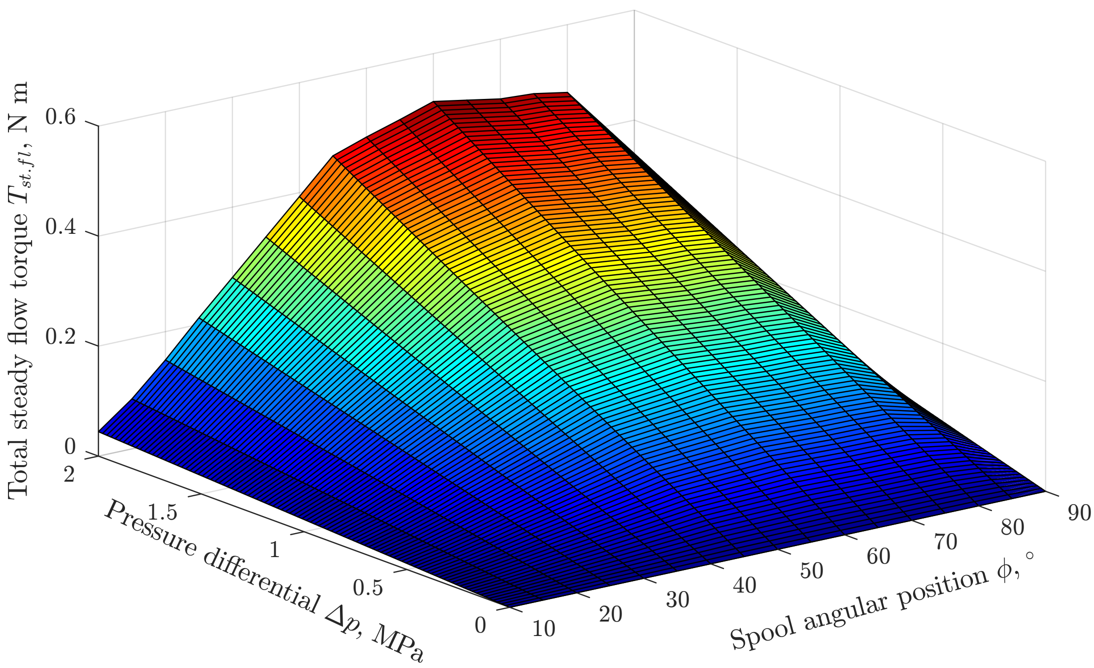

Figure 4.25: Total steady flow torque function $T_{st.fl.}(\phi, \Delta p)$

and the drawn lines represents the sought orifice jet angle.

The points on the spool external circumference are taken as the measurement points for the outlet velocity directions. The cylinders created by drawing these circumference constitute the outer bounds of the control volumes. The centers of the orifice arcs are also located far from the flow regions directly influenced by the housing walls as well as the orifice surfaces, see the Figure 4.19. Hence, the effect of the near-wall region of the casing is excluded.

As the opening of the valve exceeds $\phi = 75°$, the substitution of metering edges takes place. Before the spool position of 75°, each orifice is created by both spool and sleeve metering edges. After the point of $\phi = 75°$, the sleeve edges become concealed by the spool edges and do not contribute to the formation of the orifice and throttling. This fact affects the choice of the right plane at the graphical estimation of the jet angles.

The graphical method is considered as less accurate method to estimate the jet angle. Sources of inaccuracies come from selection of the measurement points and setting the density of the velocity vectors. Nonetheless, there is no significant deviation between values obtained graphically and derived from CFD computations of the steady flow torques.

According to the equation 8.2 and the measured jet angles functions $\alpha_i(\phi)$, the function $T_{st.fl.}(\phi, \Delta p)$ can be plotted for any operational regime of the valve. see the Figure 4.25. Thus, the steady flow torque can predicated for any load and spool position.

4.3 Cavitation

Cavitation can be defined as the process of rupturing a liquid by decrease in pressure at roughly constant temperature (Brennen 1995). The inception and development of cavitation is related to the amount of free and dissolved gas within the cavitating liquid. Cavitation inception occurs when a reduction in the liquid pressure results in a local pressure below the vapour pressure, and the liquid begins to change phase into vapour (Ceccio and Makiharju 2017). It adversely effects hydraulic components, their structure and performance. It is also associated with vibration, noise and surrounding material erosion. Particularly severe damage occurs at developed, intense cavitation.

To estimate load parameters and operational regimes on which cavitation can occur inside the valve, a cavitation number calculation has been performed according to the following equation

$$\sigma = \frac{p_a - p_v}{\frac{1}{2}\rho v^2}, \tag{4.36}$$

where p_a and p_v are ambient and oil vapour pressure respectively, v – the characteristic flow velocity. For the used fluid model of petroleum based hydraulic mineral oil, the vapour pressure is $p_v = 13\,\mathrm{Pa}$, see the Table 4.1.

In hydraulic valves the areas most prone to cavitation are the regions of the smallest cross section of the flow, where the fluid velocity reaches its maximum, *vena contracta*. In the current design, the vena contracta is split between two throttling orifices. The smaller the valve opening, the more restricted the flow cross section is and, hence, it is more likely the oil starts to cavitate at smaller spool angular positions and large flow rates. In addition to vena contracta, the regions of high vorticity identified above could be cavitation inception domains.

Numerical and experimental studies of water flow through hydraulic valves confirmed that first signs of cavitation take place at $\sigma \approx 1.2$. Below this value cavitation bubbles start to appear. This is the region of "developed" cavitation. At $\sigma < 0.75$, damaging "supercavitation" start to take place (Akira et al. 2007).

In hydrocarbon fluids, as petroleum based hydraulic oil, cavitation damage is less severe than in water, as the bubble collapse is not as sudden and can be cushioned by other dissolved vapours (Bernad and Susan-Resiga 2012). Moreover, vapour pressure of petroleum oil is smaller than the one of water (Command 1971). Therefore, petroleum oil is more cavitation-resistant than water, oil's cavitaion inception occurs at lower ambient pressure than in in water. Due to these reasons, evaluation of cavitation resistance of the valve can be performed using water's critical cavitation numbers.

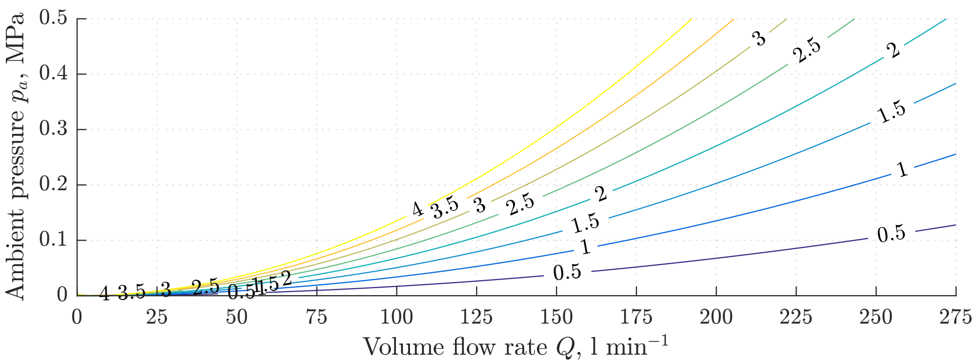

Figure 4.26: Cavitation numbers σ at the fully open state $\phi = 90°$.

According to the calculated values of the cavitation number σ at the fully opens state $\phi = 90°$, see the Figure 4.26, at the maximum rated volume flow rate of $Q = 275\,\mathrm{l\,min^{-1}}$, cavitation could start to appear at ambient pressure of $p_a = 0.25\,\mathrm{MPa}$. This value corresponds to the curve $\sigma = 1$. All operation points, i.e. combinations of p_a and Q, below this curve belong to transitional and developed cavitation domains. At this volume flow rate, the velocity at the orifice reaches $v = 24.51\,\mathrm{m\,s^{-1}}$.

The ambient pressure used in the analysis is directly related to the service port pressure, or the load pressure, in case the valve is located in the meter-in side. The oil jet leaving the orifice, as well as vena contracta of this orifice, find itself in the collecting channel, where the oil is pressurized by the load pressure. In case of the meter-in location, it is unlikely the load pressure drops below the value 0.2 MPa.

4.4 "Closed-State" Leakage

The outflow model of the valve can be further improved by evaluating the expected leakage. To estimate the amount of leakage taking place at the closed case $\phi = 0°$, the laminar flow in the spool-sleeve gap has been considered. Taking into account the small radial clearance $c = 0.1\,\text{mm}$, see the Equation 3.13, Table 3.1 and Appendix A, between the spool and the sleeve, the laminar incompressible flow configuration is regarded as a valid assumption. Thus, application of the Hagen-Poiseuille formula of the fully developed laminar flow to derive the leakage flow rate through the leaking channels is feasible.

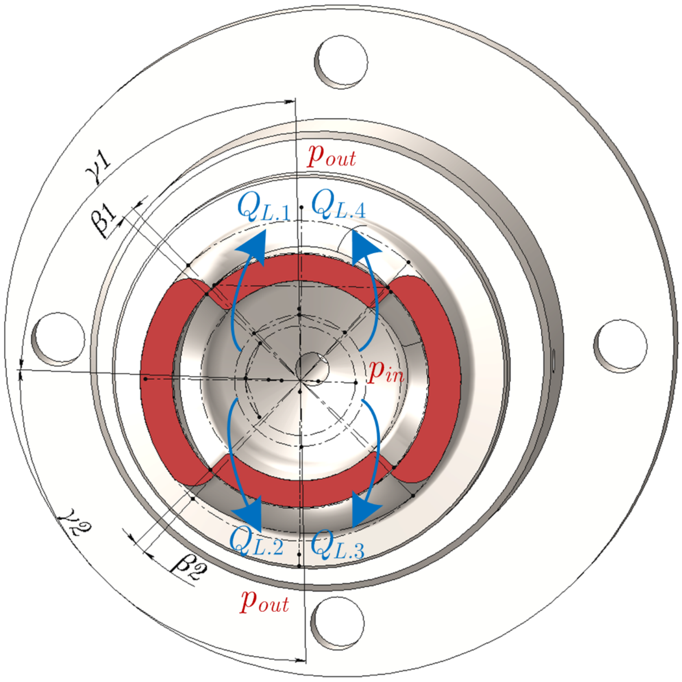

Figure 4.27: Location of the leakage channels.

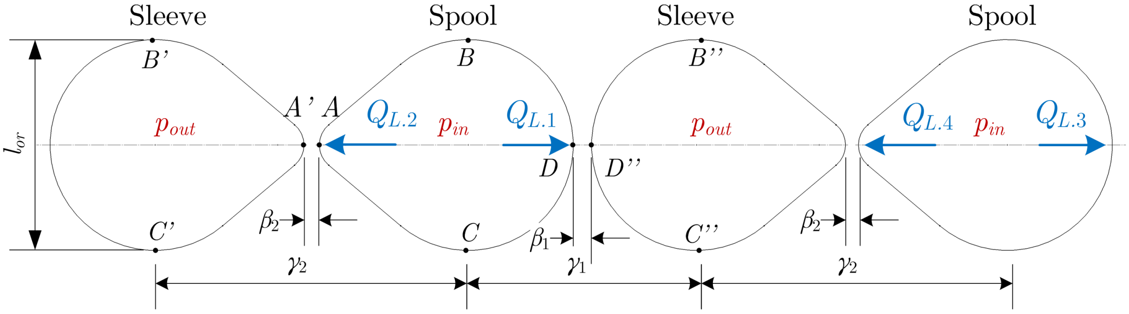

Figure 4.28: The unfolded view on the leakage channels.

In case of the fully closed valve, the leakage flow passes from the spool central cavity into the collecting channel through four leakage channels with volume flow rates $Q_{L.i}$, see the Figure 4.27, where the index $i = 1$ to 4 denotes a channel number. The cross-section of each single leakage flow is a rectangle with the height equal to the gap clearance c and the width equal to the spool orifice width $l_{or} = 12\,\text{mm}$ in the unfolded view, Appendix A. The length L of the channel varies for different leakage channels due to the drop shape of the orifices, see the Figure 4.28. For the rectangular passage the laminar leakage flow can be estimated as follows:

$$Q_{L.i} = \frac{l_{or} c^3 \Delta p}{12 \mu L_i} \tag{4.37}$$

Here $\mu = 24.68 \times 10^{-3}$ Pa s – dynamic viscosity of the oil, L – the channel length, the index $i = 1 \dots 4$ – leak channel number, $\Delta p = p_{in} - p_{out}$ – pressure difference between the central and the collecting chambers.

According to the Figure 4.28, the geometrical configuration and pressure differences for the flows $Q_{L.1}$, $Q_{L.3}$ and $Q_{L.2}$, $Q_{L.4}$ are the same. Thus, these leakage flows take same values, i.e.

$$Q_{L.1} = Q_{L.3}, \qquad Q_{L.2} = Q_{L.4}. \tag{4.38}$$

The further analysis will be focused on the single spool orifice and its leakage flows Q_2 and Q_3 estimation. Summing these two flow rates and doubling the sum will yield the total leakage through the valve.

$$Q_L = \sum_{i=1}^{4} Q_{L.i} = 2\left(Q_{L.1} + Q_{L.2}\right) = \frac{l_{or} c^3 \Delta p}{6\mu}\left(\frac{1}{L_1} + \frac{1}{L_2}\right). \tag{4.39}$$

The leakage channel length L_i is not constant and varies along the spool axis from the maximum value $L_{i.max}$ measured between the most distant points of the spool-sleeve orifices to the smallest value of $L_{i.min}$ between the tips of the drop-shaped orifices. In this study, the average value between these has been used to calculate the leakage flow rate.

$$L_i = \frac{L_{i.max} + L_{i.min}}{2} \tag{4.40}$$

Geometrically, the channel is curved and its maximum $L_{i.max}$ and minimum $L_{i.min}$ lengths are effectively arcs. According to the Figure 4.27 and the Figure 4.28, these lengths can be determined through overlap angles β forming the arcs AA', DD'' between the closest tip and back points respectively and γ, which form the arcs BB' and BB'' between the farthest points. The arc radius corresponds to the external spool radius $r_2 = 9.5$ mm. Then, the channels lengths can be calculated as follows given the angles are measured in degrees:

$$L_{i.min} = \frac{\pi r_2}{180}\beta_i, \qquad L_{i.max} = \frac{\pi r_2}{180}\gamma_i \tag{4.41}$$

According to the geometrical parameters of the leak channels, which are listed in the Table 4.3, the resultant leakage flow rate function $Q_L(\Delta p)$ was plotted in the Figure 4.30.

Parameter	Symbol	Value	Units
Gap clearance	c	0.1	mm
Orifice width	l_{or}	1.2	mm
Min overlap angle, arc DD''	β_1	3.02	°
Min overlap angle, arc AA'	β_2	2.98	°
Max overlap angle, arc BB'	γ_1	87.06	°
Max overlap angle, arc BB''	γ_2	92.94	°
Min length of the channel 1, arc length of DD''	$L_{1.min}$	5.00	mm
Min length of the channel 2, arc length of AA'	$L_{2.min}$	4.94	mm
Max length of the channel 1, arc length of BB'	$L_{1.max}$	14.44	mm
Max length of the channel 2, arc length of BB''	$L_{2.max}$	15.41	mm

Table 4.3: Geometric parameters of the leakage channels.

The graph also demonstrates the results of the computational modeling of the leakage $Q_{L.CFD}(\Delta p)$ performed for the following boundary conditions $\Delta p = 1$ MPa to 10 MPa pressure differential with the step 1 MPa and $\phi = 0°$, or the fully closed state. The CFD modelling results also allowed to visualize the leakage flow trajectories, see the Figure 4.29.

According to the Figure 4.30, it can be seen that deviations between numerical and analytical results are minimal. The average percentage error between the two relative to the analytical results

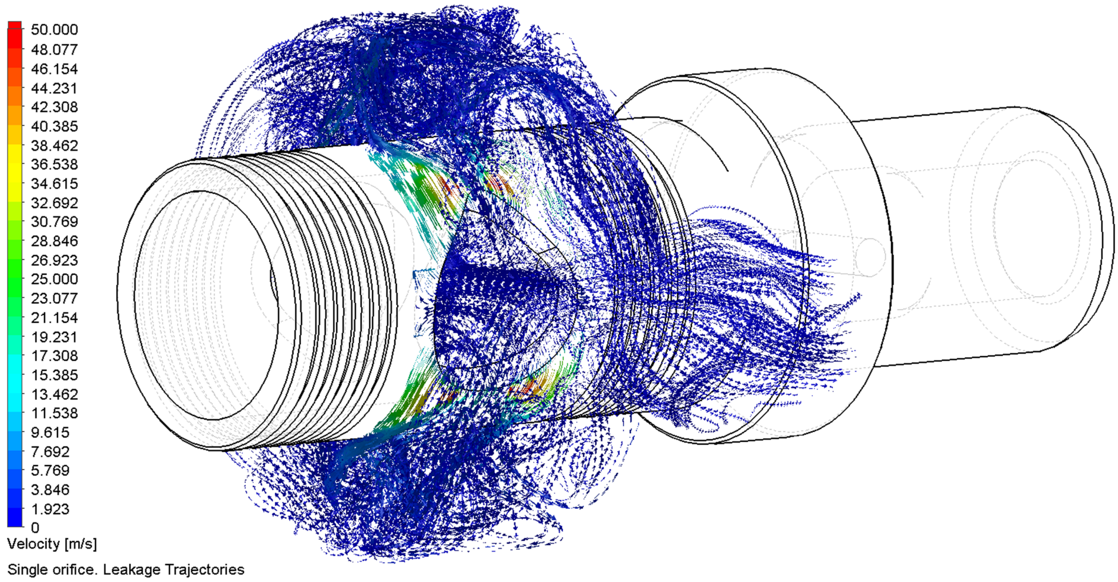

Figure 4.29: Flow trajectories visualisation of the "closed-state" leakage at the fully closed state $\phi = 0°$ and $\Delta p = 7\,\text{MPa}$ pressure differential across the valve.

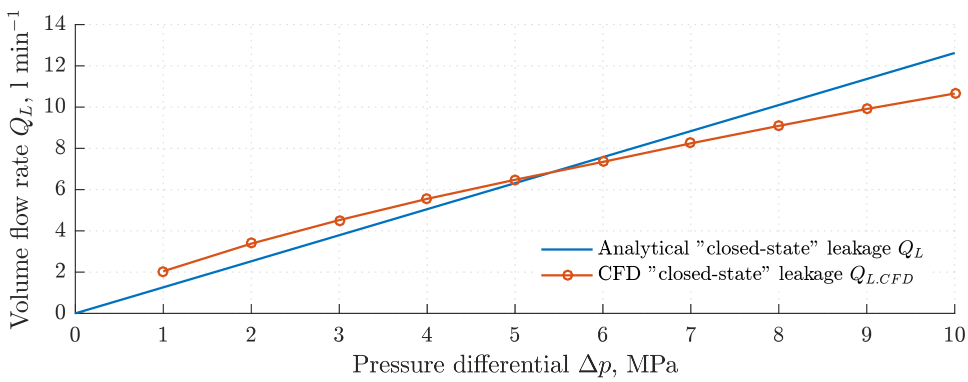

Figure 4.30: The "closed-state" leakage function $Q_L(\Delta p)$ through the valve at the fully closed state $\phi = 0°$.

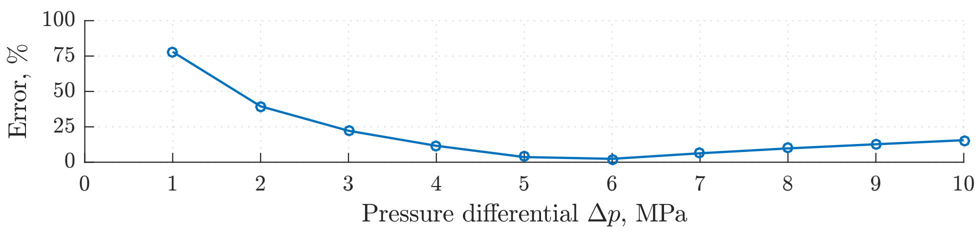

Figure 4.31: The percentage difference between the leakage estimation results from the CFD and the analytical calculation relative to the analysis.

is 20.171%, see the Figure 4.31. That serves as verification of both sets of leakage study results. The numerical and analytical results of the leakage calculation have been further validated by the experimental study, details of which are presented in the following chapters.

4.5 Chapter Conclusions

This chapter provides the metering characteristics of the valve obtained numerically, with CFD method. The applied setting of the CFD simulations, their type, the meshing process and simulations results were discussed in details. The choice of the CFD model's parameters was discussed.

The obtained metering characteristics of the valve were analysed. They provided understanding of the expected volume flow rate, the pressure drop, temperature rise functions. The outflow analysis also allowed to predict the spool-driving effort, which needs to be created by the stepper motor in order to maintain the spool position.

The derived discharge coefficients and the jet angles functions enabled prediction of valve's behaviour under all operational regimes of a hydraulic system. Cavitation and leakage properties of the valve were examined analytically. The former established the operating conditions, where valve's performance can be compromised due to cavitation. The latter provided leak-tightness characteristic of the valve.

In summary, this chapter confirmed that the chosen valve concept corresponds to the engineering specification's targets and fulfill the intended functions appropriately. In the following chapters, the comparison of the metering characteristics will be investigated.

Chapter 5

Solid Mechanics Modelling

In the previous chapter, fluid flows simulations have been conducted assuming the valve is made out of a rigid solid structure. The solid mechanics study in this chapter investigates the effects of the external loads on the internal valve components. The solid mechanics simulation allow detailed strength analysis of the valve assembly and its parts through estimation of stresses appearing in solid mechanical parts. It also examines the resultant deformations of the structure.

The purpose of the investigation conducted in this chapter is to ensure the prototype valve is able to safely carry and to withstand the applied external loading factors acting on its structure without rupturing failures and excessive deformations, which could adversely affect or impede valve performance. To verify the valve structural integrity, the internal stress and deformation distributions have been analysed for the specific loads.

The loading factors have been extracted from the fluid pressure and steady flow torques analysis in the previous chapter. This chapter represents the special case of the multidisciplinary problem of fluid-structure interaction (FSI) applied to the rotary valve. To model the effects of fluid flow on the valve structure, the load coupling has been performed within the SolidWorks (SW) solver module.

For most FSI problems, numerical simulations of complex interaction between fluids and solids may present the best insight into the fundamental physics involved. Analytical solutions to the governing equations are often impossible to obtain. Experimental studies are limited in scope and require elaborate control, data acquisition instrumentation and techniques (Hou et al. 2012).

In this chapter effects of fluid pressure inside the valve on the main valve components and influence of the steady flow torques on the spool structure have been investigated. Excessive deformations of the spool could potentially lead to warping of the spool, particularly its openings. Distortions of the spool orifice shapes could, in turn, affect metering characteristics of the valve due to change in the opening area function depicted on the Figure 3.12.

5.1 Preprocessing

In the solid mechanics modeling the static study type was used. Static studies calculate displacements, reaction forces, strains, stresses, and factor of safety distribution. Material fails at locations where stresses exceed a certain level, the material yield stress (SolidWorks 2016b).

When loads are applied to a body, the body deforms and the effect of loads is transmitted throughout the body. The external loads induce internal forces and reactions to render the body into a state of equilibrium. The static analysis in the SW module makes following assumptions (SolidWorks 2016b):

- Static assumption: All loads are applied slowly and gradually until they reach their full magnitudes. After reaching their full magnitudes, loads remain constant (time-invariant). This assumption allows us to neglect inertial and damping forces due to negligibly small accelerations and velocities.

- Linearity assumption: The relationship between loads and induced responses is linear.

5.1.1 Geometric Model

The same geometric model of the valve that has been used for the CFD studies, see the Figure 5.1, was applied in the stress estimations though the finite element analysis (FEA). The geometry of the valve main parts stayed the same with the exception of the valve body.

To replicate fully mechanical interfaces and to reproduce the configuration of connection points of the prototype valve during tests, the model of the valve body has been complemented with a set of threaded holes to simulate valves fixation to the base plate of the test rig. For this reason, the bottom plane of the model has been modified to include these holes, see the Figure 5.2. During the stress modelling, the cylinders of these holes are considered fixed, see the geometry outlined by red in the Figure 5.1. In this figure, the geometry outlined by blue lines signify the region occupied by the hydraulic oil and, hence, loaded with load pressure.

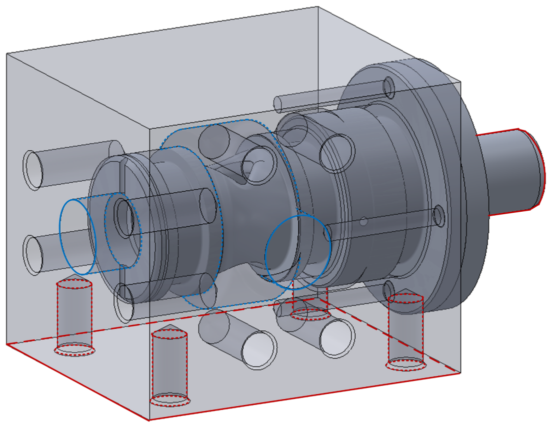

Figure 5.1: The general geometric model of the prototype valve assembly used for the stress analysis.

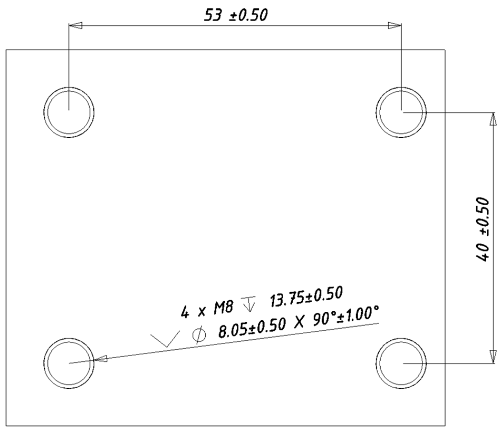

Figure 5.2: The mounting surface on the bottom plane.

5.1.2 Stress-Strain Model

The SW's simulation module uses the von Mises, or equivalent stress, yield criterion (SolidWorks 2016b). For an isotropic material, a measure of stress intensity required for the material to yield and become plastic is the von Mises stress, given by

$$\sigma_M = \sqrt{\frac{1}{2}\left[\left(\sigma_{xx}-\sigma_{yy}\right)^2+\left(\sigma_{zz}-\sigma_{xx}\right)^2+\left(\sigma_{yy}-\sigma_{zz}\right)^2+6\left({\sigma_{xy}}^2+{\sigma_{yz}}^2+{\sigma_{zx}}^2\right)\right]}, \tag{5.1}$$

where σ_{xx}, σ_{yy}, and σ_{zz} are normal stresses, and σ_{xy}, σ_{yz} and σ_{zx} are shear stresses. The first index i indicates that the stress acts on a plane normal to the i axis, and the second index j denotes the direction in which the stress acts. Conditions of material equilibrium of forces about a point require symmetry of the stress matrix, i.e. $\sigma_{ij} = \sigma_{ji}$.

According to the von Misses criterion, a material is said to start yielding when the von Mises stress σ_M reaches a yield strength of a material, σ_y, (Mises 1913). In this study, the von Mises equivalent stress is used to predict yielding of materials under complex loading. The failure criterion is based on the Von Misses equivalent stress.

According to the generalized Hooke's law for linear elasticity, displacements δ_i of the material's nodes can be calculated from the linear stress-strain relation through the material's elasticity module E, Poisson's ratio ν, the thermal expansion coefficient a and the temperature change ΔT. The displacements δ_i are calculated from the original length between the nodes ∂x, ∂y, ∂z and material strains ε_{ij} according to the following formula.

$$\varepsilon_{xx} = \frac{\partial \delta_x}{\partial x}, \qquad \varepsilon_{yy} = \frac{\partial \delta_y}{\partial y}, \qquad \varepsilon_{zz} = \frac{\partial \delta_z}{\partial z} \tag{5.2}$$

$$\varepsilon_{xy} = \varepsilon_{yx} = \frac{\partial \delta_x}{\partial y} + \frac{\partial \delta_y}{\partial x}, \quad \varepsilon_{yz} = \varepsilon_{zy} = \frac{\partial \delta_y}{\partial z} + \frac{\partial \delta_z}{\partial y}, \quad \varepsilon_{xz} = \varepsilon_{zx} = \frac{\partial \delta_x}{\partial z} + \frac{\partial \delta_z}{\partial x} \tag{5.3}$$

In the matrix form, the Hooke's law for isotropic material can be written as (Gere 2003)

$$\begin{bmatrix} \sigma_{xx} \\ \sigma_{yy} \\ \sigma_{zz} \\ \sigma_{yz} \\ \sigma_{xz} \\ \sigma_{xy} \end{bmatrix} = \begin{bmatrix} \hat{E}(1-\nu) & \hat{E}\nu & \hat{E}\nu & 0 & 0 & 0 \\ \hat{E}\nu & \hat{E}(1-\nu) & \hat{E}\nu & 0 & 0 & 0 \\ \hat{E}\nu & \hat{E}\nu & \hat{E}(1-\nu) & 0 & 0 & 0 \\ 0 & 0 & 0 & G & 0 & 0 \\ 0 & 0 & 0 & 0 & G & 0 \\ 0 & 0 & 0 & 0 & 0 & G \end{bmatrix} \begin{bmatrix} \varepsilon_{xx} \\ \varepsilon_{yy} \\ \varepsilon_{zz} \\ 2\varepsilon_{yz} \\ 2\varepsilon_{xz} \\ 2\varepsilon_{xy} \end{bmatrix} - \frac{Ea\Delta T}{1-2\nu} \begin{bmatrix} 1 \\ 1 \\ 1 \\ 0 \\ 0 \\ 0 \end{bmatrix} \tag{5.4}$$

Here $\hat{E}$ and G are the "effective" Young's modulus and the shear modulus respectively:

$$\hat{E} = \frac{E}{(1+\nu)(1-2\nu)}, \qquad G = \frac{E}{2(1+\nu)} \tag{5.5}$$

5.1.3 Mesh

The SW's mesh generator allows selection between standard (Voronoi-Delaunay) and curvature-based schemes to create a mesh. In the latter the mesher creates more elements in higher-curvature areas automatically. In both cases, a linear tetrahedral element is used as a base element. It is defined by four corner nodes connected by six straight edges (SolidWorks 2016b).

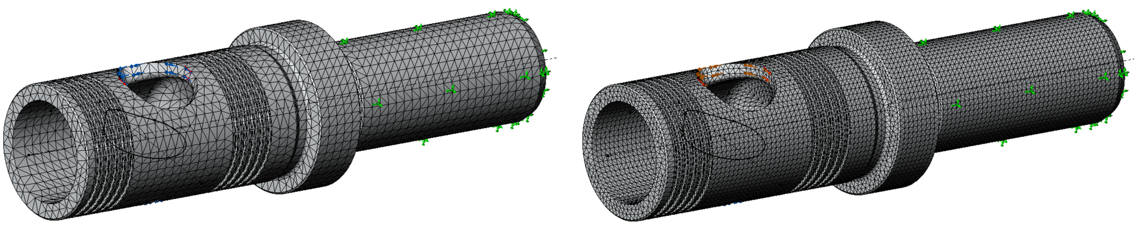

(a) 63210 elements. (b) 236840 elements.

Figure 5.3: Examples of a standard uniform mesh.

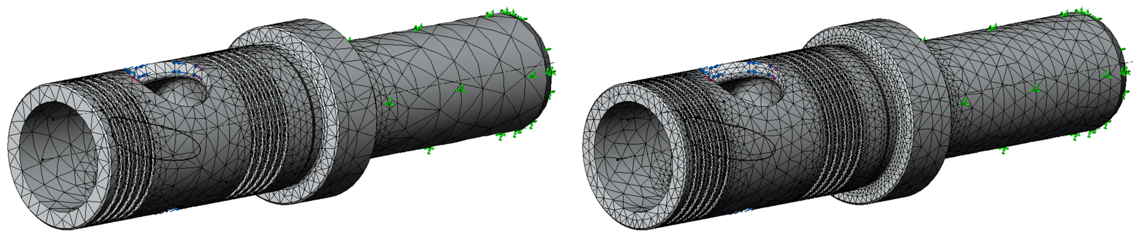

(a) 65251 elements. (b) 221683 elements.

Figure 5.4: Examples of a curved-based mesh.

For a standard mesh, see the Figure 5.3, elements are uniform in size across an entire solid model. For a curvature based mesh, see the Figure 5.4, the element size is determined mathematically by the minimum number of elements that fit in a hypothetical circle (SolidWorks 2016a). To ensure solutions accuracy, the comparison of two approaches have been conducted by means of the grid independence analysis. The internal stresses and displacements inside the spool have been selected as parameters to compare.

Grid Independence

In grid independence analysis the following FSI problem formulation has been applied. The spool's shaft is fixed, see the green arrows on the Figures 5.3 and 5.4, the metering faces are loaded with the steady flow torques, blue and orange arrows. The aluminum alloy (AA) 7075-T651 has been assigned as the spool material. Then, two types of meshes with different and increasing number of elements were applied to the entire model of the spool and simulations for the equivalent stress and displacements were performed. These steps are summarized in the Figure 5.5.

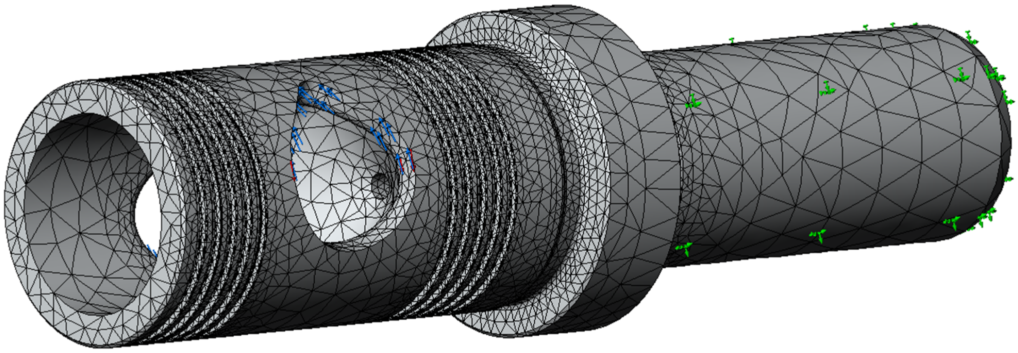

(a) Boundary conditions and meshing. Total number of elements 163369.

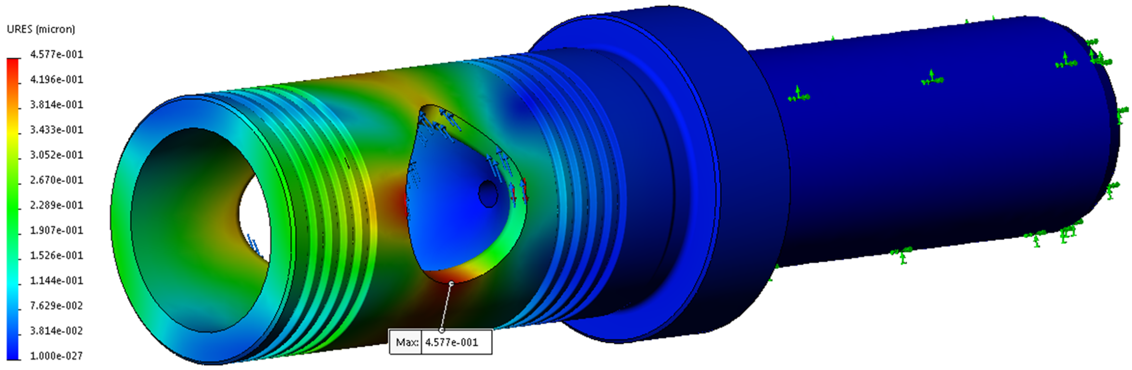

(b) Displacements in the spool.

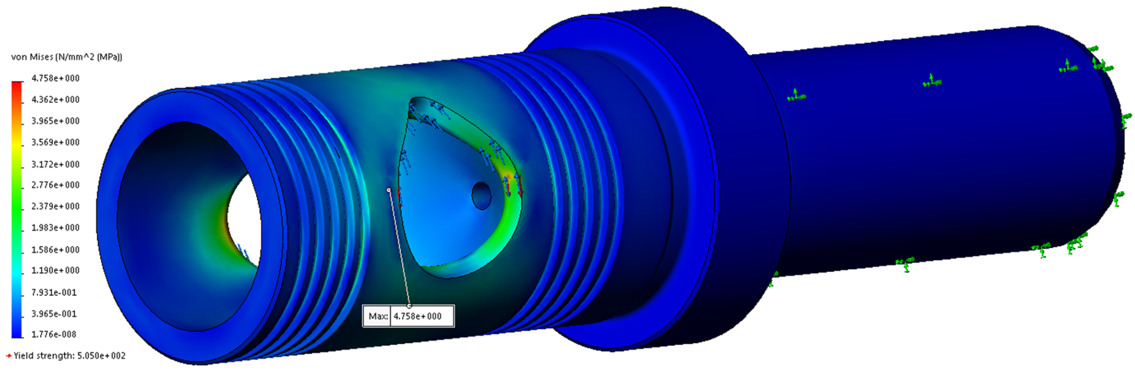

(c) Equivalent stresses in the spool.

Figure 5.5: Simulation steps and results. Flow torque effect.

For the same number of mesh elements, the minimal element size of the curvature-based mesh is comparable with the uniform elements of the standard mesh, see the Figure 5.6a, ranging from 2.3 mm to 0.5 mm. The larger the number of elements becomes, the smaller the difference in element sizes is observed for two mesh types.

The simulation results have shown larger deviations in simulation results, for both parameters: max equivalent stresses σ_M and max material displacements δ, on the coarser meshes, with smaller number of elements. Variables variations follow same trends, especially in case of displacements, where results of simulations on standard and curved-based meshes are practically coincide, see the

Figure 5.6c.

For both studied parameters, the standard mesh results in smaller deviations from the average value, see the standard deviations in the Figures 5.6b and 5.6c. The standard mesh produces more stable, consistent results compared to the curvature-based approach.

It has been also noted, that average values of the studied parameters for the standard mesh are higher comparing with the curvature-based mesh. Choosing the bigger value of simulation results for analysis and further design corrections may result in over designing the valve, which could make it heavier. On the other hand, use of larger stress values for stress studies favours resultant part's strength and reliability. For these reasons, the standard mesh was used for further analyses.

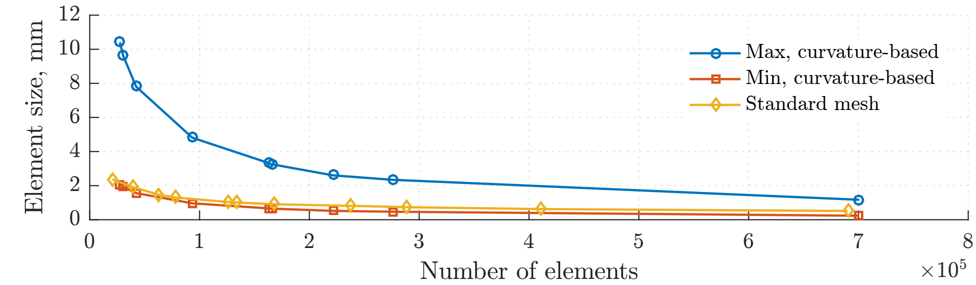

(a) Mesh element sizes for the standard and the curvature-based meshes.

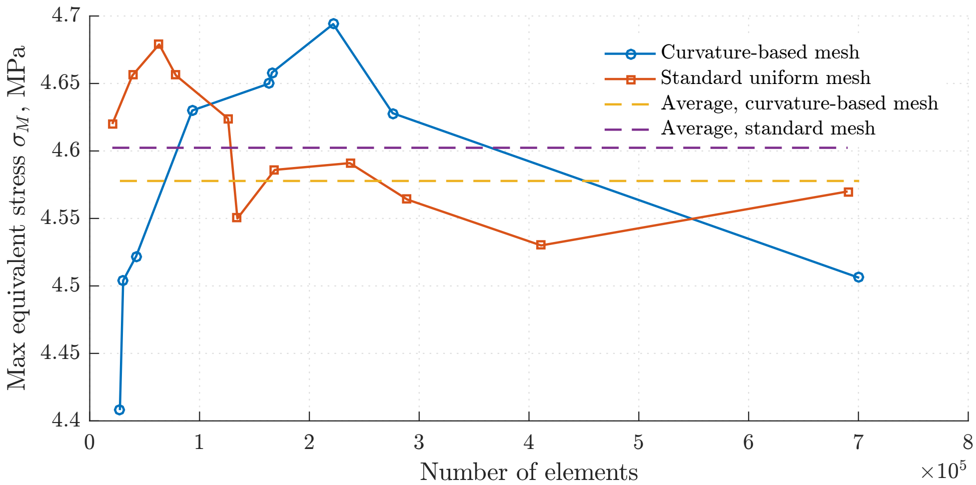

(b) Stresses. Average values for the standard and the curved-based meshes: $\mu_{st} = 4.602\,\text{MPa}$, $\mu_{curv} = 4.578\,\text{MPa}$. Standard deviations for the standard and the curved-based meshes: $\sigma_{st} = 0.048\,\text{MPa}$, $\sigma_{curv} = 0.095\,\text{MPa}$.

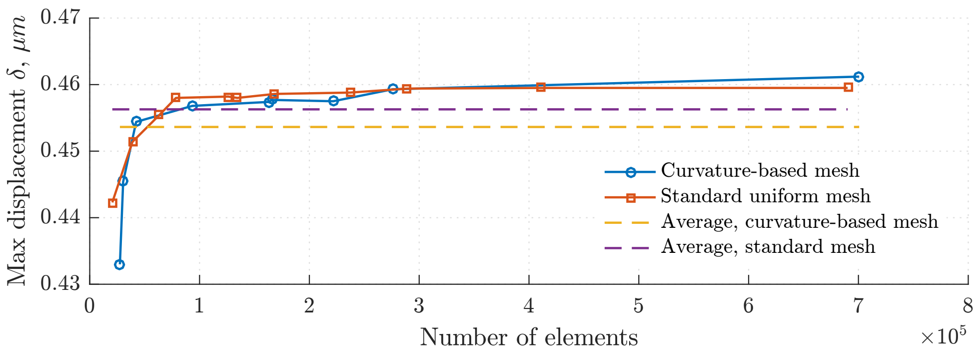

(c) Displacements. Average values for the standard and the curved-based meshes: $\mu_{st} = 0.456\,\mu\text{m}$, $\mu_{curv} = 0.454\,\mu\text{m}$. Standard deviations for the standard and the curved-based meshes: $\sigma_{st} = 5.21 \times 10^{-3}\,\mu\text{m}$, $\sigma_{curv} = 8.939 \times 10^{-3}\,\mu\text{m}$.

Figure 5.6: Grid independence results.

5.1.4 Boundary Conditions

Before running the stresses development simulation via (FEA), the boundary conditions for the simulation had to be identified in order to replicate the working conditions during operation of the prototype. General boundary conditions common to all cases were based on the assumptions that the prototype valve assembly is mounted on the test bench, surrounded by air at a room temperature and atmospheric pressure. The external pressure of $p_{atm} = 0.1\,\mathrm{MPa}$ and the room temperature $T = 20\,^{\circ}\mathrm{C}$ were applied to the external faces of the valve. Other boundary conditions include the "no penetration" condition for the adjacent mechanical parts and the global constant friction coefficient.

Material Model

Materials choice was justified by the required balance between manufacturability, structural strength. The used materials must endure imposed loading without failure and large deformations. At the same time, parts materials should allow application of simple and widespread manufacturing processes. Materials need to satisfy design for cost, manufacture and assembly (DFX) techniques.

For these reasons, the main material for the purpose of prototype manufacturing has been chosen wrought aluminum alloy AA 7075-T651, which is one of the most commonly used non-ferrous metals in the design of mechanical products (Ullman 2009). The list of mechanical properties of this alloy is listed in the Table 5.1.

Although for prototype manufacturing and test purposes aluminum is regarded as a suitable option, the final product is intended to be fabricated from high-tensile steel for the main throttling parts and cast iron for the valve body. The body's design incorporates an intricate and cavernous geometry, which favours the use of casting as manufacturing process. The main moving parts require high tensile material as these parts are the most responsible, need to carry the largest loads. Design's ability resist deformations and to keep geometry of these parts constant is the key factor to the valve performance.

Since the material of the moving parts in the final product, especially the spool, is steel, and in order to reduce friction between moving and static parts, the anti-friction material pair has been chosen for the spool-thrust bearing pair. Therefore, the thrust bearings's material is brass. The bill of materials (BOM) can be found on the assembly drawing of the prototype valve in the Appendix A.

Property	Symbol	Value	Units
Mass density	ρ	2810	$\mathrm{kg\,m^{-3}}$
Tensile strength	σ_t	570	MPa
Yield strength	σ_y	505	MPa
Elastic modulus	E	72	GPa
Poisson's ratio	ν	0.33	
Shear modulus	G	26.9	GPa
Thermal expansion coefficient	a	2.36×10^{-5}	$\mathrm{K^{-1}}$
Thermal conductivity	k	130	$\mathrm{W\,m^{-1}\,K^{-1}}$
Specific heat capacity	c	960	$\mathrm{J\,kg^{-1}\,K^{-1}}$

Table 5.1: Mechanical properties of the AA 7075-T651.

Loads

Transferring the loads from fluid flow simulations represents the special case of FSI problem applied to the developed rotary valve. Here, the extracted static pressure distribution from pressurized oil, which occupies the internal cavities of the valve, is transmitted to the stress analysis as the primary load factor. Another loading factor, which was taken from CFD simulations, is steady flow torque $T_{st.fl.i}$.

In the analysis of the spool strength, the spool was subjected to the steady flow torques on the metering surfaces $T_{st.fl.i}$ and the load pressure $p_{fl.}$. For each orifice, there are two torques originated from the flowing fluid: opening and closing. The maximum values of these torques were transferred from the CFD simulations. Thus, each orifice is exposed to the closing $T_{st.fl.cl.} = 0.22\,\mathrm{N\,m}$ and opening $T_{st.fl.op.} = 0.2\,\mathrm{N\,m}$ torques.

In the static stress analysis of the prototype valve assembly, the working pressure of the hydraulic fluid is set to $p_{fl.} = 20\,\mathrm{MPa}$, a value derived from the most extreme possible load configuration. To simulate the fluid pressure effect, this load pressure was applied to every surface wetted by the hydraulic oil, see the the geometry outlined in blue in the Figure 5.1. Additionally, the steady flow torques were applied on spool metering surfaces.

Fixtures

Fixed geometrical elements, i.e fixtures, were specified during the preprocessing stage. Selection of these is justified by a planned location on a test rig and within a machine of intended use. During testing, the prototype will be mounted on a base plate mechanically through the four fixture holes at the bottom of the body component, see the Figures 5.2 and 5.1. Therefore, these holes along with the bottom plane of the valve body are fixed in the stress simulation of the entire assembly.

In the spool strength analysis, it is assumed the spool's shaft opposite to the central cavity is fixed. The spool is mechanically connected to the stepper motor through the shaft using either a direct keyway link, or an additional coupling part.

To conclude the preprocessing stage, the settings of the solid model are summarized in the Table 5.2.

Simulation type	Static stress simulation, FOS analysis
Geometric models	The spool, the valve assembly
Mesh	Standard solid mesh with uniform tetrahedral elements • Spool: $N \approx 660000$ cells, cell size $0.520\,\mathrm{mm} \pm 0.026\,\mathrm{mm}$ • Valve: $N \approx 100000$ cells, cell size $2.50\,\mathrm{mm} \pm 0.15\,\mathrm{mm}$
Main material	Aluminum alloy AA7075-T651 see the Table 5.1
Boundary conditions	Loads • Static pressure on the oil wetted surfaces of $p_{fl} = 20\,\mathrm{MPa}$ • Steady flow torques on the spool metering surfaces: opening $T_{st.fl.op.} = 0.2\,\mathrm{N\,m}$, closing $T_{st.fl.cl.} = 0.22\,\mathrm{N\,m}$ Restraints • Spool: The shaft is fixed • Valve: The bottom plane, 4xM8, the spool's shaft are fixed Contact conditions • No penetration • Global friction coefficient 0.05

Table 5.2: Preprocessing setting of the solid model.

5.2 Postprocessing

The SW FEA solver represents a problem by a set of algebraic equations that must be solved simultaneously. There are two classes of solution methods available: direct and iterative. Direct methods solve the equations using exact numerical techniques. Iterative methods solve the equations using approximate techniques where in each iteration, a solution is assumed and the associated errors are evaluated. The software selects the solver based on the study type, analysis options, contact conditions, etc (SolidWorks 2016b).

The results of simulation provide insight into stresses and deformation of solid material under various configurations of loads and fixtures. In the postprocessing stage, strength of the spool and the entire prototype valve assembly were evaluated. In particular, analysis of stress and deformation distributions within the spool and the entire prototype valve assembly were performed.

5.2.1 Spool Strength

To study the spool strength, two main loading factors, i.e. steady flow torques $T_{st.fl}$ and the oil pressure p_{fl}, acting on the spool were investigated independently. An individual effect of each load on the structure of the spool was investigated.

Steady Flow Torque Effect

Stress and deformation fields within the spool under influence of the steady flow torques were investigated. The distributions of stresses and displacements can be taken from the grid independence analysis for the case of the standard mesh with 163369 elements, see the Figure 5.5.

The biggest equivalent stress and displacement occurs on the edge of the orifice opening. These reach values of $\sigma_{M.max} = 4.758\,\mathrm{MPa}$ and $\delta_{max} = 0.4577\,\mu\mathrm{m}$ respectively. The value of the maximum equivalent stress is far below the yield stress of the AA 7075-T651, i.e. $\sigma_y = 505\,\mathrm{MPa}$.

Therefore, the spool material does not yield under the applied load from flowing fluid. The maximum deformation can not lead to significant distortions in spool material. Hence, such deformations will not change the shape of the throttling opening on the spool and the spool can withstand the steady flow torques without failure to control the volume flow rate through the valve. The spool's design and assigned material can be considered strong enough to carry out its function in presence of the steady flow torques.

Pressurized Oil Effect

The effect of the hydraulic oil pressure $p_{fl} = 20\,\mathrm{MPa}$ on the spool structure was studied. In this study, the load is transferred from pressurized oil. The oil pressure was applied to all internal chambers and channels and to the external surfaces, which are wetted by oil, see the Figure 5.7. The standard mesh was applied with ≈ 650000 elements. The element size is $0.520\,\mathrm{mm} \pm 0.026\,\mathrm{mm}$.

According to the displacement distribution in the Figure 5.7, the spool part forming the central cavity is compressed in the axial direction. Its leftmost end is compressed with the maximum displacement of $\delta_{max} = 5.277\,\mu\mathrm{m}$. Such small deformation will not result in substantial distortion of the throttling orifice. Therefore, influence of the pressurized oil on the metering characteristics is negligible.

Another location of the relatively noticeable deformation is located on the spool central shoulder, from the compensating chamber side. There, the material displacement makes up around $3\,\mu\mathrm{m}$. Slight deformation in this regions would benefit oil tightness of the valve due to additional squeeze of the sealing rings.

It was noted, that the central oil channel, which supplies the oil to the spool back chamber, is being distorted, see the view on the deformed spool in the Figure 5.7e. It causes the channel's cross-section to contract radially on around $3\,\mu\mathrm{m}$. Since the diameter of the channel was selected equal to $2\,\mathrm{mm}$, the passage will not be blocked and oil can be fed to the compensating camber. Therefore, the balancing function of the channel is not violated.

In the case of the oil effect, the areas of the biggest internal stress are located in the back chamber and in the region along the central channel. This fact accounts for stress concentration around geometrical discontinuities, see the Figure 5.7d and 5.7e.

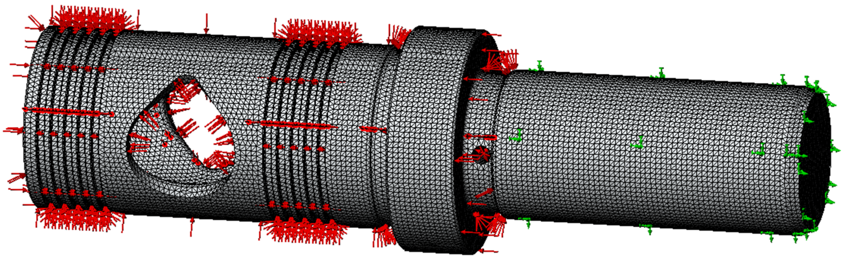

(a) Boundary conditions and mesh.

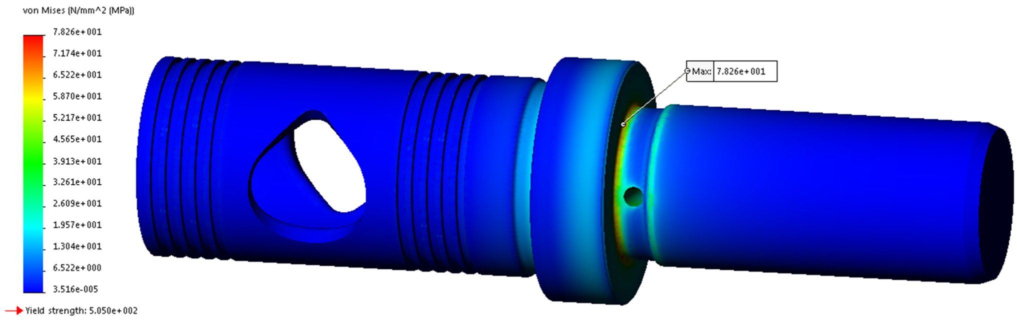

(b) Equivalent stresses distribution.

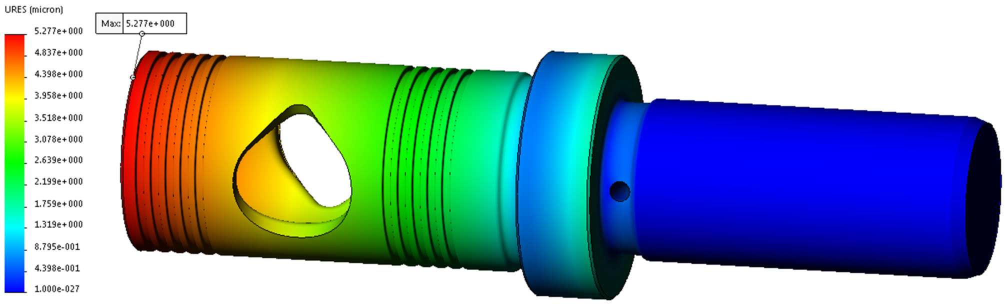

(c) Displacements distribution.

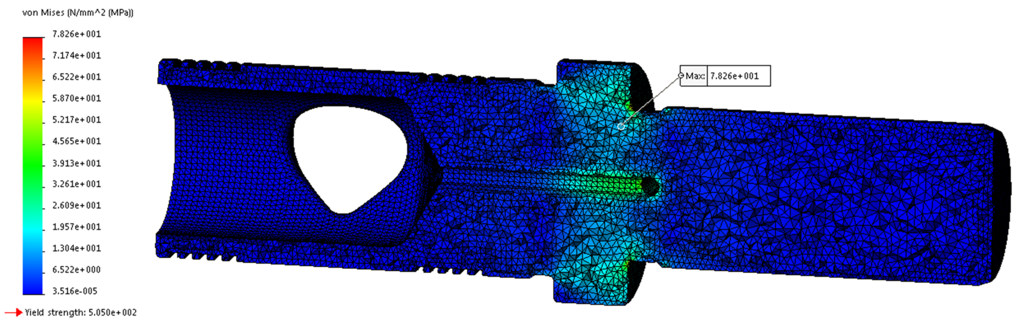

(d) Equivalent stresses distribution inside the spool.

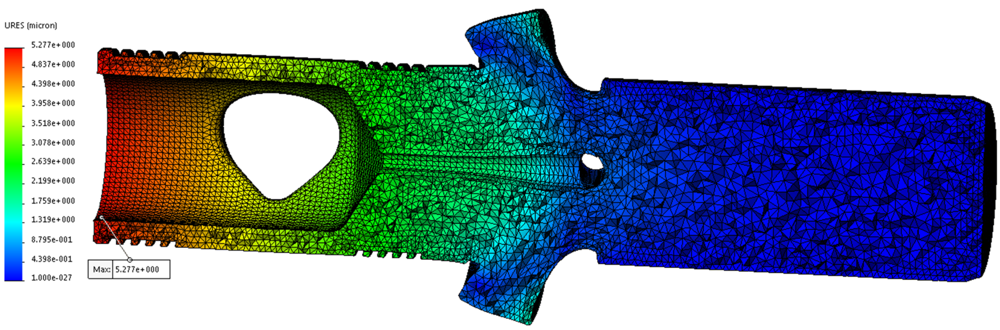

(e) Displacements distribution inside the deformed spool. The scale factor 1500

Figure 5.7: Effect of the pressurized oil on the spool. Green arrows – fixed surfaces, red arrows – surfaces subjected to the oil pressure. Total number of elements in the standard mesh 664326.

Combined Effect

The cumulative effect of two loads acting simultaneously on the spool was analysed. The mesh settings were the same as for the previous study, i.e. total number of elements ≈ 660000, the element size $0.520\,\mathrm{mm} \pm 0.026\,\mathrm{mm}$. The spool shaft is fixed.

Between the two applied loads, the oil pressure plays bigger role due to its magnitude. Thus, the results of application both loads simultaneously resemble the effect of the oil alone. The two loads result in the deformed spool, the exaggerated displacement view is illustrated in the Figure 5.8. The maximum displacement in the spool is $\delta_{max} = 5.183\,\mu\mathrm{m}$ on the spool rim at the flow entrance to central cavity. The effect is considered as insignificant as such deformation cannot cause notable distortion of the throttling windows. It also would not make the spool to get stuck inside the sleeve as the radial clearance between these parts is of larger order, i.e. $0.1\,\mathrm{mm}$. The oil supply channel is not being blocked.

Therefore, the spool material and its design are considered strong enough to carry imposed loads, perform appropriately its functions without failures.

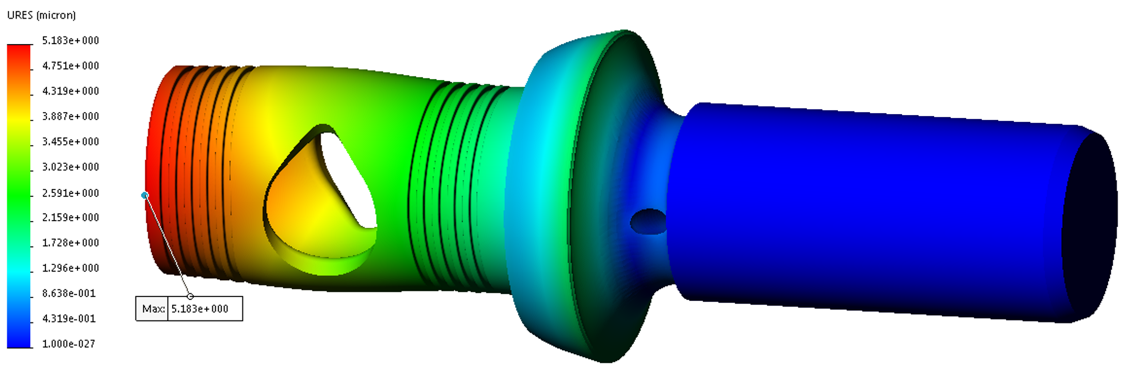

Figure 5.8: The deformed spool due to the combined load. The scale factor 1500.

5.2.2 Prototype Assembly Strength

To analyse the prototype strength, the following assumptions were made. All cavities, which are housing the elastic sealing (rubber O-rings and plastic anti-extrusion rings), are left empty. Elasticity of these chambers was neglected. The effect of empty sealing grooves is considered insignificant and not influencing the general stresses and displacements distributions though the prototype. The “no penetration” condition as well as global friction coefficient of 0.05 between neighboring mechanical parts were applied.

In this study the standard mesh was used with ≈ 100000 elements and the element size of $2.50\,\mathrm{mm} \pm 0.15\,\mathrm{mm}$. Then the fluid pressure of $p_{fl} = 20\,\mathrm{MPa}$ was applied to all internal cavities of the valve wetted with oil. The main parts included the spool, the sleeve, the valve body, the lid, the guiding sleeve and the thrust bearing. The valve body is fixed on the base plate via four threaded holes M8, it bottom plane is considered fixed as well. The spool takes the “fully open” position, i.e. $\phi = 90°$. Its shaft, which is connected to the stepper motor, was fixed too.

Distributions of the equivalent stress and displacements within the prototype assembly were plotted, see the Figures 5.9a and 5.9b respectively, and analysed. It was noted, that the largest internal equivalent stress of $\sigma_{max} = 466.2\,\mathrm{MPa}$ occurs in the spool, around its openings. The internal pressure has a local increase on the spool, other parts are stressed uniformly with slight stress rises in the domains of stress concentrations, which are sealing grooves on the sleeve and the lid. The stresses on these parts do not exceed values of $300\,\mathrm{MPa}$.

In case of displacements, non-uniform distribution of displacements was observed. As for the stress distribution, the biggest displacement $\delta_{max} = 54.84\,\mu\mathrm{m}$ takes place in the spool, around its orifices. Although, its the biggest deformation throughout the entire assembly, this value is

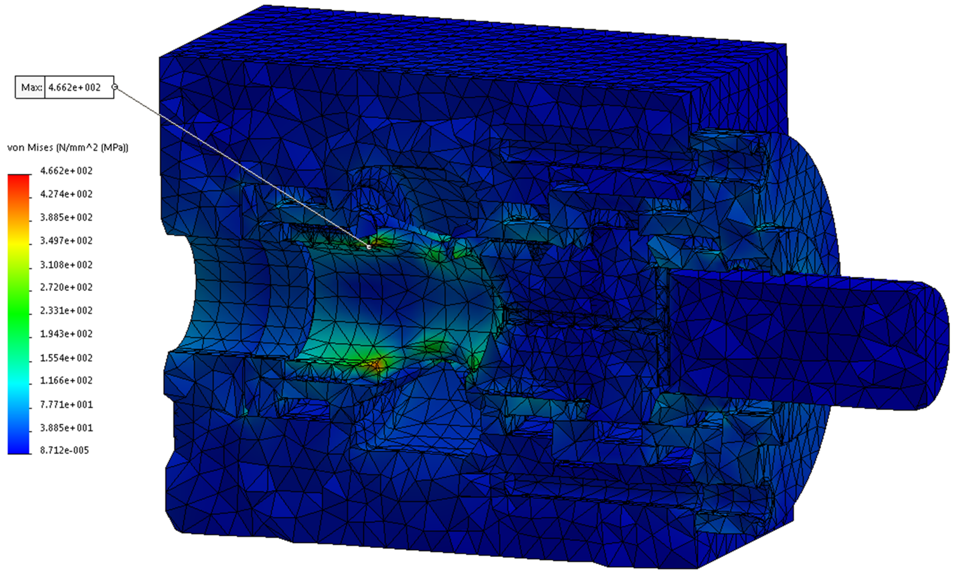

(a) Equivalent stresses distribution.

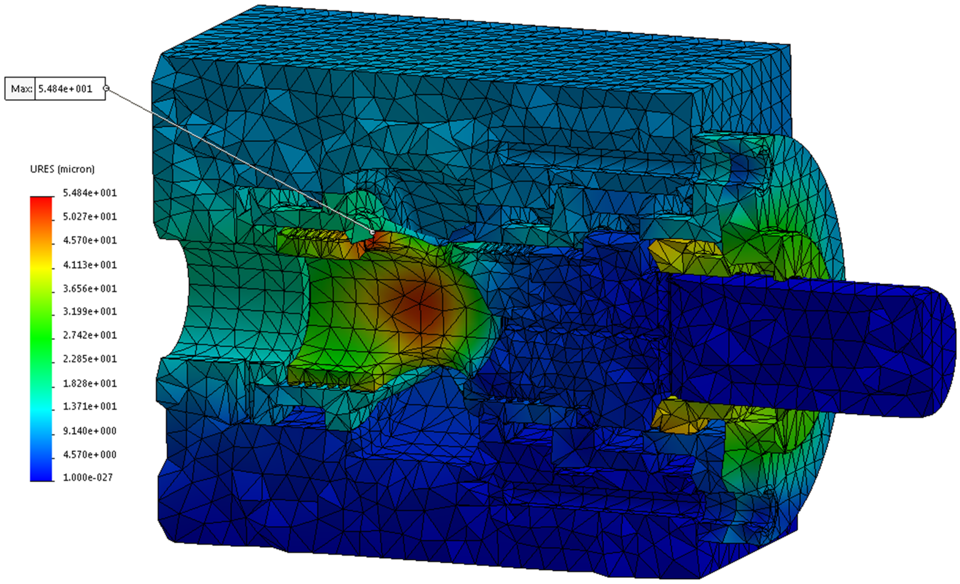

(b) Displacements distribution.

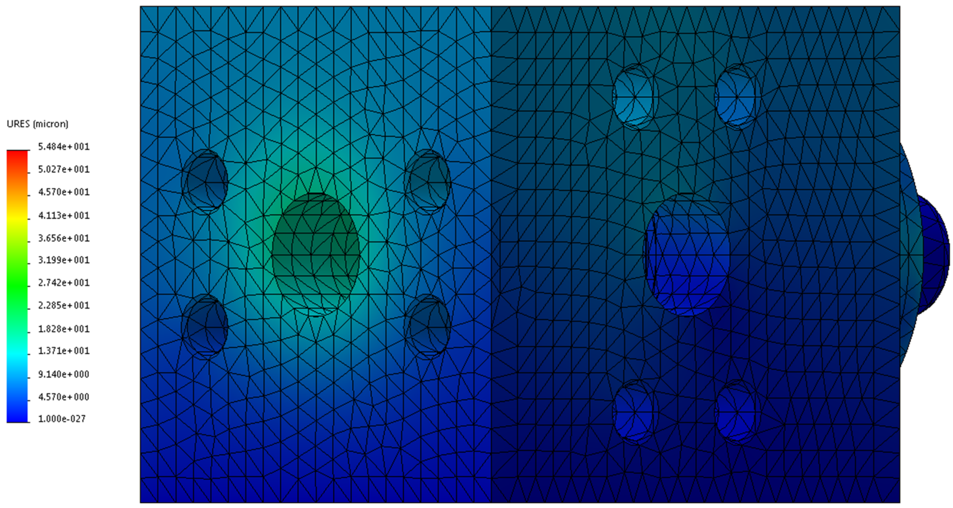

(c) Displacements distribution around the hydraulic connection ports.

Figure 5.9: Effect of the pressurized oil on the valve assembly.

smaller than the radial clearance $c = 0.1\,\mathrm{mm}$ between the spool and the sleeve. Therefore, the oil pressure-generated deformations in the spool do not cause the jam fault.

The displacements are distributed unevenly in other parts too. For example, the upper part of the valve body is being deformed up to $20\,\mu\mathrm{m}$, whereas the bottom part is effectively fixed. Large displacements also take place in the lid. In its inner part, deformations reach values of $40\,\mu\mathrm{m}$.

Because the parts displacements are within the limit of $0.1\,\mathrm{mm}$, the deformations of the valve parts are considered insignificant. The key geometrical elements of the design would not be distorted to an extent to cause faults and impede crucial functions. For instance, deformations of the hydraulic connection ports, see the Figure 5.9c, are not bigger than $25\,\mu\mathrm{m}$. Such material displacements could not obstruct functionality of the ports.

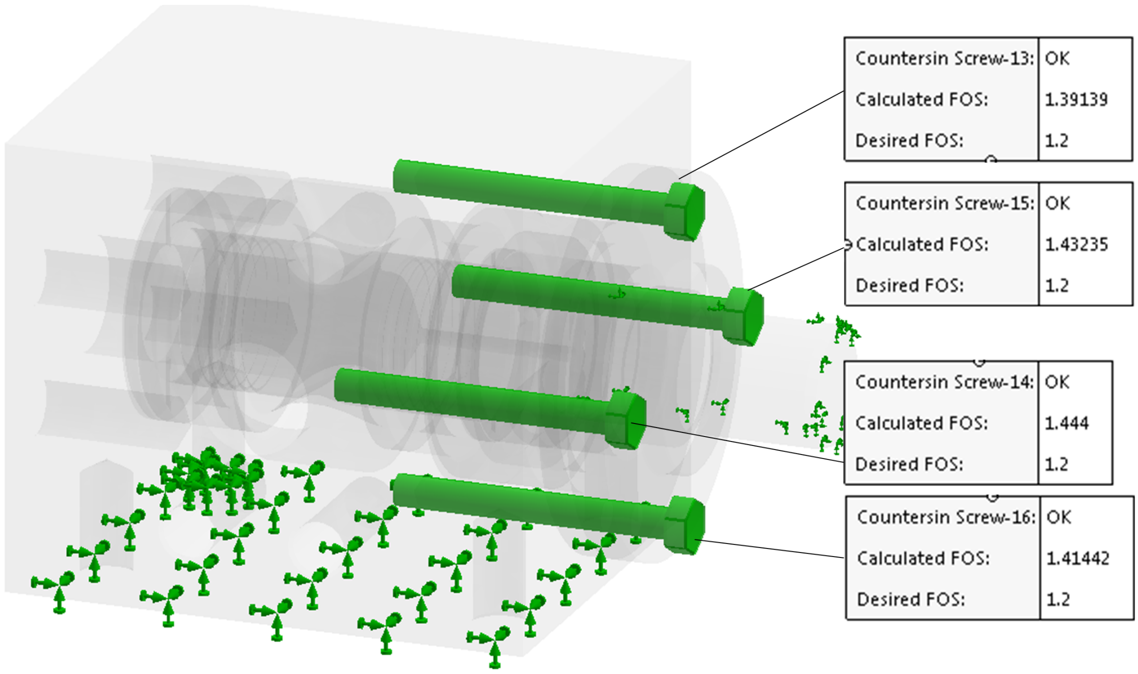

Figure 5.10: Results of the screws strength check.

Factor of Safety

Prototype strength estimation had an aim of confirming its soundness and ability to withstand specified loads during testing. It was also required to evaluate a factor of safety (FOS) of the fasteners used as these parts carry applied loads and keep the assembly together. A factor of safety less than unity indicates material failure. Large factors of safety in a region indicate low stresses and that one can remove some material from this region (SolidWorks 2016b).

The desired FOS was specified as $f_{s.des.} = 1.2$ for the set of four M4x0.7 screws with the 30 mm length, which attach the lid and the sleeve to the valve body. In the current application, the fasteners work under the tensile load. Thus, the axial force and tensile stresses were calculated from the applied load and compared with the desired FOS. FOS calculations were performed and compared with the desired FOS for each fastener, according to the following pass/no pass criterion.

$$f_s = \frac{A_T \sigma_y}{F_a} \tag{5.6}$$

$$f_s \leq f_{s.des} \tag{5.7}$$

Here, F_a – the calculated axial force, acting on the connector screw, A_T – the connector tensile area and σ_y – the yielding stress of the connector material.

Each fastener also had a pre-load torque of $T_{pre} = 1\,\mathrm{N\,m}$. If the axial force from the pre-load exceeded the load-generated force, the former was used to calculate the FOS.

The results of the pass/no pass connectors check are illustrated in the Figure 5.10. The check confirmed that the selected set of four alloy steel counterbore screws with the yield strength of $\sigma_y = 640.422\,\text{MPa}$ and the Young's module of $E = 211\,\text{GPa}$ can withstand applied oil pressure of $p_{fl} = 20\,\text{MPa}$ without yielding, even with empty sealing grooves. If the model included pre-squeezed sealing rubber O-rings and plastic anti-extrusion rings, the calculated FOS would had bigger values.

5.3 Chapter Conclusions

The strength evaluation of the spool and the entire valve assembly demonstrated that the design and chosen materials are able to carry the imposed load without material failure. According to the FOS estimation of the used screws, the selected set of connectors will not yield under the specified load. The actual deformations in the spool and the valve assembly under expected loading were evaluated and deemed acceptable. The resultant values of deformations do not violate any of the intended functions of the valve and spool design.

Therefore, the suggested design configuration of the valve can be further tested physically, in experimental environment. Its operational limits in terms of pressure can be taken as 20 MPa. Pressure levels above this value are considered risky.

Testing under more severe loading conditions would require redesigning measures, particularly for the connectors. Their total number or thread diameter can be increased. The rest of the valve parts exhibit satisfactory behaviour under the used loading. Thus, their redesign is not considered necessary in terms of structural strength and integrity.

Chapter 6

Experiments

A prototype of the valve was manufactured in order to test and validate the theoretical model of the valve described in the previous chapters. A detailed experimental procedure is designed to test the behaviour of the valve within the hydraulic system and test its modelling characteristics. This chapter discusses the manufactured valve prototype, the test parameters, the controlled and monitored variables, the instrumentation used, as well as the experimental procedure and the results.

6.1 Prototype Valve

A physical prototype of the valve was manufacture by a contractor and assembled in accordance with the design specification and the assembly scheme stated in the Appendix A and the Appendix B respectively. The prototype valve comprised original, standard and “off-the-shelf” parts.

6.1.1 Original Parts

Original parts include the designed valve’s mechanical parts required to execute the new throttling method. These were manufactured in accordance with the drawings in the Appendix A.

However, a few geometrical simplifications of the valve parts were applied. Although the valve body’s collecting channel in the prototype had a rectangular cross-section area A_{an}, see in the Figure 3.14, the area was kept the same as in the original design specification. Transition from the collecting channel to the outlet hydraulic port did not have a fillet on it. These deviations were considered as negligible and not influencing the overall valve performance. The overall length of the body was slightly shortened to reduce amount of the needed material. This resulted in small offset in the mounting threaded holes, which was taken into account during designing of the mounting base plate assembly described below.

The employed manufacturing methods used to create the original parts consisted of computer numerical controlled (CNC) milling and turning processes. The Table 6.1 summarizes the original parts produced for the valve assembly. The Figure 6.1 illustrates the main valve parts before assembly of the prototype.

To fix the prototype on the hydraulic test rig, a base plate, a shaft height compensator and a main base plate had been designed using SW to align the valve with the stepper motor (SM), see the Figure 6.3. The main purpose of the valve base plate assembly was to secure the prototype valve on the test rig.

As stated above, another function of the base plate assembly is to level the shafts of the spool and and the SM via the height difference compensator. For this, the thicknesses of the plates were calculated from the vertical positions of the motor’s and spool’s shafts. The resultant drawings of the designed complementary mounting parts can be found in the Appendix A.

#	Part	Method	Material	Extents	Q-ty
1	Body	CNC Mill	AA7075-T651	70 mm x 60 mm x 60 mm	1
2	Spool	CNC Mill	AA7075-T651	85 mm x 24.1 mm x 24.1 mm	1
3	Sleeve	CNC Lathe	AA7075-T651	62 mm x 50 mm x 50 mm	1
4	Thrust bearing	CNC Lathe	Brass Cz121	2.5 mm x 24.5 mm x 24.5 mm	1
5	Lid	CNC Lathe	AA7075-T651	16.5 mm x 50 mm x 50 mm	1
6	Guiding sleeve	CNC Lathe	AA7075-T651	5 mm x 29.51 mm x 29.51 mm	1

Table 6.1: List of the original valve parts. Tolerances of ±0.1 mm applied.

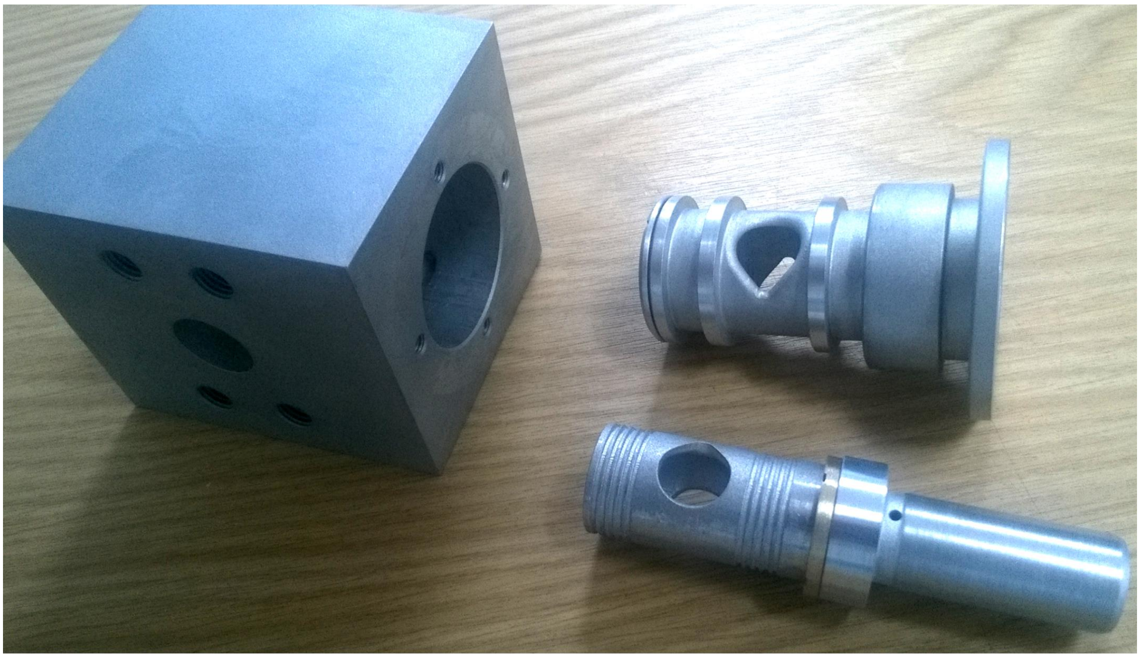

Figure 6.1: The main manufactured parts of the prototype valve: the valve body, the guiding sleeve inside the main sleeve, the spool with the thrust bearing on it.

6.1.2 "Off-the-shelf" Parts

In addition to the original valve and custom-made base plate parts, the market available or "off-the-shelf" parts needed to run the intended tests were identified. Among these parts, SM and its shaft's coupling are principal. These "off-the-shelf" parts were identified, selected and acquired. The details of these parts are summarized below.

Stepper Motor

The SM was selected based on the maximum anticipated loading torque on the spool shaft. The motor's holding torque must be able to overcome all load factors occurring on its shaft without rotation.

The used SM contained a built-in encoder allowing to monitor the spool angular position inside the valve, to detect errors and to compare it with the commanded position. This is done by comparing the command position with the encoder pulse count. If deviation exceed the set value, a "step out" signal will be gener-

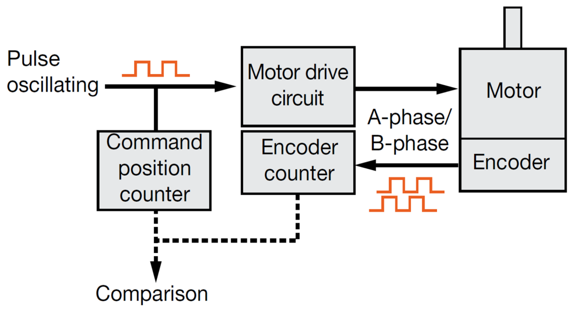

Figure 6.2: Encoder operation scheme (Oriental Motors 2017).

ated as output (Oriental Motors 2017). Therefore, the angular position feedback loop is implemented to enhance positioning precision, see the Figure 6.2. The full list of characteristics of the SM can be found in the Appendix C.

Parameter	Value	Units
Maximum holding torque	6.3	N m
Rotor inertia	3300×10^{-7}	kg m^2
Rated current	0.75	A/phase
Basic step angle	0.72±0.05	°
Power supply input (220 – 240 VAC)	2.2	A
Control power supply	24/0.2	VDC/A

Table 6.2: Key characteristics of the SM RKS5913, (Oriental Motors 2017).

Accessories

To transmit rotation from the motor to the spool and ensure reliable mechanical connection between the two shafts, an elastic coupling was selected. It uses a hard rubber spider as the elastic anti-vibration torque-transmitting element. High torsional stiffness of the spider is suitable for the required high precision positioning.

The size of the coupling was selected according to the shaft diameters of the SM and the spool. Coupling's aluminum hubs had the corresponding inner diameters. Each hub incorporated a tightening screw as a clamping mechanism, which mounts and fixes the coupling's hub onto the shaft. The whole coupling assembly has a three-pieces structure, which facilitates easy dismounting and accurate adjusting of the hub's position on the shaft.

In addition, the hard plastic mounting bracket was used to install and secure the SM onto the base plate. To attach the motor to the bracket, a set of four mounting screws M5-16 were used.

6.1.3 Standard Parts

To assemble the prototype valve, the acquired parts and to mount the entire assembly securely on the test rig, the standard fasteners were identified and selected. To ensure leak tightness of the prototype valve, sealing rings were chosen and obtained in accordance to the developed specification, see the BOM in the Appendix A. The full list of standard parts is summarized in the Table 6.3 below.

6.1.4 Assembly

To evaluate a general view and exact dimensions of the final prototype assembly, a three dimensional model of the valve with the "off-the-shelf" parts was created, see the Figure 6.3. This model was also used to identify the required set of fasteners, which is listed in the Table 6.3. It also served to estimate the dimensions of the base plate assembly and the height compensator.

As a part of the further development of the experiment design, the original model of the test valve assembly was modified by adding a torque transducer (TT) between shafts of the spool and the SM. This transducer would allow the measurement of torques acting on the spool. This was particularly useful in measuring the residual friction torque due to elastic sealing rings. TT would allow to validate the applied friction model, which is a part of the developed mathematical model of the valve, see the Appendix D. The physical representation of the prototype valve is illustrated in the Figure 6.6a.

#	Part	Standard	Material	Q-ty
	Seals: O-rings			
1	O-ring 213B 23.39x3.53-s	ISO 3601-1:2012	EPDM	3
2	O-ring 216B 28.17x3.53-s	ISO 3601-1:2012	EPDM	1
3	O-ring 114B 15.54x2.62-s	ISO 3601-1:2012	EPDM	1
4	O-ring 117B 20.29x2.62-s	ISO 3601-1:2012	EPDM	1
	Seals: Anti-extrusion rings			
5	Anti-extrusion ring T2-353-RD-002410-002960	ISO 3601-4:2008	PTFE	1
6	Anti-extrusion ring T2-353-PS-002951-002424	ISO 3601-4:2008	PTFE	2
	Fasteners			
7	Hexagon socket head cap screw M4x30-12.9	ISO 4762:2004	Alloy Steel	4
8	Hexagon socket head cap screw M6x25-12.9	ISO 4762:2004	Alloy Steel	4
9	Hexagon socket head cap screw M8x35-12.9	ISO 4762:2004	Alloy Steel	4
10	Hexagon socket countersink screw M8x20-12.9	ISO 10642:2004	Alloy Steel	4
11	Hexagon regular nut M4x30-12.9	ISO 4762:2004	Alloy Steel	4
12	Steel spring washer M4 type A	BS 4464:1969	Carbon Steel	4
13	Steel spring washer M6 type A	BS 4464:1969	Carbon Steel	4
14	Steel spring washer M8 type A	BS 4464:1969	Carbon Steel	12
15	Hexagon socket head cap screw 0.3125-24x1.25	ASME B18.3:2003	Alloy Steel	8

Table 6.3: List of standard parts.

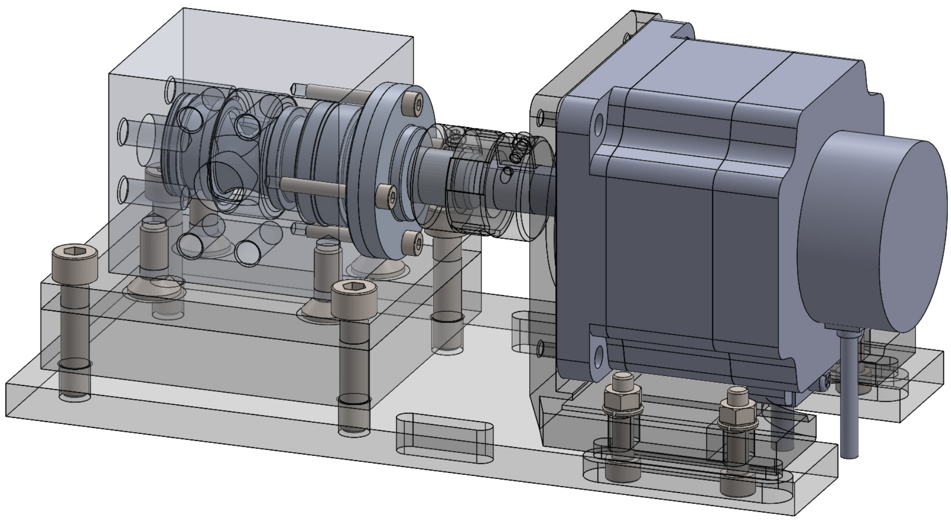

Figure 6.3: The model of the prototype valve assembly adapted for the hydraulic test rig.

6.2 Data Acquisition System

The experimental data acquisition system (DAQ) was used to collect data about the behaviour of the new valve in physical environment, as a part of a hydraulic system. The main purpose of the used DAQ is to enable safe collection of the test data since the main component of the hydraulic is the mineral oil under high pressure.

DAQ can be divided on three parts according to the physical nature of transmitted signals, see the Figure 6.4. The mechanical component was described in the preceding sections. The details of the hydraulic test bench are discussed in the following section. Depending on the characteristic of interest, the monitored and controlled variables varied. Exact sets of monitored and controlled variable are summarized in the following experiment description.

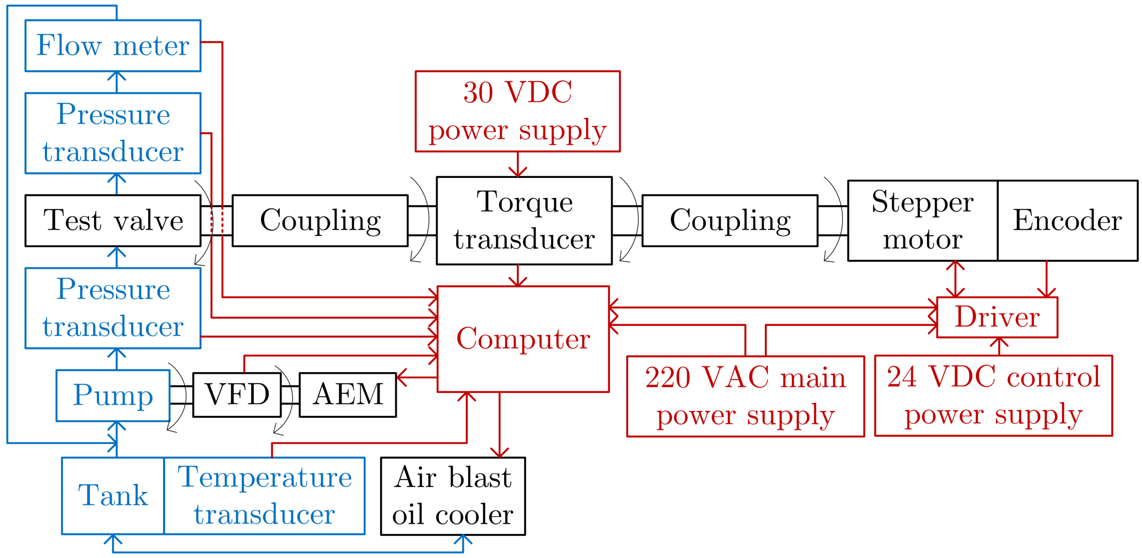

Figure 6.4: The block scheme of the data acquisition system. Blocks and signals colors correspond to: black – mechanical, blue – hydraulic, red – electric.

6.2.1 Hydraulic Test Rig

The Figure 6.6b shows the image of the hydraulic test setup used for the experiments. It can be divided on the power, oil conditioning subsystems, sensors and the test prototype valve (RTSV). The Figure 6.6 also shows the general view of the hydraulic test rig and the prototype valve.

The oil storing and conditioning subsystem includes an oil tank with an inbuilt heater, oil filters, and an air blast heat exchanger. The tank also comprised a breather that connects the tank's chamber to surrounding environment to ensure that the atmospheric pressure level is maintained in the tank and the return line of the hydraulic system.

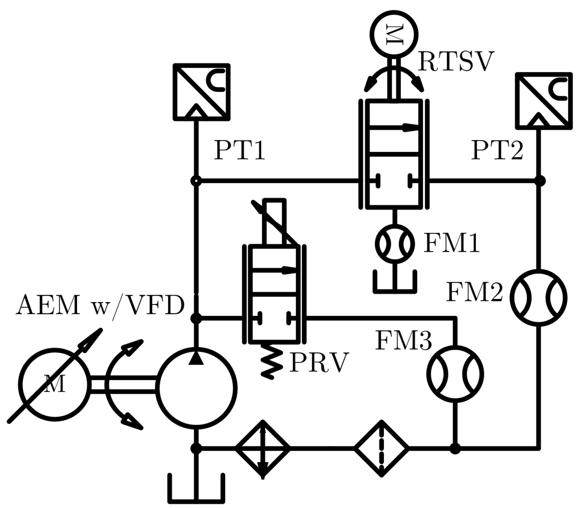

Figure 6.5: The scheme of the hydraulic test rig.

The power subsystem of the test rig was equipped with an asynchronous electric motor (AEM) with a variable frequency drive (VFD). The AEM served as a pump's driver, while the VFD allowed to set the rotational speed of the pump's shaft and, hence, to control the pump's volume flow rate supplied into the hydraulic system. The pump used here was a Hydreco's spur gear pump QR6 series with displacement of $160\,\mathrm{cm}^3\,\mathrm{rev}^{-1}$, see the yellow-painted element in the Figure 6.6b. Its operating speed range is $450\,\mathrm{rev\,min}^{-1}$ to $2750\,\mathrm{rev\,min}^{-1}$, (Hydreco 2017).

In the power subsystem, in parallel to the pump, the was a pressure relief valve (PRV), which was installed in the by-pass line. The PRV is electronically controlled proportional valve, which allowed to set the valve's inlet pressure to the desired value. It also limited the pressure level in the hydraulic system, implementing the safety function. The by-pass line also included the flow meter FM3 to monitor the amount of flow passing through this line.

The main hydraulic line incorporated the test valve, RTSV. The drain line of the RTSV featured the flow meter FM1 to measure the internal leak through the valve's parts. The origin and the route of this leakage is described in the following sections.

Up- and downstream to the prototype valve, two pressure transducers were mounted PT1 and

PT2 respectively. Additionally, the flow meter FM2 was installed in the downstream of the test line to enable measuring the volume flow rate passing through the test valve.

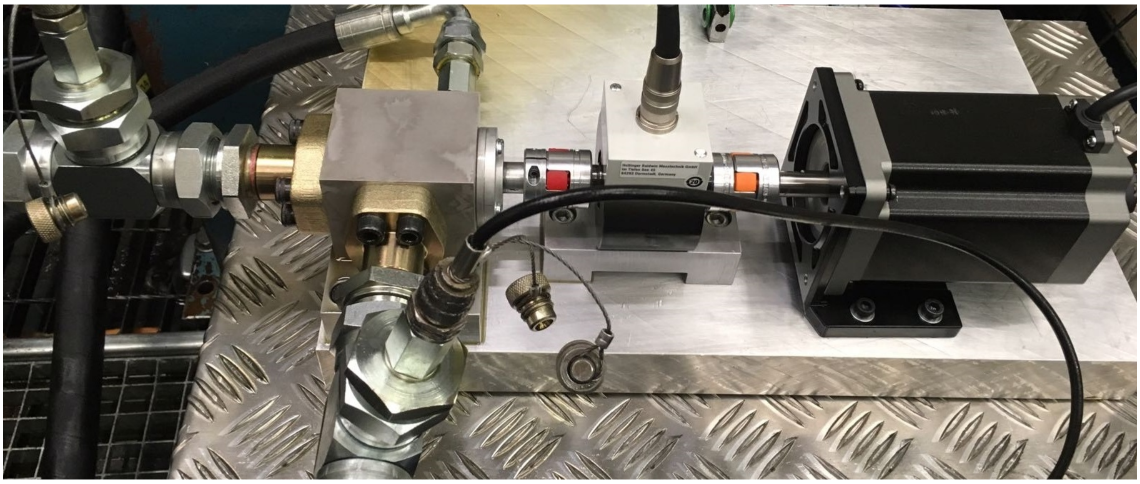

(a) The prototype valve, the RTSV.

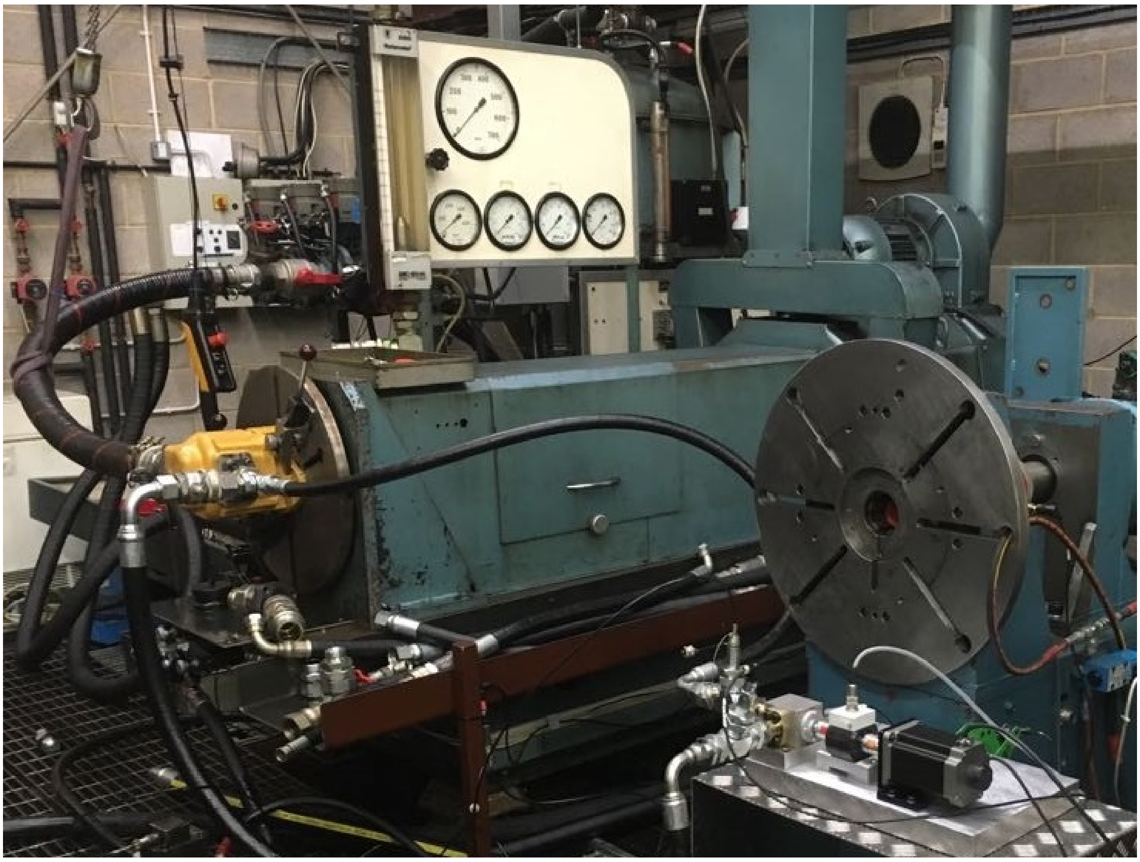

(b) The hydraulic test rig.

Figure 6.6: The photos of the used hydraulic test rig.

6.2.2 Instrumentation

The oil's supply subsystem allowed keeping the temperature level constant in time due to thermocouples, the air-blast oil cooler and the heater, which form the closed-loop temperature control system. The tank-embedded thermocouples serving as temperature sensors allowed the temperature level to stay the same throughout the length of an experiment. The working fluid was a zinc and chlorine free anti-wear hydraulic oil, Shell Tellus S2 V32 (Shell 2017).

To monitor volume flow rates circulating the hydraulic system, three gear-type flow meters FM1, FM2 and FM3 were installed in the following hydraulic lines: pumps's by-pass, test valve's line and valve's internal leakage line. The latter enabled measurement of the oil spillage from the valve's central chamber, through the spool-sleeve gap and the thrust bearing to the tank. The leak drain line allows to lubricate all mechanical contacts within the valve with the working fluid, collect the leakage flow and direct it to the tank, see the Figure 3.14.

The flow meters included two non-contacting measuring gears, which are driven by the liquid flow on the principle of a gear pump. When the measuring gear rotates by one tooth pitch, the sensor emits a signal. Then, the signal is converted into a square-wave signal by the preamplifier and fed to a computer (Kracht 2017). Apart from thermocouples and flow meters, the pressure sensors were used to collect the flow-related data, static pressure. The pressure transducers feature a sputter diaphragm, deformation of which is sensed and transformed into the pressure signal (Gems 2017).

The used instrumentation is summarized in the Table 6.4. According to the sensors' datasheets, accuracy of the used transducers can ensure a low systematic error of experiments.

Instrument	Make	Model	Range	Accuracy
Pump	Hydreco	QR6 6160	Displacement $160\,\mathrm{cm^3\,rev^{-1}}$ Speed $450\,\mathrm{rev\,min^{-1}}$ to $2750\,\mathrm{rev\,min^{-1}}$	
FM	Kracht	VC12	$2\,\mathrm{l\,min^{-1}}$ to $600\,\mathrm{l\,min^{-1}}$ Resolution $83.33\,\mathrm{impulse\,rev^{-1}}$ Tooth volume $12\,\mathrm{cm^3}$	±0.3%
PT	Gems	3100B0400	400 bar Output 0.5 V to 4.5 V 4 mA to 20 mA	±0.25%
TT	HBM	T20WN	10 N m Output ±5 V 10 mA ± 8 mA	±0.5%
SM	Oriental Motors	RKS5913R	0.72° step	±0.05°

Table 6.4: Instrumentation.

6.3 Test Procedure

The general goal during the design of the experiment stage was to replicate the valve metering characteristics obtained in the modelled environment. Test procedure development consisted of selecting and dividing the variables into controlling and recorded in order to enable recreation of the metering characteristics and, thereby, to meet the objective. The ranges of controlled variables corresponds to the boundary conditions used in the CFD parametric simulations for a particular metering function. The static parameters of interest are the volume flow rate, the pressure drop, leakages (internal and at the closed state). The summary of the test procedure is listed in the Table 6.5. During all tests the temperature of oil was kept constant at 45 °C.

6.4 Test Results

The following sections report the results of the experiments conducted as a part of this investigation. The data collection was performed in according to the test plan, see the Table 6.5. The figures shown below are the results of the static hydraulic representation of the proposed rotary flow control valve.

As a general note, visual inspection of the valve before, during and after each test did not reveal any leakages or visible deformations of the valve's parts. There were also no signs of rubber O-rings extrusions. The inspection allowed to conclude, that the valve was able to withstand

Test	Variable	Type	Instrument	Range
	p_{in}	Controlled	VFD, PRV	0.35 MPa to 1.1 MPa
$Q(\phi)$ at $\Delta p = \text{const}$	ϕ	Controlled	SM	30° to 90°
	p_{out}	Monitored	PT2	40 MPa, Table 6.4
	Q	Monitored	FM2	$600\,\mathrm{l\,min^{-1}}$, Table 6.4
	Q	Controlled	VFD, PRV	$25\,\mathrm{l\,min^{-1}}$ to $175\,\mathrm{l\,min^{-1}}$
$\Delta p(Q)$ at $\phi = \text{const}$	ϕ	Controlled	SM	50° to 90°
	p_{in}	Monitored	PT1	40 MPa, Table 6.4
	p_{out}	Monitored	PT2	40 MPa, Table 6.4
	ϕ	Controlled	SM	50° to 90°
$Q_{int.leak.}(\Delta p)$ at $\phi = \text{const}$	p_{in}	Controlled	VFD, PRV	0 MPa to 10 MPa
	p_{out}	Monitored	PT2	40 MPa, Table 6.4
	$Q_{int.leak}$	Monitored	FM1	$600\,\mathrm{l\,min^{-1}}$, Table 6.4

Table 6.5: Test plan.

highly pressurized oil without leakages and failure to operate. Therefore, the general design of the prototype was considered satisfactory and able to performs its functions.

6.4.1 Volume Flow Rate

During measurements of the volume flow rate characteristic of the valve $Q(\phi)$, the spool angular position was ranging from $\phi = 30°$ to $90°$. At every spool position ϕ, the PRV and the VFD were used to set the pressure differential across the valve equal to the values of $\Delta p = 0.25\,\mathrm{MPa}$, $0.5\,\mathrm{MPa}$ and $1\,\mathrm{MPa}$. Then, the readings from the flow meter on the main line were recorded.

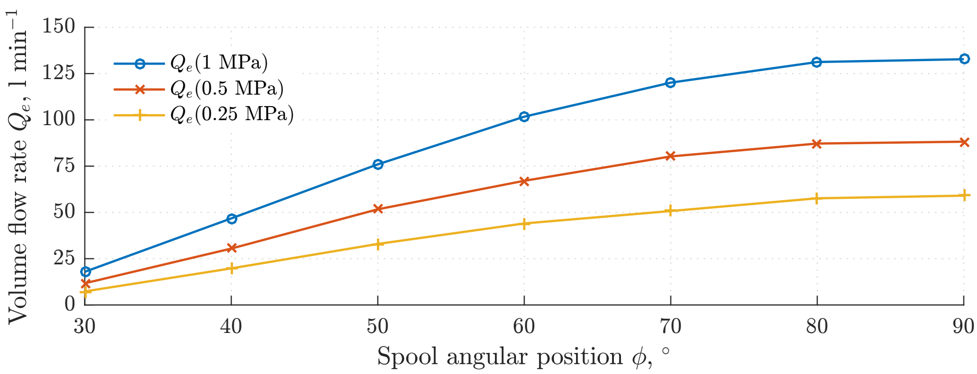

Figure 6.7: Experimental volume flow rate $Q_e(\phi)$ at $\Delta p = 0.25;\ 0.5;\ 1\,\mathrm{MPa}$

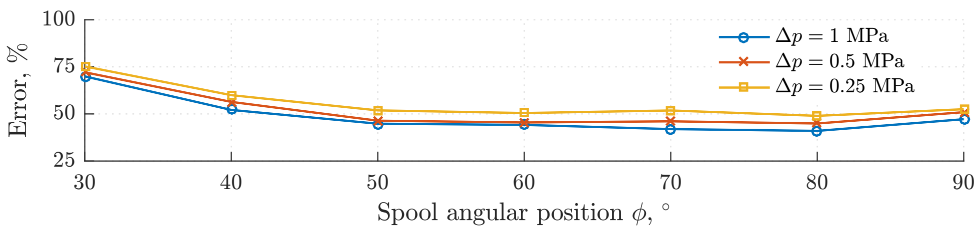

Figure 6.8: Percentage difference between simulated and tested volume flow rates $Q(\phi)$ at $\Delta p = 0.25;\ 0.5;\ 1\,\mathrm{MPa}$

Experimental graphs of the volume flow rate as a function of the spool angular position are shown in the Figure 6.7. These follow the same trend as the CFD modelled one, see the Figure

4.10. However, the magnitudes differ drastically, especially for small valve openings and the low-opening spool positions, i.e. up to $\phi = 30°$, see the Figure 6.8 showing the error between simulated and measured data.

According to the Figure 6.8, the predicted values of the volume flow rate exceed the measured values by 48.75%, 51.77% and 55.85% in average for the three pressure drops of 1 MPa, 0.5 MPa and 0.25 MPa respectively. The error between the measured, Figure 6.7, and modelled, Figure 4.10, volume flow rates does not depend on the pressure drop causing the flow. That testifies to consistent data collection.

6.4.2 Pressure Losses

During measurements of the pressure losses, VFD and PRV were simultaneously used to control the pump's discharge volume flow rate and the valve's inlet pressure respectively. The spool was put in the predetermined position in the range $\phi = 50°$ to $90°$ according to the test procedure. The spool openings below $\phi = 50°$ caused the inlet pressure to rise above 20 MPa, which was considered unsafe. The parameters monitored were the valve's outlet and inlet pressure levels. The difference between these values constituted the predicted pressure drop Δp, or the pressure loss.

The opposite tendency to the volume flow rate results was observed to the pressure drop curves. Here, the experimental values are higher than the modelled with a higher similar margin. The pressure measurements were performed with the maximum volume flow rate $175\,\mathrm{l\,min^{-1}}$. Further increase in the volume flow rate led to the inlet pressure level rise above 20 MPa, which was considered risky in terms of structural integrity of the valve. This inlet pressure was used as reference level according to the stress analysis conducted in the Chapter 5.

In case of pressure drop measurements, simulated, see the Figure 4.15 and test results, see the Figure 6.9, differ. The Figure 6.10 demonstrates the percentage error between the simulated and experimentally measured pressure losses relative to the former one. The smaller valve openings result in the highest results error of 90.25% on average, i.e. in these cases experimental results are almost two times bigger than simulated, regardless of volume flow rate.

As the opening reaches maximum, the error decreases reaching 72.69% in the range of volume flow rates from $100\,\mathrm{l\,min^{-1}}$ to $150\,\mathrm{l\,min^{-1}}$. At the fully open state and minimum volume flow rate, the error is comparable with small opening's errors, i.e. 91.68%.

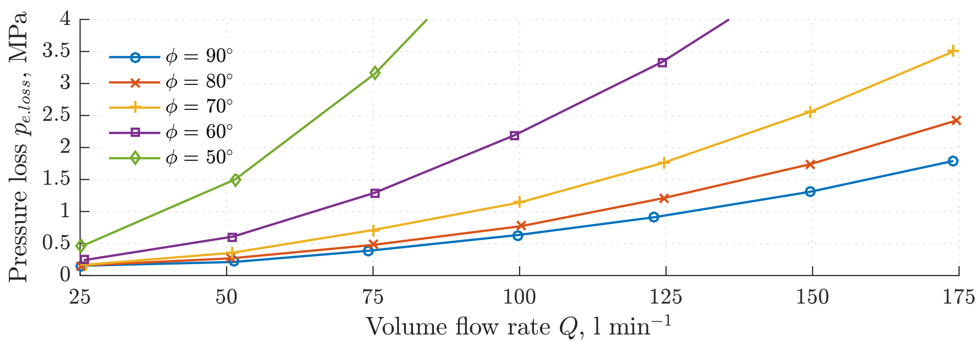

Figure 6.9: Experimental pressure loss $p_{e.loss}$ at $\phi = \text{const}$.

6.4.3 Leakage

Leakage flow, which occur during valve operation, can be divided into internal and "closed-state" leakage. The former takes place at any valve position. It passes through the valve's internal parts and lubricates them. It also helps to limit the internal pressure level and avert excessive heat. The latter leakage, as the name implies, occurs when the valve is completely closed. This parasitic leak flow passes through throttling orifices of the valve due to the annular clearance between the spool

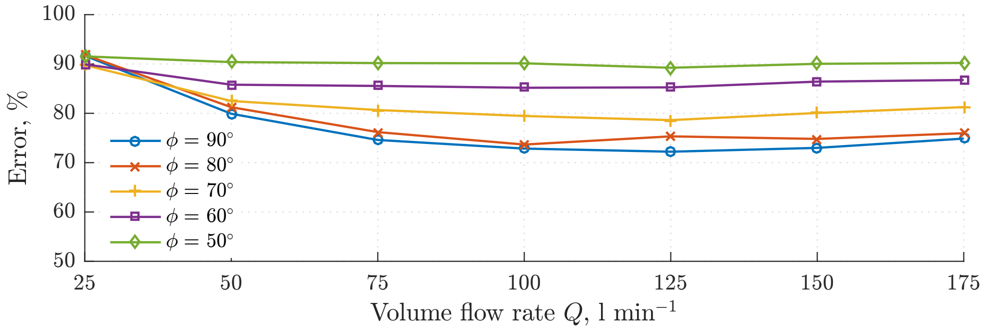

Figure 6.10: Percentage difference between simulated and tested pressure drops $\Delta p(Q)$ at $\phi =$ const.

and the sleeve. Since this gap is non-zero, this leak is unavoidable and needs to be evaluated.

Internal Leakage

During testing, measurement of internal leakage was performed. At any spool position ϕ, small portion of fluid flow passes through the spool-sleeve clearance to the chamber occupied by the thrust bearing, see the Figure 6.11. This chamber is connected to the drain line, which takes the leakage flow to the tank. Additionally, the oil under the pump pressure from the spool back chamber seeps through the sealing rings to the thrust bearing chamber. Cumulatively, the two passages constitute the internal leakage flow.

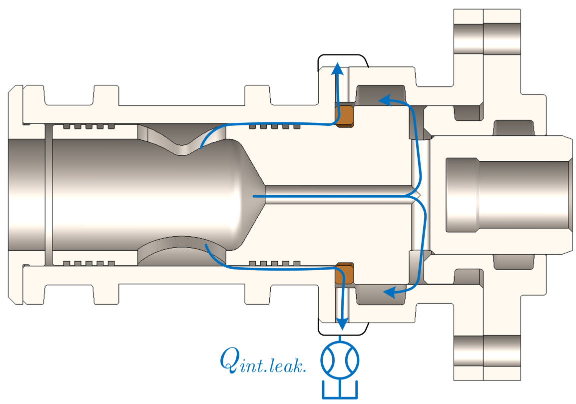

Figure 6.11: Internal leakage channels.

Presence of the internal leakage is intentional. The purpose of this leakage channels is to ensure lubrication of the thrust bearing, to compensate the axial pressure-induced force on the spool and to limit the pressure level in the internal cavities of the valve. Reducing the oil pressure in the internal cavities is crucial since high oil pressure creates surplus stresses within valve parts, hence, shortening their lifespan and worsening reliability. The drain channel collects and directs all internal leak flows to the tank.

Internal leakage was measured for spool positions $\phi = 50°$ to $90°$ and pressure differentials $\Delta p = 0.1\,\mathrm{MPa}$ to $12\,\mathrm{MPa}$. The measurement results are plotted in the Figure 6.12. Values of internal leakage follow a linear dependency with regard to the pressure differential. These increase monotonously not exceeding $Q_{int.leak.max} = 0.8\,\mathrm{l\,min^{-1}}$.

The Figure 6.13 demonstrates results of conducted comparison between the internal leakage and the total volume flow rates. It shows a portion of internal leakage $Q_{int.leak}$ in the total volume flow rate Q_{CFD} obtained from the CFD simulations, see the figure 4.12, for the case of the fully open valve with $\phi = 90°$. According to this ratio it can be concluded that the new valve design is leak-tight within the intended operational regimes. The maximum internal leakage makes up small portion of the total flow discharge, which does not exceed 0.2%. Therefore, internal leakage does not lead to excessive hydraulic power losses and material wear.

"Closed-State" Leakage

The "closed-state" leakage flow was also measured. This test would allow to confirm results of the numerical and analytical leakage estimations performed in the section 4.4.

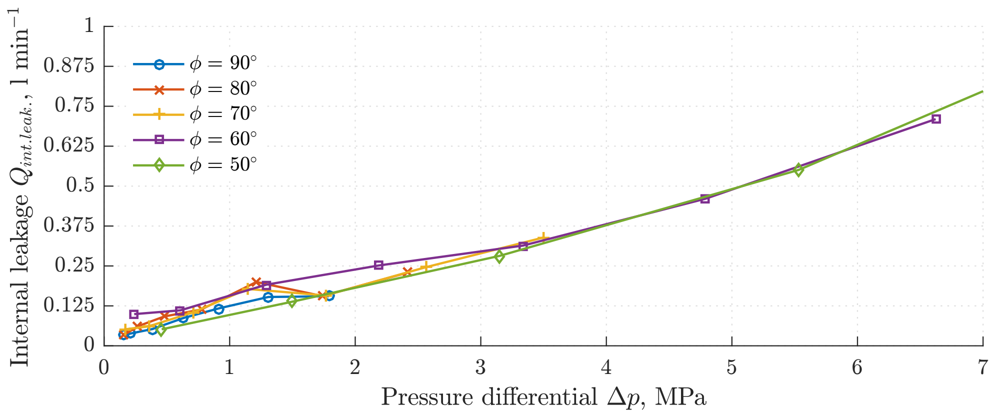

Figure 6.12: Experimental internal leakage volume flow rate $Q_{int.leak.}(\Delta p)$ at $\phi =$ const.

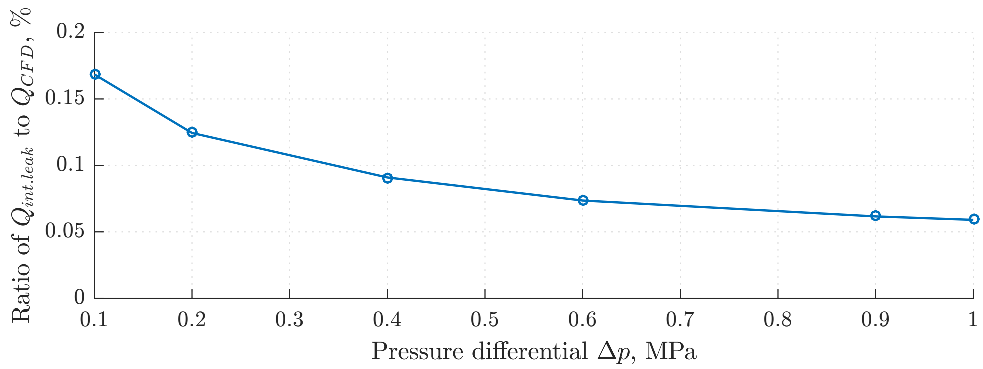

Figure 6.13: Internal leakage portion in the total volume flow rate at $\phi = 90°$.

During this test, the valve was put into the fully closed state, $\phi = 0°$, the valve return line was disconnected form the tank. Instead of the tank, the resultant leakage through the closed valve was drained into a measuring beaker. The beaker had a graduated scale, which enabled measurement of oil volume passing to the beaker from the disconnected tank line.

To measure time needed to fill the beaker up to a certain volume mark, a stopwatch was used. Two values to calculate the "closed-state" leakage were obtained. Dividing the oil volume by time yields a value of volume flow rate of this leakage.

Δp, MPa	Time, s	Volume, ml	$Q_{L.exp.}$, l min^{-1}	$Q_{L.an.}$, l min^{-1}	Δ, l min^{-1}	Δ, %
0.7	15.34	138	0.5398	0.8927	0.3529	39.53
7	8.61	955	6.655	8.672	2.017	23.26

Table 6.6: Results of the "closed-state" leakage measurement.

6.5 Correlations with Modelling

According to the Figures 6.8 and 6.10, the used simulation model overestimates the performance characteristics of the physical prototype valve by up to 90% in the case of the pressure drop test results. According to the Table 6.6, the measured "closed-state" leakage correlates well with the analytically calculated leakage, in more convergent way than the volume flow rate and pressure drop functions.

But general trends of the simulated and experimental results conform. In particular, the monotonous increase of the volume flow rate with valve opening for different values of constant pressure drops was observed. The pressure drops for a set value of the valve opening were raising with a volume flow rate growth. The linear proportionality of the leakage volume flow rate relatively to the pressure differential was confirmed.

Several factors were identified, which were causing such large errors. One factor affecting all measurements and all performed tests was related to the accuracy of the spool angular positioning. The prototype was assembled in a way that overlap angles at the closed state were impossible to measure and control. Hence, although the valve was closed, the exact lengths of the leak channels were hard to establish. Therefore, it was challenging to ensure that leak channels' lengths are equal to those used in the modelling stage. As a result, the actual "zero" position differed from the simulated. In addition, a signal noise caused by the high variability of the flow parameters in time and non-uniformity of the pump's flow rate also affects the quality of the collected data due to introduction of a random error.

In case of leakage measurements, the accuracy of the beaker-stopwatch method caused the random measurement error due to a human effect. It appears mainly at start and stop of the stopwatch and manifests clearly itself during the second measurement at $\Delta p = 7\,\mathrm{MPa}$.

However, the main reason of the tested and modelled results differences can be attributed to the imperfections of the geometric model used. Firstly, it did not include fittings into the model's geometry. These fittings connect the pressure transducers and the prototype valve to the hydraulic system. Their internal passages were non-uniform in a cross-section, their routes were not straight. Hence, their internal passages created additional disturbances to the flow, which were not accounted in the simulation model. This is the first factor causing a divergence of the modelled and experimental valve's metering characteristics.

Moreover, the simulated geometric model did not take into account surfaces roughness of mechanical parts wetted with oil. Surface's roughness creates additional pressure losses due to viscous and boundary layer-surface friction. Together, these two factors can explain the difference between experimental and simulated results. To test these assumptions, additional modelling was performed.

6.5.1 Corrected Model

To test the assumptions made, an extra run of the hydraulic behaviour modelling was performed. In this simulation the geometric model was corrected to include the instrumentation's fittings, pressure transducers' ports and adapters, which served as transition from one internal nominal diameter to another, see the Figure 6.14. These elements were created with the internal geometry as close as possible to those used in testing.

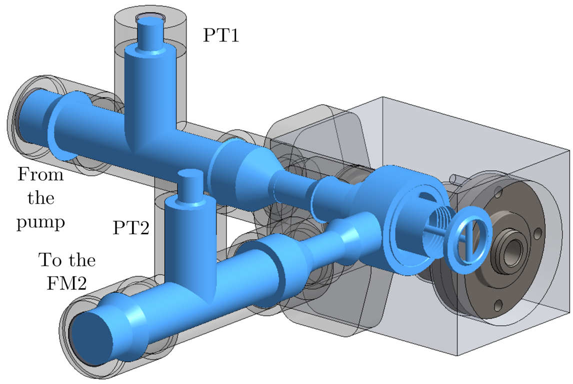

Figure 6.14: Corrected geometric model and fluid sub domain.

To fully replicate the geometry of the tested prototype, the solid model of the valve has been modified as well. In the manufactured prototype the annular collecting channel had a rectangular shape without fillets. Similarly the spool and sleeve orifices in the test valve had right edges, with no fillets. According to these deviations of the valve internal geometry from the design specification, modifications of the body, the sleeve and the spool were introduced. Adopted geometrical corrections resulted in the modified flow path, see the Figure 6.15, which reflected the test conditions more accurately.

Furthermore, roughness of $Ra25$ was assigned to all internal surfaces and passages, which are in contact with oil. The chosen roughness corresponds to finishing levels of the manufacturing processes used during prototype production – metal cutting with rough finish.

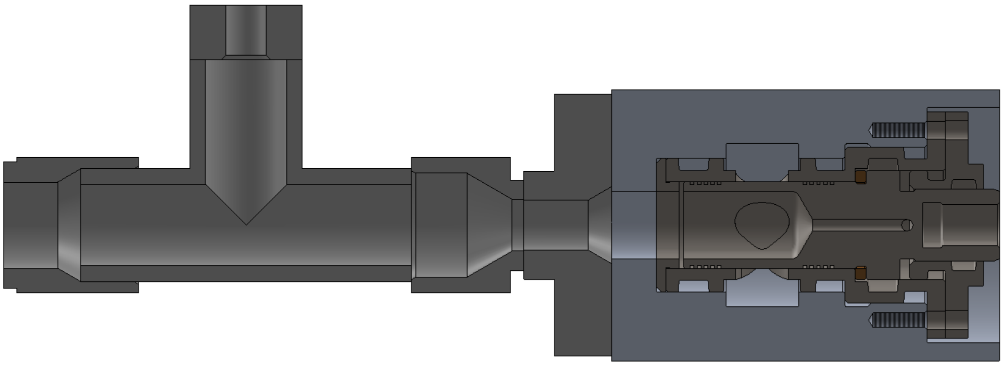

(a) Front section plane

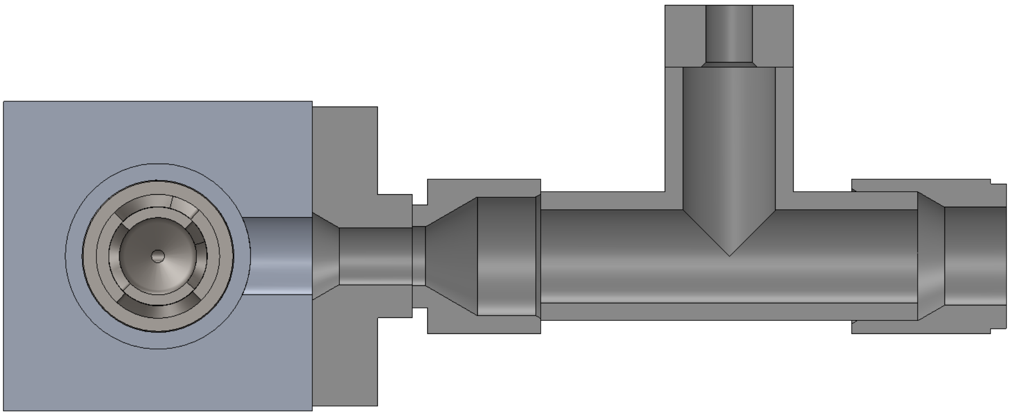

(b) Left section plane

Figure 6.15: Flow path in the corrected model

To study the influence of the corrected geometry on the pressure drop, the hydraulic problem with the following boundary conditions was solved: the spool angular position $\phi = 90°$, the volume flow rate range $Q = 25\,\mathrm{l\,min^{-1}}$ to $175\,\mathrm{l\,min^{-1}}$ and the the outlet static pressure $p_{out} = 0.101\,325\,\mathrm{MPa}$, the measured variable is the inlet pressure p_{in}. Then, the pressure difference Δp was calculated and plotted, see the Figure 6.16.

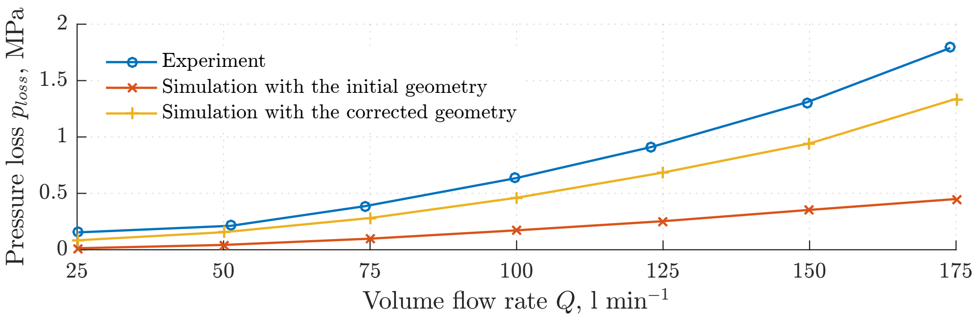

Figure 6.16: Correlation of study results for $\phi = 90°$.

According to the Figure 6.16, correcting the geometric model of the prototype valve brought the simulation results much closer to the experiment results. Taken measures to modify simulations allowed to reduce the average error between modelling and experiment by 47.75%, from 77.02% to 29.27%, see the Figure 6.17. Therefore, it can be concluded that the biggest factor contributing to the simulation and the experiment results deviations was caused by the incomplete geometric model and the "smooth wall" assumption.

After introduced modifications to the CFD settings (inclusion of the fittings to the valve geometric model and adding roughness to the internal surfaces), the percentage difference between

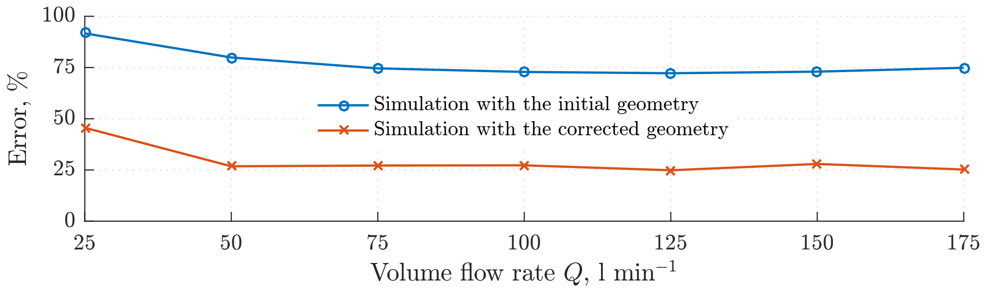

Figure 6.17: Percentage difference between simulated and test results of the pressure drop at $\phi = 90°$ relatively to the experiment data after geometry update.

the corrected simulation and the experimental results still remained quite large, average 29.27%, see the Figure 6.17. Despite this error, the applied simulation model can be considered accurate enough to predict hydraulic behaviour of the tested prototype valve. The simulation results from the previous chapters can be deemed valid too and used in further performance improvement, design optimization, etc. The obtained metering characteristics from CFD modelling hold their relevance since they pertained to the valve geometry only, excluding the elements of the hydraulic test rig and used instrumentation.

6.6 Chapter Conclusions

This chapter described the designed experimentation process. In this chapter, the original, standard and "off-the-shelf" parts needed to build the prototype valve were described and acquired for the testing stage. The test plan was developed with the general aim to safely collect the data related to the valve's metering characteristics and thereby validate the used numerical models of the valve. To implement the test plan, the data collection system was designed and its elements were assembled together on the hydraulic test rig. As a result of the experimental investigation of valve's performance, the conducted tests provided information on valve's behaviour in the physical environment.

During the tests, the volume flow rate, the pressure drop and leakage functions were obtained. The results correlation analysis was performed and reported for the special case of the pressure drop function. The initial error between modelling and testing results for the volume flow rate function reached on average 52.12%, for the pressure drop function 82.78% relative to the experiment results.

The factors causing the error were identified and their influence was studied. The corrected CFD simulation settings allowed reducing the error by 47.75% for the pressure drop at the fully open state. After the applied corrections of the CFD settings, the modelling/experiment error made up in average 29.27%. As a result of the valve performance study in the physical environment reported in this chapter, the obtained metering characteristics and modelling results were validated by experiments. It allowed to use validated modelled metering characteristics further in a concept refinement and a benchmark study, which are discussed in the following chapter.

Chapter 7

Concept Refinement

This chapter discusses the proposal to enhance the design of the new valve, to improve its performance in terms of metering characteristics. To commence the next design iteration loop in the design development process, a few design modifications to streamline the flows within the RTSV are suggested and described in this chapter as a way to improve the valve's performance by means of redesign. The effect of the design alterations was studied, analysed and reported in this chapter. The investigation of possible design improvements of the RTSV was done using the methodology of the mechanical design process, which was described in the Chapter 3, and according to the identified potential of the RTSV to achieve bigger performance gain.

In this chapter, the validated metering characteristics are compared with performance of the analogous valve to put into perspective the developed valve's performance. The performance comparison with a industrially available flow control valve was conducted by studying the pressure loss. The comparison investigation was performed according to the process used in the 4. The study details and results are reported in the following section.

7.1 Redesign

During the RTSV design development and its initial performance evaluation studies, which were described in the previous chapters, the potential to improve valve's efficiency was identified. In particular, the analysis of the turbulence intensity and the general outflow pattern in the Chapter 4 highlighted the areas of heightened turbulence and vorticity, which eventually account for the power loss inside the valve. Further design development of these regions alone and the mechanical parts forming these domains could lead to the efficiency improvement. This "local improvement" approach lets to keep the general design, leaves the throttling mechanism of the valve intact.

The results of numerical and experimental investigations of the valve performance ensured that the methodology can be used to run the second iteration in the Concept Development. The further sections present the development and results of the conducted concept refinement.

7.1.1 Separator

Among the identified regions of the valve fluid subdomain, which are prone to formations of vortices, the spool central cavity was addressed the first. According to the conducted analysis of turbulent regions inside the valve, the conical surface on the spool, which forms the central chamber, contributes to development of the swirl, which eventually covers the whole chamber. Thus, to prevent swirl formations, the fairing separator screw was suggested and designed 7.1.

The distinctive feature of the suggested separator is its a double concave blade. The blade serves as a filler of the spool cavity with material and streamlines the flow inside the spool. The primary goal of the separator is to direct the fluid right to the spool orifices. Concavity along the spool axis would reduce flow circulation along the orifices axis. Hence, the largest swirling region within the valve could be eliminated. Transverse concavity has the same aim, i.e. to facilitate elimination of swirl formation.

Although the design of the suggested extra part, separator, is challenging to manufacture due to complex surface of the blade, the possible performance gain would outweigh the incurred production costs.

While adding new mechanical parts to the original design, initially developed functionality must remain. For this reason, the separator screw includes a set of holes feeding oil to the spool back chamber in order to preserve the pressure force compensation.

The intended assembly and fixation method for the introduced screw is thread connection inside the spool. Therefore, the spool was modified too by adding an internal thread M10 instead of the conical surface.

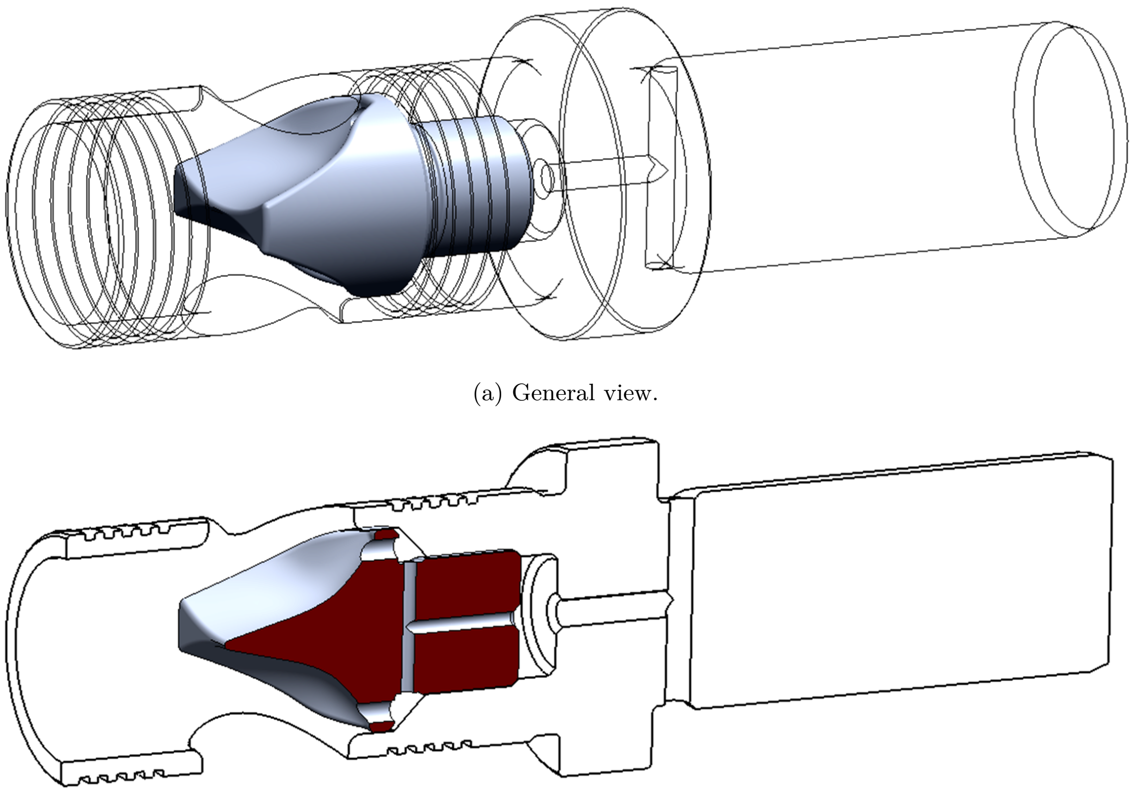

(a) General view.

(b) Cross section. Axial separator's concavity.

Figure 7.1: The separator of the modified spool.

7.1.2 Collecting Channel

The second area needed to be modified concerned the oil collecting channel. The channel's portion, which is located opposite to the service outlet port, contains a large volume of stagnant fluid, which acts as a damper in actuator's speed control. Since this regions does not take part in flow regulation and does not convey oil to the outlet port by the shortest path, the removal of this region could significantly reduce power dissipation due to viscous friction in swirls within the valve and improve valve's energy efficiency.

The collecting channel is formed by two parts: the sleeve and the valve body. Thus, both parts need to be modified. Further sections provide details of suggested design alterations for these parts separately.

Sleeve

In the new sleeve the central groove, which was cut out on the part's external cylindrical surface around orifices, was removed. That made the sleeve external cylinder flush with the body's internal cavity, see the Figure 7.2a. This modification directs the flow from the throttling orifices straight to the collecting channel. The orifice edge on the sleeve keeps fillet, which mitigates the "sharp edge" effect of the outflow. But increase in the external cylinder diameter make it possible to make the fillet radius bigger. In the modified sleeve, the fillet radius is 3 mm.

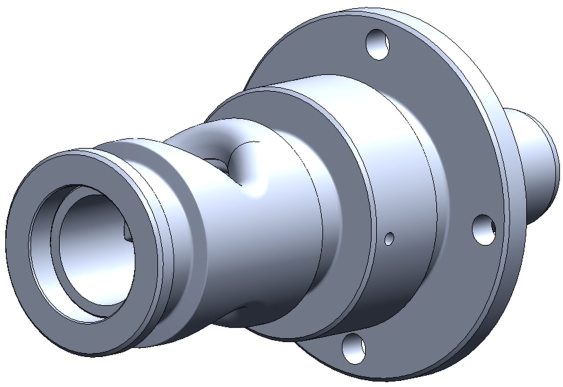

(a) Modified sleeve.

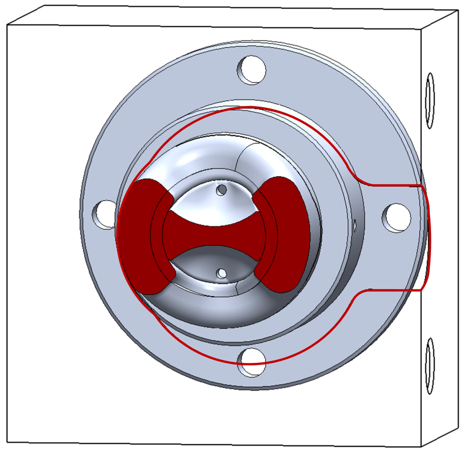

(b) Modified body. Transverse separator's concavity.

Figure 7.2: Redesign of the collecting channels.

Body

To finalize the modification of the collecting channel, the body's internal cavity was redesigned too. The design correction concerned the geometry of the collecting channel inside the body. In particular, the channel was offset closer to the outlet port, see the Figure 7.2b, so that the sleeve contacts the body channel's walls opposite to the outlet channel.

The annular cross-sectional area A_{an} of the channel's branches were kept in accordance with the dimensioning analysis in the Chapter 3 in order to disturb the outflow as little as possible. The resultant profile of the valve's collecting channel is outlined in red in the Figure 7.2b. As a result of the applied design modifications of the body and the sleeve allowed to get rid of the region of stagnant fluid within the valve's fluid subdomain.

Although the new body's design becomes more challenging to manufacture, in particular to ensure shapes and tolerances of the internal surfaces, it can be ensured by cast iron casting process. Additionally, removal of the stagnant part of the collecting channels results in smaller overall sizes of the fluid subdomain and, as a result, the whole valve body. Therefore, less material is needed to manufacture the body of the single valve, it is easier to design the four-valve assembly, which also becomes more compact.

7.1.3 Results

The applied redesign measures has resulted in the new valve geometry. The modification concerned only internal chambers of the valve involved in the throttling process. The cross section of the resultant valve design is depicted in the Figure 7.3.

To investigate how applied design modifications affect valve performance, the study of the imposed pressured drop was performed according to the process described in the Chapter 4. The percentage difference of obtained pressure drop values were then studied and analysed for the initial

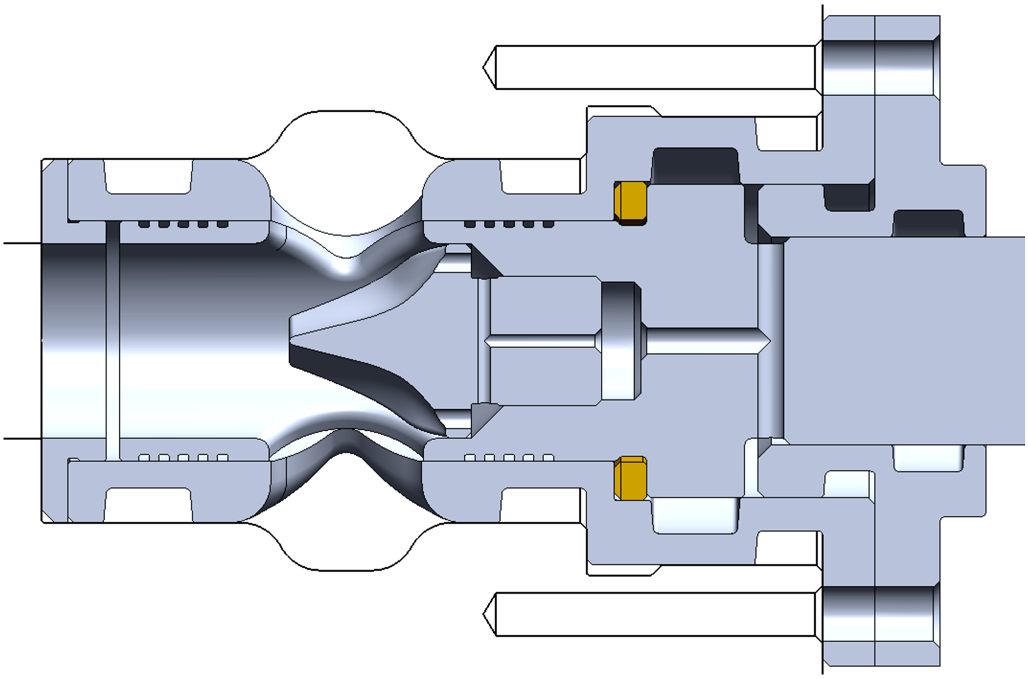

Figure 7.3: The cross section of the modified valve.

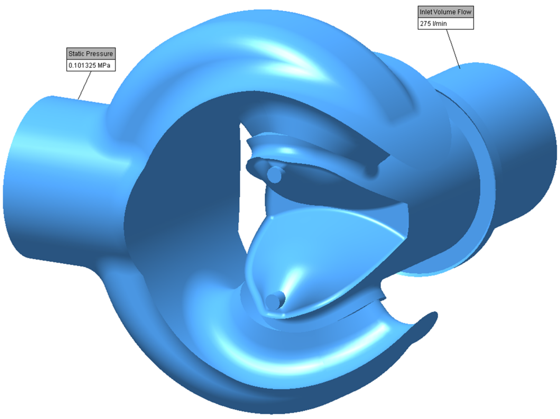

Figure 7.4: The fluid domain of the modified valve.

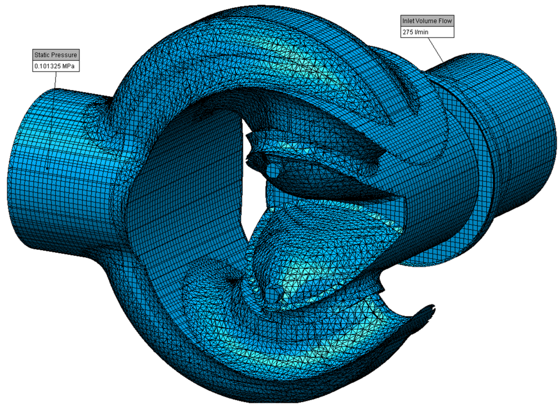

Figure 7.5: The mesh of the modified valve with ≈ 200 000 fluid cells.

and modified designs. The following sections give details of this study.

Apart from the changes reported above, the geometric model stayed intact and corresponded to the design outlined in the Chapter 3. The shapes of the orifices were kept the same as in the previous studies. The mesh settings were also translated from the metering characteristics analysis for the initial design without the elements of used instrumentation and fittings.

The Figure 7.4 illustrates the fluid subdomain, which has resulted from the applied design modifications. Its shapes became more complex with comparison to the initial valve design, see the Figure 4.1. The Figure 7.5 demonstrates the mesh, which was used in the pressure drop analysis of the new valve design.

The Figure 7.6 illustrates the effect, which has been achieved by taken design changes on the velocity field and velocity vectors distribution within the fluid subdomain of the redesigned valve. Comparing the velocity field plots in the redesigned valve, the Figure 7.6, with the same plots for the valve with the initial design, the Figure 4.8, allows to confirm that applied design modifications have yielded more streamlined fluid flow trajectories, enabled removal of the large swirl in the spool central chamber. Conducted redesigning, which was based on the analysis of the turbulent regions within the valve, enabled reduction of stagnant and turbulent regions and elimination of undesirable swirls.

The simulation results demonstrate substantial reduction of the pressure drop in the valve with the modified geometry, see the Figure 7.7. The biggest improvement was observed for the case of small valve openings, $\phi = 30°$, see the Figure 7.8. Here, the average percentage of the pressure drop reduction relatively to the initial design makes up 86.72%.

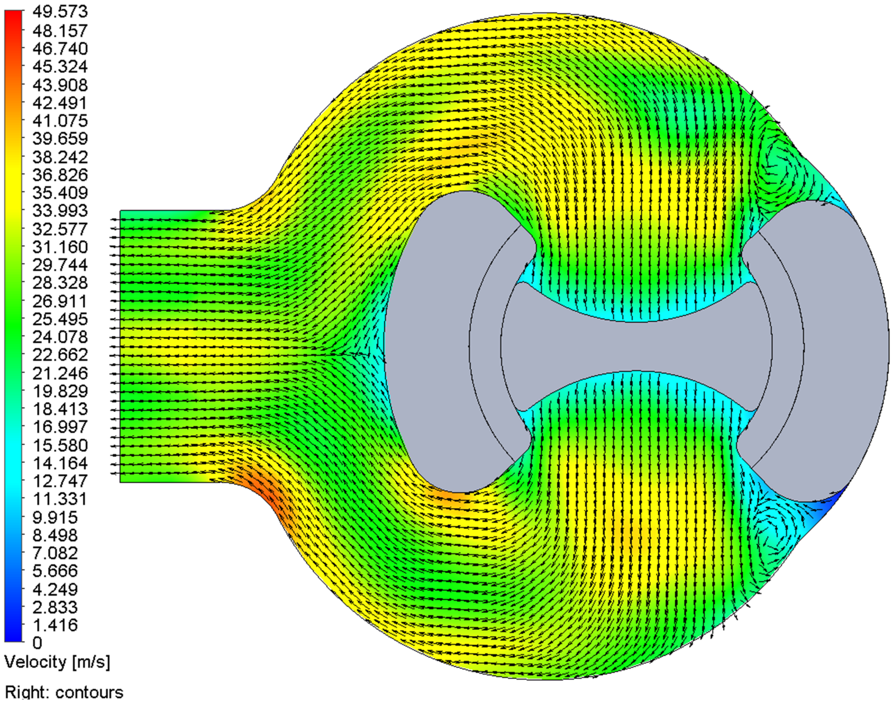

(a) The right plane.

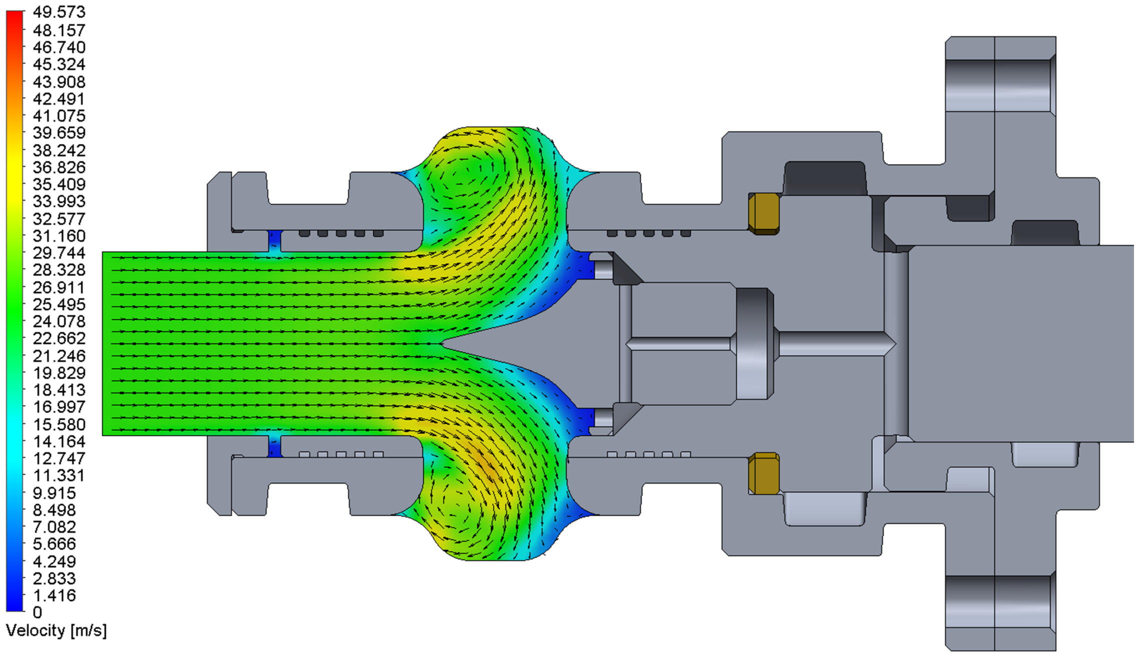

(b) The front plane.

Figure 7.6: The velocity field distributions in the redesigned valve in the main planes at the fully open state $\phi = 90°$ and $\Delta p = 1$ MPa pressure drop across the redesigned valve.

For the case of the fully open state and the maximum volume flow rate, i.e. $\phi = 90°$ and $Q = 175\,\mathrm{l\,min^{-1}}$, the initial valve creates 0.9803 MPa of the pressure loss, see the Figure 4.15. Whereas, the applied design changes allowed to reach the value of 0.7552 MPa for the same settings, which corresponds to 22.96% improvement.

Therefore, it can be concluded that applied redesign measures allowed to significantly improve valve performance. Namely it was achieved by decreasing the created pressure drop and, hence, the valve's power loss due to throttling.

Although further streamlining of internal valve surfaces may result in even bigger pressure drop reductions, the achieved values of the pressure drop in the modified valve and in the original valve design, in comparison with the benchmark valve, as it will be shown further, testify to efficacy of the suggested throttling mechanism. It also confirmed that the proposed ways of redesign can improve valve's performance.

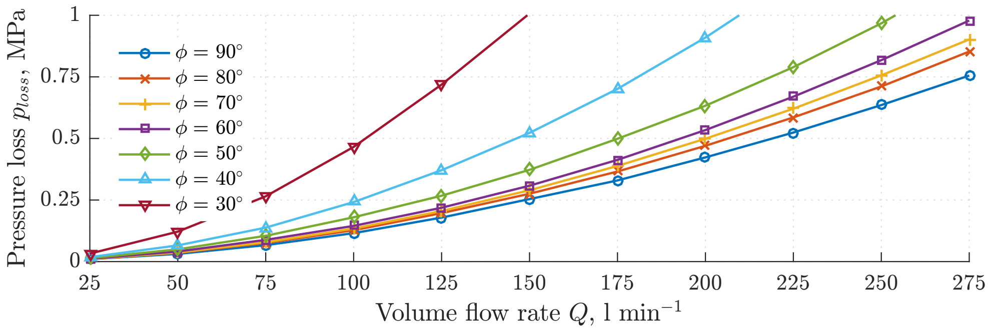

Figure 7.7: Pressure losses of the modified valve at $\phi =$ const.

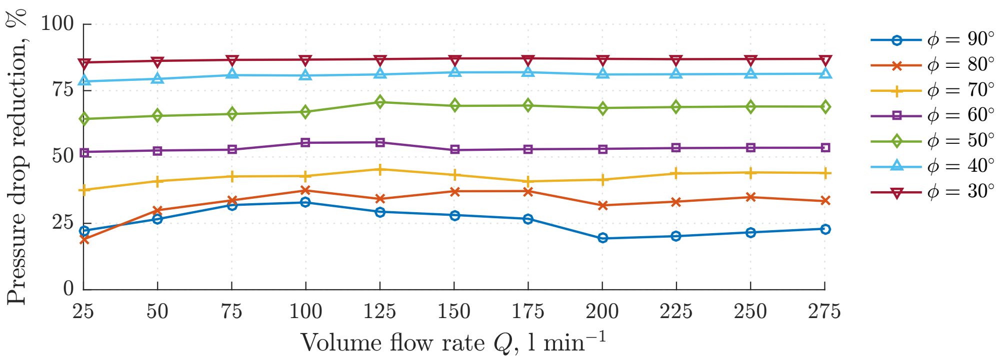

Figure 7.8: Pressure drop reduction in the modified valve relatively to the initial design at $\phi =$ const.

7.2 Influence of the Orifice Shape

The study of influence of the spool and sleeve orifice shapes was conducted to investigate what shape provides the optimal balance between controllability and energy efficiency. Three basic shapes were suggested: drop-like, circular and triangular, see the Figure 7.9. Both parts, the spool and the sleeve, in this study had the same orifices. In this study, the modified design of the valve was used with the separator and the new collecting channel's geometry.

First, the total orifice area was measured for each shape according to the process, which was used in the Chapter 3. Then, the pressure drop analysis was conducted for the selected orifice shapes.

7.2.1 Orifice Area

Within selected groups, orifices with different configurations of the basic shapes were investigated. Thus, area increase of circular orifices with ⌀11 mm and ⌀13 mm were measured. Two configuration of the triangular opening included two orientations: tip-to-tip, as it is illustrated in the Figure

7.9, and back-to-back, which is opposite to the former. Throttling of the tip-to-tip configuration at the small valve opening starts from the tips of the triangles. In the case of the latter shape, it starts from the base of the triangles.

As a reference the diameter of the inlet and outlet hydraulic ports was selected. In the current design the port size remained the same as in the previous chapters, which is equal to $d_1 = \varnothing 15\,\text{mm}$. This value results in the reference area $A_{in} = 176.71\,\text{mm}^2$, see the Table 3.1 and the Figure 7.10. The closer the total orifice area to the reference at the fully open state, when $\phi = 90°$, the less disturbances are introduced to the oil flow.

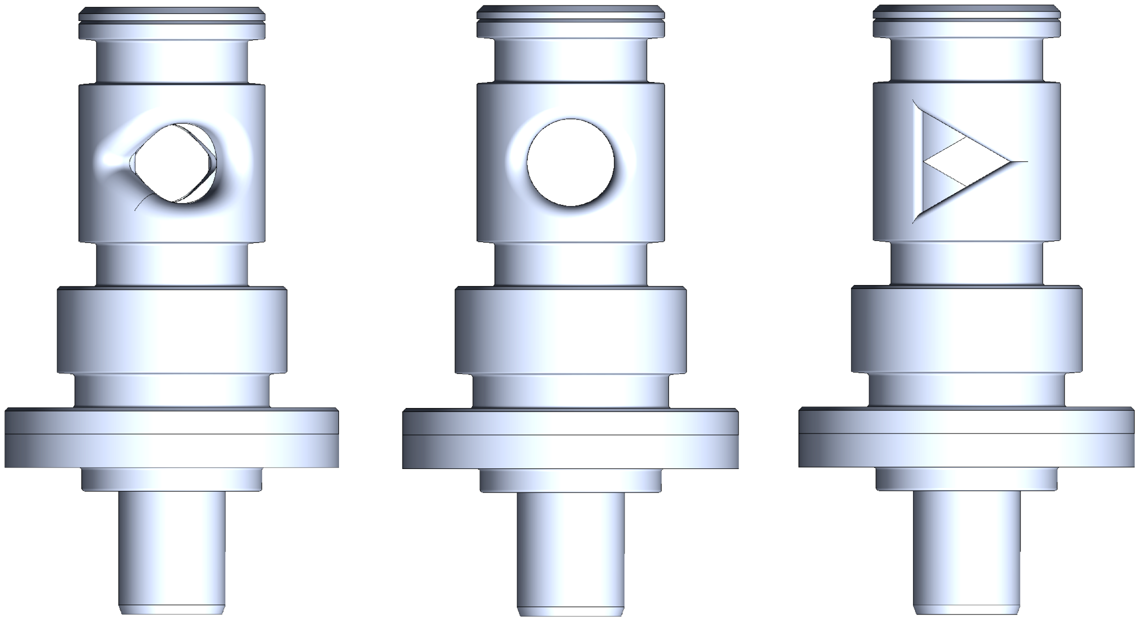

(a) Drop. (b) Circle, $\varnothing 13\,\text{mm}$. (c) Triangle, tip-to-tip.

Figure 7.9: Studied orifice shapes at the fully open state.

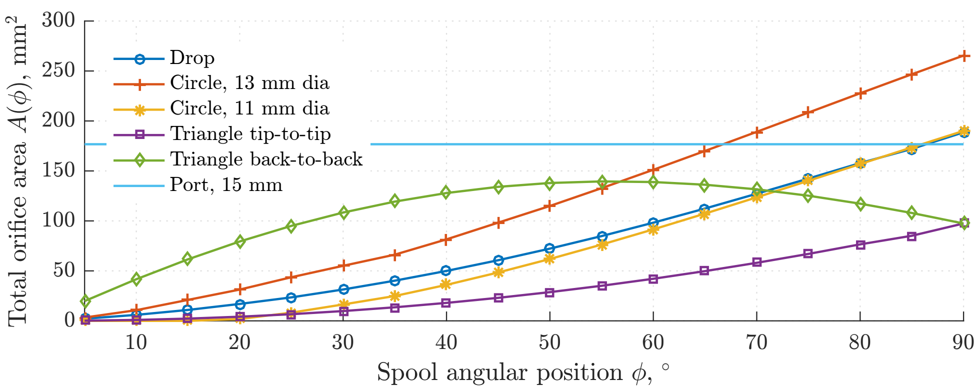

Figure 7.10: Total orifice area functions for different shapes.

The nature of the area curves development relatively to the spool stroke determines the actuator's speed characteristic according to the Bernoulli equation, see the Equation 4.16. according to the equation, the main variable defining the volume flow rate passing through the valve and reaching an actuator is the valve orifice area. According to the continuity principle, this volume flow rate directly influence the actuator's velocity. Therefore, judging by a form of the area development, or the area function, one can estimate actuator's speed gain.

The results of area measurements of different orifice shapes are illustrated in the Figure 7.10. According to this graph, the initially studied drop-like shape and the circle with $\varnothing 11\,\text{mm}$ are the closest to the reference. However, due to the small radius of the $\varnothing 11\,\text{mm}$ circle, it covers a smaller orifice angle, than the drop and the ⌀13 mm circle. Because of that, until $\phi = 15°$ the total opening is null. That results in the substantial operational dead band of the valve, which is unfavourable. For this reason, the circular orifice with ⌀11 mm was not used in the further study.

The triangular orifice with the back-to-back orientation is distinguished due to direction of parabola branches. Unlike the rest of the curves, the back-to-back triangle's parabola is pointed up, with its vertex at $\phi = 55°$. Whereas, other studied area functions resemble downward pointed parabolas with vertices at $\phi = 0°$.

The throttling process for the back-to-back design starts with the sudden increase of the total area at the small valve opening. It accounts for the fact, that in the beginning of opening triangles' bases start to overlap first. Hence, the smallest opening of the valve could results in the sudden increase of the actuator velocity, which is undesirable, can be dangerous as it could lead to actuator's motion with impacts. Therefore, such arrangement is not considered further.

7.2.2 Pressure Losses

For each shape, which is left for further investigations, the pressure drop analysis was conducted. The pressure drop, which is created by the drop-like shape, was studied in the previous section. The results are illustrated above in the Figure 7.7.

The Figure 7.11 illustrates the pressure drop function of the ⌀13 mm circular orifice. Although, the results are similar to the drop-like shape, it was noted the circular orifice produces more scattered curves. Namely, the fully open state curve at $\phi = 90°$ of the circle creates smaller pressure drop than the initial drop-like shape. At the same time, the small valve openings, i.e. $\phi = 30°$ result in bigger pressure losses.

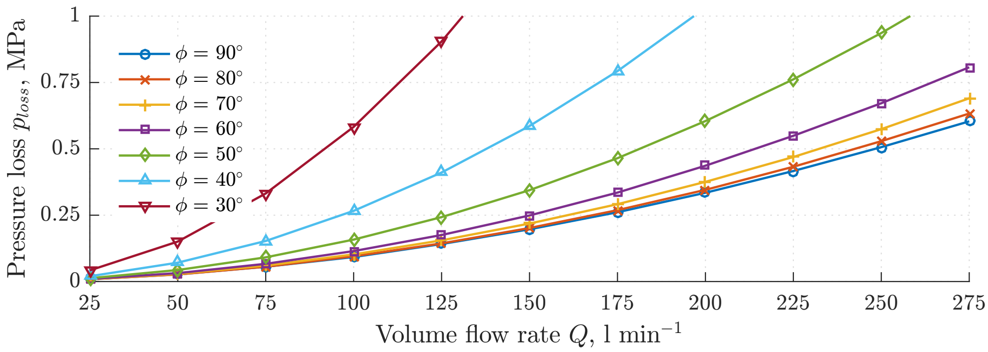

Figure 7.11: Pressure losses for the circular ⌀13 mm orifice at ϕ = const.

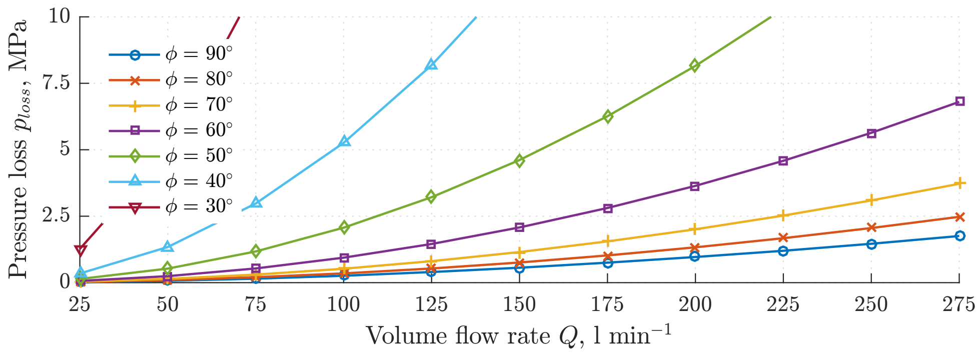

Figure 7.12: Pressure losses for the triangular "tip-to-tip" orifice at ϕ = const.

Therefore, it can be concluded that the initially selected drop-like shape is more efficient at small valve openings and power dissipation during fine speed control is smaller comparing with the drop-like shape. Contrary applies to the large openings, close to the fully open state.

The studied pressure loss due to throttling for the triangular shape showed significant pressure losses, see the Figure 7.12. It results from the sharp and straight edges as well as angles, which form the triangles. These, particularly angles, enhance the throttling phenomenon regardless of the spool position.

7.2.3 Results

The study concludes that among the shapes studied, those, which include no straight, angular and sharp geometric elements in the orifices, create the least pressure drop and, hence, represent more efficient design solution of the throttling orifice. Following this design guideline, it is possible improve valve performance further.

7.3 Benchmark

As a benchmark valve, Tecnord's products were selected as the company is one of market leaders in hydraulic components design and production. Moreover, Tecnord's manual rotary spool valves SJ-MRA (Tecnord 2017) represent the closest analog to the developed valve both structurally and in terms of specification.

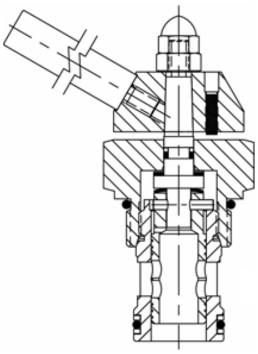

(a) Cross-section.

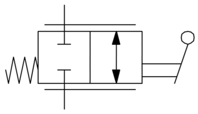

(b) Hydraulic symbol.

Figure 7.13: Tecnord's SJ-MRA rotary flow control valve, (Tecnord 2017).

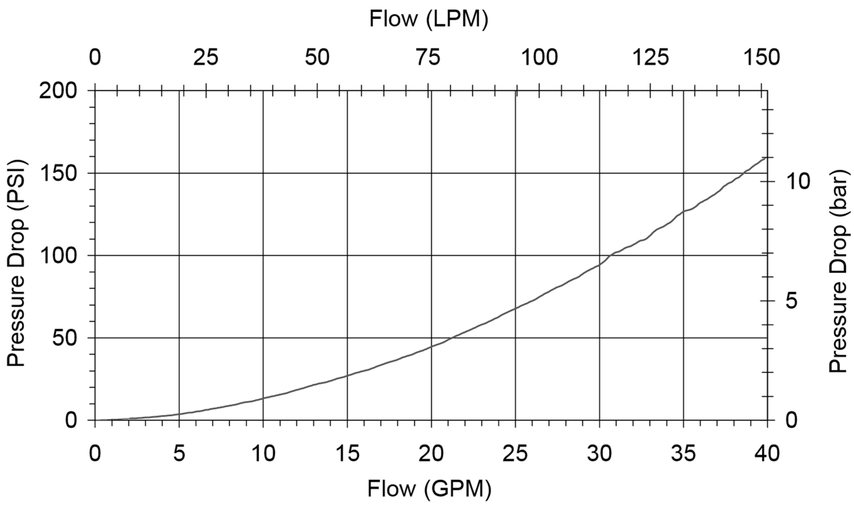

Figure 7.14: Test data of the pressure drop of SJ-MRA (Tecnord 2017).

According to the data sheet, the valve is two ways, two positions, proportional cartridge flow control valve with a rotary, tubular spool, see the Figure 7.13. It has a cartridge-nest assembly method, the valve includes the movable hollow spool inside the static sleeve as the main throttling pair. The outside diameter of the sleeve in this valve is determined by the thread 1" 5/16, which corresponds to 32 mm. The same outer sleeve diameter in the developed RTSV is 29.51 mm. The spool has two orifices, which are located opposite to each other. Its nominal volume flow rate is $151\,\mathrm{l\,min^{-1}}$, the rated operational pressure is 20.7 MPa. Despite many similarities, the Tecnord's valve is manually driven, which substantially limits its ability for fine control and, hence, its application area.

According to the performance data of this valve, in the fully open state at the rated flow rate of $150\,\mathrm{l\,min^{-1}}$ the created pressure drop by the valve makes up 1.1 MPa. Whereas in the original design of the RTSV the corresponding pressure drop constitutes 0.35 MPa, see the Figure 4.15, with 67.9% difference relatively to the Tecnord's valve. In this comparison, the simulated data for the valve geometry without the elements belonging to the test rig instrumentation was used. The comparison results are illustrated in the Figure 7.15.

The calculated percentage of the pressure drop reduction can be directly translated into the energy efficiency gain. Since the throttling power loss is proportional to the pressure drop, the curve in the Figure 7.15 also corresponds to percentage of efficiency improvement relative to the Tecnord's reference valve.

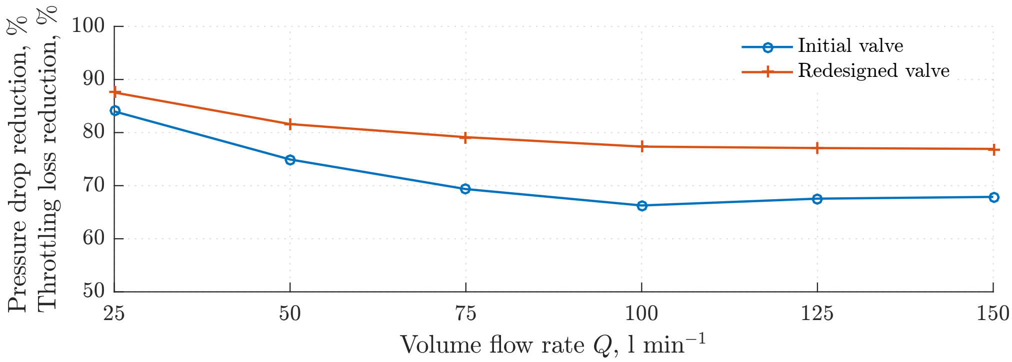

Figure 7.15: Throttling loss reduction in the initial and redesigned RTSV relatively to the Tecnord's SJ-MRA.

Percentage of pressure drop reduction in the modified valve with the drop-like shaped orifice comparing with the benchmark valve reaches even bigger values, see the Figure 7.15.

7.4 Chapter Conclusions

This chapter discussed the ways to improve the performance of the valve with the new design through concept design modifications. The analysis of the pressure drop of the modified valve proved efficacy of the applied design alterations. After applied redesign, average pressure drop reduction, depending on the spool angular position, reached values from 25.63% to 86.72% at 90° and 30° of the valve opening respectively, see the Figure 7.8. Therefore, the the applied design modifications resulted in bigger performance improvement for the small valve openings.

Using the modified RTSV, the investigation of orifice shape influence on the pressure drop was performed. This study gave insights into the valve performance dependence on the throttling shape used on the spool and the sleeve. Among initial drop-like, circular and triangular, the originally selected drop-like shaped orifice was proved to be optimal. It enables smooth increase of the area function, i.e. smooth speed control of an actuator, and relatively small pressure drop. It was also proved that the smoother the orifice shapes are, the less throttling losses occur and, hence, the more efficient the valve becomes.

The comparison of the valve pressure drop in the initial and modified versions with the analogous benchmark valve demonstrated substantial pressure drop reduction too, which was equal to 71.66% and 79.94% respectively, see the Figure 7.15. The values prove that the suggested valve designs are capable to improve energy efficiency of a flow control valve, lessen throttling losses and, thereby, power consumption of an entire hydraulic system. In this chapter, it was also confirmed that the methodology used to analyse the valve design with the aim to improve its performance through the pressure drop investigation is viable and can be applied for the further valve design development.

Chapter 8

Conclusions

Research and development of alternative design solutions of hydraulic valves used for flow control is being driven by the issue of climate change and the need for more energy efficiency and fuel consumption reduction in NRMM of the industrial sector. This chapter summarizes the outcomes of the investigation of the new valve's performance with the aim to improve energy efficiency of hydraulic systems. This chapter also outlines the future work and checks on objectives completion.

8.1 Discussion

The thesis presents a numerical and experimental investigation of the novel rotary flow control valve for IM hydraulic systems. IM systems have caught the attention of the scientific and industrial communities because of its capability to enhance hydraulic efficiency and reduce emissions. However, the transition to this architectural concept in the industrial field is hampered by the lack of studies looking at how it can be applied to the high flow rate regimes.

In this research, the design and basic principles of the stepper motor driven rotary tubular-spool valve were suggested and studied to address the issue. The aim was to develop a main component of an IM hydraulic system, which can be used in high flow rate hydraulics of industrial mobile working machines. The main approaches in valve designing were to implement a low-inertia rotary tubular spool and, thereby ensure a single-staged direct driving method.

The performance evaluations during testing of the new valve, referred as the Rotary Tubular-Spool Valve (RTSV), allowed to validate the numerical models. The simulated performance characteristics of the valve agree well with experiments. The analytical functions of the discharge coefficient and the jet angles were derived from CFD modelling and tested. Therefore, the models could be further used to analyse other aspect of RTSV's functionalities.

The simulation results confirmed the that developed RTSV can successfully perform the required functions of a flow control valve in hydraulic systems and, thereby control the speed of a hydraulic actuator and a rotary motor. The assumptions used were considered as relevant and not compromising quality of the modelling results.

The numerical analysis of stresses and displacement, which are created in the valve by anticipated loads, was validated by experiment as well. In particular, the manufactured prototype enabled to safely collect and study the hydraulic characteristics of the valve. Valve's strength was enough to perform intended functions during testing in the physical environment. Therefore, the adopted design approach can be used further to develop the four-valve assembly.

Although the benchmark performance comparison study showed significant increase in energy efficiency of the new valve, it can differ for other valves designed by other manufacturers. Nevertheless, the obtained results confirm the potential of the new valve to become the industry standard, to replace single-spool valves with the independent metering arrangement of RTSVs to control the actuator's speed.

8.2 Conclusions

The overall aim of the conducted research was to develop and examine ways to improve the energy efficiency of a control valve used in a fluid power system of mobile machinery operating at high flow rates. This was achieved by:

1. Reviewing the state of the art of fluid power architectures, their components to identify possible design solution with potential to improve performance of hydraulic systems and components.
2. Designing flow control valve with the unconventional throttling mechanism.
3. Studying performance characteristics of the valve.
4. Proposing an efficient design and evaluating its throttling losses.

The first objective was fulfilled in the Chapter 2. The reviewed literature revealed that a few examples of a tubular-spool structure in a rotary valve have been suggested and fewer have been studied so far. Although there is a clear potential of this type of valves to become the industry standard, there is a lack in studies looking at performance evaluation of these valves. The conducted research in this thesis demonstrates that flow and actuator's speed control is possible with rotary hollow-spool valves.

The assessed architectural concepts of hydraulic systems also demonstrated advantages of the independent metering and its capabilities to improve hydraulics's efficiency by breaking the mechanical link between actuator's meter-in and meter-out channels. This promising concept is still in the initial stage of development, but opens opportunities to reduce greatly power losses in hydraulic systems. In this research, the way to expand the concepts's operational regimes was suggested and proved to be feasible.

A novel throttling mechanism of flow control within the rotary valve was detailed in the Chapter 3. The process adopted to generate and evaluate the new innovative valve design incorporating the new throttling mechanism was also discussed in this chapter. The RTSV includes the specially profiled orifices on the hollow spool to implement smooth flow and actuator's speed control with minimal pressure losses. The design focused on implementation of direct, single-stage control of high flow rate flows by means of rotary tubular-spool structure.

The third objective was met in the Chapter 4. This was done by investigating the three-dimensional fluid dynamics of internal flows within the valve to determine the initial metering characteristics and pressure losses it creates. A flow pattern and performance properties of the throttling mechanism in tubular valves were modelled by CFD. The simulation results demonstrated RTSV's flow control feasibility as well as its ability to operate in the high-flow rate operational domain, with the volume flow rate reaching $250\,\mathrm{l\,min^{-1}}$ at $1\,\mathrm{MPa}$ pressure differential. At the fully open state and the rated volume flow rate, valve's pressure drop was $0.81\,\mathrm{MPa}$. Its performance was deemed comparable with industry available valves and having great potential to compete with benchmark hydraulic components.

Investigation of the strength of the new valve as the special case of a fluid-structure interaction problem in the Chapter 5, made it possible to confirm its readiness to be manufactured and tested in the physical environment. The desired FOS 1.2 of the used fasteners was ensured. The expected loading and fixation settings did not cause the internal stress to exceed the yield stress of chosen materials.

The experimental investigation focused on characterising the RTSV's hydraulic performance. The prototype valve was built. The test rig and the data acquisition system were designed and assembled. These enabled to replicate simulation set-up and collect performance characteristics simulated before.

Manufacturing and testing of the prototype proved its relative design simplicity and modelled strength, its ease of manufacture and operation. The results of tests, although differing from initial simulations in average by 52.12% for the volume flow rate function and by 82.78% for pressure drops, followed same trends as modelled. The factors causing the error were identified. To address these factors, the CFD modelling settings were corrected. These corrections to the model significantly reduced simulation/experiment errors in average by 47.75% for the pressure drop function. Thereby the initial simulation results were validated.

The concept refinement and complementary study of orifice shape influence were completed in the Chapter 7 addressing the fourth objective. The applied redesign proved to be successful as it allowed to reduce throttling losses in the modified RTSV by 55.69% in average.

The comparison study with the selected industrially available flow control valve having the similar structure and performance proved superior qualities of the developed RTSV. The ability of the novel valve to improve energy efficiency of hydraulic control system was demonstrated by evaluating and comparing throttling losses occurring in the RTSV and the reference valve. The average pressure drop reduction of the initial and modified RTSV amounted to 71.66% and 79.97% respectively. This confirms, the initial hypothesis was correct. Therefore, the suggested hypothesis can be accepted as the collected and analysed data support it.

8.3 Contribution to Knowledge

This thesis makes the following contributions to knowledge:

- Assessment of suitability and readiness of the IM to be adopted by hydraulic systems and components manufacturers as the effective and simple way to reduce fuel consumption of the mobile working machines.

Examination of state of the art and advanced architectural concepts of mobile hydraulics demonstrated that the IM configuration of flow control valves can resolve issues associated with commonly used spool valves by breaking the mechanical linkage between meter-in and meter-out orifices. Nevertheless, industrial adoption lags behind partly due to the fact that up to now only small flow rate IM systems were suggested and studied. The new valve, on the other hand, can become a foundation for the four-valve IM assembly capable of fine and efficient control of high flow rate hydraulics, which can serve as a replacement of flow control valves with a single sliding spool.

- Proposal of the novel single-stage rotary valve design capable to expand application of the IM concept in fluid power systems of mobile working machinery.

The alternative throttling mechanism and based on it the novel valve design were presented and discussed. The RTSV was deemed to have several advantages for IM fluid power control. The single-stage stepper-driven design provides simple and direct fine flow control capabilities suitable for high-flow rate applications in NRMM, while creating small pressure drops, throttling losses and requiring less driving effort than commonly used sliding spool valves.

- Investigation of the novel valve's performance in terms of fluid dynamics, the factors affecting its throttling losses, driving effort and overall efficiency.

The valve metering characteristics with the proposed design were extensively investigated and evaluated through a mixture of numerical and experimental studies. Its ability to reduce throttling losses in average by 75.85% comparing with the selected benchmark valve was confirmed. The valve's volume flow rate and pressure drop functions were deemed suitable for the intended use and capable to compete with industry standard valves.

8.4 Future Work

This thesis had demonstrated that the RTSV can be used to control the actuator's speed and suggests that an optimised valve may be capable of providing sufficient energy efficiency to be used as a standard flow regulating device. A considerable amount of further work must be done if this is to be achieved, however, and the following suggestions are therefore provided. The possible directions of the future work are suggested as following.

- Design development of the four-valve assembly.

Further evolution of the RTSV as a part of IM system has a potential to increase hydraulics' efficiency even further. For this, the single valve body incorporating four RTSV in the IM layout and two check valves needs to be redesigned. With casting method, it is possible to ensure the least material, cast iron, is used so that the mass and compactness of the entire assembly is minimal. Casting would also enable smooth flow routes within the valve body.

- Investigation of dynamic properties of the single valve.

The thesis discusses the quasi-static operation of the valve. It means only steady flow state regimes were considered. However, in order to gain insights into valve responses to transient processes in hydraulic and mechanical environments, the dynamics modelling needs to be performed. As a premise, the thesis includes a draft of the valve's mathematical model, see the Appendix D. Additionally, it is possible to improve this model by detailing transient flow torques, choosing the friction model, which accounts for more friction phenomena in rubber O-rings at rotary motion.

The test rig and data acquisition system can be used to obtain the experimental data about dynamic properties of the single RTSV. The transducers and instrumentation used have sufficient bandwidth and dynamic range to collect such data. Therefore, comparison and improvement of the dynamic model of the valve can be performed.

- Evaluation of friction torques induced by sealing: rubber O-rings and plastic anti-extrusion rings.

During development of the mathematical model in the Appendix D, it has been found that currently the friction phenomenon of elastic sealing rings is scarcely studied for the rotary motion, despite the large number of studies focused on the translational motion. Modelling and analytical investigation of the case can be coupled with experimental validation since the test rig can be modified to conduct such tests.

Within the friction effect study, the fatigue analysis of the valve can be performed. Investigation of the inception of the fatigue failure can give insights into valve's endurance, durability and an anticipated service life.

- Performance evaluation of the four-valve assembly.

According to the used design evaluation methodology, the criteria to estimate assembly's performance need to be chosen and justified. Since the purpose of the assembly is to ensure speed control of the actuator, the assembly's performance needs to be studied in conjunction with the actuator's dynamics.

- Testing of the four-valve assembly.

With the developed housing of four RTSV, the prototype can be built and tested. However, before that the test plan needs to be drawn according to the selected performance criteria. This step would conclude the first design iteration step in the product development process.

References

Aardema, J. and Koehler, D., 1999. System and method for controlling an independent metering valve. US5960695A.

Abdalla, M. O., Nagarajan, T. and Hashim, F., 2011. Numerical investigation of pressure drop in hydraulic spool valve. *Solid State Science and Technology*, 19 (2), 48–60.

Akira, S., Shigeo, H. and Akio, T., 2007. Effects of cavitation in a nozzle on liquid jet atomization. *International Journal of Heat and Mass Transfer*, 50 (17), 3575–3582.

Al-Ghathian, Faisal, Tarawneh and Muafag, 2005. Friction Forces in O-ring Sealing. *American Journal of Applied Sciences*, 2 (3), 626–632.

Altpeter, F., 1999. *Friction modeling, identification and compensation*. Ph.D. thesis, Swiss Federal Institute of Technology in Lausanne.

Amirante, R., Andrea Catalano, L. and Tamburrano, P., 2014. The importance of a full 3D fluid dynamic analysis to evaluate the flow forces in a hydraulic directional proportional valve. *Engineering Computations*, 31 (5), 898–922.

Amirante, R., Distaso, E. and Tamburrano, P., 2016. Sliding spool design for reducing the actuation forces in direct operated proportional directional valves : Experimental validation. *Energy Conversion and Management*, 119, 399–410.

Amirante, R., Moscatelli, P. G. and Catalano, L. a., 2007. Evaluation of the flow forces on a direct (single stage) proportional valve by means of a computational fluid dynamic analysis. *Energy Conversion and Management*, 48 (3), 942–953.

Ansaloni, G., Marani, P. and Paoluzzi, R., 2008. Proportional Valve with Axial Flow and Rotational Metering. *Proceedings of the 7th JFPS International Symposium on Fluid Power*, Toyama, 591–596.

Armstrong-Helouvry, B., Dupont, P. and Wit, C. C. D., 1994. A survey of models, analysis tools and compensation methods for the control of machines with friction. *Automatica*, 30 (7), 1083 – 1138. URL `http://www.sciencedirect.com/science/article/pii/0005109894902097`.

Axin, M., 2013. *Fluid Power Systems for Mobile Applications with a Focus on Energy Efficiency and Dynamic Characteristics*. Dissertation, Linköping University.

Axin, M., 2015. *Mobile Working Hydraulic System Dynamics*. Dissertation, Linköping University.

Axin, M., Eriksson, B. and Krus, P., 2014. Flow versus pressure control of pumps in mobile hydraulic systems. *Proceedings of the Institution of Mechanical Engineers, Part I: Journal of Systems and Control Engineering*, (228), 245–256.

Beck, B. and Weber, S. J., 2017. Safety and reliability of independent metering systems in mobile machinery. *Risk, Reliability and Safety: Innovating Theory and Practice*, London, UK: Taylor & Francis Group, 2602–2609.

Bernad, S. and Susan-Resiga, R., 2012. Numerical Model for Cavitational Flow in Hydraulic Poppet Valves. *Modelling and Simulation in Engineering*.

Bisztray-Balku, S., 1995. Tribology of hydraulic seals for alternating motion. *Periodica Polytechnica, Mechanical Engineering*, 39 (3-4), 225–246.

Book, R. and Goering, C. E., 1999. Programmable electrohydraulic valve. *SAE Technical Paper*, SAE International. URL https://doi.org/10.4271/1999-01-2852.

Bordovsky, P., Scmitz, K. and Murrenhoff, H., 2016. CFD Simulation and Measurement of Flow Forces Acting on a Spool Valve. *10th International Fluid Power Conference*, Dresden, Germany, 473–484.

Bosch Rexroth, 2016. Datasheet RE 64122/07.2016. Open center control block in sandwich plate design SM12. URL https://www.boschrexroth.com/various/utilities/mediadirectory/index.jsp?language=en-GB.

Brennen, C. E., 1995. *Cavitation and bubble dynamics*. Oxford University Press.

Budynas, R., Nisbett, J. and Shigley, J., 2006. *Shigley's Mechanical Engineering Design*. McGraw-Hill series in mechanical engineering, the eighth edition. URL https://books.google.co.uk/books?id=m5ZVAAAAMAAJ.

Burrows, C., 2004. Fluid power–some reflections. *The 6th International Conference on Hydraulic Machinery and Hydrodynamics*, Timisoara, Romania, February, 51–56.

Caterpillar, 2017. URL https://www.cat.com/en_GB/products/new/equipment.html.

Ceccio, S. L. and Makiharju, S. A., 2017. Experimental methods for the study of hydrodynamic cavitation. L. d'Agostino and M. V. Salvetti, eds., *Cavitation Instabilities and Rotordynamic Effects in Turbopumps and Hydroturbines: Turbopump and Inducer Cavitation, Experiments and Design*, Springer International Publishing, 35–64.

Chen, M. and Zhao, D., 2017. The gravitational potential energy regeneration system with closed-circuit of boom of hydraulic excavator. *Mechanical Systems and Signal Processing*, 82, 178–192. URL http://dx.doi.org/10.1016/j.ymssp.2016.05.017.

Choi, K., Seo, J., Nam, Y. and Kim, K. U., 2015. Energy-saving in excavators with application of independent metering valve. *Journal of Mechanical Science and Technology*, 29 (1), 387–395.

CITGO, 2015. Product Information. CITGO A/W Hydraulic oils.

Command, U. S. A. M., 1971. *Engineering Design Handbook: Hydraulic Fluids*. AMC Pamphlet, U.S. Government Printing Office.

Crosser, J., 1992. Hydraulic circuit and control system therefor. US5138838.

Das, D., Alam, M. W. and Iftekher, R., 2015. Modeling and controlling of an electro-hydraulic actuator novel by using independent metering valve. *International Conference on Mechanical Engineering and Renewable Energy (ICMERE)*, Chittagong, Bangladesh, November.

Dell, T., 2017. Load-Sensing Pressure-Compensating (LSPC) Hydraulic Systems. *Hydraulic Systems for Mobile Equipment*, Goodheart-Willcox, chapter 18.

Dell' Amico, A., Carlsson, M., Norlin, E. and Sethson, M., 2013. Investigation of a Digital Hydraulic Actuation System on an Excavator Arm. *The 13th Scandinavian International Conference on Fluid Power, SICFP2013*, 505–511.

Deng, J., Shao, X. M., Fu, X. and Zheng, Y., 2009. Evaluation of the viscous heating induced jam fault of valve spool by fluid-structure coupled simulations. *Energy Conversion and Management*, 50 (4), 947–954. URL http://dx.doi.org/10.1016/j.enconman.2008.12.033.

Department for Business Energy & Industrial Strategy, 2017. Digest of United Kingdom energy statistics 2017. Technical report, Department for Business Energy and Industrial Strategy. URL https://www.gov.uk/government/uploads/system/uploads/attachment_data/file/643414/DUKES_2017.pdf.

Ding, R., Xu, B., Zhang, J. and Cheng, M., 2016. Bumpless mode switch of independent metering fluid power system for mobile machinery. *Automation in Construction*, 68, 52–64. URL http://www.sciencedirect.com/science/article/pii/S0926580516300693.

Do, H. T., Park, H. G. and Ahn, K. K., 2014. Application of an adaptive fuzzy sliding mode controller in velocity control of a secondary controlled hydrostatic transmission system. *Mechatronics*, 24 (8), 1157–1165.

Driest, E. R. V., 1956. On Turbulent Flow Near a Wall. *Journal of the Aeronautical Sciences*, 23 (11), 1007–1011.

Durfee, W. and Sun, Z., 2009. *Fluid Power System Dynamics*. Department of Mechanical Engineering, University of Minnesota: Center for Compact and Efficient Fluid Power (CCEFP).

EATON, 2010. Ultronics ™ZTS16 Twin Spool Valve 130 Technical Catalog. URL http://www.eaton.com/ecm/groups/public/@pub/@eaton/@hyd/documents/content/pll{_}2008.pdf.

Eriksson, B., 2007. *Control Strategy for Energy Efficient Fluid Power Actuators - Utilizing Individual Metering*. Ph.D. thesis, Linköping University.

Eriksson, B., 2010. *Mobile Fluid Power Systems Design with a Focus on Energy Efficiency*. Doctoral dissertation, Linkopings University.

Erwin, R. and Husley, E., 1958. Rotary sleeve valves. US3005468A.

European Parliament, 2016. Regulation (EU) 2016/1628 on requirements relating to gaseous and particulate pollutant emission limits and type-approval for internal combustion engines for non-road mobile machinery. *Official Journal of the European Union*, (September), 53–117. URL http://eur-lex.europa.eu/eli/reg/2016/1628/oj.

Fichmann, B., 2012. Annual Energy Review 2011. Technical report. URL http://www.eia.gov/totalenergy/data/annual/pdf/aer.pdf.

Filho, J. and De Negri, V., 2013. Model-Based Fault Detection for Hydraulic Servoproportional Valves. *The 13th Scandinavian International Conference on Fluid Power, SICFP2013*, Linköping, Sweden, 389–398.

Garcia, C., 2008. Comparison of friction models applied to a control valve. *Control Engineering Practice*, 16 (10), 1231–1243.

Geerling, G. and Biedermann, O., 1998. Power control units with secondary controlled hydraulic motors – a new concept for application in aircraft high lift system. *Recent Advances in Aerospace Hydraulics*.

Gems, 2017. 3100 Series and 3200 Heavy Duty Series Compact OEM Pressure Transmitters. URL https://www.gemssensors.co.uk/~/media/files/resources/na_english/catalogpages/catalog-h_3100series-3200series.ashx.

Gere, J., 2003. *Mechanics of Materials*. Cengage Learning, sixth edition.

Habibi, S., 1999. Design of a new high performance electrohydraulic actuator. *IEEE/ASME transactions on mechatronics*, 5 (2), 158–164.

Haessig, D. A. and Friedland, B., 1991. On the modeling and simulation of friction. *Journal of Dynamic Systems Measurement and Control*, 113 (3), 354–362.

Heikkilä, M. and Linjama, M., 2013. Hydraulic Energy Recovery in Displacement Controlled Digital Hydraulic System. *The 13th Scandinavian International Conference on Fluid Power, SICFP2013*, Linköping, Sweden, 513–519.

Herakovič, N., 2009. Flow-Force Analysis in a Hydraulic Sliding-Spool Valve. *Strojarstvo*, 51 (6), 555–564.

Herakovič, N., 2015. CFD simulation of flow force reduction in hydraulic valves. *Tehnicki vjesnik - Technical Gazette*, 22 (2), 453–463.

Heybroek, K., 2008. *Saving Energy in Construction Machinery using Displacement Control Hydraulics*. Ph.D. thesis, Linkopings University.

Hippalgaonkar, R. and Ivantysynova, M., 2013. A Series - Parallel Hydraulic Hybrid Mini - Excavator with Displacement Controlled Actuators. *The 13th Scandinavian International Conference on Fluid Power*, 31–42.

Ho, T. H. and Ahn, K. K., 2012. Design and control of a closed-loop hydraulic energy-regenerative system. *Automation in Construction*, 22 (2012), 444–458.

Hou, G., Wang, J. and Layton, A., 2012. Numerical Methods for Fluid-Structure Interaction — A Review. *Communications in Computational Physics*, 12 (2), 337–377.

HUSCO, 2007. INCOVA®Hydraulic control system for excavators.

Husley, E., 1962. Rotary control valve. US3135293A.

Hydreco, 2017. Q Series Hydraulic Gear Pumps. URL `https://www.hydreco.com/info-downloads/technical-data-sheets/`.

Jansson, A. and Palmberg, J.-O., 1990. Separate Controls of Meter-in and Meter-out Orifices in Mobile Hyraulic Systems. *SAE Technical Paper 901583*, SAE International. URL `http://papers.sae.org/901583/`.

Ji, H., Cao, Y., Wang, Z. and Wang, Y., 2011. Numerical analysis of temperature rise by throttling and deformation in spool valve. *Proceedings of 2011 International Conference on Fluid Power and Mechatronics, FPM 2011*, 752–756.

Johanastrom, K. and de Wit, C. C., 2008. Revisiting the lugre friction model. *IEEE Control Systems*, 28 (6), 101–114.

Johnston, N. and Pan, M., 2015. Theoretical Studies of a Switched Inertance Hydraulic System in a Four-Port Valve Configuration. *The Seventh Workshop on Digital Fluid Power*, October.

Kayihan, A. and Doyle, F. J., 2000. Friction compensation for a process control valve. *Control Engineering Practice*, 8 (7), 799 – 812. URL `http://www.sciencedirect.com/science/article/pii/S0967066100000381`.

Ketonen, M. and Linjama, M., 2017. Simulation study of a digital hydraulic independent metering valve system on an excavator. *The 15th Scandinavian International Conference on Fluid Power, SICFP'17*, Linköping, Sweden.

Khan, Z. A., Chacko, V. and Nazir, H., 2017. A review of friction models in interacting joints for durability design. *Friction*, 5 (1), 1–22.

Koehler, D. and Krone, J., 1997. Tilt priority scheme for a control system. US5678470.

Kracht, 2017. Gear Type Flow Meter VC. URL `http://www.krachtcorp.com/wp-content/uploads/2012/05/VC_USA_02-12_view.pdf`.

Lam, C. K. G. and Bremhorst, K., 1981. A Modified Form of the $k - \varepsilon$ Model for Predicting Wall Turbulence. *Journal of Fluids Engineering*, 103 (3), 456.

Lantto, B., 1994. *On Fluid Power Control with Special Reference to Load-Sensing Systems and Sliding Mode Control*. Ph.D. thesis, Linkopig University.

Launder, B. E. and Spalding, D. B., 1974. The numerical computation of turbulent flows. *Computer Methods in Applied Mechanics and Engineering*, 3 (2), 269–289.

Lin, Y., Shi, Y. and Burton, R., 2013. Modeling and robust discrete-time sliding-mode control design for a fluid power electrohydraulic actuator (EHA) system. *IEEE/ASME Transactions on Mechatronics*, 18 (1), 1–10.

Linjama, M., 2011. Digital Fluid Power – State of the Art. *The 12th Scandinavian International Conference on Fluid Power*, Tampere, Finland, 331–354.

Linjama, M. and Huhtala, K., 2009. Digital pump-motor with independent outlets. *The 11th Scandinavian International Conference on Fluid Power, SICFP'09, June 2-4, 2009, Linköping, Sweden*.

Linjama, M. and Huhtala, K., 2010. Digital hydraulic power management system–towards lossless hydraulics. *The Third Workshop on Digital Fluid Power, October 13 - 14, 2010, Tampere, Finland*, Tampere, Finland, 5–22.

Linjama, M., Huova, M., Pietola, M., Juhala, J. and Huhtala, K., 2015. Hydraulic Hybrid Actuator: Theoretical Aspects and Solution Alternatives. *The 14th Scandinavian International Conference on Fluid Power*, Tampere, Finland.

Linjama, M., Laamanen, A. and Vilenius, M., 2003. Is it Time for Digital Hydraulics? *Proceedings of the 8th Scandinavian International Conference on Fluid Power, SICFP '03*, Tampere, Finland, 347–366.

Lisowski, E., Czyzycki, W. and Rajda, J., 2013. Three dimensional CFD analysis and experimental test of flow force acting on the spool of solenoid operated directional control valve. *Energy Conversion and Management*, 70, 220–229.

Lisowski, E. and Filo, G., 2016a. Analysis of a proportional control valve flow coefficient with the usage of a CFD method. *Flow Measurement and Instrumentation*, (February), 1–10. URL `http://linkinghub.elsevier.com/retrieve/pii/S0955598616303016`.

Lisowski, E. and Filo, G., 2016b. CFD analysis of the characteristics of a proportional flow control valve with an innovative opening shape. *Energy Conversion and Management*, 123, 15–28.

Lisowski, E., Filo, G. and Rajda, J., 2015. Pressure compensation using flow forces in a multi-section proportional directional control valve. *Energy Conversion and Management*, 103 (August), 1052–1064.

Liu, K., Gao, Y., Tu, Z. and Lin, P., 2016. Energy-saving analysis of the independent metering system with pressure compensation for excavators manipulator. *Proceedings of the Institution of Mechanical Engineers, Part I: Journal of Systems and Control Engineering*, 230 (9), 905–920. URL `http://pii.sagepub.com/lookup/doi/10.1177/0959651816658191`.

Lodewyks, J. and Zurbrügg, P., 2016. Decentralized energy-saving hydraulic concepts for mobile working machines. *10th International Fluid Power Conference*, Dresden, Germany, 79–90.

Love, L., Lanke, E. and Alles, P., 2012. *Estimating the Impact (Energy, Emissions and Economics) of the US Fluid Power Industry*. December.

Lynch, L. A. and Zigler, B. T., 2017. Estimating Energy Consumption of Mobile Fluid Power in the United States. Technical Report NREL/TP-5400-70240, National Renewable Energy Laboratory.

Marani, P., Ansaloni, G. and Paoluzzi, R., 2008. Load Sensing With Active Regeneration System. *Proceedings of the 7th International Symposium on Fluid Power*, Toyama, Japan, volume 2008, 617–622.

Marques, F., Flores, P., Pimenta Claro, J. C. and Lankarani, H. M., 2016. A survey and comparison of several friction force models for dynamic analysis of multibody mechanical systems. *Nonlinear Dynamics*, 86 (3), 1407–1443.

McCloy, D. and Martin, H., 1973. *The control of fluid power*. London: Longman Group Limited, first edition.

McWilliams, D., 1991. Pressure compensated hydraulic system. WO911/1622 (A1).

Merritt, H. E., 1968. *Hydraulic Control Systems*. New York: John Wiley & Sons, Inc.

Mises, R. v., 1913. Mechanik der festen körper im plastisch-deformablen zustand. *Nachrichten von der Gesellschaft der Wissenschaften zu Göttingen, Mathematisch-Physikalische Klasse*, 1913, 582–592.

Munson, B., Young, D., Okiishi, T. and Huebesch, W., 2012. *Fundamentals of Fluid Mechanics*. NJ: John Wiley&Sons, Inc., the sevent edition.

Murrenhoff, H., Sgro, S. and Vukovic, M., 2014. An Overview of Energy Saving Architectures for Mobile Applications. *9th International Fluid Power Conference (9th IFK)*, Aachen, Germany, 238–249.

Nielsen, B., 2005. *Controller Development for a Separate Meter-In Separate Meter-Out Fluid Power Valve for Mobile Applications*. Ph.D. thesis, Aalborg University.

Olsson, H., Åström, K. J., Canudas de Wit, C., Gäfvert, M. and Lischinsky, P., 1998. Friction Models and Friction Compensation. *European Journal of Control*, 4 (3), 176–195.

Oriental Motors, 2017. URL `https://www.oriental-motor.co.uk/media/files/rk2_uk_062016.pdf`.

Owen, W. S. and Croft, E. A., 2003. The reduction of stick-slip friction in hydraulic actuators. *IEEE/ASME Transactions on Mechatronics*, 8 (3), 362–371.

Paloniitty, M., Karvonen, M., Linjama, M. and Tiainen, T., 2012. Laminated manifold for digital hydraulics – principles, challenges and benefits. *The Fifth Workshop on Digital Fluid Power*, Tampere, Finland.

Paloniitty, M., Linjama, M. and Huhtala, K., 2015. Equal Coded Digital Hydraulic Valve System – Improving Tracking Control with Pulse Frequency Modulation. *Procedia Engineering*, 106, 83–91.

Palumbo, A., Paoluzzi, R., Borghi, M. and Milani, M., 1996. Forces on a hydraulic valve spool. *Proceedings of the JFPS International Symposium on Fluid Power*, 1996 (3), 543–548.

Pan, M., Johnston, N., Plummer, A., Kudzma, S. and Hillis, a., 2013. Theoretical and experimental studies of a switched inertance hydraulic system. *Proceedings of the Institution of Mechanical Engineers, Part I: Journal of Systems and Control Engineering*, 228 (1), 12–25. URL http://pii.sagepub.com/lookup/doi/10.1177/0959651813500952.

Pan, M., Johnston, N., Robertson, J., Plummer, A., Hillis, A. and Yang, H., 2015. Experimental Investigation of a Switched Inertance Hydraulic System With a High-Speed Rotary Valve. *Journal of Dynamic Systems, Measurement, and Control*, 137 (12), 121003.

Pettersson, K. and Tikkanen, S., 2009. Secondary control in construction machinery – design and evaluation of an excavator swing drive. *The 11th Scandinavian International Conference on Fluid Power, SICFP'09, June 2-4, 2009, Linköping, Sweden*, 1–10.

Piatkowski, T., 2014. Dahl and LuGre dynamic friction models - The analysis of selected properties. *Mechanism and Machine Theory*, 73, 91–100. URL http://dx.doi.org/10.1016/j.mechmachtheory.2013.10.009.

Plummer, A., 2016. Electrohydraulic servovalves–past, present, and future. *10th International Fluid Power Conference, IFK2016*, Dresden, Germany.

Posa, A., Oresta, P. and Lippolis, A., 2013. Analysis of a directional hydraulic valve by a Direct Numerical Simulation using an immersed-boundary method. *Energy Conversion and Management*, 65, 497–506.

Rampen, W., 2006. Gearless Transmissions For Large Wind Turbines - The History and Future of Hydraulic Drives. Artemis IP Ltd.

Rannow, M. B., Tu, H. C., Wang, M., Li, P. Y. and Chase, T. R., 2010. Optimal design of a high-speed on/off valve for a hydraulic hybrid vehicle application. *Proceedings of the 7th International Fluid Power Conference*, Aachen, Germany, 1–14.

Reichert, M., 2010. *Development of high-response piezo-servovalves for improved performance of electrohydraulic cylinder drives*. Ph.D. thesis, Aachen University, Aachen, Germany.

Roemer, D. B., Johansen, P., Pedersen, H. C. and Andersen, T. O., 2013. Design and modelling of fast switching efficient seat valves for digital displacement pumps. *Transactions of the Canadian Society for Mechanical Engineering*, 37 (1), 71–88.

Rydberg, K.-E., 2015. Energy Efficient Hydraulics – System solutions for loss minimization. *National Conference on Fluid Power*, Linköping, Sweden.

Sakurai, Y., Nakada, T. and Tanaka, K., 2002. Design method of an intelligent oil-hydraulic system (load sensing oil-hydraulic system). *Proceedings of the IEEE Internatinal Symposium on Intelligent Control*.

Schneider, M., Koch, O. and Weber, J., 2016. Green Wheel Loader–improving fuel economy through energy efficient drive and control concepts. *The 10th International Fluid Power Conference*, Dresden, Germany, 63–78.

Shell, 2017. Industrial Hydraulics Fluid Shell Tellus S2 V32. URL http://www.epc.shell.com/.

Shenouda, A., 2006. *Quasi-Static Hydraulic Control Systems and Energy Savings Potential Using Independent Metering Four-Valve Assembly Configuration*. Doctor of philosophy thesis, Woodruff School of Mechanical Engineering, Georgia Institute of Technology.

Simic, M. and Herakovic, N., 2015. Reduction of the flow forces in a small hydraulic seat valve as alternative approach to improve the valve characteristics. *Energy Conversion and Management*, 89 (JANUARY), 708–718.

Sitte, A. and Weber, J., 2013. Structural design of independent metering control systems. *The 13th Scandinavian International Conference on Fluid Power, SICFP2013*, (September), 261–270.

Smith, D., 1999. Electrohydraulic valve arrangement. US5868059.

Sobachkin, A. and Dumnov, G., 2013. Numerical Basis of CAD-Embedded CFD. *NAFEMS World Congress 2013*, (February), 1–20.

SolidWorks, 2013a. Advanced Boundary Cartesian Meshing Technology in SolidWorks Flow Simulation.

SolidWorks, 2013b. Enhanced Turbulence Modeling in SolidWorks Flow Simulation.

SolidWorks, 2015. SolidWorks Flow Simulation.

SolidWorks, 2016a. Introduction to simulation. SolidWorks Simulation.

SolidWorks, 2016b. Theoretical manual. SolidWorks Simulation.

Taylor, J., Rampen, W., Robertson, A. and Caldwell, N., 2011. Digiatl displacement® hydraulic hybrids. Parallel hybrid drives for commercial vehicles. *JSAE Annual Congress*, (1).

Tecnord, 2017. SJ-MRA Manual Rotary Spool Valve, 2 Way. URL `https://www.tecnord.com/tabelle/cartridge-valves/mechanical-directional-pdf/SJ-MRA.pdf`.

Tennis, F., 1969. Pilot controllable valve mechanism. US3464444.

Trancossi, M., 2011. An Overview of Scientific and Technical Literature on Coanda Effect Applied to Nozzles. *SAE Technical Papers*, 1–13.

Tu, H. C., Rannow, M. B., Van de Ven, J. D., Wang, M., Li, P. Y. and Chase, T. R., 2007. High speed rotary pulse width modulated on/off valve. *Proceedings of the International Mechanical Engineering Congress*, Seattle, Washington, 1–13.

Tu, H. C., Rannow, M. B., Wang, M., Li, P. Y., Chase, T. R. and Cheong, K. L., 2011. High-Speed 4-Way Rotary On/Off Valve for Virtually Variable Displacement Pump/Motor Applications. *ASME 2011 Dynamic Systems and Control Conference and Bath/ASME Symposium on Fluid Power and Motion Control*, 1 (January), 201–208.

Tu, H. C., Rannow, M. B., Wang, M., Li, P. Y., Chase, T. R. and Van de Ven, J. D., 2012. Design, Modeling, and Validation of a High-Speed Rotary Pulse-Width-Modulation On/Off Hydraulic Valve. *Journal of Dynamic Systems, Measurement, and Control*, 134 (6), 061002. URL `http://dynamicsystems.asmedigitalcollection.asme.org/article.aspx?articleid=1478019`.

Ullman, D., 2009. *The Mechanical Design Process*. McGraw-Hill series in mechanical engineering, McGraw-Hill Education. URL `https://books.google.co.uk/books?id=dQcoAQAAMAAJ`.

Vukovic, M., Leifeld, R. and Murrenhoff, H., 2016. STEAM – a hydraulic hybrid architecture for excavators. *10th International Fluid Power Conference*, Dresden, Germany, 151–162.

Vukovic, M. and Murrenhoff, H., 2015. The Next Generation of Fluid Power Systems. *Procedia Engineering*, 106, 2–7.

Wang, H., Gong, G., Zhou, H. and Wang, W., 2016. Steady flow torques in a servo motor operated rotary directional control valve. *Energy Conversion and Management*, 112, 1–10.

Wang, M. and Li, P. Y., 2009. Duty ratio control of a rotary pwm valve with periodic measurement error. *Proceedings of the American Control Conference*, 5073–5078.

Wang, M. and Li, P. Y., 2012. Displacement Control of Hydraulic Actuators Using a Passivity Based Nonlinear Controller. *ASME 2012 5th Annual Dynamic Systems and Control Conference joint with the JSME 2012 11th Motion and Vibration Conference, DSCC2012-MOVIC2012*, Fort Lauderdale, Florida, USA, 1–7.

Wang, M., Tu, H., Rannow, M., Li, P. and Chase, T., 2010. CFD analysis of a novel high speed rotary on/off valve. *Proceedings of the 6th FPNI-PhD Symposium*, 283–294.

Wang, T. and Wang, Q., 2014. Efficiency analysis and evaluation of energy-saving pressure-compensated circuit for hybrid hydraulic excavator. *Automation in Construction*, 47, 62–68. URL `http://dx.doi.org/10.1016/j.autcon.2014.07.012`.

White, F., 1999. *Fluid Mechanics*. McGraw-Hill series in mechanical engineering, the fourth edition.

Wilcox, D. C., 2006. *Turbulence Modeling for CFD*. DCW Industries, Inc, third edition.

de Wit, C. C., Olsson, H., Astrom, K. J. and Lischinsky, P., 1995. A new model for control of systems with friction. *IEEE Transactions on Automatic Control*, 40 (3), 419–425.

Xu, B., Ding, R., Zhang, J., Cheng, M. and Sun, T., 2015. Pump/valves coordinate control of the independent metering system for mobile machinery. *Automation in Construction*, 57, 98–111. URL `http://dx.doi.org/10.1016/j.autcon.2015.04.012`.

Yang, H.-Y. and Pan, M., 2015. Engineering research in fluid power: a review. *Journal of Zhejiang University - Science A: Applied Physics & Engineering*, 16 (6), 427–442.

Yang, Y., Guglielmino, E., Dai, J. S., Boaventura, T. and Caldwell, D. G., 2010. Modeling of a novel 3-way rotary type electrohydraulic valve. *2010 IEEE International Conference on Information and Automation, ICIA 2010*, Harbin, China, 1463–1468.

Yu, J., Zhuang, J. and Yu, D., 2014. Modeling and analysis of a rotary direct drive servovalve. *Chinese Journal of Mechanical Engineering*, 27 (5), 1064–1074.

Yu, J., Zhuang, J. and Yu, D., 2015. State feedback integral control for a rotary direct drive servo valve using a Lyapunov function approach. *ISA Transactions*, 54, 207–217.

Appendices

Appendix A. Drawings of the Prototype

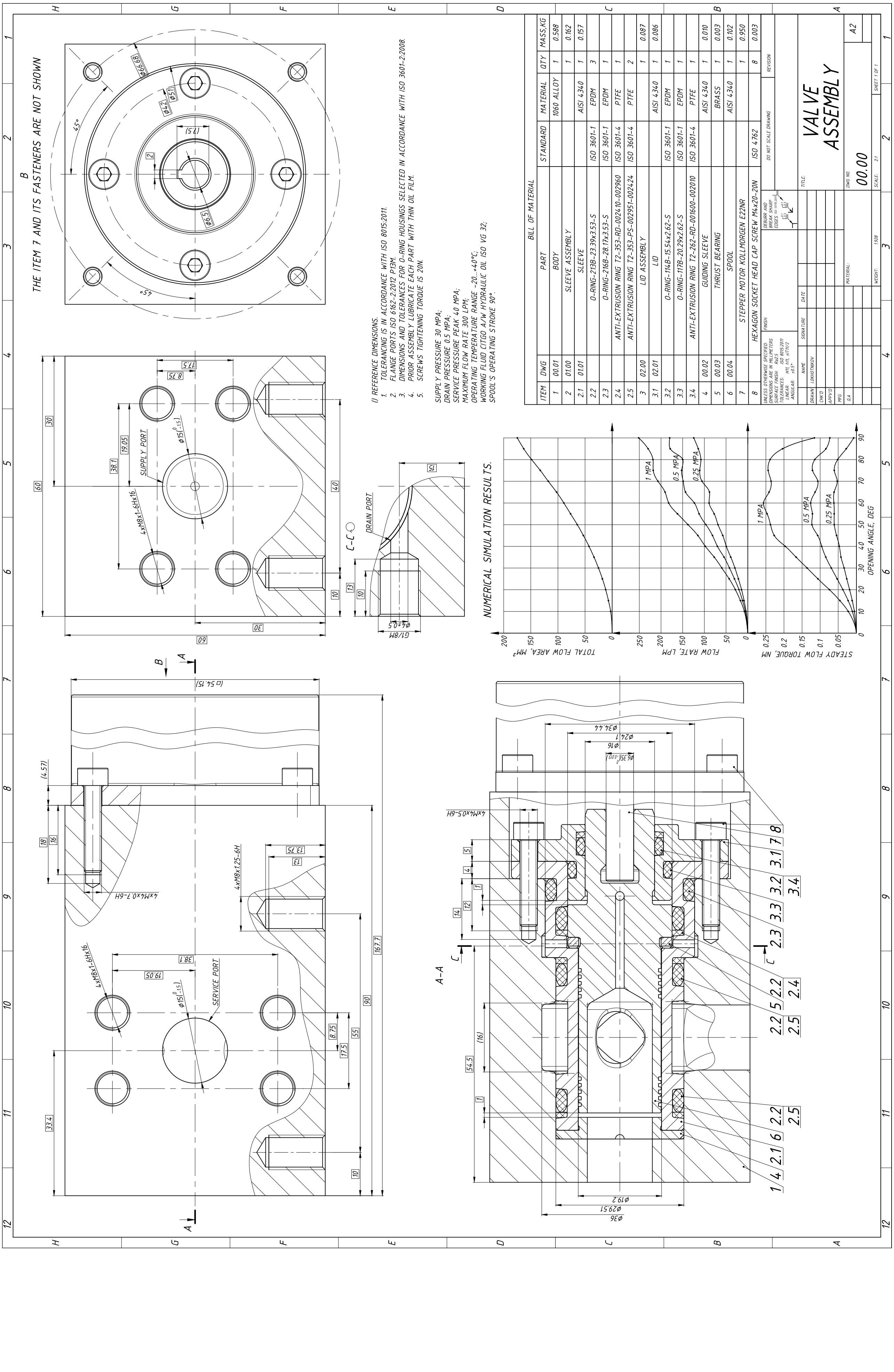
B
THE ITEM 7 AND ITS FASTENERS ARE NOT SHOWN
SUPPLY PORT
SERVICE PORT
DRAIN PORT
C–C
A–A
() REFERENCE DIMENSIONS.
1. TOLERANCING IS IN ACCORDANCE WITH ISO 8015:2011.
2. FLANGE PORTS ISO 6162-2:2012 P13M.
3. DIMENSIONS AND TOLERANCES FOR O-RING HOUSINGS SELECTED IN ACCORDANCE WITH ISO 3601-2:2008.
4. PRIOR ASSEMBLY LUBRICATE EACH PART WITH THIN OIL FILM.
5. SCREWS TIGHTENING TORQUE IS 20N.
SUPPLY PRESSURE 30 MPA;
DRAIN PRESSURE 0.5 MPA;
SERVICE PRESSURE PEAK 40 MPA;
MAXIMUM FLOW RATE 300 LPM;
OPERATING TEMPERATURE RANGE -20...+40°C;
WORKING FLUID CITGO A/W HYDRAULIC OIL ISO VG 32;
SPOOL'S OPERATING STROKE 90°.
NUMERICAL SIMULATION RESULTS.
TOTAL FLOW AREA, MM²
FLOW RATE, LPM
STEADY FLOW TORQUE, NM
OPENING ANGLE, DEG
1 MPA
0.5 MPA
0.25 MPA
BILL OF MATERIAL
ITEM | DWG | PART | STANDARD | MATERIAL | QTY | MASS,KG
1 | 00.01 | BODY | | 1060 ALLOY | 1 | 0.588
2 | 01.00 | SLEEVE ASSEMBLY | | | 1 | 0.162
2.1 | 01.01 | SLEEVE | | AISI 4340 | 1 | 0.157
2.2 | | O-RING-213B-23.39x3.53-S | ISO 3601-1 | EPDM | 3 |
2.3 | | O-RING-216B-28.17x3.53-S | ISO 3601-1 | EPDM | 1 |
2.4 | | ANTI-EXTRUSION RING T2-353-RD-002410-002960 | ISO 3601-4 | PTFE | 1 |
2.5 | | ANTI-EXTRUSION RING T2-353-PS-002951-002424 | ISO 3601-4 | PTFE | 2 |
3 | 02.00 | LID ASSEMBLY | | | 1 | 0.087
3.1 | 02.01 | LID | | AISI 4340 | 1 | 0.086
3.2 | | O-RING-114B-15.54x2.62-S | ISO 3601-1 | EPDM | 1 |
3.3 | | O-RING-117B-20.29x2.62-S | ISO 3601-1 | EPDM | 1 |
3.4 | | ANTI-EXTRUSION RING T2-262-RD-001600-002010 | ISO 3601-4 | PTFE | 1 |
4 | 00.02 | GUIDING SLEEVE | | AISI 4340 | 1 | 0.010
5 | 00.03 | THRUST BEARING | | BRASS | 1 | 0.003
6 | 00.04 | SPOOL | | AISI 4340 | 1 | 0.102
7 | | STEPPER MOTOR KOLLMORGEN E22NR | | | 1 | 0.950
8 | | HEXAGON SOCKET HEAD CAP SCREW M4x20-20N | ISO 4762 | | 8 | 0.003
DO NOT SCALE DRAWING
REVISION
DRAWN LOKHOTNIKOV
TITLE:
VALVE
ASSEMBLY
DWG NO
00.00
A2
SCALE: 2:1
SHEET 1 OF 1

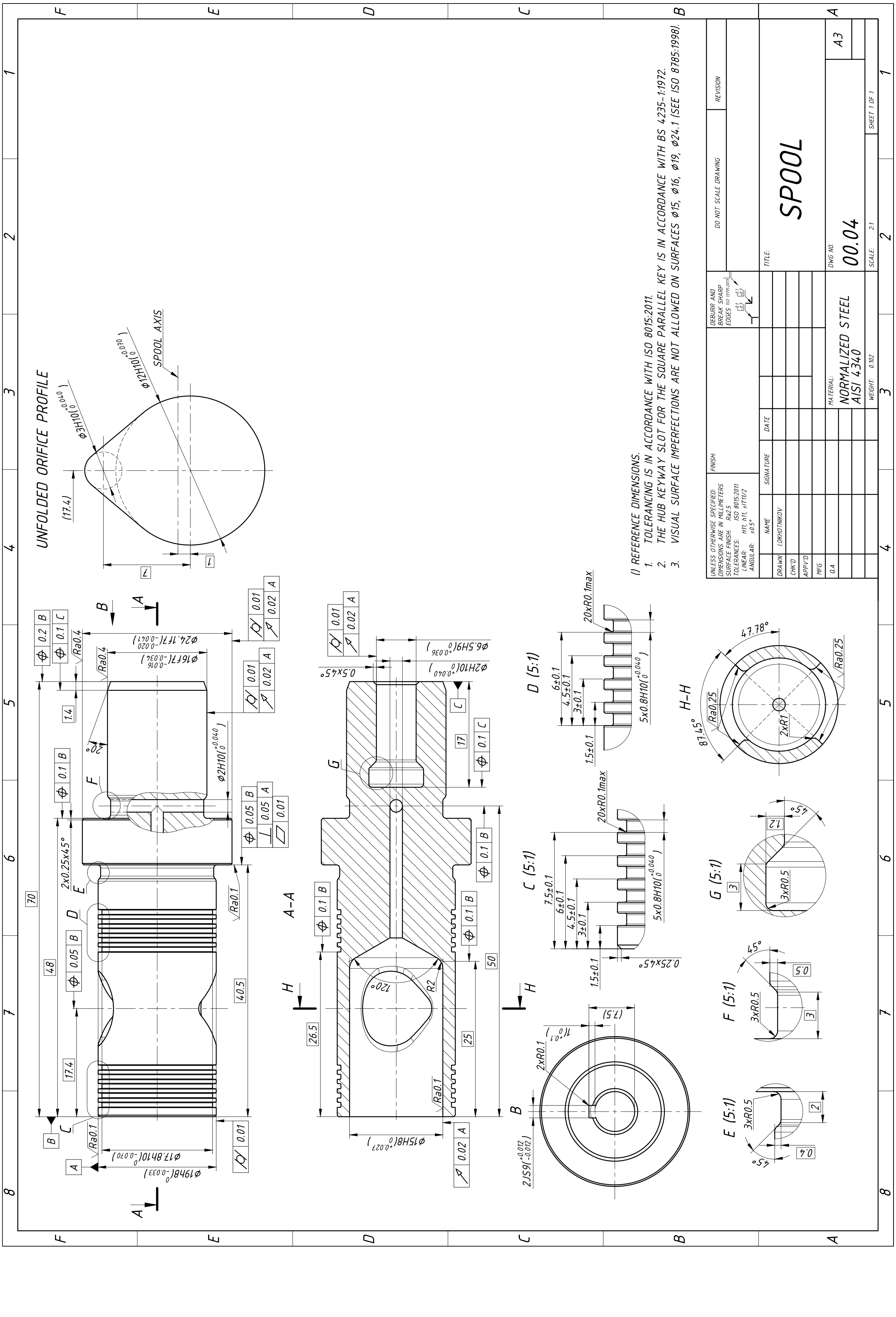
UNFOLDED ORIFICE PROFILE
SPOOL AXIS
A–A
H–H
D (5:1)
C (5:1)
G (5:1)
F (5:1)
E (5:1)
() REFERENCE DIMENSIONS.
1. TOLERANCING IS IN ACCORDANCE WITH ISO 8015:2011.
2. THE HUB KEYWAY SLOT FOR THE SQUARE PARALLEL KEY IS IN ACCORDANCE WITH BS 4235-1:1972.
3. VISUAL SURFACE IMPERFECTIONS ARE NOT ALLOWED ON SURFACES ⌀15, ⌀16, ⌀19, ⌀24.1 (SEE ISO 8785:1998).
UNLESS OTHERWISE SPECIFIED:
DIMENSIONS ARE IN MILLIMETERS
SURFACE FINISH: Ra2.5
TOLERANCES: ISO 8015:2011
LINEAR: H11, h11, ±IT11/2
ANGULAR: ±0.5°
FINISH:
DEBURR AND BREAK SHARP EDGES
DO NOT SCALE DRAWING
REVISION
NAME
SIGNATURE
DATE
DRAWN LOKHOTNIKOV
CHK'D
APPV'D
MFG
Q.A
TITLE:
SPOOL
MATERIAL:
NORMALIZED STEEL AISI 4340
DWG NO.
00.04
A3
WEIGHT: 0.102
SCALE: 2:1
SHEET 1 OF 1

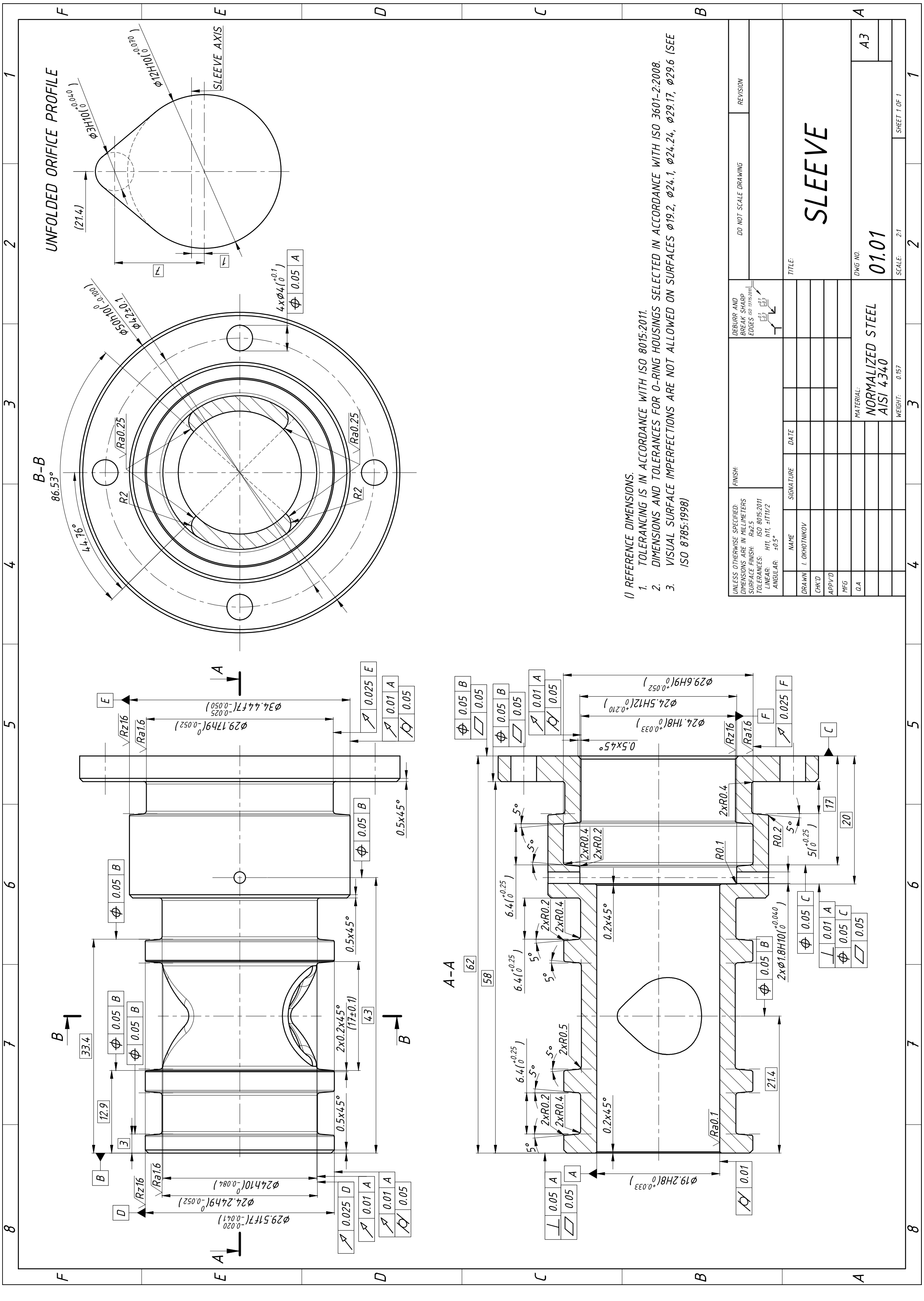
UNFOLDED ORIFICE PROFILE
SLEEVE AXIS
B-B
A-A
() REFERENCE DIMENSIONS.
1. TOLERANCING IS IN ACCORDANCE WITH ISO 8015:2011.
2. DIMENSIONS AND TOLERANCES FOR O-RING HOUSINGS SELECTED IN ACCORDANCE WITH ISO 3601-2:2008.
3. VISUAL SURFACE IMPERFECTIONS ARE NOT ALLOWED ON SURFACES Ø19.2, Ø24.1, Ø24.24, Ø29.17, Ø29.6 (SEE ISO 8785:1998)
DO NOT SCALE DRAWING
REVISION
TITLE:
SLEEVE
MATERIAL:
NORMALIZED STEEL
AISI 4340
DWG NO.
01.01
A3
DRAWN I. OKHOTNIKOV

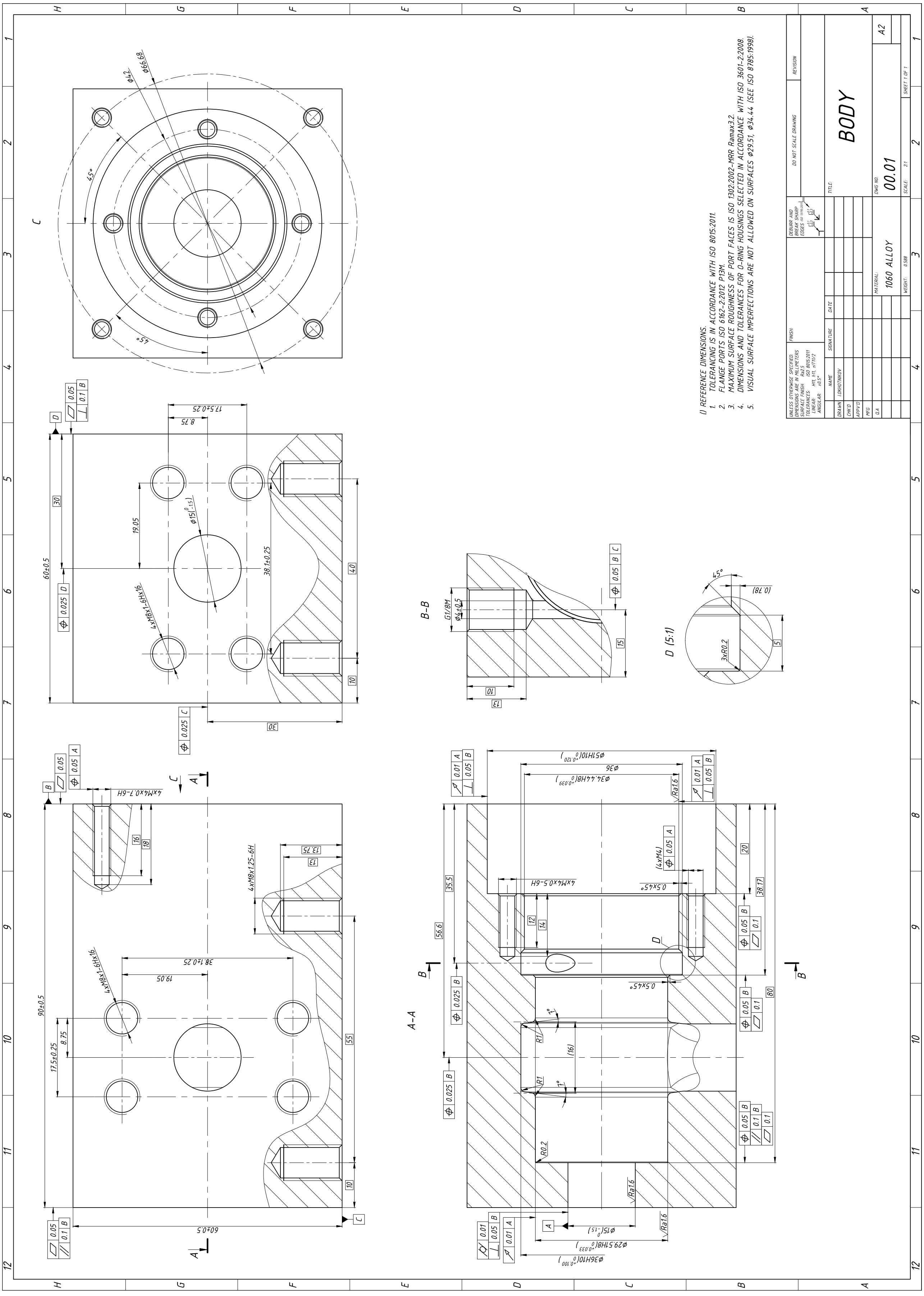
() REFERENCE DIMENSIONS.
1. TOLERANCING IS IN ACCORDANCE WITH ISO 8015:2011.
2. FLANGE PORTS ISO 6162-2:2012 P13M.
3. MAXIMUM SURFACE ROUGHNESS OF PORT FACES IS ISO 1302:2002-MRR Ramax3.2.
4. DIMENSIONS AND TOLERANCES FOR O-RING HOUSINGS SELECTED IN ACCORDANCE WITH ISO 3601-2:2008.
5. VISUAL SURFACE IMPERFECTIONS ARE NOT ALLOWED ON SURFACES Ø29.51, Ø34.44 (SEE ISO 8785:1998).
BODY
00.01
1060 ALLOY
A2
A-A
B-B
D (5:1)

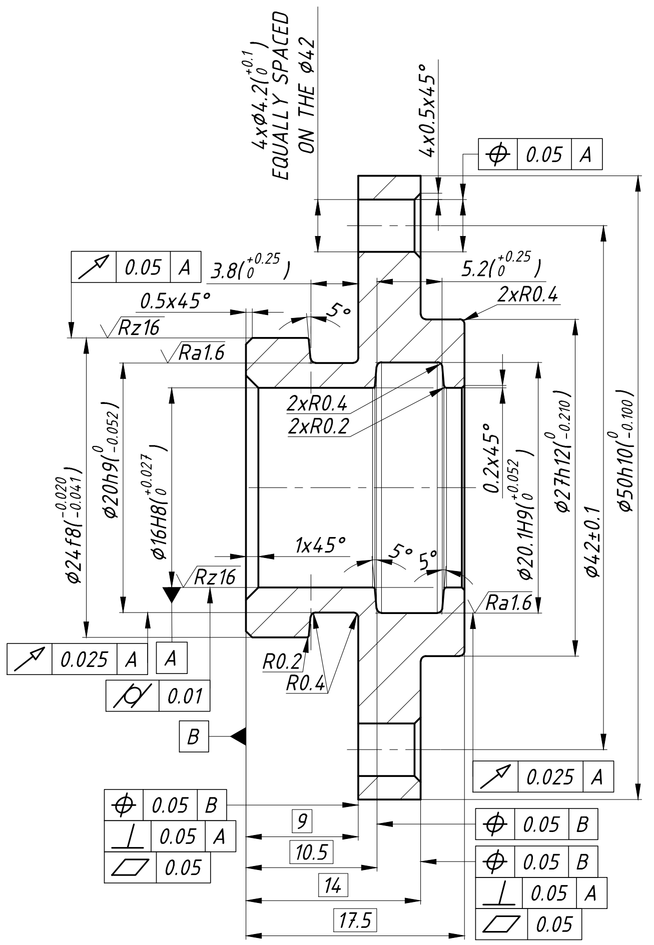

() REFERENCE DIMENSIONS.

1. TOLERANCING IS IN ACCORDANCE WITH ISO 8015:2011.
2. DIMENSIONS AND TOLERANCES FOR O-RING HOUSINGS SELECTED IN ACCORDANCE WITH ISO 3601-2:2008.
3. VISUAL SURFACE IMPERFECTIONS ARE NOT ALLOWED ON SURFACES Ø20, Ø20.1 (SEE ISO 8785:1998).

UNLESS OTHERWISE SPECIFIED:
DIMENSIONS ARE IN MILLIMETERS
SURFACE FINISH: Ra2.5
TOLERANCES: ISO 8015:2011
LINEAR: H11, h11, ±IT11/2
ANGULAR: ±0.5°

FINISH:

DEBURR AND BREAK SHARP EDGES ISO 13715:2011

DO NOT SCALE DRAWING

REVISION

	NAME	SIGNATURE	DATE
DRAWN	I.OKHOTNIKOV		
CHK'D			
APPV'D			
MFG			
Q.A			

TITLE: LID

MATERIAL: NORMALIZED STEEL AISI 4340

DWG NO. 02.01

A4

WEIGHT: 0.086

SCALE: 2:1

SHEET 1 OF 1

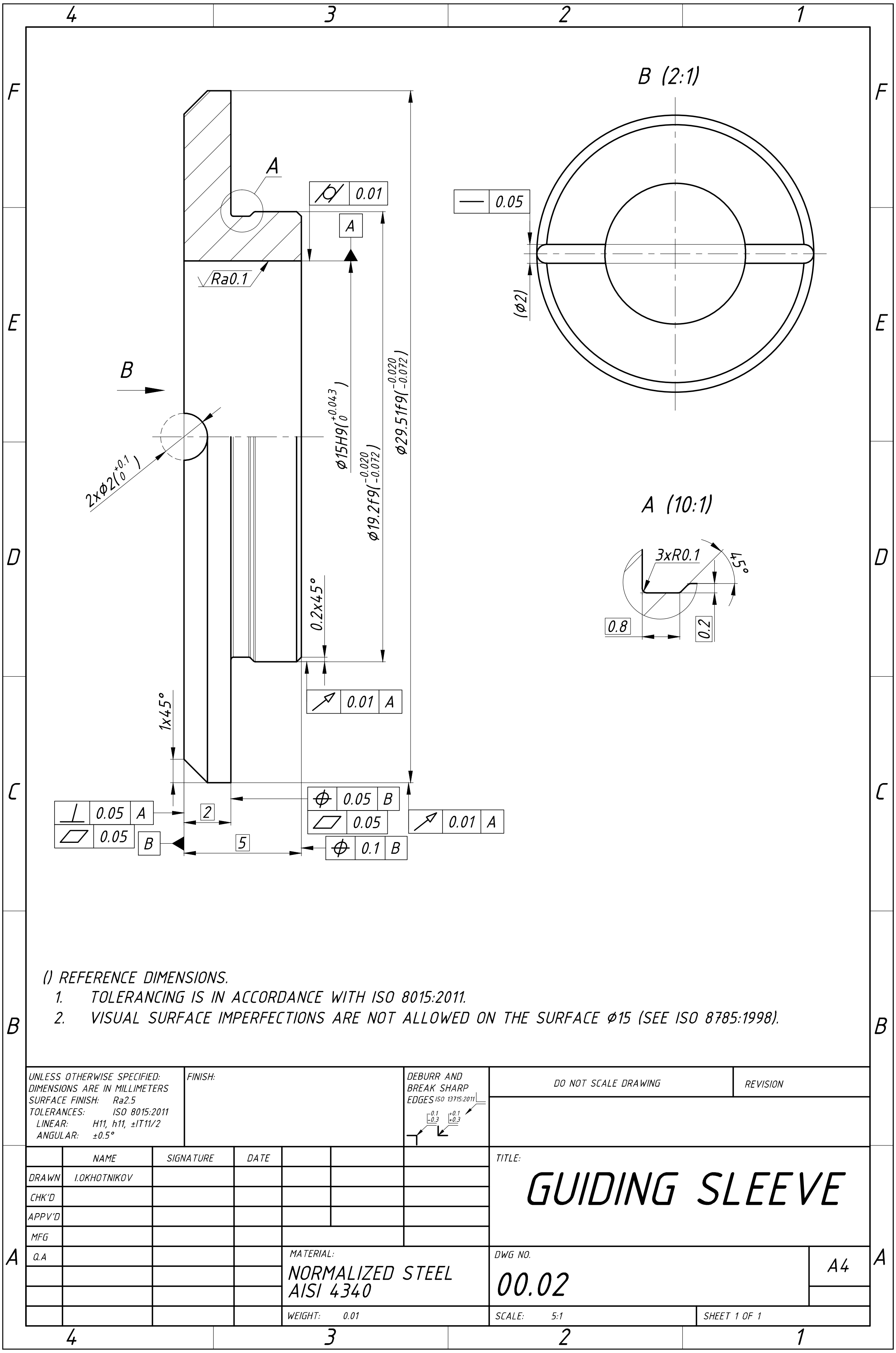
B (2:1)
A (10:1)
A
B
0.01
0.05
(Ø2)
Ra0.1
Ø15H9(+0.043 0)
Ø19.2f9(−0.020 −0.072)
Ø29.51f9(−0.020 −0.072)
2xØ2(+0.1 0)
3xR0.1
45°
0.8
0.2
0.2x45°
1x45°
0.01 A
0.05 A
0.05 B
0.05
0.1 B
2
5
() REFERENCE DIMENSIONS.
1. TOLERANCING IS IN ACCORDANCE WITH ISO 8015:2011.
2. VISUAL SURFACE IMPERFECTIONS ARE NOT ALLOWED ON THE SURFACE Ø15 (SEE ISO 8785:1998).
UNLESS OTHERWISE SPECIFIED:
DIMENSIONS ARE IN MILLIMETERS
SURFACE FINISH: Ra2.5
TOLERANCES: ISO 8015:2011
LINEAR: H11, h11, ±IT11/2
ANGULAR: ±0.5°
FINISH:
DEBURR AND BREAK SHARP EDGES ISO 13715:2011
DO NOT SCALE DRAWING
REVISION
NAME
SIGNATURE
DATE
DRAWN I.OKHOTNIKOV
CHK'D
APPV'D
MFG
Q.A
TITLE:
GUIDING SLEEVE
MATERIAL:
NORMALIZED STEEL AISI 4340
DWG NO.
00.02
A4
WEIGHT: 0.01
SCALE: 5:1
SHEET 1 OF 1

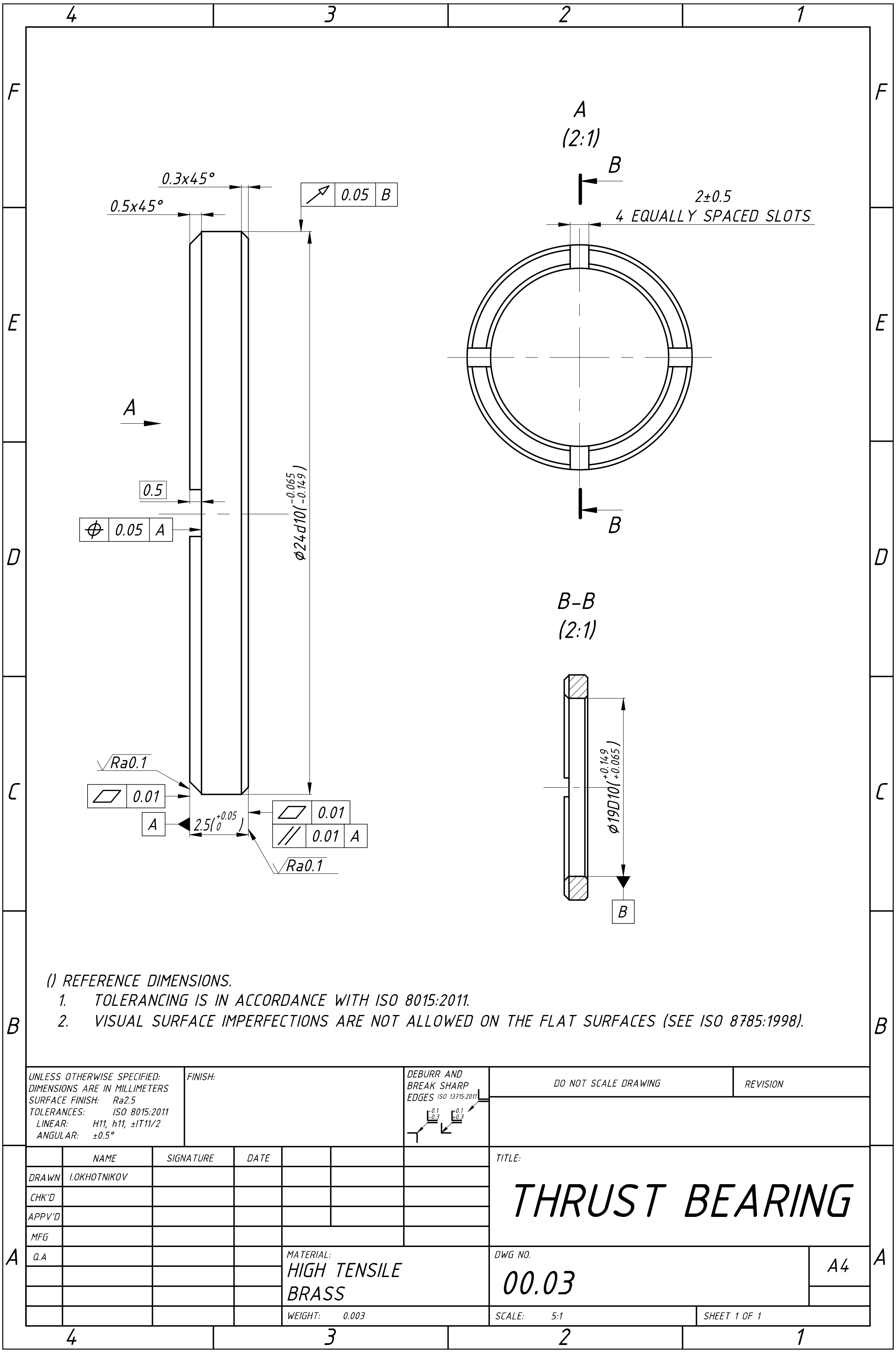
A
(2:1)
B
2±0.5
4 EQUALLY SPACED SLOTS
0.3x45°
0.5x45°
0.05 B
A
0.5
0.05 A
Ø24d10(-0.065 -0.149)
Ra0.1
0.01
A
2.5(+0.05 0)
0.01
0.01 A
Ra0.1
B
B-B
(2:1)
Ø19D10(+0.149 +0.065)
B
() REFERENCE DIMENSIONS.
1. TOLERANCING IS IN ACCORDANCE WITH ISO 8015:2011.
2. VISUAL SURFACE IMPERFECTIONS ARE NOT ALLOWED ON THE FLAT SURFACES (SEE ISO 8785:1998).
UNLESS OTHERWISE SPECIFIED:
DIMENSIONS ARE IN MILLIMETERS
SURFACE FINISH: Ra2.5
TOLERANCES: ISO 8015:2011
LINEAR: H11, h11, ±IT11/2
ANGULAR: ±0.5°
FINISH:
DEBURR AND BREAK SHARP EDGES ISO 13715:2011
DO NOT SCALE DRAWING
REVISION
NAME
SIGNATURE
DATE
DRAWN I.OKHOTNIKOV
CHK'D
APPV'D
MFG
Q.A
TITLE:
THRUST BEARING
MATERIAL:
HIGH TENSILE BRASS
WEIGHT: 0.003
DWG NO.
00.03
A4
SCALE: 5:1
SHEET 1 OF 1

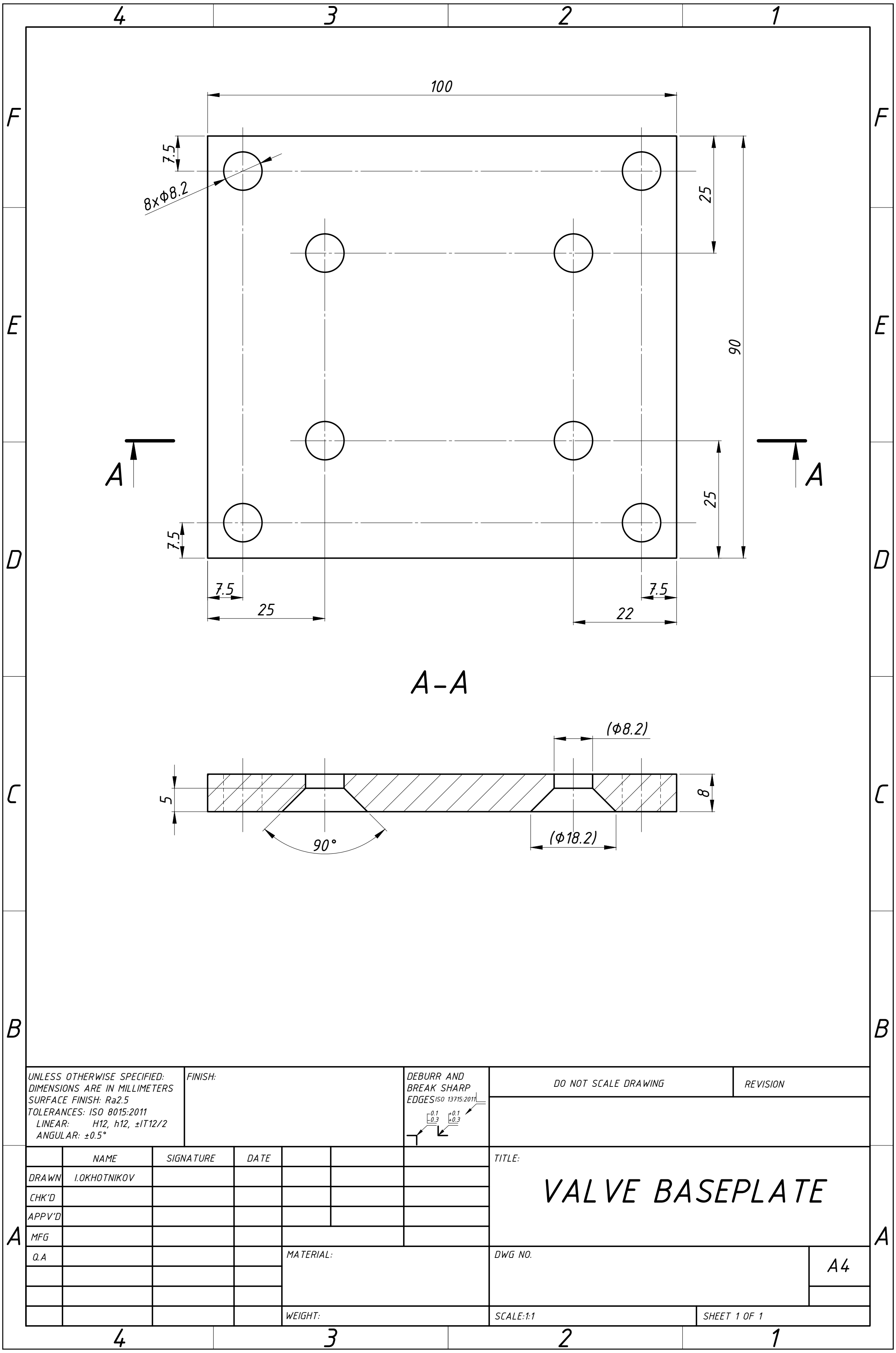
100
7.5
8xΦ8.2
25
90
A
A
25
7.5
7.5
25
7.5
22
A-A
(Φ8.2)
5
8
90°
(Φ18.2)
UNLESS OTHERWISE SPECIFIED:
DIMENSIONS ARE IN MILLIMETERS
SURFACE FINISH: Ra2.5
TOLERANCES: ISO 8015:2011
LINEAR: H12, h12, ±IT12/2
ANGULAR: ±0.5°
FINISH:
DEBURR AND
BREAK SHARP
EDGES ISO 13715:2019
DO NOT SCALE DRAWING
REVISION
NAME
SIGNATURE
DATE
DRAWN
I.OKHOTNIKOV
CHK'D
APPV'D
MFG
Q.A
TITLE:
VALVE BASEPLATE
MATERIAL:
DWG NO.
A4
WEIGHT:
SCALE:1:1
SHEET 1 OF 1

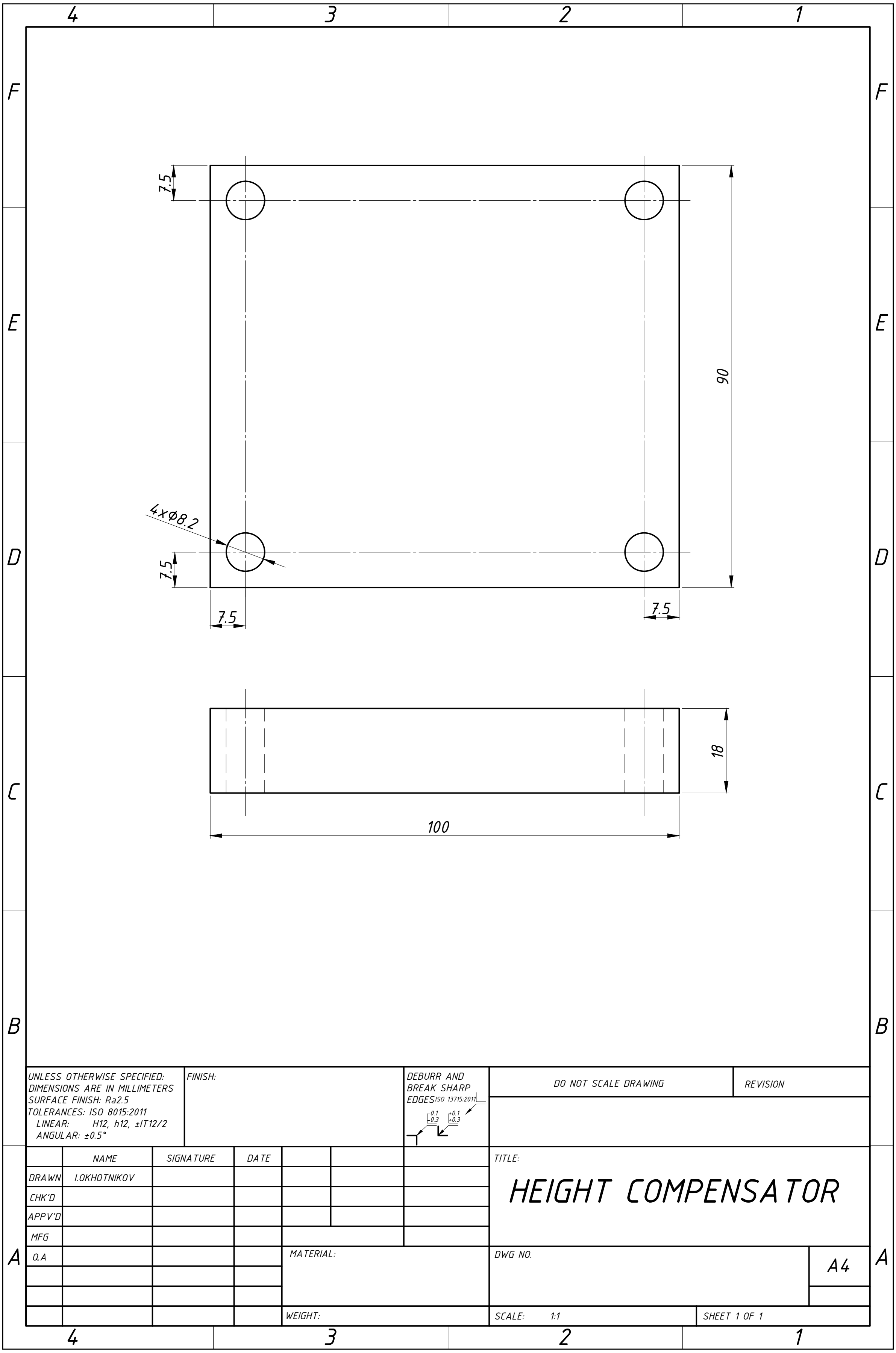

7.5
7.5
4xØ8.2
7.5
7.5
90
18
100
UNLESS OTHERWISE SPECIFIED:
DIMENSIONS ARE IN MILLIMETERS
SURFACE FINISH: Ra2.5
TOLERANCES: ISO 8015:2011
LINEAR: H12, h12, ±IT12/2
ANGULAR: ±0.5°
FINISH:
DEBURR AND BREAK SHARP EDGES ISO 13715:2011
DO NOT SCALE DRAWING
REVISION
NAME
SIGNATURE
DATE
DRAWN I.OKHOTNIKOV
CHK'D
APPV'D
MFG
Q.A
TITLE:
HEIGHT COMPENSATOR
MATERIAL:
DWG NO.
A4
WEIGHT:
SCALE: 1:1
SHEET 1 OF 1

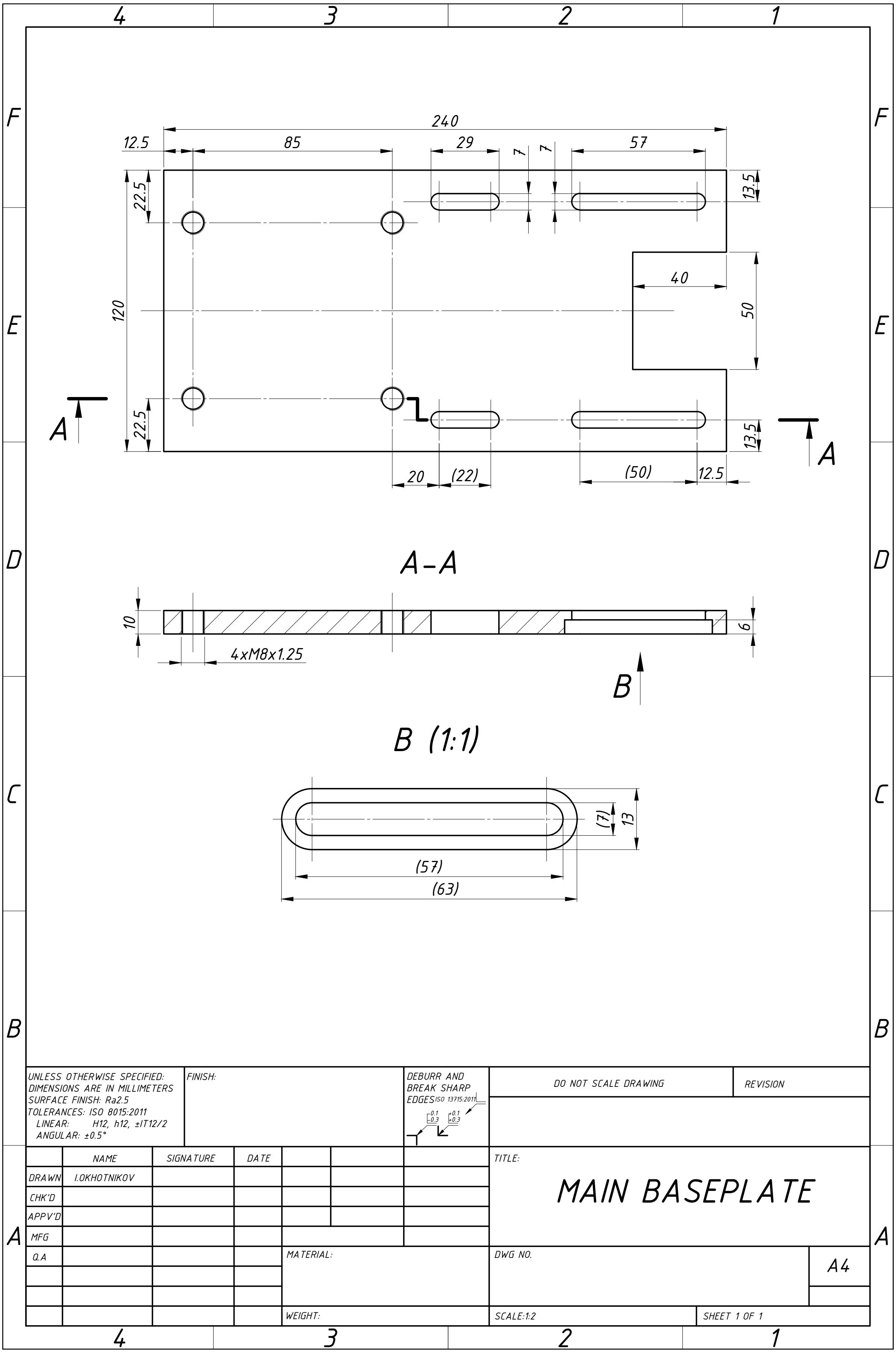
240
12.5
85
29
57
22.5
120
13.5
40
50
20
(22)
(50)
12.5
A
A-A
10
6
4xM8x1.25
B
B (1:1)
(7)
13
(57)
(63)
UNLESS OTHERWISE SPECIFIED:
DIMENSIONS ARE IN MILLIMETERS
SURFACE FINISH: Ra2.5
TOLERANCES: ISO 8015:2011
LINEAR: H12, h12, ±IT12/2
ANGULAR: ±0.5°
FINISH:
DEBURR AND BREAK SHARP EDGES ISO 13715:2019
DO NOT SCALE DRAWING
REVISION
NAME
SIGNATURE
DATE
DRAWN
I.OKHOTNIKOV
CHK'D
APPV'D
MFG
Q.A
TITLE:
MAIN BASEPLATE
MATERIAL:
DWG NO.
A4
WEIGHT:
SCALE:1:2
SHEET 1 OF 1

Appendix B. Prototype Assembly Scheme

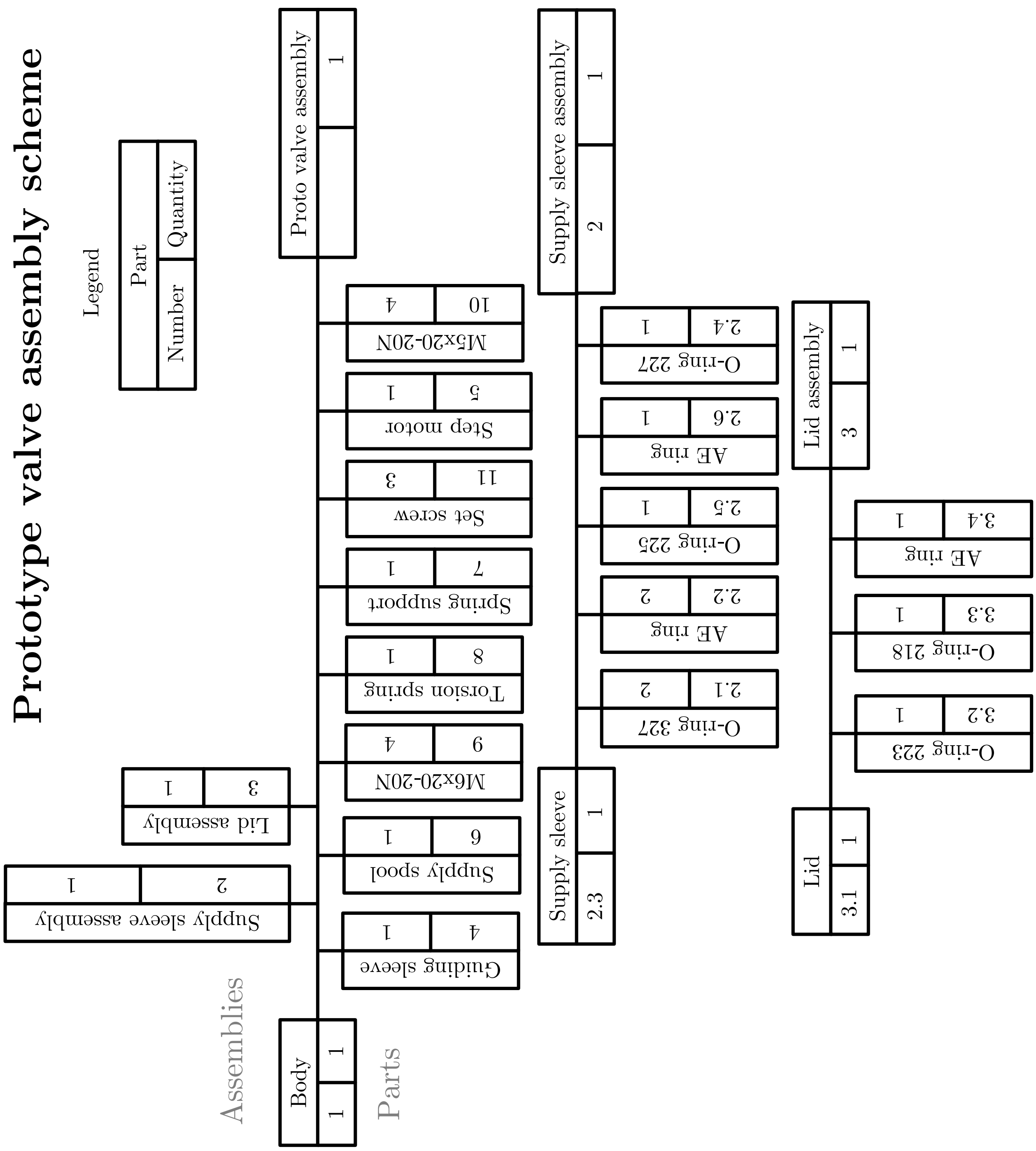
Prototype valve assembly scheme
Legend
Part
Number
Quantity
Assemblies
Parts
Proto valve assembly
1
Supply sleeve assembly
2
1
Lid assembly
3
1
Body
1
1
Guiding sleeve
4
1
Supply spool
6
1
M6x20-20N
9
4
Torsion spring
8
1
Spring support
7
1
Set screw
11
3
Step motor
5
1
M5x20-20N
10
4
Supply sleeve
2.3
1
O-ring 327
2.1
2
AE ring
2.2
2
O-ring 225
2.5
1
AE ring
2.6
1
O-ring 227
2.4
1
Lid
3.1
1
O-ring 223
3.2
1
O-ring 218
3.3
1
AE ring
3.4
1

Appendix C. Stepper Motor Specification, (Oriental Motors 2017)

Speed -Torque Characteristics fs: Maximum Starting Frequency

RKS596

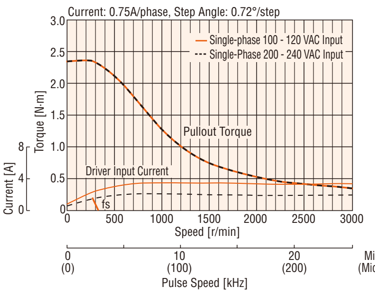

RKS599

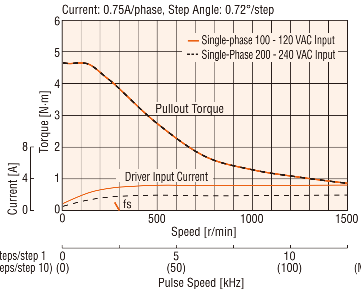

RKS5913

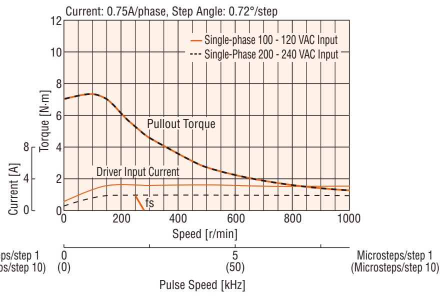

Note

- Pay attention to heat dissipation from the motor as there will be a considerable amount of heat under certain conditions. Be sure to keep the temperature of the motor case under 100˚C.
  For the Encoder type, in order to protect encoder, be sure to keep the temperature of the motor case under 85˚C.
  [When conforming to the UL or CSA Standards, it is required to keep the temperature of the motor case at 75°C or less, since the motor is recognized as Thermal class 105 (A).]

Definition

Maximum Holding Torque	: Maximum Holding Torque (holding power) while motor standstill (power supplied at the Rated Current).	
Permissible Torque	: Maximum Torque load applied to Gear Output Shaft	
Maximum Torque	: Maximum Torque load applied to Gear Output Shaft when up/reduce the speed (i.e.. start-up or shut-down of Load Inertia).	
Holding Torque at Motor Standstill	Power ON	: Holding Torque under Automatic Current Cutback function is operated.
	Electromagnetic Brake	: Static friction torque generated by Electromagnetic Brake at motor standstill. (Power Off Activated Type Electromagnetic Brake)

Specifications (RoHS)

Product Name			RKS596□ □D■-◇	RKS599□ □D■-◇	RKS5913□ □D■-◇
Product Name	Built-In Controller Type		RKS596□ □D■-◇	RKS599□ □D■-◇	RKS5913□ □D■-◇
	Pulse Input Type		RKS596□ □-◇	RKS599□ □-◇	RKS5913□ □-◇
Maximum Holding Torque		N·m	2.1	4.1	6.3
Holding Torque at Motor Standstill	Power ON	N·m	1.05	2.05	3.15
	Electromagnetic Brake	N·m	1.05	2.05	3.15
Rotor Inertia		J : kg·m²	1100×10⁻⁷ [2200×10⁻⁷]*1 (1100×10⁻⁷)*2	2200×10⁻⁷ [3300×10⁻⁷]*1 (2200×10⁻⁷)*2	3300×10⁻⁷ [4400×10⁻⁷]*1 (3300×10⁻⁷)*2
Rated Current		A / Phase	0.75		
Basic Step Angle			0.72˚		
Power Supply Input	Voltage / Frequency		Single-Phase 100-120 VAC, Single-Phase 200-240 VAC –15~+10% 50/60 Hz		
	Input Current A	Single-Phase 100-120 VAC	3.6	3.5	3.5
		Single-Phase 200-240 VAC	2.1	2.2	2.2
Excitation Mode			Microstep		
Control Power Supply*3			24 VDC±5% 0.2 A		
Electromagnetic Brake*4	Power Supply Input		24 VDC±5%*5 0.42 A		

Frame Size 85 mm

Product Name	Motor Product Name	L	Mass kg
RKS596R□D2-◇	PKE596RC2	90	2.0
RKS599R□D2-◇	PKE599RC2	120	3.1
RKS5913R□D2-◇	PKE5913RC2	150	4.2

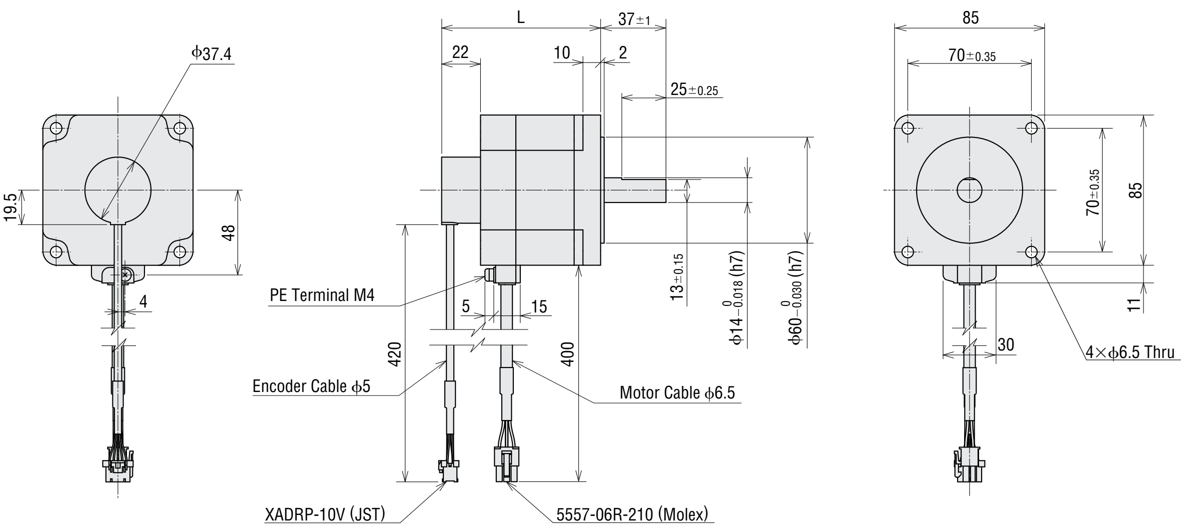

Driver Specification

	Built-in Controller type	Pulse-input Type
Maximum Input Pulse Frequency	–	Line Driver Output from controller: 500kHz (at 50% duty) Open-collector Output from controller: 250kHz (at 50% duty) Active low pulse-input
Input Signal	Photocoupler input Input signal voltage : 11.4 VDC~26.4 VDC	Photocoupler, Open-collector output: 11.4 VDC~26.4 VDC (AWO, CS, FREE, ALM-RST) Photocoupler, Open-collector output: 3 VDC~5.25 VDC (CW (PLS) + 5 V, CCW (DIR) + 5 V) Photocoupler, Open-collector output: 21.6 VDC~26.4 VDC (CW (PLS) + 24 V, CCW (DIR) + 24 V)
Output Signal	Photocoupler · Open-collector output External use condition: 30 VDC maximum, 10 mA maximum	Photocoupler · Open-collector output External use condition: 30 VDC maximum, 10 mA maximum (READY, ALM, TIM)
Number of Positioning Program	64	–
Positioning Operation	One-shot operation, Linked operation, Linked operation 2, Sequential mode, Direct mode	–
Other operation	Continuous Operation, JOG Operation, Return-To-Home Operation, Test Operation	–
Control Module **OPX-2A**	○	–
Data Setting Software **MEXE02**	○	–

Built-In Controller Type RS-485 Communication Specifications

Protocol	Modbus protocol (Modbus RTU mode)
Electrical Characteristics	EIA-485 compliance Twisted-pair wire (TIA/EIA-568B CAT5e or greater recommended) is used up to a total extension length of 50 m.
Transmission/ Reception Mode	Half-duplex communication Asynchronous mode (data: 8-bit, stop bit: 1-bit/2-bit, parity: none/odd/even)
Baud Rate	9600 bps/19200 bps/38400 bps/57600 bps/115200 bps
Connection Type	Up to 31 units can be connected to one programmable controller (master equipment).

General Specifications

		Motor	Driver	
			Built-In Controller Type	Pulse Input Type
Thermal Class		130 (B) [Recognized as 105 (A) by UL]	–	
Insulation Resistance		100 MΩ or more when 500 VDC megger is applied between the following places: · Case – Motor windings · Case – Electromagnetic brake windings✻1	100 MΩ or more when 500 VDC megger is applied between the following places: · PE terminal – Power supply terminal · Signal I/O terminal – Power supply terminal	
Dielectric Strength		Sufficient to withstand the following for 1 minute: · Case – Motor windings 1.5 kVAC 50 Hz or 60 Hz · Case – Electromagnetic brake windings 1.5 kVAC 50 Hz or 60 Hz✻1	Sufficient to withstand the following for 1 minute: · PE terminal – Power supply terminal 1.5 kVAC 50 Hz or 60 Hz · Signal I/O terminal – Power supply terminal 1.8 kVAC 50 Hz or 60 Hz	· PE terminal – Power supply terminal 1.8 kVAC 50 Hz or 60 Hz · Signal I/O terminal – Power supply terminal 1.9 kVAC 50 Hz or 60 Hz
Operating Environment (In Operation)	Ambient Temperature	−10~+50°C (non-freezing): Standard Type, **TS** and **PS** Geared Type 0~+50°C (non-freezing): Package with Encoder 0~+40°C (non-freezing): Harmonic geared type	0~+55°C✻2 (non-freezing)	
	Ambient Humidity	85% or less (non-condensing)		
	Atmosphere	No corrosive gases, dust. Avoid contact with water or oil.		
Temperature Rise		Temperature rise of the windings are 80˚C or less. Measured at rated current, at standstill, five phases energized measured (by the resistance change method).	–	
Degree of Protection		IP20	IP10	IP20
Stop Position Accuracy✻3		±3 arc minutes (±0.05°)		
Shaft Runout		0.05 T.I.R (mm)✻4	–	
Radial Play✻5		0.025 mm Max. (Load 5 N)	–	
Axial Play✻6		0.075 mm Max. (Load 10 N)	–	
Concentricity for Shaft in the Mounting Pilot		0.075 T.I.R (mm)✻4	–	
Perpendicularity for Shaft of the Mounting Surface		0.075 T.I.R (mm)✻4	–	

✻1 Only for Built-in Controller Package
✻2 When attaching a heat sink 200 mm x 200 mm x 2 mm, made from aluminum plate or higher.
✻3 This value is measured at step angle 0.72°, under no load. (The value changes depends on the size of the load.)
✻4 T.I.R. (Total Indicator Reading) : The total dial gauge reading when the measurement section is rotated one revolution centered on the reference axis center.
✻5 Radial Play : Displacement in shaft position in the radial direction, when a 5 N load is applied in the vertical direction to the tip of the motor's shaft.
✻6 Axial Play : Displacement in shaft position in the axial direction, when a 10 N load is applied to the motor's shaft in the axial direction.

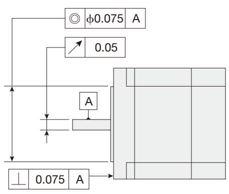

Note

- Do not measure insulation resistance or perform the dielectric strength test while the motor and driver are connected.

Encoder Specifications

Resolution	500 P/R
Output mode	Incremental
Output signal	3 channels
Output Circuit type	Line Driver

Permissible Radial Load and Permissible Axial Load

Unit=N

Type	Frame Size	Model	Gear Ratio	Permissible Radial Load					Permissible Axial Load
				Distance from tip of shaft mm					
				0	5	10	15	20	
Standard Type	42 mm	**RKS543**	–	35	44	58	85	–	2.5 (3.9) [3.1]
		RKS544							3.1 (4.5) [3.7]
		RKS545							3.7 (5.1) [4.3]
	60 mm	**RKS564**		90	100	130	180	270	6.9 (9.8) [7.5]
		RKS566							8.8 (11.8) [9.4]
		RKS569							13.7 (16.7) [14.7]
	85 mm	**RKS596**		260	290	340	390	480	18.6 (26.5) [19.6]
		RKS599							29.4 (37.3) [30.4]
		RKS5913							40.2 (48.1) [41.2]
TS Geared Type	42 mm	**RKS543**	**3.6, 7.2, 10**	20	30	40	50	–	15
			20, 30	40	50	60	70	–	
	60 mm	**RKS564**	**3.6, 7.2, 10**	120	135	150	165	180	40
			20, 30	170	185	200	215	230	
	90 mm	**RKS596**	**3.6, 7.2, 10**	300	325	350	375	400	150
			20, 30	400	450	500	550	600	
PS Geared Type	42 mm	**RKS545**	**5, 7.2, 10**	73	84	100	123	–	50
		RKS543	**25, 36, 50**	109	127	150	184	–	
	60 mm	**RKS566**	**5**	200	220	250	280	320	100
			7.2, 10	250	270	300	340	390	
		RKS564	**25, 36, 50**	330	360	400	450	520	
	90 mm	**RKS599**	**5, 7.2, 10**	480	540	600	680	790	300
		RKS596	**25**	850	940	1050	1190	1380	
			36	930	1030	1150	1310	1520	
			50	1050	1160	1300	1480	1710	
Harmonic Geared Type	42 mm	**RKS543**	**50, 100**	180	220	270	360	510	220
	60 mm	**RKS564**		320	370	440	550	720	450
	90 mm	**RKS596**		1090	1150	1230	1310	1410	1300

● The values inside the brackets ( ) represent the specification for the electromagnetic brake type.
The values inside the brackets [ ] represent the specification for the encoder type.

Appendix D. Mathematical Model of the Valve

The study of dynamic properties requires, as a prerequisite, construction of a mathematical model of the RTSV from the first principles. Presentation of this model in the state-space form allows analysis of stability of the systems. The previous chapter allowed to validate valve's performance functions derived during numerical modelling. Using these functions, namely the jet angles and the discharge coefficient functions, the mathematical model of the valve can be built. This chapter discusses development and analysis of the mathematical model of the valve.

The model of the valve was developed with the following assumptions: physical properties of the oil are constant, pressure fluctuations in the supply line are negligible, there is no internal and external leakages, pressure losses in conduits are insignificant.

The mathematical model developed in this chapter illustrates how spool loading factors, in the form of torques, influence the spool position and the resultant volume flow rate through the valve. It also describes how responsive the valve is with presence of loading torques.

Flow Torque

The flow torque acting on the spool from oil flowing through its orifices is a sum of the steady state torque and the transient one:

$$T_{fl} = T_{st.fl.} + T_{tr.fl.}. \tag{8.1}$$

The former takes place in steady state regimes, when flow streamlines are invariable in time (White 1999). The steady flow torque is a result of a momentum change in liquid entering and leaving the control volume. The total control volume in case of two orifices on the hollow rotary spool is split on two volumes: CV1 and CV2. Each control volume is considered as a circular sector of a hollow cylinder with radii corresponding to the spool's ones.

Steady Flow Torque

According to the analysis conducted in the previous chapter, the total steady flow torque acting on the spool of the hollow rotary spool from both orifices can be evaluated through the jet angle functions α_i as following:

$$T_{st.fl.} = C_d^2 A \Delta p r_2 \sum_{i=1}^{2} \sin \alpha_i(\phi). \tag{8.2}$$

Transient Flow Torque

The transient torque occurs due to acceleration of the fluid control volume. For the sliding spool valves the transient flow force is proportional to a spool velocity and a rate of pressure changes acting on a small fluid element inside the control volume (Merritt 1968). It is applicable for rotary valves as well with substitution of linear motion to angular one.

However, pressure changes in down- and upstream channels do not lead to formation of a tangential force and, hence, a torque on the hollow rotary spool. The reason for that is that pressure drop alterations do not cause a significant torque difference on the edges of the rotary orifice because of their small thickness. Therefore, the only contributor to the transient flow torque is the fluid inertial component, which can be determined through a moment of inertia I_{fl} of a fluid volume and a spool angular acceleration:

$$T_{tr.fl.} = I_{fl} \frac{d\omega}{dt}. \tag{8.3}$$

The moment of inertia of the fluid body, which is a hollow cylinder or a tube, along its longitudinal, or main valve, axis is equal to (Budynas et al. 2006)

$$I_{fl} = m_{fl} \frac{r_2^2 + r_1^2}{2}. \tag{8.4}$$

It depends on external and internal radii of the spool r_2, r_1 respectively and the total fluid mass m_{fl} in control volumes under acceleration, which is

$$m_{fl} = \rho V_{fl}. \tag{8.5}$$

Here, V_{fl} – the total volume of tubular control volumes in both spool openings, ρ – oil density.

Each of control volumes represents a portion of a hollow cylinder, which is located within an angle λ covering by the spool window. Since there are two control volumes, the total volume of the fluid within hollow cylindrical elements being accelerated during spool motion is calculated as:

$$V_{fl} = 2\left(r_2^2 - r_1^2\right) \frac{\pi \lambda h}{180°}. \tag{8.6}$$

The height of the fluid hollow cylinder h is variable along the central arc with the length l in the symmetry plane of the opening. The central arc length is.

$$l = \frac{\pi \lambda}{180°} r_2. \tag{8.7}$$

Effectively, this cylinder height h is equal to the width of the spool throttling window, see the Figure 8.1. It can be expressed through an equivalent area $A_{sp.eq}$, which is a rectangle with the sides h and l and equal to $A_{sp.op}$, the area of the spool single window opening $A_{sp.op}$. Hence, the sought height h is a ratio of the spool opening $A_{sp.op}$ to the central axis arc length l.

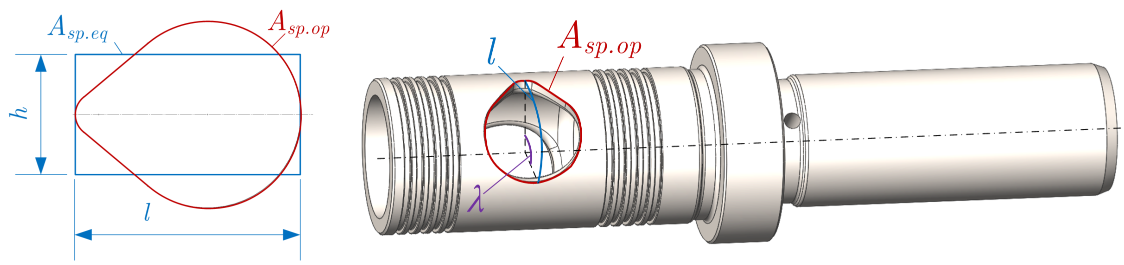

Figure 8.1: Spool single opening geometry.

$$A_{sp.op} = A_{sp.eq} = hl \tag{8.8}$$

$$h = \frac{A_{sp.op}}{l} = \frac{180° A_{sp.op}}{\pi \lambda r_2} \tag{8.9}$$

Then, after inserting the Equation 8.9 into the Equation 8.6 the total volume of tubular fluid elements becomes

$$V_{fl} = 2\left(r_2^2 - r_1^2\right) \frac{A_{sp.op}}{r_2}. \tag{8.10}$$

Finally, inserting equations 8.4, 8.5 and 8.10 into 8.3 yields a function of the inertial transient flow torque in the considered valve on the spool angular acceleration:

$$T_{tr.fl.} = \frac{\left(r_2^4 - r_1^4\right) A_{sp.op} \rho}{r_2} \frac{d\omega}{dt}. \tag{8.11}$$

The area of the single spool opening for the case of drop-shaped orifice is $A_{sp.op} = 123.86\,\mathrm{mm}^2$.

Friction Model

The applied friction model should provide a satisfactory trade-off between accuracy and an ability to be implemented. The accuracy requirement implies that essential frictional phenomena of the pre-sliding elastic displacement, the frictional lag, or hysteresis, and the "stick-slip" effect should be addressed and captured in the chosen model.

Based on numerous comparison studies of recently suggested friction models (Armstrong-Helouvry et al. 1994), (Olsson et al. 1998), (Marques et al. 2016), (Garcia 2008), (Piatkowski 2014), (Khan et al. 2017), the dynamic LuGre model (de Wit et al. 1995), (Johanastrom and de Wit 2008) was selected as it provides a reasonable compromise between model complexity influencing on computational time needed to implement the model and accuracy of friction behaviour modelling or completeness of phenomena included in the model. It has been also proved to be suitable for a state-space approach in dynamic analysis (Owen and Croft 2003).

The applied LuGre model originates from an elastic bristle model (Haessig and Friedland 1991) that uses the average deflection of the asperities on two contacting surfaces z as the key parameter modelled by

$$\frac{dz}{dt} = \omega - \frac{\sigma_0 \left|\omega\right|}{g\left(\omega\right)} z. \tag{8.12}$$

Since the considered design deals with rotation as the main type of motion, all terms in the LuGre model need to be angular. Thus, in the previous formula, ω is the relative angular velocity between the two rubbing surfaces, σ_0 – bristle stiffness, that is a function of the normal force (Altpeter 1999) or a function of the fluid working pressure and pre-squeeze after assembly, $g(\omega)$ – the velocity dependent function describing Coulomb friction and the Stribeck effect as following

$$g\left(\omega\right) = T_C + \left(T_S - T_C\right) e^{-\left(\frac{\omega}{\omega_S}\right)^2}. \tag{8.13}$$

The LuGre model completes the description of a total friction force generated due to bending of bristles and a relative motion with several additional coefficients: a bristle damping coefficient σ_1, a viscous friction coefficient σ_2, the Stribeck characteristic velocity ω_S, the level of stiction or static friction torque T_S and the level of Coulomb friction torque T_C:

$$T_{fr} = \sigma_0 z + \sigma_1 \frac{dz}{dt} + \sigma_2 \omega. \tag{8.14}$$

In the steady state of motion, i.e. when ω and z are constant, the friction torque takes the following form.

$$T_{fr.s} = \mathrm{sign}\left(\omega\right)\left(T_C + \left(T_S - T_C\right) e^{-\left(\frac{\omega}{\omega_S}\right)^2}\right) + \sigma_2 \omega \tag{8.15}$$

In order to achieve continuity of the model and its derivatives, the smooth hyperbolic tangent approximation of the sign function used (Kayihan and Doyle 2000):

$$T_{fr.s} = \tanh\left(\omega\right)\left(T_C + \left(T_S - T_C\right) e^{-\left(\frac{\omega}{\omega_S}\right)^2}\right) + \sigma_2 \omega \tag{8.16}$$

Viscous Friction

The viscous friction torque $T_{fr.v}$ is incorporated in the LuGre model in the third term of the equation 8.14.

$$T_{fr.v} = \sigma_2 \omega \tag{8.17}$$

Assuming the spool and the sleeve are concentric parts with a small radial clearance $c = 0.1\,\mathrm{mm}$ between them, the viscous friction torque $T_{fr.v}$ acting on the spool from the annular liquid volume at motion can be considered as laminar Couette flow and calculated according to the Newton's law of viscosity:

$$T_{fr.v} = \tau A_{sp} r_2 = \frac{\mu r_2^2 A_{sp} \omega}{c}. \tag{8.18}$$

Here τ is shear stress, μ – the fluid dynamic viscosity coefficient, A_{sp} – the total area of the spool external cylinder subjected to the shear stress in the annual gap with a clearance c, defined by 3.13.

The viscous shear stress τ acts on the spool cylindrical surfaces in the annular gap with the clearance c. The spool external cylinder houses two sets of balancing grooves that prevent formation of a hydraulic lock and centre the spool concentrically inside the sleeve (Merritt 1968), as well as two throttling orifices. These regions do not contribute to the viscous friction torque $T_{fr.v}$ on the spool since the radial distance from the spool to the sleeve there is not equal to the clearance c. Thus, the total area of interest is

$$A_{sp} = 2\pi r_2 \left(L - nw\right) - 2A_{sp.op}. \tag{8.19}$$

This expression includes the length of the spool located inside the sleeve L; n, w are the total number and the width of the balancing grooves respectively.

In terms of the LuGre friction model, the viscous friction coefficient becomes

$$\sigma_2 = \frac{2\mu r_2^2 \left(\pi r_2 \left(L - nw\right) - A_{sp.op}\right)}{c}. \tag{8.20}$$

Dry Friction

The solid-to-solid sliding Coulomb friction, in the case of the considered valve design, takes place between the spool and elastomer O-ring seals and back-up rings. Sealing between moving mechanical parts is ensured by squeezed elastomer and plastic back-up rings during assembly. This squeeze produces the drag dry friction torque from a elastomer ring on the sealant mechanical part (Al-Ghathian et al. 2005).

To quantify parameters of the friction model, i.e. the Coulomb and static friction torques, one needs to consider every source of static friction. As for the rotary valve we study, static friction acting on the spool is a sum of friction forces generated from every O-ring and back-up ring contacting with the spool.

In the applied method of estimation, the dry friction torque from sealing, running friction is evaluated via Stribeck diagrams used for an oil pressure up to 16 MPa and O-rings design of sealing. The break-out friction is derived then from the running one.

The Coulomb (or running) friction torque T_C is defined through stabilized (running) friction force F_C, which depends on the friction coefficient μ_w and the normal force F_t generated by the squeezed sealing ring after assembly compression and application of oil pressure on it (Bisztray-Balku 1995).

$$T_C = F_C R_{sp} = \mu_w F_t R_{sp} \tag{8.21}$$

In this expression R_{sp} is a spool shaft radius, on which the contact between the spool and the sealing ring takes place. In the design of the considered valve, all seals are of rod type, i.e. sealing rings are housed in parts surrounding the spool.

The normal force (expected friction force at the middle of the spool stroke) may be determined as following:

$$F_t = 2\pi R_{sp} b p_w, \tag{8.22}$$

where p_w is working, operating pressure, which can be considered for high-pressure hydraulic applications equal to pressure difference between chambers separated by the sealing ring and b is the total compressed seal width.

For O-rings, the seal width b_o is approximated through its cross-section diameter d_2:

$$b_o = \sqrt{\frac{\pi d_2^2}{4}}$$

The back-up ring seal width is the same as the ring's width b_b (Bisztray-Balku 1995) as its compression is negligible comparing to rubber seal's one. Thus, the total seal width is $b = b_o + b_b$.

In case of application of O-rings with PTFE back-up rings in high-pressure and low-speed conditions, the friction coefficient becomes mostly dependent on the working pressure. Taking the operating pressure p_w equal to 20 MPa, the friction coefficient is $\mu_w = \mu_{20} = 2.7 \cdot 10^{-2}$.

The static friction can be considered proportional to the Coulomb friction force F_C with proportionality coefficient c, which represents the friction force hysteresis when the motion direction changes. The value of the change coefficient is taken equal to $c = 1.2$ at the relative linear velocity is in range from 0.05 m/s to 0.3 m/s, i.e. $F_S = cF_C = 1.2F_C$.

Appendix E. Data Analysis Code

```
%% Load data
addpath('C:\Users\iokhotnikov\Thesis\matlab\data');
run auxiliary.m
run geometry.m
run fuel_consumption.m
run im_studies.m
run oil_model.m
run area_measurements.m
run grids.m
run cfd_results.m
run exp_results.m
%% Calculations of alpha(phi), deg; Cd(phi); theor Q(p), lpm; Q(phi), lpm; Re
%Hydraulic diameter, mm^2
Dh=4*area25./s;
for ii=1:3
   ja1(ii,:)=radtodeg(asin(((sft1(ii,:)/r2).*(area5*10^(-6))/2)./(rho(8)*(q_ang_cfd(ii,:)/120000).^2)));
   ja2(ii,:)=radtodeg(asin(((sft2(ii,:)/r2).*(area5*10^(-6))/2)./(rho(8)*(q_ang_cfd(ii,:)/120000).^2)));
   cdsim(ii,:)=(q_ang_cfd(ii,:)./(area5*10^(-6)))*(1/60000)*sqrt(rho(8)/(2*(0.5)^(ii-1)*10^6));
   q_p_th(ii,:)=cdsim(1,(23-6*ii))*area5(23-6*ii)*10^(-6)*sqrt((2*dp1*10^6)/rho(8))*60000;
   q_ang_th(ii,:)=0.62*area5*10^(-6)*sqrt(2*(0.5)^(ii-1)*10^(6)/rho(8))*60000;
   Re(ii,:)=q_ang_cfd(ii,:).*(Dh(3:2:end)*10^(-3))./(60*10^(3)*area5*10^(-6)*nucst(8)*10^(-6));
end
%% Cavitation number calculation
v=(q/60000)./(area5(17)*1e-6);
for ii=1:100
   for jj=1:100
      cav(ii,jj)=(pa(ii)*1e6-pv)./(0.5*rho(8)*v(jj).^2);
   end
end
%% Calculations of Q(phi, dp), lpm, and Tst.fl.(phi, dp), Nm, functions
for ii=1:17
   for jj=1:100
   qphidp(ii,jj)=cdsim(1,ii).*area5(ii)*1e-6*sqrt(2*dp(jj)*1e6/rho(8))*6e4;
   sftphidp(ii,jj)=cdsim(1,ii)^2*area5(ii)*1e-6*r2*dp(jj)*1e6*(sin(pi*ja1(1,ii)/180)+sin(pi*ja2(1,ii)/180));
   end
end
%% Power loss calculation, kW
[m, n]=size(ploss);
for ii=1:m
    for jj=1:n
    power(ii,jj)=ploss(ii,jj)*q25(jj)/60;
    end
 end
%% Leakage calculation
% Lengths calculations, m
L(:)=pi*r2*bg(:)/180;
L1=mean([L(1) L(3)]);
L2=mean([L(2) L(4)]);
% Leakage flow calculation, lpm
ql=(l_or*c^3*((1/L1)+(1/L2))/(6*mucp(8)*1e-3))*dpl*1e6*6e4;
% Error between the CFD and analytical results relative to the analytical.
for ii=1:10
er_l(ii)=abs(ql(ii*10)-qlcfd(ii+1))./ql(ii*10);
end
%% Correlation between experiment and modelling Relative to the experiment
%dp(Q) 90deg->50deg, 25LPM-175LPM
for ii=1:5
   er_exp_dp(ii,:)=abs(dpe(ii,:)-ploss(ii,[1:7]))./dpe(ii,:);
end
```

```
%Q(phi) 1MPa-0.25MPa, 30deg-90deg
for ii=1:3
   er_exp_cfd(ii,:)=abs((qe((ii+5),:)-q_ang_cfd(ii,[5 7 9 11 13 15 17]))./q_ang_cfd(ii,[5 7 9 11 13 15 17]);
end
%dp(Q)@90 deg new geometry
er_exp_sim(1,:)=(dpe(1,:)-ploss(1,1:7))./dpe(1,:);
er_exp_sim(2,:)=(dpe(1,:)-ploss_cfd_upd)./dpe(1,:);
%% Comparison with SJ-MRA
tec1_sim_dp=(dp_tec-ploss(1,1:6))./dp_tec;
tec2_sim_dp=(dp_tec-ploss2(7,1:6))./dp_tec;
power_tecnord=q25(1:6).*dp_tec/60;%kW 25LPM->150LPM
%% Effect of redesign 90deg->30deg, relative to the initial design
for ii=1:7
   er_ploss2(ii,:)=abs(ploss(ii,:)-ploss2((8-ii),:))./ploss(ii,:);
end
%% Default plotting settings
set(groot,'defaulttextinterpreter','latex');
set(groot,'defaultAxesTickLabelInterpreter','latex');
set(groot,'defaultLegendInterpreter','latex');
set(groot,'defaultLineLineWidth',1);
set(groot,'DefaultLineMarkerSize',4);
```

Appendix F. Published article

International Journal of Heat and Fluid Flow 64 (2017) 89–102

Contents lists available at ScienceDirect

International Journal of Heat and Fluid Flow

journal homepage: www.elsevier.com/locate/ijhff

Evaluation of steady flow torques and pressure losses in a rotary flow control valve by means of computational fluid dynamics

Ivan Okhotnikov[a,*], Siamak Noroozi[a], Philip Sewell[a], Philip Godfrey[b]

[a] Bournemouth University, Faculty of Science and Technology, BH12 5BB, United Kingdom
[b] Hydreco Hydraulics Limited, 32 Factory Road, Poole, Dorset, BH16 5SL, United Kingdom

A R T I C L E I N F O

Article history:
Received 4 July 2016
Revised 22 December 2016
Accepted 17 February 2017

Keywords:
Rotary flow control valve
Computational fluid dynamics
Pressure drop
Steady flow torques
Discharge coefficient
Jet angle

A B S T R A C T

In this paper, a novel design of a rotary hydraulic flow control valve has been presented for high flow rate fluid power systems. High flow rates in these systems account for substantial flow forces acting on the throttling elements of the valves and cause the application of mechanically sophisticated multi-staged servo valves for flow regulation. The suggested design enables utilisation of single-stage valves in power hydraulics operating at high flow rates regimes. A spool driver and auxiliary mechanisms of the proposed valve design were discussed and selection criteria were suggested. Analytical expressions for metering characteristics as well as steady flow torques have been derived. Computational fluid dynamics (CFD) analysis of steady state flow regimes was conducted to evaluate the hydraulic behaviour of the proposed valve. This study represents a special case of an independent metering concept applied to the design of power hydraulic systems with direct proportional valve control operating at flow rates above 150 litres per minute. The result gained using parametric CFD simulations predicted the induced torque and the pressure drops due to a steady flow. Magnitudes of these values prove that by minimising the number of spool's mobile metering surfaces it is possible to reduce the flow-generated forces in the new generation of hydraulic valves proposed in this study. Calculation of the flow jet angles was analytically verified by measuring the deflection of the velocity vector using flow velocity field distribution, obtained during visualisation of the results of CFD simulations. The derived calculation formulas can predict metering characteristics, values of steady flow torques and jet angles for the specified design and geometry of the suggested valve. The proposed novel structure of the flow control valve promises to attain improved controllability, reliability and efficiency of the hydraulic control units of heavy mobile machinery operating at high flow rates regimes.

1. Introduction

Fluid power systems are a major element in the design and development of all heavy off road, earthmoving, agricultural and construction machinery. Their contribution to the overall performance of such machines is hard to overestimate. These industrial applications require hydraulics functioning at high-pressure and high-flow rates in order to operate multiple drives of a single mobile machine such as manipulator arms, wheels, crawlers, transmission and other appliances simultaneously. These large flow rates require a significant amount of energy to achieve and consequently result in a substantial loss of flow energy or pressure drops, which is quite common in such hydraulic systems (Merritt, 1968). These losses are usually due to viscous friction, swirls formation, sudden changes in flow direction and cross-section (Lisowski and Rajda, 2013). Large flow rates also account for considerable flow forces acting on the regulating elements of the control valves (Rajda and Lisowski, 2013).

In order to overcome these large resisting forces, an indirect pilot hydraulic actuation of the main sliding spool is employed. In this solution, the design of flow control valves lacks mechanical reliability due to the introduction of an additional hydraulic stage, what causes immense pressure losses, poor energy efficiency and rigorous requirements to the level of oil contamination due to sophisticated and narrow internal channelling (Filho and De Negri, 2013). Furthermore, production of such valves demands high-precision manufacturing processes. That increases the overall cost of these flow control units. Manual assembly of torque motor driven two-stage valves and their adjustment also motivates investigations of alternative technologies (Plummer, 2016).

* Corresponding author at: Department of Design and Engineering, Faculty of Science and Technology, Bournemouth University, Poole House, Talbot Campus, Fern Barrow, Poole, Dorset, BH12 5BB, United Kingdom.

E-mail addresses: iokhotnikov@bournemouth.ac.uk (I. Okhotnikov), snoroozi@bournemouth.ac.uk (S. Noroozi), psewell@bournemouth.ac.uk (P. Sewell), pgodfrey@hydreco.com (P. Godfrey).

http://dx.doi.org/10.1016/j.ijheatfluidflow.2017.02.005
0142-727X/

Nomenclature

Latin symbols

$A(\varphi)$	Function of the opening area, m^2
A_v	Van Driest coefficient
$C_{\varepsilon1}, C_{\varepsilon2}, C_\mu$, C_B	Constant empirical closure coefficients in the $k-\varepsilon$ turbulence model
C_d	Discharge coefficient
C_v	Velocity coefficient
F_{fl}	Steady flow force, N
f_μ	Turbulent viscosity factor
f_1, f_2	Lam and Bremhorst's damping functions
g_i	The component of gravitational acceleration in direction of i, m/s^2
K	Karman constant
k	Turbulent kinetic energy, m^2/s^2
$\dot{m}$	Fluid mass flow rate, kg/s
P_B	Buoyancy-generated turbulence production term in the $k-\varepsilon$ turbulence model, $1/s^2$
Δp	Pressure differential, Pa
Q	Volume flow rate, litres/minute
R_y, R_T	Turbulent Reynolds numbers
$R_{sl.ext}$	Sleeve external diameter, m
$R_{sp.ext}, R_{sp.in}$	Spool external and internal diameters respectively, m
T_{fl}	Steady state flow torque, N·m
t	Time, s
u_i	The ith component of the fluid velocity, m/s
u^+	Dimensionless longitudinal wall velocity
v_1, v_2	Average inlet and outlet velocities of a control volume respectively, m/s
x_i	The ith component of the Cartesian coordinate system
y^+	Dimensionless distance from wall surface

Greek symbols

α	Angle, occupied by the spool window in the outflow section, °
β	Angle, occupied by the sleeve window in the outflow section, °
γ	Backlash angle, °
δ_{ij}	The ijth component of the Kronecker delta function
ε	Turbulent dissipation rate, m^2/s^2
η	General variable
θ	Jet angle, °
μ	Dynamic viscosity coefficient, kg/(m·s)
μ_t	Turbulent eddy viscosity coefficient, kg/(m·s)
ρ	Fluid density, kg/m^3
$\sigma_\epsilon, \sigma_k, \sigma_B$	Constant empirical closure coefficients in the $k-\varepsilon$ turbulence model
τ_w	Wall shear stress, Pa
τ_{ij}^R	The ijth component of the Reynolds-stress tensor, Pa
φ	Spool angular position, °

Subscripts and superscripts

fl	Steady state flow
fl.tan	Tangential component of the flow force
i, j, k	Directions of the Cartesian coordinate system
w	At the wall
single	Single orifice parameter
total	Entire valve parameter

Abbreviations

+	Dimensionless wall parameter
CFD	Computational fluid dynamics
DC	Direct current
LPM	Litres per minute

One way to reduce losses in such valves is to optimise the flow paths through them in order to lessen flow disturbances (Simic and Herakovic, 2015). One promising method to enhance the valve's performance in terms of losses, flow disturbance reduction, and simplification of the valve geometry for manufacture is to utilise specially profiled sliding spools with special geometrical features. A number of studies have shown the positive impact of sleek spool geometry, especially smooth change of diametrical sizes of a spool along its length, on the fluid's rate of momentum change, hence reducing the flow forces experienced by the spool's driver. The introduction of a compensation profile on the sliding spool's shaft diminishes the flow forces by creating a pressure drop in the downstream cavity (Amirante et al., 2007). It was proven experimentally, that geometrical optimisation of central conical surfaces on the spool shank can provide higher axial velocities at the inlet of the meter-in chamber and the outlet of the meter-out chamber of the spool, which alleviates a net flow force, and lowers dynamic overshoot in step response (Amirante et al., 2016). Cone surfaces on the spool's control edges and returning oil jet back in spool's cavity on the meter-out edges enables application of direct actuation of the spool for larger nominal valve sizes (Herakovič, 2009).

Adding a supplementary parallel channel to the return line in the valve's body allows extension of the valve's operational flow range by improving the carrying capacity or conductivity of the drain line without resorting to more powerful solenoids (Lisowski et al., 2013). The geometrical optimisation of flow regulating parts has a notable effect on flow forces in seat valves as well (Simic and Herakovic, 2015).

Other viable ways to lessen the effect of flow forces are improvement of electromagnetic actuator's performance (Reichert, 2010), advanced regulation of spring rates of the return mechanism and geometrical optimisation of the spool's ambient parts and channels, inlet and outlet spool chambers (Abdalla et al., 2011) to make them less prone to formation of eddies, vortices and flow disturbances.

Advanced architectural approaches to design and control high-flow rate hydraulic systems are demonstrated in concepts of independent metering (Shenouda, 2006; Choi et al., 2015) and digital hydraulics (Linjama, 2011). The former utilises separate control of flows into and from actuator's chambers. The latter consists in incremental modulation of the flows in hydraulic lines by switching on and off individual valves connected in a parallel layout. Generally, these concepts rely on two-way valve setups. These two new concepts have had limited application due to the low flow rates used to date. Nevertheless, these concepts need further advancement in order to be effectively implemented within high flow rate systems as these approaches are considered promising in performance improvement of current hydraulic systems.

Despite the vast number of design studies all looking to minimise the flow forces and static pressure losses, the application of conceptually alternative construction of throttling elements and their arrangements are still rare in current literature. The use of valves with rotary spools to solve the problems associated with large flow forces that exist in high flow rate regimes has been studied (Yu et al., 2014, 2015; Yang et al., 2010; Wang et al., 2016). Unlike conventional designs, a rotating spool configuration creates a much smaller net area of surfaces subjected to the flow forces. So far, employment of rotary spools industrially is restricted to manually driven on-off valves, flow dividers, and automotive steering valves.

However, there are alternative proposals to utilise rotary valves. In a study of a three-way electronically driven hydraulic rotary valve, a detailed mathematical model of a DC-driven spool was presented (Yang et al., 2010). In the research of direct drive servo valves a single, axisymmetric spool works on a similar principle as a 4/3 directional valve. It modulates proportionally and simultaneously flow areas of both meter-in and meter-out hydraulic lines of an actuator (Yu et al., 2014, 2015). Spool shoulders contain several axially oriented grooves overlapping with corresponding holes on the static bush. In these structures, the single spool incorporates several fluid paths in it. That makes the structure of the spool larger for the same volume flow rate application and generates tangible pressure drops of the whole valve. A similar approach to the spool design was described in the analysis of a rotary directional control valve driven by a servo motor (Wang et al., 2016).

The introduction of switched inertia hydraulic systems provokes numerous studies of rotary fast-switching valves since the rotary arrangement of spools provide faster and less resistant shift between open and closed states. This concept is analogous with an electric buck converter and inherent fluid inertia in hydraulic tubes and hoses to control supply pressure and flow to a hydraulic motor (Pan et al., 2013). Experimental studies of switched inertia suggest fast switching can cause noise and cavitation problems (Pan et al., 2015; Johnston and Pan, 2015).

The above-mentioned studies comprise detailed computational fluid dynamics (CFD) and experimental analyses of driving torques of spools at flow rates not exceeding 150 litres per minute (LPM). For noted design solutions, the formation of lateral or radial forces on the spool causing flexion and jamming of the spool inside the bush seems to be a common potential problem.

Minimisation of the mobile surfaces subjected to the flow forces as an approach to overcome flow forces was used in the research of an axial flow valve with rotational metering (Ansaloni et al., 2008). The proportional two-way, two-position valve in this study has an in-line setup of regulating parts. The valve design implies inbuilt hydraulic control of the rotor's angle by means of the reducer ring sliding along helical grooves in a gap between the stator and the rotor. This design might pose problems of rotor blocking and internal leakages.

There is a proposal in the study of the three-way pulse-width-modulated directional valve to harvest the fluid flow energy by embedded turbines in order to establish the spool's translational and rotary positions (Tu et al., 2012) and eventually modulate its duty ratio (Wang and Li, 2009). This design features a self-spinning turbine with rhombic slots forming throttling orifices (Wang et al., 2010; Tu et al., 2007; Rannow et al., 2010) and finds application in virtually variable displacement pump/motors (Tu et al., 2011).

In the current research, the emphasis was placed on the actual geometrical design of the valve's throttling elements. The aim is, by better design, to ensure slow, gradual opening/closing of the valve and flow variation to enable smoother operation and improve reliability due to simpler construction. The latter would greatly simplify manufacture and reduce the cost of these devices in the longer term. This paper both proposes and presents a new design of rotary valve and its simulated performance. The authors believe that this design is significantly different in many respects to all existing rotary valves especially in the details of the spool-sleeve assembly design.

Current research aims to develop further the concept of reduction of flow forces in high flow rate applications through the implementation of the novel design of the throttling orifice. The main impetus for this research is the detailed design investigation of a structure of the spool-sleeve assembly in order to minimise the number of spool's surfaces exposed to the flow forces and the implementation of direct control of spool position.

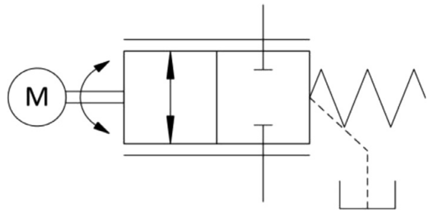

Fig. 1. Graphical, schematic representation of the developed valve.

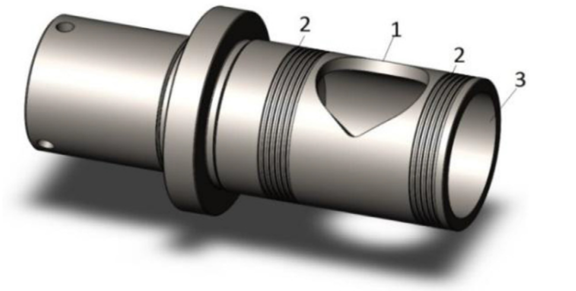

Fig. 2. The spool of the rotary control valve: 1 – orifice opening, 2 – anti-silting grooves, 3 – flow entrance to the spool's chamber from the oil supply channel.

This study also attempts to advance the innovative concept of independent metering structurally. The research presents a strong case for that architectural approach to be the most suitable valve system in the high flow rate domain of power hydraulics. The paper addresses one of the biggest challenges in the design of fluid power systems, namely the size or compactness and weight of the components (Yang and Pan, 2015), which influences energy efficiency and the work cycle of mobile machines carrying power hydraulics, especially operating at high flow rates operational regimes.

2. Proposed valve design

The design of the developed flow control unit represents a normally closed two-position, two-way flow control valve with direct electromagnetic proportional control of the regulating spool, with a non-variable spring return mechanism to the valve's closed state. Applying terms and symbols of BS ISO 1219-1:2012, the graphical symbol for the valve was drawn, Fig. 1. All key parts are housed in a valve's casing. It supplies working fluid to the spool, collects and directs oil to the hydraulic actuator via built-in channels after throttling orifices. The valve design implies a cartridge assembly method allowing multi-valve arrangement in a single body given enough valve socket ports and matching internal channelling. Manufacturers usually favour such assembly method because such valves are easy and fast to manufacture, repair, maintain or replace in the event of a mechanical failure.

In this new proposed valve's structure, liquid enters the hollow cylindrical spool's central cavity through the end face opening from the supply channel, Fig. 2. Then it outflows from two specially profiled cut-outs on the outer surface of the spool's cylinder and passes through the sleeve windows to the collecting chamber of the valve body. The flow rate is regulated by the opening area, which is formed by the overlap between the slots of the spool and the sleeve. The orifice area is also a function of each window profile. Consequently, the angular position of the spool in the sleeve defines the output oil's flow rate.

In order to minimise and compensate the reactive lateral, radially directed, flow forces, which might lead to flexion and jamming of the cantilevered spool inside the sleeve, two slots are located on diametrically opposite sides of the spool's cylindrical surface.

Such a symmetrical pattern also increases the strength of the spool by reducing the mechanical stress in the material of the part, compared to a case with a single larger orifice or multiple smaller cut-outs. The suggested spool works under torsion conditions from a steady flow torque. Its throttling cross-section in a double-orifice arrangement has higher polar, or second, moment of inertia than a single orifice design with the same throttling opening area. Additionally, a two slot configuration halves the total discharge passing through the single orifice which in turn amplifies the valve's conductance and lowers pressure drop across the valve.

The spool also incorporates two sets of circumferential grooves cut on both sides of the throttling holes. The purpose of the grooves is to lower coulomb friction in the spool-sleeve assembly and prevent silting of the spool inside the sleeve due to the small radial clearance between those parts (Merritt, 1968). The grooves also play a role of labyrinth sealing, which prevents leakages to spool bearing housing and flow over to the supply channel.

The profile of the sleeve's throttling holes is identical in shape to the spool's windows, but the openings on the spool and the sleeve are pointed towards each other, Fig. 3. In the current study, drop-shaped windows are used on both the spool and the sleeve. This allows a very smooth increase of the opening area when throttling begins. In turn, this ability provides the smooth start of actuation, as well as accurate velocity control of a hydraulic motor.

Location of the throttling windows on the cylindrical surfaces makes it easier to cut complex opening profiles what improves manufacturability of the flow regulating parts. The combination of the windows' shapes, nonlinear nature of the total opening area, the stroke angle and the rate of spool rotation makes the developed orifices' arrangement unique in its class. Mentioned features and flow regulation potential are currently unobtainable by any ordinary linear sliding spools. The needed flow rate can be achieved in this valve through the realisation of a specific value of the opening area, which depends on the input control signal.

The flow regulation is attained by turning the spool to a preset angle. The spool is controlled by a rotary electric motor. The spool angular position corresponds to a finite value of the opening area that can be calculated and established in accordance with the required metering characteristics by a controller. In this proposed new design solution, the rotational movement of the spool is accomplished via a stepper motor.

The electromechanical motor has to ensure accurate positioning of the spool. It also has to maintain a specified angle even in the presence of significant disturbing fluctuating torques originated from fluid flow, inertia torques in rotary transmission and both mechanical and viscous friction factors. Furthermore, it has to transmit the input signal quickly and with minimal deviations from the intended values. The complex, mutable and unsteady nature of the controlled medium favours application of stepper motors with a high holding torque. Other requirements for the spool driver is its ability to withstand a high holding torque providing short settling time during state switch.

To be able to maintain the exact angular position of the spool at the steady flow regime, the driver holding torque must exceed the torques induced by the flow, viscous friction torque in the spool cavity and in the annular gap between the spool and the sleeve as well as the spring torque turning the spool into the initial, closed position. For that reason, the *holding torque* is the main characteristic affecting selection of the stepper motor. Its detent torque determines operability of the stepper motor in the inactivated state, which corresponds to the closed state of the valve.

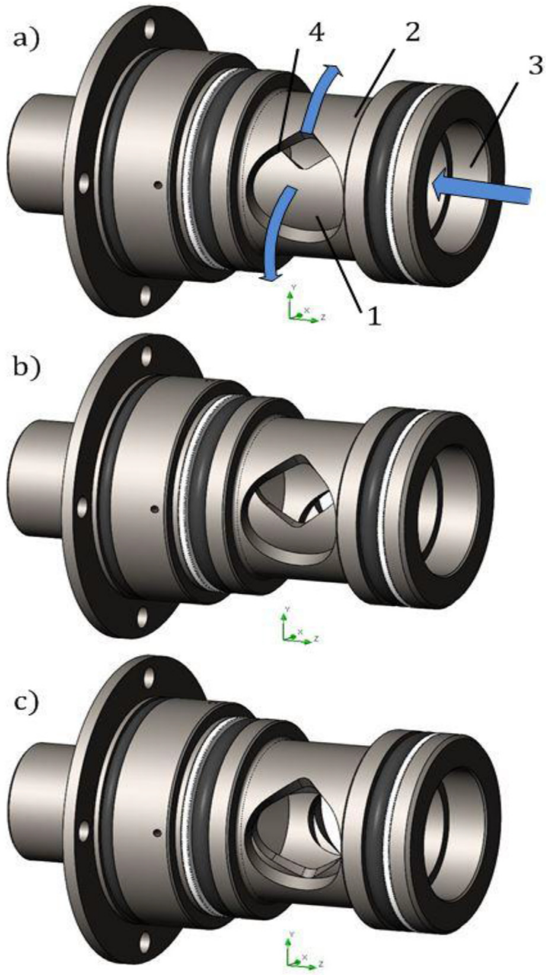

Fig. 3. The spool-sleeve assembly and the gradual increase in overlap between the parts: (a) spool angular position is $\varphi = 30°$, 1 – the spool, 2 – the sleeve assembly, 3 – inlet to the spool's cavity (connection to the flow supply port), 4 – outlet from the valve's cavity (connection to the service port). Blue arrows indicate directions of the fluid paths inside the spool-sleeve assembly; (b) intermediate position $\varphi = 60°$; (c) fully open state, $\varphi = 90°$.

In conventional valves, the spool's return to a neutral state is performed with compression centring springs. This is to assure, that in the absence of an input signal on the spool actuator or its failure the spool closes all hydraulic ports of the valve. That will guarantee there is no flow between them during the no-control condition.

Thus, the spring fulfils a safety function. In the rotary valve, a torsion spring is used for the same purpose. Selection of the torsion spring is based on maximum torque needed at the extreme angular positions. The spring must possess enough stiffness in order to generate a return elastic torque and be able to surmount the torques originated from oil flow, viscous and coulomb friction between contacting parts, and eventually close the valve.

Among the listed torque disturbances acting on the spool, steady flow torque is considered as the most prominent. In force terms, for sliding spools steady flow force prevails over the rest force factors and affects the selection of the spool driver mechanism and its control method.

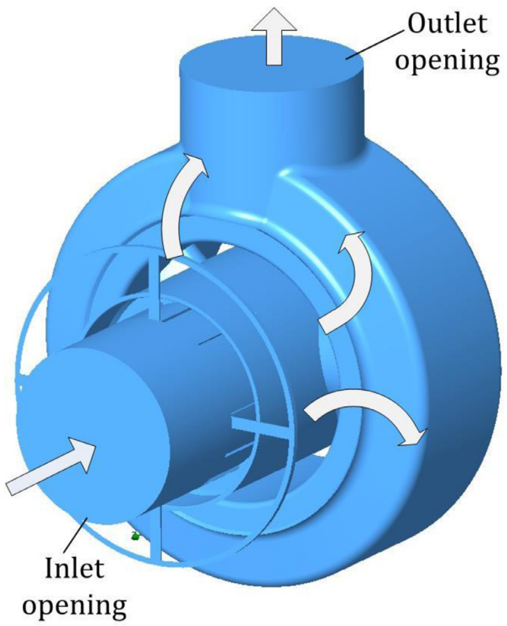

Fig. 4. Fluid subdomain, fluid flow direction. White arrows are fluid flow directions in the fluid subdomain.

3. CFD simulation

In this study parametric CFD analysis of the developed hydraulic valve is used since this method makes it possible to obtain performance characteristics of the valve theoretically and optimise them before prototype production and experimental investigation. The purpose of the CFD in this study is to establish the performance of the proposed valve design by computing metering characteristics and steady flow torques in a modelled environment.

In the case of the control valves study, the properties of interest are pressure drop imposed to the hydraulic system by the considered valve and magnitude of steady flow torques acting on the rotary spool at steady-state regimes. The latter eventually is sensed by the spool driver and affects selection criteria of the spool motor. In order to estimate these values a series of parametric simulations have been conducted. Visualisation capabilities of CFD packages help to establish fluid flow behaviour for the novel design with the original geometry of internal channels and chambers, define areas of further geometrical improvement.

According to the preceding description of the design concept, a detailed three-dimensional solid geometrical model of the valve was constructed using the SolidWorks software suite by Dassault Systems SolidWorks Corp., Waltham, Massachusetts, USA. A full three-dimensional flow model was utilised, rather than the simplified fluid subdomain to study a planar case of the orifice flow or axis-symmetrical flow model. This approach eliminates all the assumption made in the 2d flow analysis such as uniformity of the flow paths in any adjacent planes without compromising calculation accuracy (Amirante et al., 2014).

Parametric CFD analyses have been conducted in the Flow Simulation module of SolidWorks software. Based on the depicted novel valve's geometrical model, the internal regions occupied by the oil, which is the fluid subdomain, are modelled showing the flow paths throughout the domain as seen in, Fig. 4. CFD simulations allow the visualisation of the changing flow paths corresponding to different spool's angular positions while maintaining the same overall fluid subdomain intact. At any angular position of the spool, a new fluid subdomain is extracted from the geometrical solid model altering just in the orifice area of the valve.

3.1. Turbulence model

Taking into account expected application of the developed valve, that is high pressures and high flow rates, the fluid flow inside the valve is considered as turbulent. In the Flow Simulation module, the Favre-averaged Navier–Stokes equations are used, where time-averaged effects of the flow turbulence on the flow parameters are considered. To close this system of equations, transport equations for the turbulent kinetic energy and its dissipation rate is employed, the so-called $k-\varepsilon$ model (SolidWorks, 2015). The adopted model meets accuracy and reliability requirements in the considered valve study and performs satisfactorily in solving fluid power problems (Palumbo et al., 1996).

In SolidWorks Flow Simulation the classical two-equation $k-\varepsilon$ empirical model for simulating turbulence effects in fluid flow CFD simulation (Wilcox, 2006) is used as it requires the minimum amount of additional information to calculate the flow (SolidWorks, 2013a). The modified $k-\varepsilon$ turbulence model with damping functions (Lam and Bremhorst, 1981) describes laminar, turbulent, and transitional flows of homogeneous fluids consisting of the following turbulence conservation laws (Sobachkin and Dumnov, 2013):

$$\frac{\partial \rho k}{\partial t}+\frac{\partial \rho k u_i}{\partial x_i}=\frac{\partial}{\partial x_i}\left(\left(\mu+\frac{\mu_t}{\sigma_k}\right)\frac{\partial k}{\partial x_i}\right)+\tau_{ij}^{R}\frac{\partial u_i}{\partial x_j}-\rho\varepsilon+\mu_t P_B, \tag{1}$$

$$\frac{\partial \rho \varepsilon}{\partial t}+\frac{\partial \rho \varepsilon u_i}{\partial x_i}=\frac{\partial}{\partial x_i}\left(\left(\mu+\frac{\mu_t}{\sigma_\varepsilon}\right)\frac{\partial \varepsilon}{\partial x_i}\right)+C_{\varepsilon 1}\frac{\varepsilon}{k}\left(f_1\tau_{ij}^{R}\frac{\partial u_i}{\partial x_j}+C_B\mu_t P_B\right)-f_2 C_{\varepsilon 2}\frac{\rho\varepsilon^2}{k}. \tag{2}$$

Here P_B represents the turbulent generation due to buoyancy forces and can be written as

$$P_B=-\frac{g_i}{\sigma_B}\frac{1}{\rho}\frac{\partial\rho}{\partial x_i}. \tag{3}$$

where g_i is the component of gravitational acceleration in direction of x_i. The empirical $k-\varepsilon$ constants have the following typical values (SolidWorks, 2015): $\sigma_k=1$, $\sigma_B=0.9$, $\sigma_\varepsilon=1.3$, $C_\mu=0.09$, $C_{\varepsilon 1}=1.44$, $C_{\varepsilon 2}=1.92$ and constant $C_B=1$ if $P_B>0$, and 0 otherwise.

Following Boussinesq assumption, the Reynolds-stress tensor for Newtonian fluids has the following form:

$$\tau_{ij}^{R}=\mu\left(\frac{\partial u_i}{\partial x_j}+\frac{\partial u_j}{\partial x_i}-\frac{2}{3}\delta_{ij}\frac{\partial u_k}{\partial x_k}\right)-\frac{2}{3}\delta_{ij}\rho k. \tag{4}$$

Here δ_{ij} is the Kronecker delta function (it is equal to unity when $i=j$, and zero otherwise), μ is the dynamic viscosity coefficient, k is the turbulent kinetic energy and μ_t is the turbulent eddy viscosity coefficient, which is determined from

$$\mu_t=f_\mu\frac{C_\mu\rho k^2}{\varepsilon}. \tag{5}$$

Here f_μ is a turbulent viscosity factor. It is defined by the expression

$$f_\mu=\left(1-e^{-0.0165R_y}\right)^2\cdot\left(1+\frac{20.5}{R_T}\right), \tag{6}$$

$$R_y=\frac{\rho\sqrt{k}y}{\mu}, \tag{7}$$

$$R_T = \frac{\rho k^2}{\mu \varepsilon}. \quad (8)$$

The distance from the point to the wall is y and Lam and Bremhorst's damping functions are determined from

$$f_1 = 1 + \left(\frac{0.05}{f_\mu}\right)^3, \quad (9)$$

$$f_2 = 1 - e^{-R_T^2} \quad (10)$$

Lam and Bremhorst's damping functions $f_\mu f_1 f_2$ decrease turbulent viscosity and turbulence energy and increase the turbulence dissipation rate when the Reynolds number R_y based on the average velocity of fluctuations and distance from the wall becomes too small. When $f_\mu = 1,\ f_1 = 1,\ f_2 = 1$ the approach obtains the original $k - \varepsilon$ model.

To simulate fluid boundary layer effects near solid bodies, solve the Navier–Stokes equations with a two-equation $k - \varepsilon$ turbulence model and evaluate skin friction in these regions a "wall function" approach (Launder and Spalding, 1974) is utilized in the Flow Simulation module. But SolidWorks Flow Simulation employs Van Driest's profiles (Driest, 1956) instead of a logarithmic profile. Additionally, a "two-scale wall functions" approach to describe a turbulent boundary layer and fit a fluid's boundary layer profile relative to the main flow's properties is employed (SolidWorks, 2013a).

When the number of cells across the boundary layer is sufficient (more than ~10) the simulation of laminar boundary layers is done via Navier–Stokes equations as part of the core flow calculation. For turbulent boundary layers proceeding from the Van Driest mixing length (Driest, 1956) SolidWorks Flow Simulations uses following dependency of the dimensionless longitudinal velocity u^+ on the dimensionless wall distance y^+ (SolidWorks, 2013a)

$$u^+ = \frac{u}{\sqrt{\frac{\tau_w}{\rho}}} = \int_0^{y^+} \frac{2d\eta}{1 + \sqrt{1 + 4K^2\eta^2\left(1 - e^{-\frac{\eta}{A_v}}\right)^2}} \quad (11)$$

Here $K = 0.4504$ is the Karman constant and the Van Driest coefficient is $A_v = 26$.

3.2. Mesh generation

Before processing, a mesh or a grid of the fluid subdomain needs to be built. The Flow Simulations module enables splitting the fluid domain into cells with adjustable resolution. Then, flow governing partial differential equations, that are the Navier–Stokes and transport equations, are solved in knots, in centres of the cells of the mesh.

The Flow Simulation solves the governing equations with a discrete numerical technique based on the finite volume discretization method as it satisfies requirements of conservation nature of the governing differential equations. The mesh cells are rectangular parallelepipeds with faces orthogonal to the specified axes of the Cartesian coordinate system. The near-boundary cells are portions of the original parallelepiped cells that are cut by the solid matter geometry boundary. Thus, the resulting near-boundary cells are polyhedrons with both axis-oriented and arbitrary oriented plane faces, partial cells. All physical and inertial parameters are referred to the mass centres of the cells within the control volume (SolidWorks, 2015). The module uses the immersed body meshing approach and yields the structured and ununiformed Cartesian mesh with an irregular distribution of mesh nodes, which results in the much faster calculation of mesh-based information required by the solver, as well as speeds up the search for data associated with neighbour cells. The Cartesian-based approach has been shown to deliver the lowest local truncation error when the

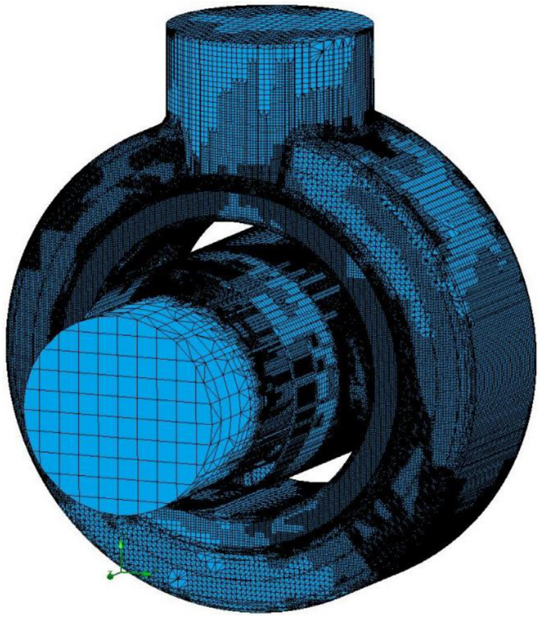

Fig. 5. Mesh of the fluid subdomain with approximately two million fluid cells.

Navier–Stokes equations are discretized onto the mesh, simplify navigations on the mesh, ensure robustness of the differencing scheme by the absence of secondary skewed faces (SolidWorks, 2013b).

Automatically constructed initial meshes in SolidWorks vary in level of fineness, i.e. cell sizes. The built-in mesh generating algorithms enable mesh optimisation and obtaining the fine enough mesh for purposes of valves design and simulation without resorting to any further mesh refinement. However, in this study, the manual specification of the meshing parameters has been used based on the eighth level of fineness, Fig. 5. Minimum gap size and minimum wall thickness of the mesh are equal to 1 mm and 0.01 mm respectively. Both parameters influence the characteristic cell's size and computational domain resolution in narrow channels. Flow Simulation generates the mesh in order to have a minimum of two cells per the specified minimum gap size. The wall thickness parameter defines the refinement level of the mesh at the fine geometrical elements such as sharp edges and small protrusions (SolidWorks, 2015).

Applied solution-adaptive refinement process allows splitting the mesh cells in the high-gradient flow regions, which cannot be resolved prior to the calculation, and merging the mesh cells in the low-gradient regions. It serves to minimize the spatial error arising from the discretization of the governing differential equations (SolidWorks, 2013b).

A grid independence study has been conducted for the case of 1 MPa pressure drop between inlet and outlet openings of the valve and the spool angular position equal to 50°. For specified conditions, several meshes have been created differing in a number of fluid cells from 12,000 up to 3,300,000. The average value of the computed flow rate between different meshes is equal to 671.92 LPM with 3.5% fluctuations of extreme values around the mean one. The result of the mesh independence study is shown in Fig. 6. The obtained values ensure the independence and convergence of the found solutions with regard to the mesh resolutions with reasonable accuracy.

Mesh cells are not uniform in sizes across the fluid subdomain but maintain the Cartesian structure with the orthogonal faces. Ar-

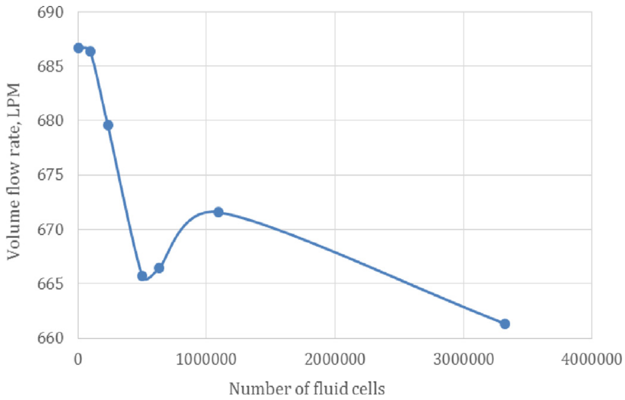

Fig. 6. Grid independence study results.

eas adjacent to the throttling orifices are subjected to further automated solution adaptive refinement with the aim to optimize mesh distribution by increasing the number of fluid cells in areas with high variable changes and flow restrictions.

The meshing algorithm for further hydraulic boundary condition settings in parametric studies was selected with up to 1.5 million fluid cells and three million partial cells on the bordering surfaces of solid matter. Chosen meshing setting guarantees a sensible trade-off between computational time and accuracy for the multitude of simulations described further.

3.3. Boundary conditions

The specification of boundary conditions establishes a hydraulic problem in the Flow Simulation module and applies the desired magnitude of known or pre-set flow parameters for the openings. In this study, a wall roughness and slip conditions were not imposed. It is also considered that there are no leakages through external sealing lids of fluid domain.

The first objective was to gain an understanding of the hydraulic performance of the valve and to predict areas of further geometrical optimisation to reduce hydraulic pressure losses. A feature of interest was its discharge coefficient. Together with orifice area, this coefficient completes the geometrical description of the valve for the Bernoulli equation.

The second problem was to set a criterion for selection of the spool driving mechanism. Here it was desired to evaluate a jet angle of the single orifice as the determinant factor influencing the magnitude of flow torques.

In parametric simulations for both tasks, Dirichlet boundary conditions for steady state fluid flow have been implemented. Namely, boundary conditions for the valve inlet were selected as static pressure of 0.25, 0.5 and 1 MPa; the valve outlet opening is subjected to a static pressure of 0.1 MPa. This set of spatial hydraulic boundary conditions provided varying values of the pressure difference, which dictated the volume flow rate passing through the orifice. For each variation of specified input factors, the angular position of the spool was added as a geometrical parameter varying from 10° to full open state of 90° with a 5° step.

The oil was treated as a compressible fluid, CITGO Hydraulic Oil Grade 32. The temperature field in the fluid subdomain is non-uniform and the temperature rise has been proven to be local in small areas close to throttling edges (Ji et al., 2011). The initial fluid's temperature was taken equal to 313 K that corresponds to normal operational conditions of fluid power systems. For this value of oil temperature, according to manufacturer's datasheet ("Product Information. CITGO A/W Hydraulic oils," 2012), kinematic viscosity is 32.9 cSt and density is 853 kg/m^3. The mentioned manufacturer data also provides information concerning fluid properties changes with regard to temperature variations.

3.4. Goals

The final step in the Flow Simulation module's pre-processing stage of simulations is goals specification, which are physical parameters of interest at points, on surfaces or in the specified volumes. The module initially considers any steady state flow problem as a time-dependent problem. The solver module iterates on an internally determined time step to seek a steady state flow field, so it is necessary to have a criterion for determining that a steady state flow field is obtained in order to stop the calculations. Convergence of the goals is considered as attaining a steady state solution as well as a condition for finishing the calculation (SolidWorks, 2015). For chosen features, convergence studies are conducted automatically for every simulation with automatically set criterion values.

Depending on a nature of the simulation, the goals vary. In the case of the analysis of the metering characteristics of the valve, the volume flow rate of the outlet opening has been selected and measured. The boundary conditions for this set of simulations are pressure differences, the orifices area, and fluid's parameters. The obtained volume flow rate completes the Bernoulli equation for calculation of the discharge coefficient of the valve with regard to the spool angular position.

Using the same set of boundary conditions, but different goals, i.e. torques on metering faces relatively to the spool axis, CFD yields all needed parameters for determining the jet angle of the orifice, both graphically through the field of the velocity vector and analytically through the mathematical formula for steady state torque derived in the following section.

The selected set of boundary conditions and the goals provides a complete description of the functionality for the designed valve structure at any hydraulic operational regime. These parameters set a basis for the further detailed development of the valve and optimisation of its geometry.

4. Theoretical analysis

4.1. The steady-state flow torque

In order to derive the mathematical expressions for estimation of the steady flow torques acting on the spool of the developed valve analytically, the law of conservation of fluid flow momentum is used for control volumes (White, 1999). According to this law and referring to control volumes CV1 and CV2 on the Fig. 7,

$$\vec{F_{fl}} = \dot{m}\left(\vec{v_2} - \vec{v_1}\right), \tag{12}$$

where $\vec{F_{fl}}$ is the vector of the net force acting on the flow stream tube causing a change of fluid flow's direction, $\dot{m}$ is change of mass of fluid in the control volume or the mass flow, $\vec{v_1}$, $\vec{v_2}$ – average flow velocity vectors on the inlet and the outlet section of the control volume respectively. The Eq. (12) refers to either control volumes.

According to Newton's third law, a force with the same magnitude but opposite direction acts on a structure ambient to the fluid flow. Hence, this opposite force acts on the spool, prompting the closure of the valve. The fluid density ρ is taken as a constant and distributed uniformly across the fluid subdomain and the expression for the mass flow is

$$\dot{m} = \rho Q. \tag{13}$$

Radial projections of the flow force $\vec{F_{fl}}$ cancel out each other since in the proposed design there are two orifices, located on op-

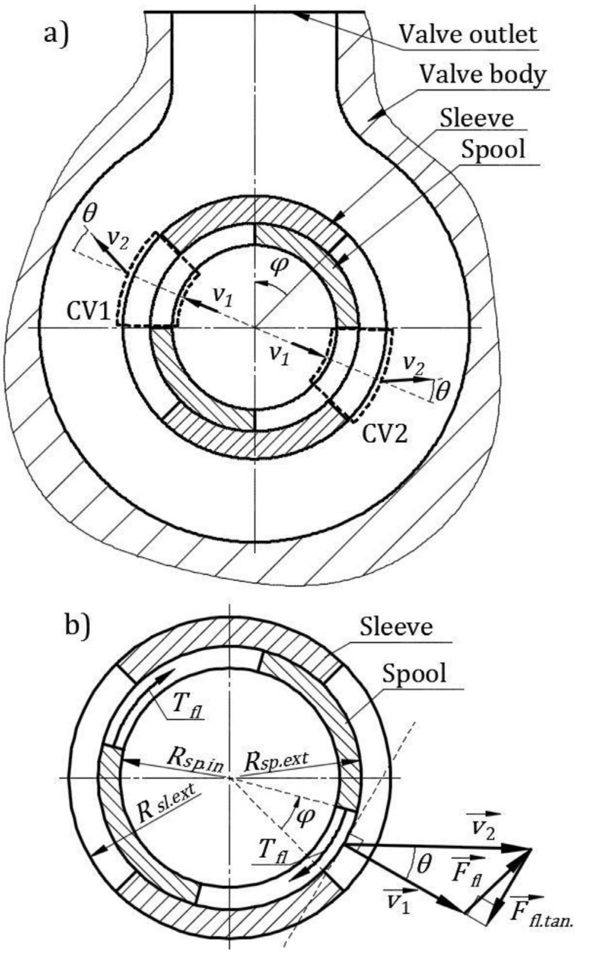

Fig. 7. Outflow scheme: (a) locations of control volumes in the fluid subdomain; (b) detailed outflow scheme.

posite sides of the spool's cylinder. Radial components do not contribute to the formation of steady flow torques as they intersect with the axis of rotation, the spool axis. Thus, the spool does not perceive them and only tangential projections of the flow force produce the flow torques. Hence, flow force acting on the single orifice can be expressed as

$$F_{fl.tan} = \dot{m}v_2 \sin\theta = \rho Q_{single} v_2 \sin\theta \tag{14}$$

where θ is a jet angle or the angle of streamline's deflection due to the obstacle to the flow. In the derived equation, the orifice inlet velocity disappears, because the inlet velocity vector is directed radially. Therefore, it takes no part in the generation of the tangential flow force and the steady flow torque.

It is assumed, that the velocity profile on the spool's inlet face is uniform and total discharge $Q_{total}$of the whole valve is split equally between two orifices, with discharge Q_{single} passing through the single window, i.e.

$$Q_{total} = 2Q_{single}. \tag{15}$$

According to Bernoulli relation, the output, efflux velocity of the orifice is

$$v_2 = C_v\sqrt{\frac{2\Delta p}{\rho}}, \tag{16}$$

where velocity coefficient $C_v = 0.98$, which accounts for pressure losses in the orifice (Lienhard, 1984) and Δp is a pressure difference between inlet and outlet ports of the valve.

Combining equations for the output velocity (16) and the flow force expression (14) multiplied by the spool external radius $R_{sp.ext}$ yields the expression for the steady state flow torque acting on the spool, i.e.

$$T_{fl} = C_v Q_{total}\sqrt{2\Delta p\rho}R_{sp.ext} \sin\theta. \tag{17}$$

This expression takes into account influence of both orifices during the development of the total steady flow torque.

Direct analytical or theoretical estimation of the jet angle on the metering edges poses numerous challenges (Amirante et al., 2006). In valves with complex geometry, jet angles are obtained based on the velocity vector field distribution from CFD simulation. Since the jet angle of the fluid is the function of spool position and does not depend on pressure difference (Lisowski et al., 2015), the arbitrary configuration of boundary conditions during CFD can be used in order to estimate the jet angle versus the spool angular position. It is noteworthy, that the jet angle in the considered rotary spool design highly depends on the location of a sink channel since it defines the direction of the fluid flow from the throttling orifices.

Rearranging equation for the flow torques relative to the jet angle yields analytical expression of the jet angle:

$$\theta = \arcsin\left(\frac{T_{fl}}{C_v Q_{total}\sqrt{2\Delta p\rho}R_{sp.ext}}\right). \tag{18}$$

Given the torque and the hydraulic parameters and the geometry of the throttling elements, the jet angle magnitude for any spool position can be evaluated analytically. Comparison with measured jet angles on velocity vector plots determines validation criterion for the derived expression. The validated jet angle function can be used further as the main descriptor of the valve's orifice.

4.2. The opening area

The Bernoulli's law describes behaviour of the flow parameters during fluid efflux from an orifice

$$Q = C_d A(\varphi)\sqrt{\frac{2\Delta p}{\rho}}. \tag{19}$$

Here the discharge coefficient C_d is a function of the orifice shape and flow parameters (White, 1999). However, it has been shown through CFD simulations that in developed turbulent flows the discharge coefficient becomes independent of the flow conditions (Borghi et al., 1998). Thus, the total orifice area $A(\varphi)$ and the discharge coefficient complete the independent geometrical description of the valve and predict the valve's performance at any operational regime of the hydraulic control system.

Given a flow regime, i.e. flow rate, pressure difference, and the opening area are all set; Eq. (19) can be rearranged to calculate the discharge coefficient C_d.

$$C_d = \frac{Q}{A(\varphi)}\sqrt{\frac{\rho}{2\Delta p}}. \tag{20}$$

The opening area $A(\varphi)$, which is a function of the spool angular position φ, is an undetermined quantity. The remaining values in Eq. (20) are either taken as constant or defined through CFD computations.

Due to the specific shape of the individual profiles of the windows, the total opening area has a nonlinear dependency with regard to the spool angular position. This fact allows implementation of the desired flow rate gain during valve operation.

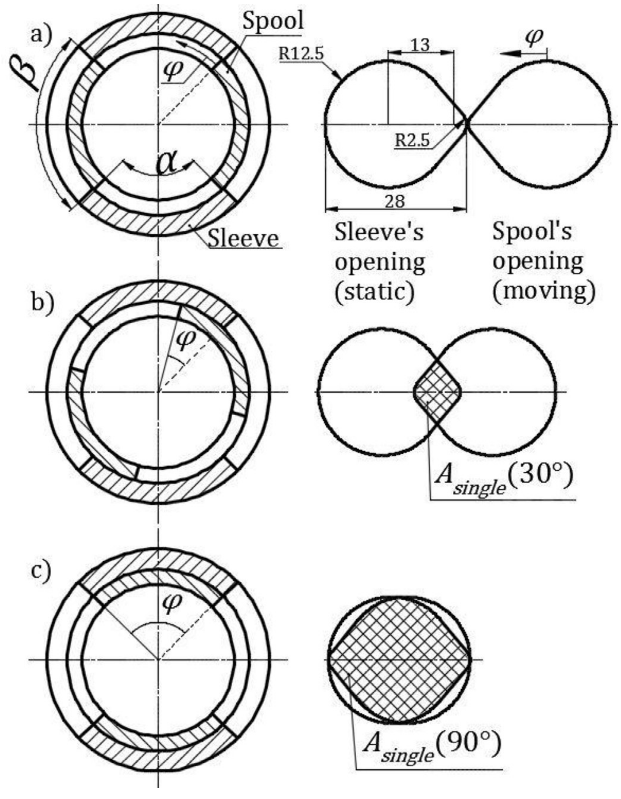

Fig. 8. Openings of the fixed sleeve (left profile) and the moving spool (right profile): (a) the valve is closed, spool's angular position is $\varphi = 0°$; (b) cross-hatched region – single orifice's opening area at spool's position $\varphi = 30°$; (c) the valve is fully open at spool's angular position $\varphi = \varphi_{max} = 90°$.

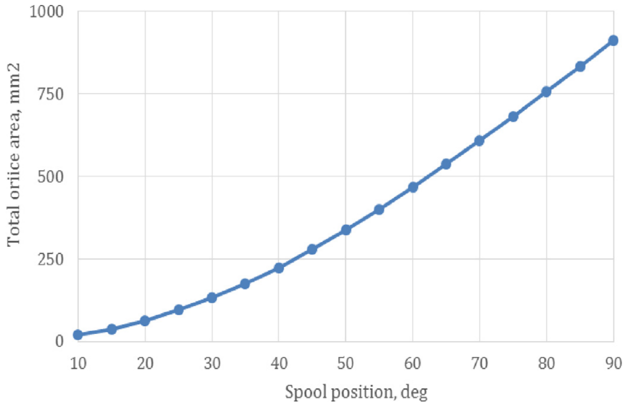

Fig. 9. The opening area of the valve.

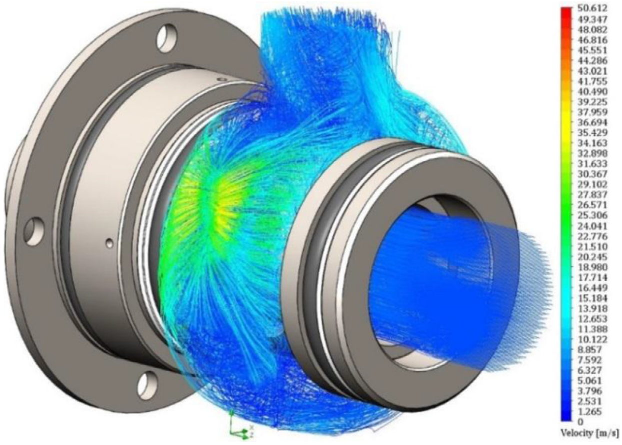

Fig. 10. Flow streamlines inside the valve at the spool position of 25° and pressure difference of 1 MPa.

Easy access to the external cylindrical surfaces of the sleeve and the spool at the production stage enables cutting windows of almost any shape. This opens opportunities to implement virtually any regulation curves of the flow rate.

In this study opening profiles have been chosen identical geometrically. Sizes of the sleeve opening are introduced in Fig. 8. Since these profiles are projected on cylinders of different diameters, exact dimensions vary depending on a value of the radial clearance between the spool and the sleeve. Referring to Fig. 7, internal and external radii of the spool and the sleeve are $R_{sp.in} =$ 15 mm, $R_{sp.ext} = 18$ mm and $R_{sl.ext} = 22$ mm respectively. However, the valve dimensions are scalable leading to a variety of output flow values' ranges. The only principal prerequisite is superiority of a stepper motor holding torque over a net drag torque.

Selected profiles produce negative overlap at the spool's initial position, at $\varphi = 0°$, Fig. 8a. This creates a disparity between angles occupied by windows on the cylinders of the spool $\alpha =$ 89.14° and the sleeve $\beta = 88.88°$ measured along their circumferences in symmetry planes of the profiles. According to these values of window angles of the parts, the overlap angle or backlash angle is

$$\gamma = \frac{\alpha - \beta}{2} = \frac{89.14° - 88.88°}{2} = 0.13°. \quad (21)$$

In order to determine the relation between the single orifice area and rotational angle of the spool, swept or unrolled profiles of the windows have been used in a planar study, Fig. 8. Overlaying spool and sleeve profiles and replacing angular displacement with linear displacement, the intersection area can be assessed, which is equal to the single orifice opening. Doubling intersection area of the single orifice yields the total opening of the valve depending on the spool position, Fig. 9.

It can be seen from the graph of Fig. 9, that the rate of increase in the opening area of the valve is gradual, but not even. The smooth increase of the opening, up to 40° of spool position, results in a much smoother change of actuator cylinder's speed. This slow nonlinear change in the area at the start of actuation is a special design feature of this novel valve. The dependency, beyond 40° angular position of the spool, is steeper and much closer to a linear rate of opening. The maximum opening area is 912.7 mm^2 at the spool position $\varphi = 90°$, which is the fully open valve state.

The developed relation offers finer regulation and better controllability of the hydraulic actuator at the low-speed regime and at the start of motion of a cylinder rod. Realisation of this shape of the opening area gain is attained by use of smooth profiles of throttling windows with small radii, where intersection begins between profiles. Smooth and continuous increase of the orifice area prevents peaks, which can lead to a hydraulic hammer effect and shocks in hydraulic cylinder motion.

5. Results and discussion

The results of the CFD study provide information regarding the distribution of the flow paths, Fig. 10, velocity field, Fig. 11, and velocity vector field inside the valve structure. Although the outflow is three dimensional, the plots of velocity features have been built in the middle plane of the throttling windows, which form the ori-

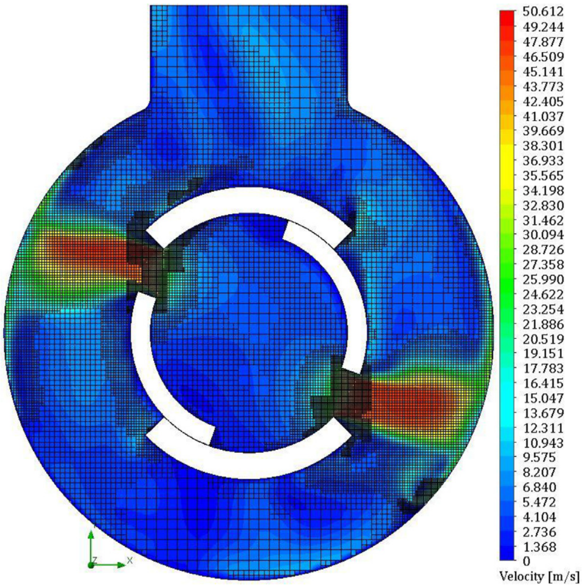

Fig. 11. Velocity field and the mesh distribution in the middle plane of the throttling windows. Spool position is 25° and pressure difference is 1 MPa. The number of fluid cells is approximately two million.

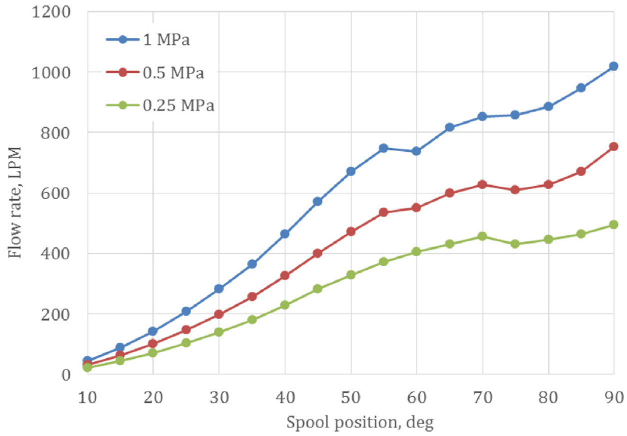

Fig. 12. Volume flow rate through the valve.

fices. This choice for the middle plane for analysis is vindicated as this domain gives a better visualisation of the flow pattern at the orifice.

According to the depicted efflux model, the fluid flows radially to the throttling area inside the spool's inner cavity. This justifies the assumption taken in the theoretical analysis of the flow torques. Two jets are being formed with maximum fluid velocity inside the jets reaching values of 50 m/s depending on the opening area and volume flow rate passing the orifices. These jets then hit the housing walls. At that point, the jet flow splits. Streamlines stick to the casing surface due to Coanda effect (Trancossi, 2011). This effect coupled with the collision of the jets with the walls, at almost right angles, results in a split of the jets.

In the plane of throttling, one portion of the flow from the single jet is guided to the valve's outlet. The other part of the jet is routed downward, to the area opposite to the sink channel. Due to the jet's separation, there are multiple areas of the fluid subdomain, which are highly prone to the constitution of significant fluid circulations and subsequently highly turbulent regions.

These are the bottom region opposed to the sink channel, the domains of merging fluid streamlines close to the sink channel and sleeve orifices, where flow separations take place. These regions account for flow energy losses due to viscous friction in multiple swirls formed there. Fluctuating local fluid particle velocities in the swirls reach 120% of time averaged velocity, what is reflected on the graph of the turbulence intensity or the level of the turbulence (Munson et al., 2012), Fig. 17a. Computed turbulent time or the period of the velocity fluctuations (the ratio of the turbulent kinetic energy k to its dissipation rate ε) and the turbulent length in the specified areas equal to values up to 0.003 s and 2.5 mm respectively, Fig. 17.

It is also noted based on the CFD visualization that areas adjoining to the sleeve metering edges close to the sink channel as well as transition domain between the metering chamber and the sink channel are prone to flow separation especially at high values of the opening area as the volume flow rate increases. The mentioned regions represent areas for further geometrical optimization to improve fluid flow trajectories by introduction of smooth fillets.

Due to vorticity in the inner cavity of the spool, there is a deviation from the assumption of equality of the volume flow rates passing through the orifices. Another contributing factor to this is linked with the asymmetric disposition of the orifices with regard to the sink channel on the small angular displacement of the spool. Partition of the discharge is not constant during the course of the spool opening. Up to 50° of opening, the left orifice's area contains a larger domain of high fluid velocity compared to the right orifice since the left orifice is located closer to the sink channel and constitutes lower resistance to the flow. However, inequality of the flows passing through two orifices does not affect the derivation of the analytical expression of the steady flow torques. Furthermore, at the fully open state the location of the valve's orifices becomes symmetric relative to the axis of the sink channel as well as the flow model.

During the CFD simulation studies of the valve, the spool angular position is considered as the main parameter ranging from 0° to 90° with an increment of 5°. The pressure drop across the orifice had definite values of 0.25 MPa, 0.5 MPa, and 1 MPa. The volume flow rate as a function of the spool position has been found for specified pressure drops. Interpolation plots for discrete data points of calculated flow rates can be found in Fig. 12. The discharge increases as the opening area grows. From 25° and up to 60° of valve's opening, volume flow rate exhibits an almost linear rise. Domains close to extreme spool positions have smoother flow rate gain. This benefits controllability of a hydraulic motor at small and maximum speed regimes.

Derived flow rate characteristics of the valve allow calculation of the discharge coefficient of the orifice for any given spool angular position, Fig. 13. For any pressure drop across the valve, computed discharge-coefficient curves coincide and decrease as the valve opens. The maximum value of the coefficient is 0.81 at 10° opening, the minimal value is 0.37 at the valve's open state. With the predetermined orifice area and the discharge coefficient relation, hydraulic behaviour of the valve can be predicted for any operational regime of the hydraulic system.

In order to estimate pressure drop imposed by the valve to the hydraulic circuit it is installed in, another set of simulations has been conducted. In this case, the flow rate passing through the valve and the outlet pressure of 0.1 MPa have been selected as the boundary conditions. Volume flow rate here alters from 100 LPM to 500 LPM with a step of 100 LPM. The measured goal is the magnitude of inlet pressure. The resultant pressure drop curves for indicated discharges decline nonlinearly, with the relation close to exponential, and do not exceed 0.5 MPa at the fully open state of the valve, Fig. 14.

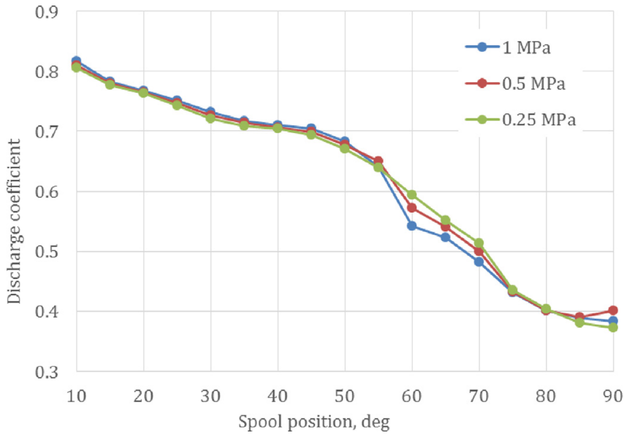

Fig. 13. Discharge coefficient of the valve.

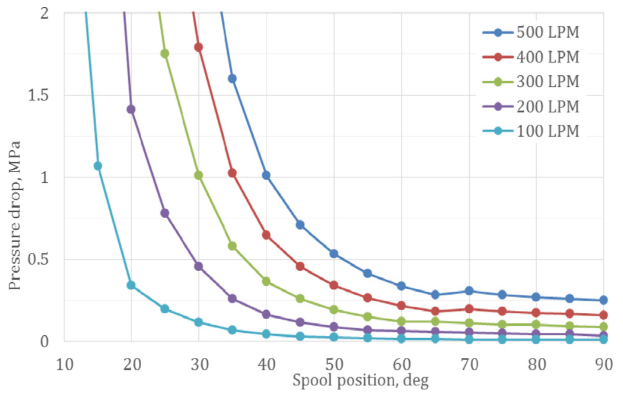

Fig. 14. Pressure drop created by the valve as a function of the spool position and volume flow rate.

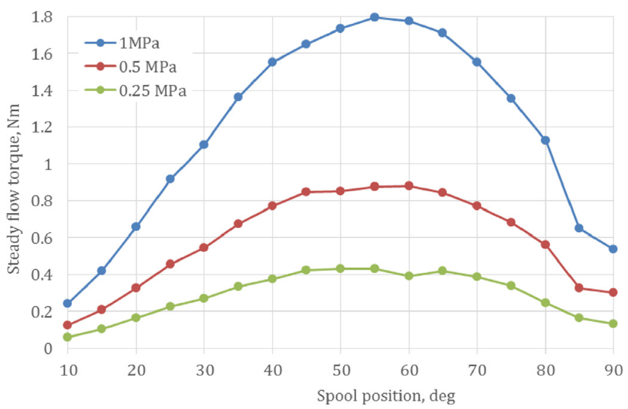

Fig. 15. Steady flow torque as a function of the spool position and the given pressure drops across the valve.

The calculations of steady flow torques have been performed for the same range of pressure drops and spool positions as for computations of the volume flow rate. The only difference is the set of goals. In this case, the metering faces of the spool have been selected on both orifices and the obtained data is plotted, Fig. 15. These faces are features of interest because at steady state flow the rest of the spool surfaces are cylindrical and do not contribute to the steady torque formation. Measurement of the torques was performed relative to the axis of the spool.

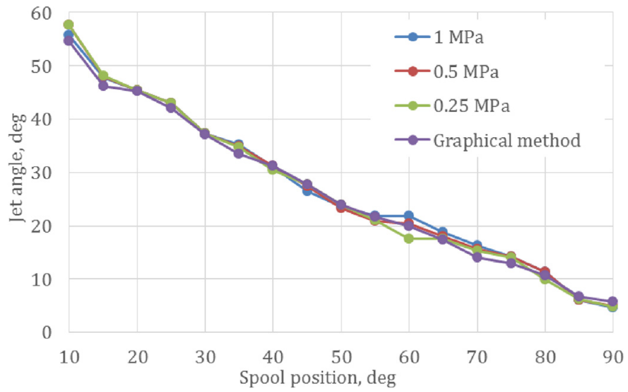

Fig. 16. Jet angle as a function of the spool position and the given pressure drops across the valve.

As the flow passes the throttling edges, two torques act on the spool in opposite directions: opening and closing the valve. The difference between them accounts for the total steady flow torque perceived by the spool driver. Results show that the closing torque prevails over the opening torque. This fact takes place since the metering faces adjacent to high-velocity jets are subjected to a lower pressure than the metering surfaces outside the throttling region.

The steady flow torque has a dependency close to parabolic to the spool position. The maximum value of the flow torque is noted when the spool is positioned in the middle of the opening range, that is 50°. This domain of spool positions distinguishes itself due to the influence of both volume flow rate and deflection of the flow reaching its maximum. The largest steady flow torque for the 1 MPa pressure difference across the valve does not exceed 1.8 Nm.

Similar parabolic dependency of the steady flow torque on the spool angular position and discharge coefficient function were reported for rotary valve directional valve (Wang et al., 2016). The parabolic torque function distinguished the rotary type of spools from other valve classes as these entire valves tend to be overcompensated.

Based on the obtained values of flow torques it is possible to calculate the jet angle of the flow for any given spool position, according to the Eq. (18). Given that the direction of diverted streamlines does not depend on flow characteristics as flow rates and pressure drops, calculated jet angle curves overlap for different pressure drops across the valve, Fig. 16. The jet angle curves vary continuously from 57° at 10° of the spool opening to 4° at the fully open state of the valve. Independently to pre-set pressure drops, jet angle curves descend on the whole range of the spool angular position. The described relation of jet angles to spool positions applies for the chosen arrangement of the throttling elements, windows' profiles, and housing geometry. The main housing geometrical parameters affecting jet angle magnitudes are cross-section shape of the collecting channels and the location of the sink port. The influence of the pressure drop value on the discharge coefficient Fig. 13 as well as on the jet angle Fig. 16 is negligible, which was reported in a similar study of a directional control valve by a direct numerical simulation (Posa et al., 2013).

With the use of a CFD study of flow torques, an alternative graphical method has been employed to find the jet angles, Fig. 18. The method was used in a number of studies considering jet angles evaluation in flow control valves in order to determine flow forces acting on the valve's regulating elements (Lisowski and Filo, 2016; Lisowski et al., 2015; Amirante et al., 2007; Wang et al., 2016). Distribution of the velocity vectors of the flow has been extracted from the series of spool positions. For each plot of the vector field,

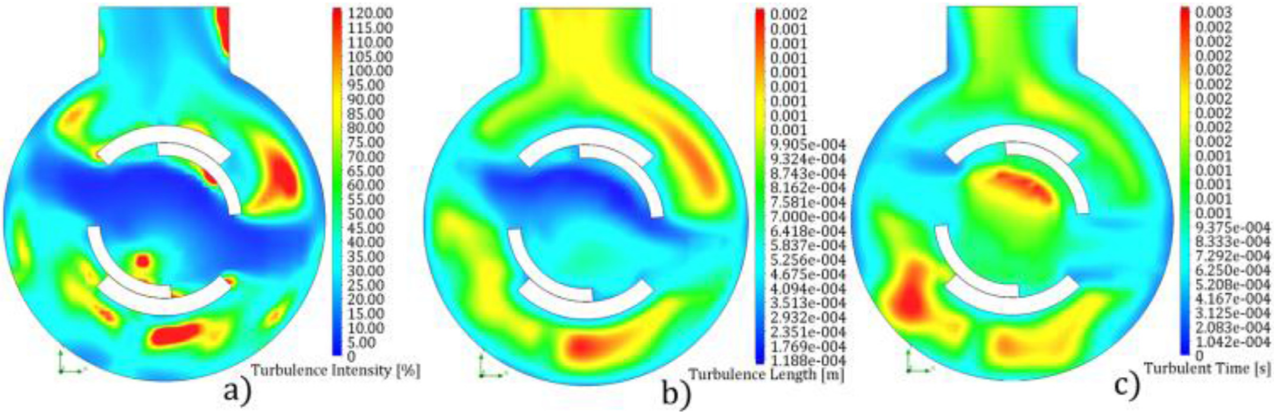

Fig. 17. Turbulence parameters of the flow inside the valve: a) turbulence intensity; b) turbulence length; c) turbulence time.

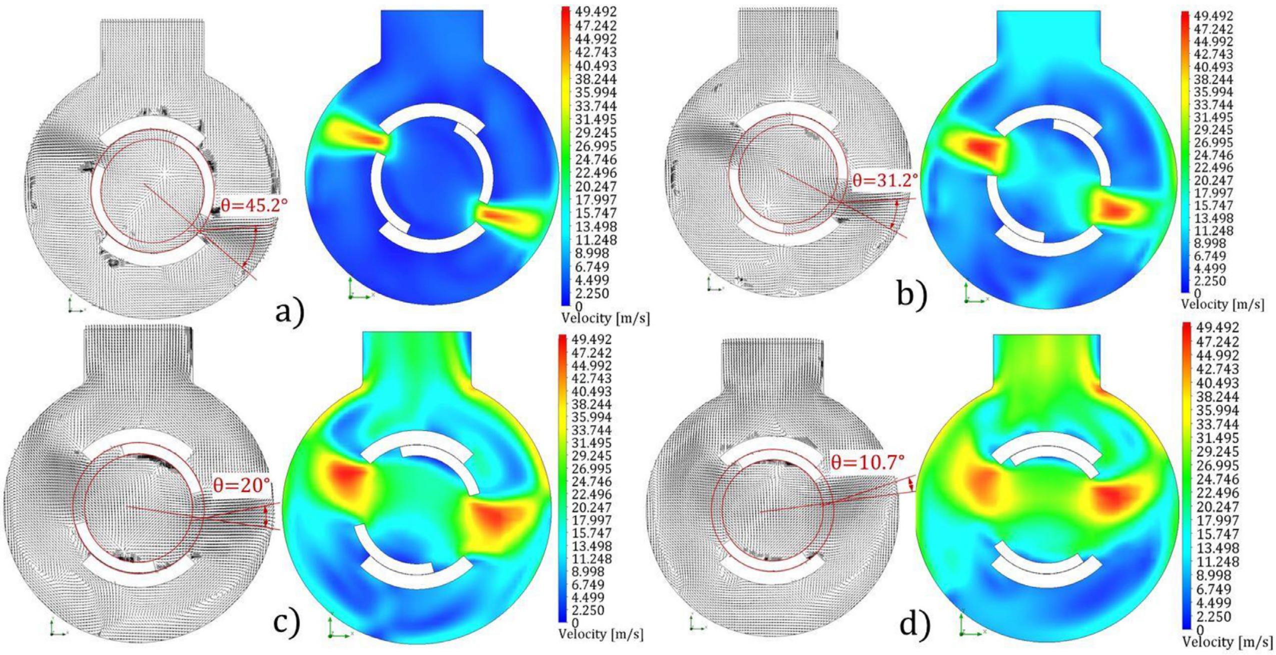

Fig. 18. Velocity vectors and velocity distribution fields for different spool positions: a) 20°, b) 40°, c) 60°, d) 80°. Measurement of the jet angle graphically.

the deflection angle of the flow has been quantified. Radial direction of the fluid flow at the orifice plane is considered as the orientation of inlet velocity for the control volumes. Then the orifice outlet velocity direction was drawn coinciding with velocity vectors at the outlet of the orifice. Thus, the angle between the radial and the drawn line represents the sought orifice jet angle. Points of external sleeve circumference are taken as measurement points for directions of the outlet velocity as they are far from the flow regions directly influenced by the housing walls as well as the orifice area itself. Hence, the effect of the near-wall region of the casing is excluded.

As the opening of the valve progresses further from 75°, the substitution of metering edges takes place. Before the spool position of 75°, each orifice is created by both spool and sleeve metering edges. After this point, the sleeve edges are concealed by the spool edges and do not contribute to the formation of the orifice and throttling. This fact affects the choice of the orifice plane at a graphical estimation of the jet angles. The graphical method imposes an accuracy challenge during the evaluation of the jet angle. Namely, it appears in the selection of the measurement points and setting the density of the depicted velocity vectors. Nonetheless, there is no significant deviation between values obtained graphically and during CFD computations of the steady flow torques and jet angles.

6. Conclusions

The flow modelling study conducted confirms the appropriateness of the structural approach to expanding the application of the directly controlled valves to the high flow rate operational domains. In particular, the proposed rotary arrangement of the throttling edges coupled with the hollow spool structure allows using less power demanding spool control without compromising the valve's hydraulic performance.

Derived graphs of opening area, discharge coefficient, and jet angle constitute the complete definition of the functionality of the proposed valve design in the steady flow regimes. The CFD simulations verified the obtained theoretical model of the valve. Utilisation of this tool gave an understanding of the flow pattern in the fluid subdomain of the valve by visualisation of the flow paths.

Simulation based analysis shows small pressure losses in the suggested valve design along with low steady flow torques. The nonlinear opening area promises to improve controllability in actuator speed control. The developed valve design presents the feasible and sound structure of control valves for high flow rate power hydraulic systems. Its construction ensures improved controllability and maintainability due to the utilisation of a stepper motor and cartridge assembly. Furthermore, grouping four proposed valves in the independent metering arrangement also opens the opportunity to advance the efficiency of the fluid power systems by the implementation of energy regeneration and recuperation in the regulation of hydraulic motors. All in all noted factors prove the effectiveness of the proposed approach for designing of unconventional throttling orifices in flow control valves of high flow rate fluid power systems.

However, the presented geometrical model of the throttling parts can be further optimised in identified areas with the aim to achieve even smaller pressure drop values and consequently smaller flow torques on the spool. During selection of the spool driving rotary motor, it is recommended to evaluate dynamic properties of the valve assembly, conduct a more detailed study of transient flow regimes, and estimate effects of viscous and mechanical friction torques on the spool during position change. The operation of multiple rotary two-way valves in one arrangement is also of interest. Estimation of dynamics and efficiency of such modules develops further the independent metering approach in construction of hydraulic control systems.

References

Abdalla, M.O., Nagarajan, T., Hashim, F., 2011. Numerical investigation of pressure drop in hydraulic spool valve. Solid State Sci. Technol. 19, 48–60.

Amirante, R., Andrea Catalano, L., Tamburrano, P., 2014. The importance of a full 3D fluid dynamic analysis to evaluate the flow forces in a hydraulic directional proportional valve. Eng. Comput. 31, 898–922. doi:10.1108/EC-09-2012-0221.

Amirante, R., Del Vescovo, G., Lippolis, a., 2006. Flow forces analysis of an open center hydraulic directional control valve sliding spool. Energy Convers. Manage. 47, 114–131. doi:10.1016/j.enconman.2005.03.010.

Amirante, R., Distaso, E., Tamburrano, P., 2016. Sliding spool design for reducing the actuation forces in direct operated proportional directional valves: experimental validation. Energy Convers. Manage. 119, 399–410. doi:10.1016/j.enconman.2016.04.068.

Amirante, R., Moscatelli, P.G., Catalano, L.a., 2007. Evaluation of the flow forces on a direct (single stage) proportional valve by means of a computational fluid dynamic analysis. Energy Convers. Manage. 48, 942–953. doi:10.1016/j.enconman.2006.08.024.

Ansaloni, G., Marani, P., Paoluzzi, R., 2008. Proportional valve with axial flow and rotational metering. In: Proceedings of the 7th JFPS International Symposium on Fluid Power. Toyama, pp. 591–596. doi:10.5739/isfp.2008.591.

Borghi, M., Cantore, G., Milani, M., Paoluzzi, R., 1998. Analysis of hydraulic components using computational fluid dynamics models. Proc. Inst. Mech. Eng. 212, 619–629. doi:10.1243/0954406981521583.

Choi, K., Seo, J., Nam, Y., Kim, K.U., 2015. Energy-saving in excavators with application of independent metering valve. J. Mech. Sci. Technol. 29, 387–395. doi:10.1007/s12206-014-1245-5.

Van Driest, E.R., 1956. On turbulent flow near a wall. J. Aeronaut. Sci. (Institute Aeronaut. Sci. doi:10.2514/8.3713).

Filho, J., De Negri, V., 2013. Model-based fault detection for hydraulic servoproportional valves. In: The 13th Scandinavian International Conference on Fluid Power, SICFP2013. Linköping, Sweden, pp. 389–398.

Herakovič, N., 2009. Flow-force analysis in a hydraulic sliding-spool valve. Strojarstvo 51, 555–564.

Ji, H., Cao, Y., Wang, Z., Wang, Y., 2011. Numerical analysis of temperature rise by throttling and deformation in spool valve. In: Proc. 2011 Int. Conf. Fluid Power Mechatronics, 2011. FPM, pp. 752–756. doi:10.1109/FPM.2011.6045861.

Johnston, N., Pan, M., 2015. Theoretical studies of a switched inertance hydraulic system in a four-port valve configuration. The Seventh Workshop on Digital Fluid Power.

Lam, C.K.G., Bremhorst, K., 1981. A modified form of the k-ε model for predicting wall turbulence. J. Fluids Eng. 103, 456. doi:10.1115/1.3240815.

Launder, B.E., Spalding, D.B., 1974. The numerical computation of turbulent flows. Comput. Methods Appl. Mech. Eng. 3, 269–289. doi:10.1016/0045-7825(74)90029-2.

Lienhard, J.H., 1984. Velocity coefficients for free jets from sharp-edged orifices. J. Fluids Eng. 106, 13. doi:10.1115/1.3242391.

Linjama, M., 2011. Digital fluid power – state of the art. In: The 12th Scandinavian International Conference on Fluid Power. Tampere, Finland, pp. 331–354.

Lisowski, E., Czyzycki, W., Rajda, J., 2013. Three dimensional CFD analysis and experimental test of flow force acting on the spool of solenoid operated directional control valve. Energy Convers. Manage. 70, 220–229. doi:10.1016/j.enconman.2013.02.016.

Lisowski, E., Filo, G., 2016. CFD analysis of the characteristics of a proportional flow control valve with an innovative opening shape. Energy Convers. Manage. 123, 15–28. doi:10.1016/j.enconman.2016.06.025.

Lisowski, E., Filo, G., Rajda, J., 2015. Pressure compensation using flow forces in a multi-section proportional directional control valve. Energy Convers. Manage. 103, 1052–1064. doi:10.1016/j.enconman.2015.07.038.

Lisowski, E., Rajda, J., 2013. CFD analysis of pressure loss during flow by hydraulic directional control valve constructed from logic valves. Energy Convers. Manage. 65, 285–291. doi:10.1016/j.enconman.2012.08.015.

Merritt, H.E., 1968. Hydraulic Control Systems. John Wiley & Sons, Inc., New York doi:10.1115/1.3601167.

Munson, B., Young, D., Okiishi, T., Huebesch, W., 2012. Fundamentals of Fluid Mechanics, seventh ed. John Wiley & Sons, Inc., NJ.

Palumbo, A., Paoluzzi, R., Borghi, M., Milani, M., 1996. Forces on a hydraulic valve spool. In: Proc. JFPS Int. Symp. Fluid Power. doi:10.5739/isfp.1996.543.

Pan, M., Johnston, N., Plummer, A., Kudzma, S., Hillis, A., 2013. Theoretical and experimental studies of a switched inertance hydraulic system. Proc. Inst. Mech. Eng. Part I J. Syst. Control Eng. 228, 12–25. doi:10.1177/0959651813500952.

Pan, M., Johnston, N., Robertson, J., Plummer, A., Hillis, A., Yang, H., 2015. Experimental investigation of a switched inertance hydraulic system with a high-speed rotary valve. J. Dyn. Syst. Meas. Control 137, 121003. doi:10.1115/1.4031325.

Plummer, A., 2016. Electrohydraulic servovalves – past, present, and future. 10th International Fluid Power Conference, IFK2016.

Posa, A., Oresta, P., Lippolis, A., 2013. Analysis of a directional hydraulic valve by a direct numerical simulation using an immersed-boundary method. Energy Convers. Manage. 65, 497–506. doi:10.1016/j.enconman.2012.07.012.

Product Information. CITGO A/W Hydraulic oils, 2012.

Rajda, J., Lisowski, E., 2013. Flow forces acting on the spool of directional control valve. Czas. Tech. Mech. Tech. Trans. Mech. 349–356.

Rannow, M.B., Tu, H.C., Wang, M., Li, P.Y., Chase, T.R., 2010. Optimal design of a high--speed on/off valve for a hydraulic hybrid vehicle application. In: Proceedings of the 7th International Fluid Power Conference. Aachen, Germany, pp. 1–14.

Reichert, M., 2010. Development of High-Response Piezo-Servovalves For Improved Performance of Electrohydraulic Cylinder Drives. Aachen University, Aachen, Germany.

Shenouda, A., 2006. Quasi-Static Hydraulic Control Systems and Energy Savings Potential Using Independent Metering Four-Valve Assembly Configuration Dr. Philos. Thesis. Woodruff School of Mechanical Engineering, Georgia Institute of Technology.

Simic, M., Herakovic, N., 2015. Reduction of the flow forces in a small hydraulic seat valve as alternative approach to improve the valve characteristics. Energy Convers. Manage. 89, 708–718. doi:10.1016/j.enconman.2014.10.037.

Sobachkin, A., Dumnov, G., 2013. In: Numerical Basis of CAD-Embedded CFD, 2013. NAFEMS World Congr., pp. 1–20.

SolidWorks, 2015. SolidWorks Flow Simulation.

SolidWorks, 2013a. Enhanced Turbulence Modeling in SolidWorks Flow Simulation.

SolidWorks, 2013b. Advanced Boundary Cartesian Meshing Technology in SolidWorks Flow Simulation.

Trancossi, M., 2011. An overview of scientific and technical literature on coanda effect applied to nozzles. SAE Tech. Pap. 1–13. doi:10.4271/2011-01-2591.

Tu, H.C., Rannow, M.B., Van de Ven, J.D., Wang, M., Li, P.Y., Chase, T.R., 2007. High speed rotary pulse width modulated on/off valve. In: Proceedings of the International Mechanical Engineering Congress. Seattle, Washington, pp. 1–13. doi:10.1115/IMECE2007-42559.

Tu, H.C., Rannow, M.B., Wang, M., Li, P.Y., Chase, T.R., Cheong, K.L., 2011. High-speed 4-way rotary on/off valve for virtually variable displacement pump/motor applications. In: ASME 2011 Dyn. Syst. Control Conf. Bath/ASME Symp. Fluid Power Motion Control, 1, pp. 201–208. doi:10.1115/DSCC2011-6109.

Tu, H.C., Rannow, M.B., Wang, M., Li, P.Y., Chase, T.R., Van de Ven, J.D., 2012. Design, modeling, and validation of a high-speed rotary pulse-width-modulation on/off hydraulic valve. J. Dyn. Syst. Meas. Control 134, 61002. doi:10.1115/1.4006621.

Wang, H., Gong, G., Zhou, H., Wang, W., 2016. Steady flow torques in a servo motor operated rotary directional control valve. Energy Convers. Manage. 112, 1–10. doi:10.1016/j.enconman.2015.11.054.

Wang, M., Li, P.Y., 2009. Duty ratio control of a rotary PWM valve with periodic measurement error. Proc. Am. Control Conf. 5073–5078. doi:10.1109/ACC.2009.5160693.

Wang, M., Tu, H., Rannow, M., Li, P., Chase, T., 2010. CFD analysis of a novel high speed rotary on/off valve. In: Proc. 6th FPNI-PhD Symp., pp. 283–294.

White, F., 1999. Fluid Mechanics, fourth ed. McGraw-Hill series in mechanical engineering.

Wilcox, D.C., 2006. Turbulence Modeling for CFD, third ed. DCW Industries, Inc.

Yang, H., Pan, M., 2015. Engineering research in fluid power: a review. J. Zhejiang Univ. - Sci. A Appl. Phys. Eng. 16, 427–442. doi:10.1631/jzus.A1500042.

Yang, Y., Guglielmino, E., Dai, J.S., Boaventura, T., Caldwell, D.G., 2010. Modeling of a novel 3-way rotary type electrohydraulic valve. In: 2010 IEEE International Conference on Information and Automation, ICIA 2010. Harbin, China, pp. 1463–1468. doi:10.1109/ICINFA.2010.5512286.

Yu, J., Zhuang, J., Yu, D., 2015. State feedback integral control for a rotary direct drive servo valve using a Lyapunov function approach. ISA Trans. 54, 207–217. doi:10.1016/j.isatra.2014.08.006.

Yu, J., Zhuang, J., Yu, D., 2014. Modeling and analysis of a rotary direct drive servovalve. Chin. J. Mech. Eng. 27, 1064–1074. doi:10.3901/CJME.2014.0725.127.